

Université Lille 1 Sciences et Technologies

THÈSE

pour obtenir le grade de :

Docteur de l'Université de Lille 1

Spécialité:

**Sciences de la Matière, du Rayonnement
et de l'Environnement**

Soutenue le 16 décembre 2013 par

Yana KAROL

Titre :

**Determination of optical and microphysical
properties of atmospheric aerosols from
multi-wavelength airborne sun photometer**

Jury :

Aliaksandr SINYUK	<i>Rapporteur</i>
Victoria E. CACHORRO REVILLA	<i>Rapporteur</i>
Jean-Claude ROGER	<i>Examineur</i>
Hervé DELBARRE	<i>Examineur</i>
Didier TANRE	<i>Directeur de thèse</i>
Anatoly CHAIKOVSKY	<i>Directeur de thèse</i>
Philippe GOLOUB	<i>Co-directeur de thèse</i>

Laboratoire d'Optique Atmosphérique

U.F.R de Physique Fondamentale

Université Lille 1 Sciences et Technologies

59655 Villeneuve d'Ascq, France

Laboratory of Optics of Scattering Media

B.I. Stepanov Institute of Physics, National Academy of Sciences of Belarus

220072 Minsk, Belarus

The earth has music for those who listen.

George Santayana

Acknowledgements

This work was possible through everyday help of many people.

First of all, I would like to express my gratitude to my supervisor Didier Tanré for his guidance of my thesis and support in my personal problems. I thank my belarusian supervisor Anatoly Chaikovsky, through whom I had the opportunity to work in LOA as well as for his advices. Of course, my work would not be possible without fellowship provided by CNRS and CNES.

I am grateful to Philippe Goloub for his great organizational skills which made possible our field experiments with PLASMA.

I thank Oleg Dubovik, an outstanding scientist and my countryman, for his invaluable assistance in my work with his inversion code.

I especially thank Christian Vervaerde, talent engineer, who created PLASMA and an experienced pilot, with whom we spent many hours in the sky.

I am grateful to engineers Luc Blarel and Thierry Podvin for their continued technical support of the instrument and for their attention to all of my numerous requests.

I will never forget the assistance of Tatiana Lapionak and Yevgeni Derimian in the development of the inversion code, as well as essential advices of Anton Fedarenka and Anton Lapatsin.

I thank Augustin Mortier for providing lidar data and handling of PLASMA during DRAGON campaign and also Benjamin Torres for his work with the PLASMA in my absence and for his assistance in analyzing the data.

I thank Isabelle Jankoviak for her hearty participation and assistance in my first steps in the laboratory and in general in France.

And finally, thanks to all laboratory staff for their hospitality and friendliness that I was surrounded by all the 3 years in LOA.

Abstract

Atmospheric aerosols still represents one of the greatest uncertainty in the study of the processes of climate change. The diversity of aerosol sources and their formation mechanisms make the spatial distribution of aerosols very inhomogenous and requires numerous instruments and different approaches for their analysis.

A new multi-wavelength airborne sun photometer PLASMA (Photomètre Léger Aéroporté pour la Surveillance des Masses d'Air) developed in the Laboratory of Atmospheric Optics, Lille University of Sciences and Technologies allows providing on-board measurements of aerosol optical depth over a wide ($0.34 - 2.25 \mu m$) spectral range and at different altitudes (Karol et al., 2013). The information of vertical distribution of aerosol optical properties can be then used to validate the lidar processing algorithms. Moreover, it is possible to retrieve from PLASMA measurements the size distribution of the aerosol particles at different levels. Also, the instrument can be installed on an automobile in order to measure the horizontal profiles of AOT.

This study is dedicated to characterization and calibration of PLASMA and to the analysis of several data sets. Numerous ground-based (Lille, Izaña, Beijing, Washington, Dakar, Cagliari), airborne (Lille, Dakar) and automobile (Izaña, Washington) measurements were held and compared with other instruments (sun photometers, lidars).

Sensitivity study of the Dubovik's inversion algorithm (Dubovik and King, 2000; Holben et al., 1998) showed that it is possible to get the particle's size distribution from only AOD measurements in the range of $0.34 - 1.64 \mu m$ (in some cases $0.34 - 1.02 \mu m$) assuming a value of the refractive index within a limited domain. Airborne PLASMA measurements were inverted and size distributions of the aerosol particles were obtained at different altitudes. This new information is helpful to better understand the formation and spatial distribution of aerosols in the atmosphere.

Résumé

Les aérosols atmosphériques constituent l'une des plus grandes incertitudes dans l'étude des processus de changement climatique. La diversité des sources d'aérosols et de leurs mécanismes de formation rendent la distribution spatiale des aérosols très inhomogène ce qui nécessite la mise en place d'une instrumentation et de méthodes d'observation sophistiquées.

Un nouveau photomètre solaire aéroporté avec 15 longueur d'onde PLASMA (Photomètre Léger Aéroporté pour la Surveillance des Masses d'Air) développé au Laboratoire d'Optique Atmosphérique, permet d'effectuer des mesures d'épaisseur optique des aérosols sur une large gamme spectrale ($0.34-2.25 \mu m$) et à différentes altitudes (Karol et al., 2013). La détermination de la distribution verticale des propriétés optiques des aérosols peut ainsi être utilisée pour valider les algorithmes d'inversion des mesures lidar. En outre, il est possible de remonter à la distribution de taille des particules d'aérosol à différents niveaux. En outre, l'instrument peut être installé sur un véhicule afin de mesurer les profils horizontaux du contenu et de la granulométrie des aérosols.

Cette étude est consacrée à la caractérisation et à l'étalonnage de l'instrument et à l'analyse de plusieurs jeux de données. De nombreuses mesures au sol (Lille, Izaña, Pékin, Washington, Dakar, Cagliari), aéroportées (Lille, Dakar) et depuis un véhicule (Izaña, Washington) ont réalisées et sont comparées aux mesures d'autres instruments (photomètres solaires, lidars).

L'étude de la sensibilité de l'algorithme d'inversion de Oleg Dubovik (Dubovik and King, 2000; Holben et al., 1998) a montré qu'il est possible d'obtenir la distribution en tailles des particules sur une gamme de rayons à partir de mesures d'épaisseur optique sur le domaine spectral de $0.34 - 1.64 \mu m$ (dans certains cas de $0.34 - 1.02 \mu m$) quand l'indice de réfraction est connu avec une certaine précision. Les

mesures aéroportées ont ainsi été inversées et les distributions de tailles obtenues pour différentes altitudes. Cette information permettra de mieux comprendre les processus de formation et la répartition spatiale des aérosols dans l'atmosphère.

Contents

1	Introduction	15
1.1	Scientific interest	15
1.2	Thesis context	18
2	Aerosol properties and impact	21
2.1	Physical properties of aerosols	21
2.1.1	Aerosol origin	21
2.1.2	Chemical composition	23
2.1.3	Size distribution	25
2.1.4	Refractive index	28
2.1.5	Vertical distribution	29
2.2	Optical properties of aerosols	30
2.2.1	Aerosol optical depth and extinction coefficient	31
2.2.2	Angstrom parameter	32
2.2.3	Single-scattering albedo	33
2.2.4	Phase function	35
2.3	Aerosol impact	36
2.3.1	Radiative impact	36
2.3.2	Impact to the environment and peoples' health	37
2.4	Instruments and methods	39
2.4.1	Sunphotometer CIMEL CE-318	40
2.4.2	Lidars	42
2.4.3	Airborne instruments	43
2.4.4	Space-borne instruments	45
2.4.5	In-situ measurements	46
3	Airborne sun photometer PLASMA	49
3.1	Introduction and objectives	49
3.2	Technical description	51
3.3	Data processing	55
3.4	Calibration	56
3.4.1	Langley calibration	56
3.4.2	Intercalibration	58
3.4.3	Evolution of the instrument and calibration campaigns	59

3.5	Analysis of PLASMA ground-based, airborne and automobile measurements. Comparison with other instruments.	61
3.5.1	Ground-based measurements	61
3.5.2	Airborne measurements	64
3.5.2.1	Airborne measurements in Lille region	65
3.5.2.2	M'Bour airborne experiment	69
3.5.3	Automobile measurements	74
3.5.3.1	Tenerife experiment	75
3.5.3.2	DRAGON campaign	77
3.6	Conclusion	81
4	Inversion of aerosol size distribution from spectral AOD measurements	83
4.1	Introduction	83
4.2	Inversion algorithm	84
4.2.1	Forward problem	85
4.2.2	Inversion problem	87
4.2.3	Inversion products	91
4.3	Sensitivity study of the inversion code	94
4.3.1	Description of the chosen aerosol types	94
4.3.2	Methodology of the sensitivity study	98
4.3.3	Sensitivity to the refractive index	100
4.3.4	Sensitivity to the AOD noise	104
4.3.4.1	Sensitivity to the AOD noise $\Delta\tau = 0.05\tau$	105
4.3.4.2	Sensitivity to the AOD noise $\Delta\tau = 0.1\tau$	105
4.3.4.3	Sensitivity of the inversion code with $\tau = \langle \tau \rangle$ and standard instrumental noise $\Delta\tau = 0.005$ and $\Delta\tau = 0.01$	107
4.3.5	Conclusion of the sensitivity study	109
4.4	Inversion of PLASMA ground-based measurements	110
4.5	Inversion of the DRAGON campaign data	111
4.6	Inversion of airborne measurements	113
4.6.1	Flights over Lille	113
4.6.2	Flights over M'Bour –Dakar	115
4.7	Conclusion of PLASMA data inversion	118
5	General conclusion	119
A	Illustrations for the sensitivity study to the refractive index and AOD noise	123
B	The paper published during the study	161
	Bibliography	169

List of Figures

1.1	Global average radiative forcing in 2005 (From IPCC, 2007).	17
2.1	Schematic view of the size ranges of atmospheric aerosols in the vicinity of the source and the principal processes involved A: ultra fine particles; B: accumulation mode; C: coarse particles (after Kacenenbogen (2008)).	26
2.2	Schema of the vertical structure of the troposphere: the area near the Earth surface define the atmospheric boundary layer and the rest is called free troposphere (after Stull (1988)).	30
2.3	Aerosol radiative forcing. (From IPCC, 2007, modified from Haywood and Boucher, 2000).	36
2.4	Sunphotometer CIMEL CE-318.	40
2.5	Distribution of AERONET stations in the world (September 2012).	41
2.6	Micro Lidar CIMEL CE 370-2	42
2.7	NASA Ames Airborne Tracking Sunphotometer AATS-14.	44
2.8	FUBISS-ASA2	45
2.9	A-Train constellation.	46
3.1	PLASMA scheme.	51
3.2	PLASMA filter's transmission.	51
3.3	PLASMA without jacket.	52
3.4	Scheme of the main hardware blocks.	53
3.5	Screenshot of the program.	54
3.6	Langley plot provided by Demonstrat 26/03/2010.	57
3.7	Illustration of the automatic calibration in Demonstrat.	59
3.8	PLASMA vs. CIMEL digital count.	59
3.9	Examples of PLASMA ground-based measurements in Lille, Beijing and Dakar stations compared to CIMEL measurements at the same location.	62
3.10	Comparison of simultaneous ground-based measurements of PLASMA (colored lines) and CIMEL CE-318 (black lines) 18/04/2011.	63
3.11	PLASMA on the plane.	65
3.12	PLASMA AOD at 550 nm (left) and extinction coefficient compared with lidar (right) 28th of May 2010.	66
3.13	Timebase of lidar measurements in Lille 28th of May 2010.	66

3.14	The picture taken during the flight over Lille 28th of May 2010 from an altitude around 1500 m.	67
3.15	PLASMA AOD (left), aerosol extinction coefficient (center) at 7 channels and aerosol extinction coefficient compared with lidar (right) as a function of the altitude acquired near Lille region the 12th October 2010, 28th September, 29th September and 15th October 2011.	68
3.16	PLASMA AOD (left) and aerosol extinction coefficient (right) at 8 channels as a function of the altitude acquired near M'Bour region the 27th of March 2013.	69
3.17	PLASMA AOD (left) and aerosol extinction coefficient (right) at 8 channels as a function of the altitude acquired near M'Bour region the 28th of March 2013.	70
3.18	PLASMA AOD (left) and aerosol extinction coefficient (right) at 8 channels as a function of the altitude acquired near M'Bour region the 30th of March 2013.	71
3.19	PLASMA AOD (left) and aerosol extinction coefficient (right) at 8 channels as a function of the altitude acquired near M'Bour region the 3rd of April 2013.	71
3.20	PLASMA AOD (left) and aerosol extinction coefficient (right) at 8 channels as a function of the altitude acquired near M'Bour region the 4th of April 2013.	72
3.21	PLASMA AOD (left) and aerosol extinction coefficient (right) at 8 channels as a function of the altitude acquired near M'Bour region the 5th of April 2013.	73
3.22	a) Installation on the AEMET car; b) PLASMA route on Tenerife and AERONET sites.	75
3.23	Vertical profiles of AOD during car experiment 13/01/2011 in Tenerife island, Spain.	76
3.24	Installation of PLASMA and mobile lidar in the roof of the automobile (a) and PLASMA route 20/07/2011 and the closest AERONET stations during DRAGON campaign (b).	77
3.25	Comparison of PLASMA and AERONET AOD. AERONET measurements were at the distance 2-10 km.	78
3.26	Comparison of PLASMA and AERONET Ångström exponent.	78
3.27	Attenuated backscattered lidar signal measured between Hyattsville (G) and Edgewood (E) with PLASMA AOD (white diamonds). From Mortier et al. (2012)	79
4.1	Size distributions of aerosol standard types when $AOD(440) = 0.2$ (biomass burning and urban aerosols) and $AOD(1020) = 0.2$ (desert dust and maritime aerosols).	98
4.2	Scheme of the sensitivity study.	99
4.3	Effective radii retrieved from 8 and 11wl with different fixed refractive indices (desert dust).	101

4.4	Effective radii retrieved from 8 and 11wl with different fixed refractive indices (biomass burning).	102
4.5	Effective radii retrieved from 8 and 11wl with different fixed refractive indices (urban clean).	102
4.6	Effective radii retrieved from 8 and 11wl with different fixed refractive indices (urban industrial).	103
4.7	Effective radii retrieved from 8 and 11wl with different fixed refractive indices (maritime).	104
4.8	Distribution of the AOD noise.	104
4.9	Size distributions of aerosol standard types when $AOD(\lambda) = <$ $AOD(\lambda) >$	107
4.10	Aerosol size distribution derived from PLASMA ground-based measurements in Lille 19/04/2011.	110
4.11	Aerosol size distribution derived from PLASMA ground-based measurements in Beijing 11/05/2011.	111
4.12	Comparison between PLASMA inversion on 7 and 8 wavelengths with the AERONET inversion.	112
4.13	Size distributions at different altitudes obtained during the airborne measurements by PLASMA sunphotometer over Lille.	114
4.14	Example of the size distribution retrieved from airborne measurements including 1640 nm channel that has wrong calibration.	115
4.15	Size distributions at different altitudes obtained during the airborne measurements by PLASMA sunphotometer over M'Bour on 28/03/2013.	116
4.16	Size distributions at different altitudes obtained during the airborne measurements by PLASMA sunphotometer over M'Bour on 06/04/2013.	116
4.17	Size distributions at different altitudes obtained during the airborne measurements by PLASMA sunphotometer over M'Bour on 07/04/2013.	117
A.1	Size distributions retrieved from 8 wl with different refractive indices (fixed) - Solar Village.	125
A.2	Size distributions retrieved from 11 wl with different refractive indices (fixed) - Solar Village.	127
A.3	Size distributions retrieved from 8 wl with different initial refractive indices (retrieved together with size distributions) - Solar Village.	128
A.4	Size distributions retrieved from 8 wl with different refractive indices (fixed) - Mongu.	130
A.5	Size distributions retrieved from 11 wl with different refractive indices (fixed) - Mongu.	132
A.6	Size distributions retrieved from 8 wl with different initial refractive indices (retrieved together with size distributions) - Mongu.	133
A.7	Size distributions retrieved from 8 wl with different refractive indices (fixed) - GSFC.	135

A.8	Size distributions retrieved from 11 wl with different refractive indices (fixed) - GSFC.	137
A.9	Size distributions retrieved from 8 wl with different initial refractive indices (retrieved together with size distributions) - GSFC.	138
A.10	Size distributions retrieved from 8 wl with different refractive indices (fixed) - Mexico.	140
A.11	Size distributions retrieved from 11 wl with different refractive indices (fixed) - Mexico.	142
A.12	Size distributions retrieved from 8 wl with different initial refractive indices (retrieved together with size distributions) - Mexico.	143
A.13	Size distributions retrieved from 8 wl with different refractive indices (fixed) - Lanai.	145
A.14	Size distributions retrieved from 11 wl with different refractive indices (fixed) - Lanai.	147
A.15	Size distributions retrieved from 8 wl with different initial refractive indices (retrieved together with size distributions) - Lanai.	148
A.16	Sensitivity to the AOD noise $\Delta\tau = 0.05\tau$ - Solar Village.	149
A.17	Sensitivity to the AOD noise $\Delta\tau = 0.05\tau$ - Mongu.	149
A.18	Sensitivity to the AOD noise $\Delta\tau = 0.05\tau$ - GSFC.	150
A.19	Sensitivity to the AOD noise $\Delta\tau = 0.05\tau$ - Mexico.	150
A.20	Sensitivity to the AOD noise $\Delta\tau = 0.05\tau$ - Lanai.	151
A.21	Sensitivity to the AOD noise $\Delta\tau = 0.1\tau$ - Solar Village.	152
A.22	Sensitivity to the AOD noise $\Delta\tau = 0.1\tau$ - Mongu.	153
A.23	Sensitivity to the AOD noise $\Delta\tau = 0.1\tau$ - GSFC.	154
A.24	Sensitivity to the AOD noise $\Delta\tau = 0.1\tau$ - Mexico.	155
A.25	Sensitivity to the AOD noise $\Delta\tau = 0.1\tau$ - Lanai.	156
A.26	Sensitivity of 11 wl inversion to the AOD noise $\Delta\tau = 0.005$ when $\tau = \langle \tau \rangle$	157
A.27	Sensitivity of 8 wl inversion to the AOD noise $\Delta\tau = 0.005$ when $\tau = \langle \tau \rangle$	158
A.28	Sensitivity of 11 wl inversion to the AOD noise $\Delta\tau = 0.01$ when $\tau = \langle \tau \rangle$	159
A.29	Sensitivity of 8 wl inversion to the AOD noise $\Delta\tau = 0.01$ when $\tau = \langle \tau \rangle$	160

List of Tables

2.1	Estimated annual global emission of the main types of aerosols ((IPCC, 2001, 2007))	22
2.2	Aerosol refractive index from AERONET network (Dubovik et al., 2002a).	29
2.3	Range of aerosol optical thickness and average AOT from AERONET network (Dubovik et al., 2002a).	32
2.4	Range of Ångström parameter from AERONET network (Dubovik et al., 2002a).	33
2.5	Range single-scattering albedo parameter from AERONET network (Dubovik et al., 2002a).	34
3.1	PLASMA ground-based measurements.	61
3.2	PLASMA airborne measurements.	64
3.3	PLASMA automobile measurements.	74
4.1	Optical properties of aerosol in Solar Village (after Dubovik et al. (2002a)).	95
4.2	Optical properties of aerosol in Mongu (after Dubovik et al. (2002a)).	95
4.3	Optical properties of aerosol in GSFC (after Dubovik et al. (2002a)).	96
4.4	Optical properties of aerosol in Mexico (after Dubovik et al. (2002a)).	97
4.5	Optical properties of aerosol in Lanai (after Dubovik et al. (2002a)).	97
A.1	Sensitivity study results: 8 wl inversion (Solar Village)	124
A.2	Sensitivity study results: 11 wl inversion (Solar Village)	126
A.3	Sensitivity study results: 8 wl inversion (Mongu)	129
A.4	Sensitivity study results: 11 wl inversion (Mongu)	131
A.5	Sensitivity study results: 8 wl inversion (GSFC)	134
A.6	Sensitivity study results: 11 wl inversion (GSFC)	136
A.7	Sensitivity study results: 8 wl inversion (Mexico)	139
A.8	Sensitivity study results: 11 wl inversion (Mexico)	141
A.9	Sensitivity study results: 8 wl inversion (Lanai)	144
A.10	Sensitivity study results: 11 wl inversion (Lanai)	146

Chapter 1

Introduction

Science never solves a problem
without creating ten more.

George Bernard Shaw

1.1 Scientific interest

Interest to the aerosols originated in the late nineteenth - early twentieth century after the works of R. Millikan in determining the value of a single electric charge ([Millikan, 1910](#)), and J. Wilson in the creation of an ionization chamber ([Wilson, 1901](#)). The great stimulus for the development of research of physicochemical properties of aerosols was their use for military purposes (in the form of smoke and masking agents). As part of the science of the Earth's atmosphere aerosol physics began to develop in last few decades, when it became obvious that studies of optical phenomena in the atmosphere and cloud processes can not proceed further without an understanding of the physical picture of formation and transformation of aerosols ([Mészáros, 1999](#)).

The value of the various components of the atmosphere in atmospheric processes is determined not only by their relative content in the air. Aerosol particles are tiny particles (dust, fumes, etc.) present in the atmosphere. In very dusty

regions their amount is less than 10^{-6} of air mass in which they are contained, and for the entire atmosphere, this value does not exceed 10^{-9} . It is three to four orders of magnitude smaller than the mass fraction of water vapor. And despite this, the role of aerosols in atmospheric processes is very important, especially in the processes of clouds formation and aerosol particles interaction with water vapor. Aerosols are condensation nuclei for clouds, without them clouds might occur in the atmosphere only at high altitude due to condensation of water vapor on the ions. The fact that the mass of water vapor per unit volume of air is several orders of magnitude greater than the mass of aerosol particles has a considerable effect on the variability of aerosol optical properties: for example, even at a constant concentration of solid aerosol particles with the change of external conditions (e.g. ambient temperature, and therefore, relative humidity, intensity and spectrum of incident solar radiation) the transformation of the size and composition of aerosol particles can occur due to conversion of water from a gaseous state into aerosol. The mechanisms of the growth of aerosol particles is not clear when the humidity changes, especially when it is quite far from saturation. In some cases this is determined by the specific physical and chemical properties of some aerosol particles.

The phenomena of atmospheric electricity are closely related to the presence of atmospheric aerosol particles. J. Frenkel suggested that the oriented adsorption of water molecules can cause charged particles (Frenkel, 1944). Also, the adhesion of light ions to aerosol particles leads to a decrease in the conductivity of air. Moreover, collecting the charge of definite sign on large aerosol particles ($R > 0.1\mu m$) could lead to the formation of a large volume charge in the air. Aerosol particles are also the carriers of radioactivity. In this sense, they are dangerous because of the high concentration of radioactivity transport over long distances and because of the relatively rapid lowering of radioactive aerosol particles from the upper to the lower layers of the atmosphere.

It should be emphasized that the role of aerosol particles of different sizes in atmospheric phenomena is quite different. Thus, the initial charge of the drops and electrical properties of air are determined by the content of the ions with the

radius $0.001 < R < 0.055\mu\text{m}$. In the optics of atmospheric aerosol larger particles comparable to the wavelength of the radiation have major influence on the processes of scattering and absorption of radiation. For the processes of cloud formation the presence of atmospheric cloud condensation nuclei and sublimation, which have a particle size $R > 1\mu\text{m}$ is important. This particles also determine the chemical composition of atmospheric aerosols and precipitation (Junge, 1963). The presence of aerosol particles is important for atmospheric optical phenomena: in almost whole optical range the values of aerosol extinction, scattering and absorption coefficients are approximately of the same order as for all atmospheric gases taken together, but the aerosol optical properties are much more variable both in time and in space. In addition, the angular optical characteristics of aerosols (e.g., the scattering indicatrix) are significantly different from those characteristics of gases. As a consequence, such optical phenomena as galos, rainbows, crowns, gloria, etc. are observed in the atmosphere (McCartney, 1976).

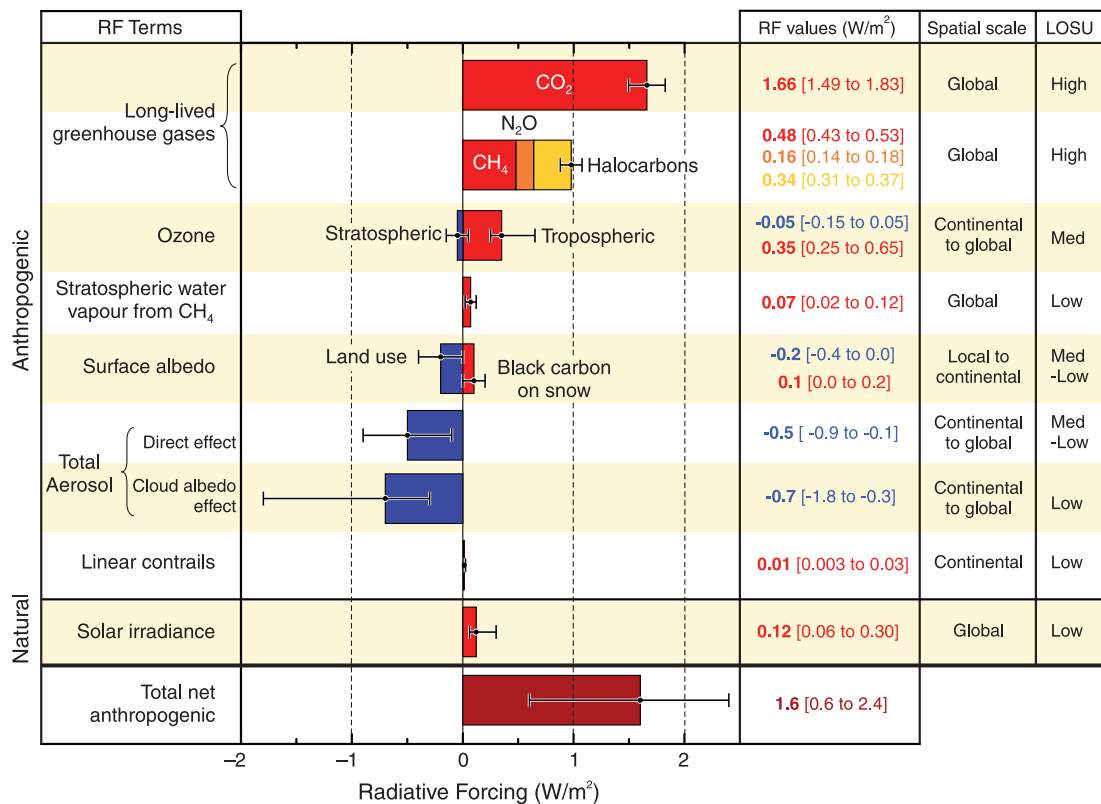


FIGURE 1.1: Global average radiative forcing in 2005 (From IPCC, 2007).

Atmospheric aerosols play an important role in the earth radiative budget

(Hansen et al., 1997). Due to their interaction with solar and thermal radiation, aerosols first cool the atmosphere-surface system (aerosol direct effect) and by absorbing sunlight in the atmosphere, they further cool the surface but warm the atmosphere and change the temperature and humidity profiles (semi-direct effect). They also impact the cloud properties by acting as cloud condensation nuclei and ice nuclei (indirect effects) (Ramanathan et al., 2001; Kaufman et al., 2002).

Fig. 1.1 shows the sign and the intensity of radiative forcing of the main constituents of the atmosphere. It shows in particular that the total radiative forcing caused by the emission of anthropogenic greenhouse gas and aerosols is considered positive to 1.6 W/m^2 (from 0.6 to 2.4 W/m^2) showing the influence of human activities on warming. From the fig. 1.1, increasing of greenhouse gas emissions in the troposphere due to human activities leads to a positive radiative forcing estimated at about 2.99 W/m^2 (from 2.62 to 3.56) (with $1.66 \pm 0.17 \text{ W/m}^2$ of carbon dioxide, $0.48 \pm 0.05 \text{ W/m}^2$ of the methane, $0.16 \pm 0.02 \text{ W/m}^2$ of nitrous oxide, $0.34 \pm 0.03 \text{ W/m}^2$ of the gas halocarbons and 0.35 W/m^2 (from 0.25 to 0.65 W/m^2) of ozone). The radiative forcing due to greenhouse gas emissions is estimated with a "strong" level of scientific understanding ("Level of Scientific Understanding", LOSU), apart from an "average" level for ozone. On the other hand the aerosols have cooling effect (-0.5 W/m^2 for direct and -0.7 W/m^2 for indirect effects in average) but the uncertainty in cooling effect estimation is high and respectively LOSU is low.

1.2 Thesis context

To understand the variability of aerosol it is important to measure the 3D distribution of its properties at global scale. The most accessible and informative methods for this are optical methods divided into active (lidar) and passive (photometer) techniques. Both active and passive instruments could be ground-based or space-borne. Middle position have airborne instruments.

Each instrument has its own scope and limitations. Lidar measures the vertical profile of extinction coefficient but has limitation in quantitative measurement because the lidar equation cannot be solved without an assumption on aerosol optical characteristics or some additional constraint such as independent optical depth measurement. Photometer gives the optical depth and particle size distribution but only in the total atmospheric column. There are several satellite sensors (imagers or scanners) that provide a 2D distribution but the vertical aerosol repartition is poorly sampled. Satellite missions that include lidars such as CALIPSO ([Winker et al., 2010](#)) are useful tools for measuring vertical profiles of aerosols on the satellite track, however, it has the same lidar limitations as ground-based instruments. Currently, serious attempts are done to combine the data of different instruments into one algorithm of processing to get more complete picture of aerosol processes in the atmosphere.

An airborne sun-tracking photometer named PLASMA (that stands for Photomètre Léger Aéroporté pour la Surveillance des Masses d’Air) was developed for validation of lidar and satellite measurements. xAerosol optical depths (AOD) in several wavelengths over a large spectral range are derived from measurements of the extinction of solar radiation by molecular and aerosol scattering and absorption processes. Of course, flying at different altitudes provides the corresponding vertical profiles of both quantities.

Algorithmically, the use of photometer is quite simple since there is no assumption regarding aerosol properties and type. With an airborne version like PLASMA, we can easily sample different locations within few minutes, which is valuable for validating AOD derived from satellite sensors like MODIS ([Remer et al., 2005](#)), MISR ([Kahn et al., 2010](#)) or PARASOL ([Tanré et al., 2011](#)). It can also be used to validate extinction vertical profiles obtained by ground-based or space-borne lidars such as CALIOP on CALIPSO ([Winker et al., 2010](#)).

Last decades similar airborne sunphotometers were successfully developed ([Matsumoto et al., 1987](#); [Schmid et al., 2003](#); [Asseng et al., 2004](#)). Compared to AATS-14 (Ames Airborne Tracking Sunphotometer) and FUBISS-ASA2 (Free

University Berlin Integrated Spectrographic System Aureole and Sun Adapter), the spectral range is similar. The main advantage of PLASMA is its small size and lightness. The weight of the optical head (mobile part) is 3.5kg and the weight of the electronic modules is around 4kg. The optical head has been designed to be easily set up on any mobile platform like a small aircraft or an automobile. It can be used for sampling in few minutes aerosol plumes that are not horizontally uniform or for precisely retrieving aerosol vertical profile.

The first part of thesis project consisted of experimental work with the instrument, its characterization, data analysis and comparison. The goal was to obtain the tool that would provide precise measurements of solar radiation in wide spectral range. The second part was the theoretical work on inversion problem. The spectral dependence of AOD gives information on the aerosol size distribution when the spectral range is large enough (King et al., 1978). There is a well-known algorithm of O. Dubovik used in AErosol RObotic NETwork (Dubovik and King, 2000; Holben et al., 1998) for inversion of optical parameters of atmospheric aerosol. Previously the inversion was made with direct-sun and angular measurements (almucantar and principal plane) in 4 channels in $0.44 - 1.02\mu m$. In this study we implement the algorithm for only direct-sun measurements but with 11 channels in wider spectral range.

The structure of the manuscript follows the chronology of the work on thesis project. The second chapter of the thesis is devoted to physical and optical properties of the aerosol, their radiative effect. In the second chapter we also introduce optical instruments and methodology for aerosol studies. In the chapter 3 we present new airborne sun photometer PLASMA which data we used in our research, its technical characteristics, calibration and evolution, the results of measurements and comparison with other instruments. Our objective is to obtain accurate vertical profiles of aerosol optical depth and aerosol extinction coefficient to use them further for validation lidar and satellite measurements. Finally, the chapter 4 consists original study of inversion of aerosol size distribution from spectral AOD and its implementation for PLASMA measurements in order to obtain this characteristics on different altitudes.

Chapter 2

Aerosol properties and impact

Study the past, if you would
divine the future.

Confucius

2.1 Physical properties of aerosols

2.1.1 Aerosol origin

The wide variety of sources and formation mechanisms leads to a significant variability in size of aerosol particles and their chemical composition. Thus, we can classify them according to their origin (natural or anthropogenic sources) or their mode of formation (primary or secondary aerosols) (Table 2.1).

Primary aerosols correspond to the direct emission of particles to the atmosphere. Natural aerosols come from mechanical effect of wind on the land surface (soil erosion and remobilization), the sea surface (sea spray), or vegetation (biogenic aerosols) (Hinds, 1999). Occasionally, the volcanoes are also natural sources of aerosols emitted during eruptions (sulphate ash).

The primary anthropogenic aerosols such as black carbon, organic carbon or industrial dust (containing metal traces) arise mainly from combustion processes (industrial, domestic, biomass burning), transport or agriculture when vegetation is suppressed by man activities.

TABLE 2.1: Estimated annual global emission of the main types of aerosols ((IPCC, 2001, 2007))

Source	Emission (Tg/year)
<i>Primary aerosols</i>	
Carbonaceous aerosols	
Organic Matter ($0 - 2\mu m$)	
Biomass burning	54
Fossil fuel	28
Biogenic ($> 1\mu m$)	56
Black Carbon ($0 - 2\mu m$)	
Biomass burning	5.7
Fossil fuel	6.6
Aircraft	0.006
Industrial Dust, etc. ($> 1\mu m$)	100
Sea Salt	
$d < 1\mu m$	54
$d = 1 - 16\mu m$	3290
Total	3340
Mineral (Soil) Dust	
$d < 1\mu m$	110
$d = 1 - 2\mu m$	290
$d = 2 - 20\mu m$	1750
Total	2150
<i>Secondary aerosols</i>	
Sulphate (as NH_4HSO_4)	200
Anthropogenic	122
Biogenic	27
Volcanic	21
Nitrate (as NO_3)	
Anthropogenic	14.2
Natural	3.9
Organic compounds	
Anthropogenic	0.6
VOC	
Biogenic VOC	16
Total natural aerosols	90-95%
Total anthropogenic aerosols	5-10%

Secondary inorganic aerosols (sulphates, nitrates, ammonium) or organic come from gas-particle transformation processes through the phenomena of nucleation, condensation or adsorption. The precursor gas can come from emissions from the soil (e.g. due to the use of fertilizers), vegetation (biogenic VOC) or human activities (combustion of fossil fuels in energy production, transport, industrial activities, etc.).

Table 2.1 reveals that only 5 to 10% of the total mass of aerosols emitted annually in the world come from human activities. However, we see that some coarse particles and the majority of fine particles having an impact on health, environment and climate as carbon soot and sulfates, are derived from anthropogenic emissions.

2.1.2 Chemical composition

Chemical composition of aerosols depends on sources of emission and the transformations they undergo in the atmosphere. We describe here the main chemical species constituting the aerosol (following IPCC, 2001). To estimate the radiative effects of aerosol, information is required about particle size, refractive index, and whether the minerals are mixed externally or as aggregates (Tegen et al., 1996; Sokolik and Toon, 1999; Jacobson, 2001).

Soil dust. Soil dust is a major contributor to aerosol loading and optical thickness. Median diameters of dust particles are $2 < d < 4\mu\text{m}$. The atmospheric lifetime of dust depends on particle size; large particles are quickly removed from the atmosphere by gravitational settling, while sub-micron sized particles can have atmospheric lifetimes of several weeks (Marticorena et al., 1997; Miller and Tegen, 1998).

Sea salt. The emission of sea salt depends of wind on the surface of the ocean. Sea salt particles cover a wide size range ($0.05 < d < 10\mu\text{m}$), and have a correspondingly wide range of atmospheric lifetimes. This aerosol is dominant contributor to both light scattering and cloud nuclei. It is very efficient CCN (cloud

condensation nuclei), and therefore characterization of their surface production is of importance for aerosol indirect effects (Gong et al., 1998).

Industrial dust, primary anthropogenic aerosols. These aerosol sources are responsible for the most conspicuous impact of anthropogenic aerosols on environmental quality, and have been widely monitored and regulated.

Carbonaceous aerosols (organic and black carbon). Organic carbon can be emitted directly into the atmosphere (OC) by sources of anthropogenic origin (burning of petroleum, wood, garbage, cooking meat, etc.) or natural (leaf abrasion by the wind). But it can also be formed by nucleation or condensation of products of photochemical degradation of volatile organic compounds (VOCs). This is called secondary organic aerosol (SOA). VOCs can come from the vegetation (terpenes, limonene, etc.) or be derived from anthropogenic sources (benzene, toluene, etc.). It comes from combustion processes (fossil fuel and biomass) and has little chemical reactivity (Andreae and Crutzen, 1997). Of particular importance for the direct effect is the light-absorbing character of some carbonaceous species, such as soot and tarry substances (Hansen et al., 1997; Haywood and Ramaswamy, 1998; Penner et al., 1998).

Primary biogenic aerosols. They consist of plant debris and microbial particles (cuticular waxes, leaf fragments, bacteria, fungi, viruses, algae, pollen, spores, etc.). The presence of humic-like substances makes this aerosol light-absorbing in the UV region (Havers et al., 1998). Primary biogenic particles are able to act both as cloud droplet and ice nuclei (Schnell and Vali, 1976). Therefore, they are important for both direct and indirect climate effects.

Sulfates. This species are formed mainly in the aqueous phase by condensation of sulfuric acid emitted primarily by industrial activities appear as particles when the droplets evaporate without precipitation. Sulphate in aerosol particles is present as sulphuric acid, ammonium sulphate, and intermediate compounds, depending on the availability of gaseous ammonia to neutralize the sulphuric acid formed from SO_2 (Adams et al., 1999). The chemical pathway of conversion of precursors to sulphate is important because it changes the radiative effects. Most

SO_2 is converted to sulphate either in the gas phase or in cloud droplets that later evaporate (Weber et al., 1999).

Nitrates. The nitric acid has two ways of formation. Firstly, it appears in the gas phase, and secondly, on heterogeneous phase in particles or water droplets in clouds. Ammonia is a base that will neutralize part of nitric acid to form particulate ammonium nitrate according to temperature and ambient relative humidity. Nitrates are not considered in assessments of the radiative effects of aerosols because they cause only 2% of the total direct forcing (Andreae, 1995). They are important only at a regional scale (ten Brink et al., 1996).

Volcanic aerosols. There are two main components of volcanic emissions: primary dust and gaseous sulphur (mainly in the form of SO_2) (Graf et al., 1997). Continuous eruptive activity is about 4 Tg/yr (Jones et al., 1994), that is three orders of magnitude smaller than soil dust emission but big eruptions can lead to significant climate effects. The well-known example is Pinatubo eruption in 1991 (Stenchikov et al., 1998).

2.1.3 Size distribution

The size of the aerosol extends over a wide range of radii ranging from several nanometers to several tens of microns. Size varies with the nature of the source of particle production and according to reactions undergone by aerosols during the time they are present in the atmosphere (nucleation, coagulation, and condensation of gas to the particulate state). Suitable for the characterization of the size of a population of aerosols, the size distribution is used to quantify the number of particles of a certain radius. It presents one or more modes. The aspect of a multi-modal distribution of aerosols in the troposphere has been shown by Jünger (1955) and more recently updated by Whitby (1978).

Fig. 2.1 presents the mass distribution of a population of particles of different aerodynamic diameters. The aerodynamic diameter is the diameter of a spherical particle with a density of 1 g/cm^3 should be to present the same settling velocity

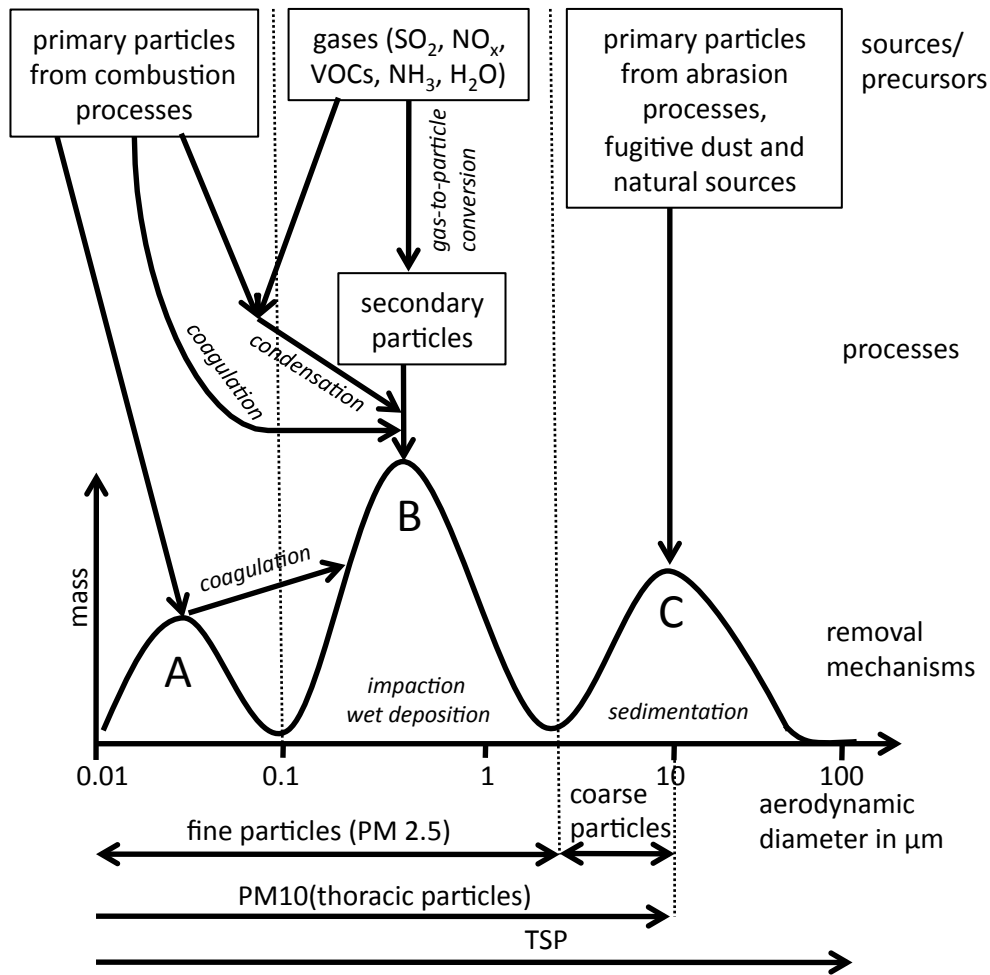


FIGURE 2.1: Schematic view of the size ranges of atmospheric aerosols in the vicinity of the source and the principal processes involved A: ultra fine particles; B: accumulation mode; C: coarse particles (after [Kacenenlobogen \(2008\)](#)).

as the particle under review. The aerodynamic diameter d_a is depending on the physical diameter d_p and density of the particle ρ (often expressed as $g \cdot \text{cm}^{-3}$), is written in the following manner: $d_a = d_p \sqrt{\rho}$.

There are three most commonly observed modes: nucleation (also called "ultrafine" or "Aitken", A), accumulation (B) and coarse mode (C). Nucleation (A) and accumulation (B) modes can be grouped into a single mode called "fine".

The nucleation mode (A) corresponds to particles of physical (not aerodynamic) radius less than $0.05 \mu\text{m}$. They are not efficient scatters in the visible and are too small to interact with terrestrial (infrared) radiation. They are, therefore, not optically active and their radiative impact can be neglected.

The accumulation mode (B) represents a physical particle radius between $0.05\mu m$ and $1\mu m$. They come from the aggregation of smaller particles, from the condensation of gases or the re-evaporation of droplets. Aerosols of this type are of great importance from the climate viewpoint because their interaction with the light is maximal (since their size is of the order of the wavelength in the visible part of the solar spectrum) and their presence time in the atmosphere is significant. Moreover, droplets form from the accumulation mode of the aerosols.

Finally, the coarse mode (C) corresponds to particles of radius more than $1\mu m$ that mostly have natural and primary type. Note that close to a source of aerosols, the size distribution of particles' population is often observed as mono-modal. The size distribution evolves into a bi-modal when the residence time of particles in the atmosphere increases or in the presence of two distinct sources of aerosols of different types.

Mathematically, the lognormal distribution can well characterize a population covering a wide range of sizes. Variation in the number of particles n as a function of the natural logarithm of the radius r can be written such as

$$n(r) = \frac{dN}{d \ln r} = \frac{n_0}{\sigma_0 \sqrt{2\pi}} \exp \left[- \frac{(\ln r - \ln r_0)^2}{2\sigma_0^2} \right] \quad (2.1)$$

where $n(r)$ is the number of particles, the natural logarithm of the radius is between $\ln r$ and $\ln r + d \ln r$, r_0 is the modal radius, σ_0 is the standard deviation of the natural logarithm of the radius (the width of the distribution) and n_0 is the number of particles in the mode considered.

A multi-modal distribution is simply described by a sum of log-normal distributions. The most used is bi-modal lognormal size distribution.

It is not always relevant to use the distribution of the number of particles. The distribution of the surface is more appropriate if we are interested in chemical

reactions involving aerosols:

$$\frac{dS}{d \ln r} = \frac{S_0}{\sigma_2 \sqrt{2\pi}} \exp\left[-\frac{(\ln r - \ln r_2)^2}{2\sigma_2^2}\right] \quad (2.2)$$

If one seeks to evaluate the mass of aerosols, the distribution of volume V will be interesting. This can be written

$$\frac{dV}{d \ln r} = \frac{V_0}{\sigma_3 \sqrt{2\pi}} \exp\left[-\frac{(\ln r - \ln r_3)^2}{2\sigma_3^2}\right] \quad (2.3)$$

where r_3 and σ_3 are defined in the same way as above, and V_0 is the volume concentration of particles. Knowing that the radius of the modal distribution of the n -th power of the radius is given for the log-normal $r_0 \exp(-n\sigma_0^2)$ and the standard deviations remain unchanged ($\sigma_3 = \sigma_0$), we pass from modal radius distribution volume for that of the distribution of the number by

$$r_3 = r_0 \exp(-3\sigma_0^2) \quad (2.4)$$

r_3 is higher than r_0 , which reflects the fact that the volume distribution is shifted towards larger particles, which contribute the most.

2.1.4 Refractive index

The refractive index is a major property of the aerosol since it impacts the phase matrix and the single scattering albedo. Its complex value is determined as:

$$m = n + ik \quad (2.5)$$

where $n = \text{Re}(m)$ is real part and $k = \text{Im}(m)$ is imaginary part of complex refractive index.

TABLE 2.2: Aerosol refractive index from AERONET network (Dubovik et al., 2002a).

Urban-industrial and mixed	GSFC , Greenbelt, USA (1993 - 2000)
n, k	$1.41 - 0.03\tau(440) \pm 0.01; 0.003 \pm 0.003$
	Mexico city (1999 - 2000)
n, k	$1.47 \pm 0.03; 0.014 \pm 0.006$
Biomass burning	African savanna , Zambia (1995 - 2000)
n, k	$1.51 \pm 0.01; 0.021 \pm 0.004$
Desert dust and oceanic	Solar Vilage , Saudi Arabia (1998 - 2000)
$n, k(440/670/870/1020)$	$1.56 \pm 0.03; 0.0029/0.0013/0.001/0.001 \pm 0.001$
	Lanai , HI, USA (1995 - 2000)
n, k	$1.36 \pm 0.01; 0.0015 \pm 0.001$

The real part $Re(m)$ defines the speed of propagation in the medium and provides information on the deflection of light by the particle. This is generally between 1.33 (aerosols saturated water) and 1.55 (mineral aerosol), but can reach 1.75 in the visible range for soot particles. The imaginary part $Im(m)$ is connected to the absorption properties of aerosols. It is 0 for purely scattering aerosols (such as sea salt) and 0.66 for the most absorbing aerosols such as soot particles.

Table 2.2 shows that the aerosol refractive index depends on the chemical composition and the source of pollution. The real part of refractive index does not show the spectral dependence. For dust and oceanic aerosol there is high spectral dependency of imaginary part. For biomass burning real part is ranged between 1.47 and 1.52. The refractive index depends also on relative humidity decreasing with its increase.

2.1.5 Vertical distribution

Among many climatological and meteorological factors (wind, local topography, etc.), the vertical distribution of aerosols is strongly influenced by the stability of the atmosphere. The atmosphere is stable if an air mass, displaced from its equilibrium position, tends to return in it. It depends on the temperature of the air mass relative to the ambient air. If the raised mass of air is colder than the

surrounding air, it will be denser and will go down again to its starting level. We say, in this case, the atmosphere is stable.

Fig. 2.2 describes the simplified vertical structure of the troposphere limited to the first 10 km. The atmospheric boundary layer is defined as the part of the troposphere directly influenced by the Earth's surface (friction, evaporation, heat transfer, emission of pollutants, etc).

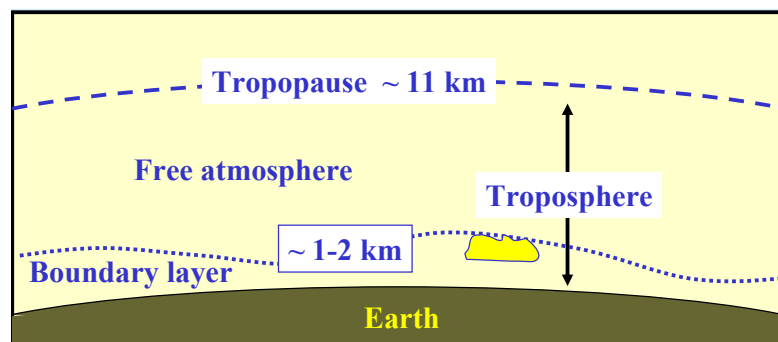


FIGURE 2.2: Schema of the vertical structure of the troposphere: the area near the Earth surface define the atmospheric boundary layer and the rest is called free troposphere (after [Stull \(1988\)](#)).

The boundary layer is generally thinner in the case of high atmospheric pressure (more than 1013.25 hPa), anticyclonic conditions with clear skies or fine weather clouds ([Stull, 1988](#)). In the case of high pressure, the vertical structure of the atmospheric boundary layer during the day is composed of three major parts: a surface layer (about 10% of the boundary layer) at its base, followed by a mixed layer and an entrainment zone. It is very difficult to define a height and boundary layer structure in the case of low pressures.

2.2 Optical properties of aerosols

The main optical parameters of aerosols for determining their radiation effects are the aerosol optical depth and extinction coefficient, Ångström parameter, single scattering albedo and the phase matrix. All these parameters depend on the wavelength of radiation when the AOD is depending on the aerosol content in

the atmosphere. It is also necessary to know the horizontal and vertical distribution of aerosol layers. For computing the aerosol radiative impact, the albedo of the cloud or of the underlying Earth's surface is required. The presence of aerosols in the atmosphere generally leads to a negative effect, i.e. to the cooling of the Earth's surface. However, partially absorbing aerosol over bright (scattering) surfaces (clouds, snow, ice, deserts) may contribute to the warming of the surface-atmosphere system.

2.2.1 Aerosol optical depth and extinction coefficient

From the Bouguer-Lambert-Beer law, the sun irradiance $E(\lambda, z)$ at wavelength λ at an altitude z above sea level is written (Bohren and Huffman, 1998):

$$E(\lambda, z) = t_g(\lambda, z)E_0(\lambda)e^{-\tau(\lambda, z)m} \quad (2.6)$$

where $E_0(\lambda)$ is the extraterrestrial sun irradiance; $t_g(\lambda, z)$ is the gaseous transmission; m is an airmass proportional to $1/\cos(\theta_s)$ when refraction is neglected; θ_s is a solar zenith angle; $\tau(\lambda, z)$ is the spectral total optical depth of the atmospheric layer from altitude z to the top of the atmosphere (TOA) and is the sum of aerosol extinction and molecular (Rayleigh) scattering optical depths:

$$\tau(\lambda, z) = \tau_{ext}^a(\lambda, z) + \tau_{ext}^m(\lambda, z) \quad (2.7)$$

The aerosol optical thickness τ_{ext}^a (AOT) is the sum of the thickness of optical absorption and scattering: $\tau_{ext}^a = \tau_{diff} + \tau_{abs}$ represents the extinction of radiation by aerosol layer integrated along the atmospheric column. It is defined as follows:

$$\tau_{ext}^a(\lambda, z) = \int_z^{TOA} \sigma_{ext}^a(\lambda, z')dz' \quad (2.8)$$

And then

$$\sigma_{ext}^a = \frac{d\tau_{ext}^a}{dz} \quad (2.9)$$

For a set of spherical aerosols, the extinction coefficient $\sigma_{ext}^a(\lambda, z)$ (m^{-1}) is written:

$$\sigma_{ext}(\lambda, z) = \int_0^{\infty} \pi r^2 Q_{ext}(m, r, z, \lambda) n(r, z) dr \quad (2.10)$$

where the extinction efficiency factor Q_{ext} depends on the refractive index m , the particle size r , the wavelength λ and altitude z . The size distribution of a set of particles $n(r, z)$ is also, strictly speaking, depending on the altitude.

It is useful to introduce the extinction cross section s_{ext} (m^2) that is the product of the geometric section of the particle (equal to πr^2 for a spherical particle of radius r) by the efficiency factor for extinction Q_{ext} .

As in the case of the extinction optical thickness one can write:

$$\sigma_{ext} = \sigma_{diff} + \sigma_{abs}, \quad Q_{ext} = Q_{diff} + Q_{abs}, \quad s_{ext} = s_{diff} + s_{abs}.$$

Table 2.3 represents the values of AOD for different types of aerosols measured in AERONET network.

TABLE 2.3: Range of aerosol optical thickness and average AOT from AERONET network (Dubovik et al., 2002a).

Urban-industrial and mixed	GSFC , Greenbelt, USA (1993 - 2000) $0.1 \leq \tau(440) \leq 1.0; \langle \tau(440) \rangle = 0.24$
	Mexico city (1999 - 2000) $0.1 \leq \tau(440) \leq 1.8; \langle \tau(440) \rangle = 0.43$
Biomass burning	African savanna , Zambia (1995 - 2000) $0.1 \leq \tau(440) \leq 1.5; \langle \tau(440) \rangle = 0.38$
Desert dust and oceanic	Solar Vilage , Saudi Arabia (1998 - 2000) $0.1 \leq \tau(1020) \leq 1.5; \langle \tau(1020) \rangle = 0.17$
	Lanai , HI, USA (1995 - 2000) $0.01 \leq \tau(1020) \leq 0.2; \langle \tau(1020) \rangle = 0.04$

2.2.2 Angstrom parameter

Ångström parameter (Ångström, 1929) α provides information on the particle size (Schuster et al., 2006) through the spectral dependence of the AOD. It can be

expressed by

$$\tau(\lambda) = \tau(\lambda_0) \left(\frac{\lambda}{\lambda_0} \right)^{-\alpha} \quad (2.11)$$

Larger the spectral dependence of the AOT, larger the Ångström coefficient, smaller are the particles.

In the case of molecules (Rayleigh scattering), AOT approximately follows a law λ^{-4} . Regarding aerosols, the Ångström parameter ranges from 0 (very large particles, for example, desert dust) to 3 (very fine particles like urban pollution aerosol). Note that a population of large particles whose number is distributed on a single mode can have a slightly negative Ångström parameter.

TABLE 2.4: Range of Ångström parameter from AERONET network ([Dubovik et al., 2002a](#)).

Urban-industrial and mixed	GSFC , Greenbelt, USA (1993 - 2000)
	$1.2 \leq \alpha \leq 2.5$
	Mexico city (1999 - 2000)
	$1.0 \leq \alpha \leq 2.3$
Biomass burning	African savanna , Zambia (1995 - 2000)
	$1.4 \leq \alpha \leq 2.2$
Desert dust and oceanic	Solar Vilage , Saudi Arabia (1998 - 2000)
	$0.1 \leq \alpha \leq 0.9$
	Lanai , HI, USA (1995 - 2000)
	$0 \leq \alpha \leq 1.55$

Examples of Ångström parameter in different regions are presented in table 2.4. In urban-polluted cities α reaches 2.5, places with only natural aerosol represent usually $\alpha < 1$.

2.2.3 Single-scattering albedo

The part of scattering in the extinction is given by the single-scattering albedo ω_0 (SSA). It is the ratio of the scattering coefficient and the extinction coefficient of a set of particles:

$$\omega_0 = \frac{\sigma_{scat}}{\sigma_{ext}} \quad (2.12)$$

The absorption properties are directly related to the chemical composition of the aerosol and its refractive index. More the aerosol is absorbing, higher the imaginary part of the refractive index is, and smaller is ω_0 . For a non-absorbing aerosol (for which imaginary part of the refractive index is equal to 0), $\omega_0 = 1$.

Most of the absorption in the aerosol compound is due to presence of black carbon ($SSA(550nm) = 0.15-0.30$) (Bond and Bergstrom, 2006) and to absorbing mineral dust ($SSA(550nm) = 0.75 - 0.99$) (Tanré et al., 2001) whereas other species such as sulphates, organic carbon and sea salt are predominantly non absorbing ($SSA(550nm) = 0.98 - 1$) (Penner et al., 2001; Cooke et al., 1999; Hess et al., 1998).

Table 2.5 presents the values of single-scattering albedo of different types of aerosol. Most regions have in majority scattering aerosols with $SSA > 0.9$. Aerosols of African savanna with usual biomass burning events contain a lot of black carbon and therefore absorb more. At the same time it has higher value of imaginary part of refractive index (see table 2.2) that is consistent with lower value of SSA.

TABLE 2.5: Range single-scattering albedo parameter from AERONET network (Dubovik et al., 2002a).

Urban-industrial and mixed $\omega_0(440/670/870/1020)$	GSFC , Greenbelt, USA (1993 - 2000) 0.98/0.97/0.96/0.95 \pm 0.02
	Mexico city (1999 - 2000) 0.90/0.88/0.85/0.83 \pm 0.02
Biomass burning $\omega_0(440/670/870/1020)$	African savanna , Zambia (1995 - 2000) 0.88/0.84/0.80/0.78 \pm 0.015
Desert dust and oceanic $\omega_0(440/670/870/1020)$	Solar Vilage , Saudi Arabia (1998 - 2000) 0.92/0.96/0.97/0.97 \pm 0.02
	Lanai , HI, USA (1995 - 2000) 0.98/0.97/0.97/0.97 \pm 0.03

2.2.4 Phase function

The angular distribution of the scattering of a particle is given by the phase function. It is normalized as follows:

$$\int_{4\pi} P(\Omega) d\Omega = 4\pi \quad (2.13)$$

where Ω notes the solid angle. By introducing scattering angle Θ that is the angle between the incident and scattering directions, and its cosine $\mu = \cos(\Theta)$, we can write

$$\int_{-1}^1 P(\mu) d\mu = 2 \quad (2.14)$$

when the phase function presents a rotation symmetry in the azimuthal angle, which is the case of spherical particles and non-spherical randomly oriented particles. The aerosol phase function is highly anisotropic and has a very sharp diffraction peak for small scattering angles between 0° and 5° .

Several quantities have been suggested to describe the phase function. The asymmetry parameter of g is defined by

$$g = \frac{1}{2} \int_{-1}^1 \mu P(\mu) d\mu \quad (2.15)$$

g is the moment of first order in the decomposition of the phase function in Legendre moments, and provides information on the symmetry forward / back distribution of the particle scattering. Scattering is fully forward if $g = 1$ and is fully back if $g = -1$. If $g = 0$, the distribution is symmetric between forward and backward directions.

2.3 Aerosol impact

2.3.1 Radiative impact

The processes of interaction between aerosols, solar and terrestrial radiation and other components of the Earth system are complex and difficult to quantify precisely. They can lead to a cooling of climate system (negative radiative forcing) or to the warming (positive radiative forcing).

Currently, aerosols are known to act on climate in three distinct ways. By their ability to scatter and absorb radiation, aerosols can directly modify the incident solar and telluric flux (direct and semi-direct radiative effects). It is linked to their ability to absorb infrared radiation and reflect or absorb visible radiation.

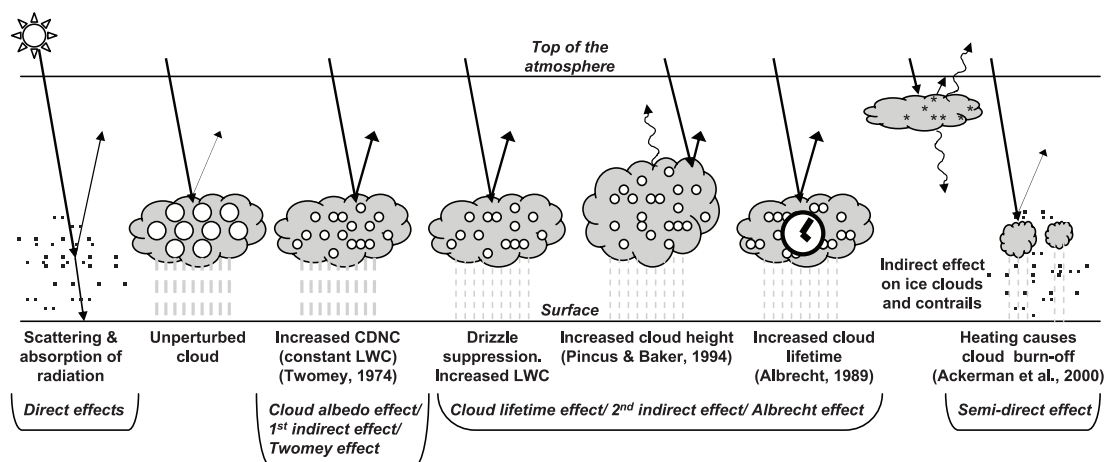


FIGURE 2.3: Aerosol radiative forcing. (From IPCC, 2007, modified from Haywood and Boucher, 2000).

Clouds to be formed use natural and anthropogenic aerosols as cloud condensation nuclei. When aerosol concentration increases, clouds contain more smaller drops for constant liquid water content. This phenomenon is called the effect Twomey (1974). As a result, the parasol effect of clouds increases. Presence of aerosols has other effects such as increase of the height of clouds (Pincus and Baker, 1994) and of the lifetime of clouds (effect Albrecht (1989)).

The indirect effect of aerosols is that they act as cloud condensation nuclei or ice nuclei which initiate the formation of droplets or ice crystals. It should be

noted that their indirect effect is important because a significant part of clouds do not precipitate and the chemical composition of aerosols is modified after passing through the liquid phase in the clouds (see Fig. 2.3).

The semi-direct effect is due to the solar absorption by aerosols that can modify the temperature profile of the atmosphere. This affects the conditions of cloud formation (Ackerman et al., 2000).

Precipitating clouds containing only large drops are not disturbed by an excess of aerosols. Therefore, the radiative properties of these clouds are not modified and return to space a small amount of light.

2.3.2 Impact to the environment and peoples' health

Aerosols can have harmful effects on human health when they are inhaled. Toxicological studies have shown their role in some lung functions, the outbreak of asthma and the increasing number of deaths due to cardiovascular diseases (Liao et al., 1999; Donaldson et al., 2001). Aerosol particles can carry toxic compounds, allergens, mutagens or carcinogens, such as polycyclic aromatic hydrocarbons and heavy metals, which can reach the lungs, where they are absorbed in the blood and tissues. The harmfulness of aerosols also depends on their concentration and size (Ramgolam et al., 2009) because the finest particles (diameter inferior to 2.5 microns) can penetrate deeply the respiratory system to reach the lung alveoli.

Health effects of air pollution were sometimes dramatic in the past. The first evident event that showed the relationship between particulate air pollution and health impacts took place in Glasgow in 1909 when nearly 1000 deaths were attributed to the sharp increase in concentrations of sulfur dioxide and particulate matter caused by very stable meteorological conditions. The term "smog" (smoke-contraction of smoke and fog, mist) was used for the first time to characterize this episode. We can identify other tragic events of the same nature, such as Donora

(USA) on 26-31 October 1948 (20 dead) or infamous episode of pollution of London that had 4000 deaths between 5 and 9 December 1952. During the episode, the particle concentrations reached $3000\mu\text{g}/\text{m}^3$ (Davis et al., 2002).

These health crisis relating to the excessive use of fossil fuels (especially coal), lead in most industrialized countries to develop policies for reducing emissions of gaseous pollutants and particulate. However, the use of fossil fuels in huge megalopolises in India, China or Africa still make the alarming pollution in these regions.

Today, in most of the major agglomerations of Western Europe, aerosol concentrations are of the order of a few tens of micrograms per cubic meter (in daily average) following the reduction efforts recently undertaken in industrial countries. However, the impact on the health of low to moderate concentrations events is not recognized. Indeed, a 2009 report by the French Agency for Health, Environment and Labour (l'Agence Francaise de Sécurité Sanitaire, de l'Environnement et du Travail, AFSSET) on the effects of particles on health (InVS/Afsse, 2005; Mulot et al., 2009) shows that there is no threshold concentration of fine particles in ambient air below which there would be no health impact.

The experts from AFSSET specify that frequent exposure at moderate levels are more dangerous than occasional exposure of peak concentrations. According to them, only 3% of health impacts would be caused by high concentrations of particles. Epidemiologists of the French Institute for Public Health Surveillance (de l'Institut francais de Veille Sanitaire, InVS) define them as to the impact of exposure to particulate matter as being "of the same order as passive smoking". In addition, fast development of nanotechnology, more and most used in industry (including nanoparticles of heavy metals) and presented way of growing in commercial products could pose an additional risk for the health (InVS/Afsse, 2005).

2.4 Instruments and methods

Optical measurements for the study of atmospheric aerosols are divided into active and passive methods. The active methods include laser (lidar) sensing when the most popular passive method is sunphotometry based on solar radiation measurements after passing through the atmosphere.

Both active and passive instruments can be performed from the surface, from space or from airplanes. Let us mention additional information to the optical measurements can be provided by in-situ measurements.

To fully describe the aerosols radiative impact on climate the following information have to be available (Veeffkind, 1999; Lacis and Mishchenko, 1995):

- the optical constants (complex refractive index) for the chemical compounds contained in aerosols, at all relevant wavelengths;
- the chemical composition, particle shape, and size distribution of aerosols species;
- a physical model to describe the effect of hygroscopical particle growth with changing relative humidity on the aerosol optical properties;
- a cloud microphysical model to determine changes in cloud droplet size, cloud optical depth, and lifetimes in response to changes in the CCN concentration.

It is clear that such information is not available on a global scale. In fact, most of the data available on aerosol properties is measured during short-term campaigns, which might not be relevant for other regions or other seasons, or even other conditions than encountered during the measurement campaign. Frequent global monitoring of aerosol properties is only achievable by satellite remote sensing. Therefore a combined effort of ground-based, airborne, satellite remote sensing, short-term intensive field observations, and three-dimensional chemistry transport modeling is needed to adequately describe the aerosols impact on climate.

2.4.1 Sunphotometer CIMEL CE-318

The CIMEL CE-318 (Fig. 2.4), the main instrument of AERONET network (Holben et al., 1998), is a portable automatic sun and sky radiometer, equipped with 8 or 9 spectral channels covering the spectral range 340 – 1640 *nm*. The photometer provides direct sun and angular measurements of distribution of sky radiance in almucantar (a circle on the celestial sphere parallel to the horizon with constant zenith angle equal to solar zenith angle) and principal plane configurations. Several versions exist within the network: old analog photometers (standard and polarized versions with 8 channels), digital 8-channel photometers (standard and polarized), the Short Wave Infrared (SWIR, also called extended instruments, with 9 channels) and finally the dual polar photometers. Independently of the version, all instruments operating within AERONET are equipped at least with the spectral channels 440, 670, 870, 936, 1020 *nm*. Apart from these, each version may have additional channels, such as 500 *nm*, 1640 *nm*, ultraviolet (340, 380 *nm*) or polarized channels. The four channels 440, 670, 870, 1020 *nm* are the core of the measurement protocol.



FIGURE 2.4: Sunphotometer CIMEL CE-318.

The instrument has solar panel and rechargeable batteries, which confers it full autonomy. It is equipped by two robot axes allowing movement in azimuth and zenith plans and can therefore cover any point in the celestial vault with an accuracy of 0.05° and a field of view of 1.2° .

The data are transmitted via geostationary satellites (or via internet link) every hour to a processing center (NASA Goddard Space Flight Center). There are different levels of data processing available: level 1 (raw data), Level 1.5 (cloud screening is automatically applied but final calibration is not necessarily available) and level 2 (the cloud screening and the final calibration are applied and data are screened manually).

The global network of photometers AERONET (AErosol ROBotic NETwork) (Holben et al., 1998) has been operating since early 1990s. The approximate total number of permanent sites is currently over 200 and around 50 sites are seasonal (like in the Amazon site where photometers are not installed during the rainy season). Fig. 2.5 presents the overall distribution of all available stations measuring network AERONET.



FIGURE 2.5: Distribution of AERONET stations in the world (September 2012).

The network are managed simultaneously in the United States by NASA (GSFC) and in Lille by the Laboratory of Atmospheric Optics (LOA). LOA also ensures the calibration, on-site installation and maintenance of several sites (including Europe and Africa). The original French component of the network is the AERONET PHOTONS network (PHOTométrie pour le Traitement Opérationnel de Normalisation Satellitaire).

The website www.aeronet.gsfc.nasa.gov allows to visualize and download the AERONET measurements (instantaneous, daily or monthly) by choosing the period and location.

2.4.2 Lidars

The Lidar (light detection and ranging) technique is an efficient tool for real-time monitoring of aerosols or gases that can be single- or multi-wavelength. The remote sensing of vertical distribution of aerosol particles, produced locally over the measuring site or transported by the atmospheric circulation can be carried out by lidar. Lidar can be used in investigation of air-quality issues as it records inversion layer and helps for the validation of regional forecasting models, in the horizontal mapping of urban and industrial areas to detect the sources of pollution and analyze the local pollution phenomena (3D tracking).



FIGURE 2.6: Micro Lidar CIMEL CE 370-2

For comparison with PLASMA we use the Cloud and Aerosol Micro-LIDAR (CAML) CE 3702 manufactured by CIMEL (Pelon et al., 2008; Léon et al., 2009). This eye-safe micro-pulse LIDAR system (Fig. 2.6) operates at 532 nm with power ranging from 50 to 100 mW. Its principle is similar to the micro-pulse LIDAR

system (Welton et al., 2001). The link from the rack to the telescope is ensured by a 10 m optical fiber and the same telescope is used for both emission and reception avoiding the alignment problem. The aerosol extinction profile as well as the effective extinction-to-backscatter ratio are retrieved using combination of lidar data and sun-photometer AOD (Léon et al., 2009).

In the European region, regular monitoring of the state of the atmosphere are carried out in the framework of international lidar and combine lidar-photometer networks EARLINET -European Aerosol Research Lidar Network (Bösenberg, 2003; Rocadenbosch et al., 2008), CIS-LiNet - CIS Lidar Network (Chaikovsky et al., 2005), GALION - GAW Aerosol Lidar Observation Network (Bösenberg and Hoff, 2007), GAW - Global Atmospheric Watch (WMO/GAW, 2007), EMEP - Cooperative Programme for Monitoring and Evaluation of the Long-range Transmission of Air Pollutants in Europe <http://www.emep.int/>, NDACC - Network for the Detection of Atmospheric Composition Change <http://www.ndsc.ncep.noaa.gov/>.

2.4.3 Airborne instruments

Several airborne sunphotometer were recently developed and we shortly describe these instruments.

AATS-6 and AATS-14

The 6- and 14-channel NASA Ames Airborne Tracking Sunphotometer AATS-6 (Matsumoto et al., 1987) and AATS-14 (Schmid et al., 2003) measure the transmission of the solar beam in 6 or 14 spectral channels. Azimuth and elevation motors controlled by differential sun sensors rotate a tracking head, locking onto the solar beam and keeping detectors normal to it. The AATS tracking head mounts outside the aircraft skin, to minimize blockage by aircraft structures and avoid data contamination by aircraft-window effects. The spectral range is 380 – 1021 *nm* for AATS-6 and 354 – 2139 *nm* for AATS-14.

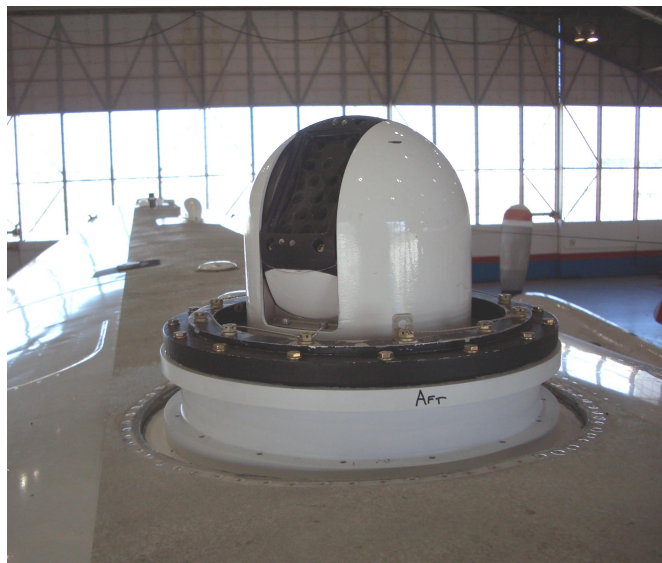


FIGURE 2.7: NASA Ames Airborne Tracking Sunphotometer AATS-14.

AATS-6 and further AATS-14 participated in numerous campaigns such as second Aerosol Characterization Experiment (ACE-2) ([Schmid et al., 2000](#)), South African Regional Science Initiative (SAFARI) 2000 ([Bergstrom et al., 2003](#)), Asian Pacific Regional Aerosol Characterization Experiment (ACE-Asia) ([Huebert et al., 2003](#)), Chesapeake Lighthouse and Aircraft Measurements for Satellites (CLAMS) ([Chowdhary et al., 2005](#)), Aerosol LIdar Validation Experiment (ALIVE) ([Waquet et al., 2009](#)) and most recently in Arctic Research of the Composition of the Troposphere from Aircraft and Satellites (ARCTAS) ([Lyapustin et al., 2010](#)).

FUBISS-ASA and FUBISS-ASA2

The system measures simultaneously the direct solar irradiance and the aureole around the sun in two different angles (4 and 6). The spectra are measured with three spectrometers in the range of 400 – 1000 nm (FUBISS-ASA ([Asseng et al., 2004](#))) or 300 – 1700 nm (FUBISS-ASA2 ([Zieger et al., 2007](#))) and 256 spectral channels simultaneously. The spectral resolution is 10 nm (FWHM). Standard products are aerosol optical thickness, angstrom coefficient and in the case of special flight profiles the extinction coefficient. The aureole measurements can be used to characterize the aerosol type.

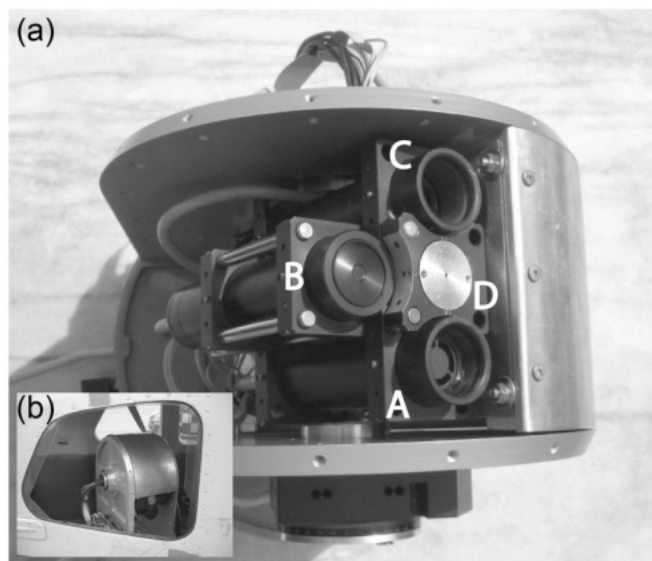


FIGURE 2.8: FUBISS-ASA2

2.4.4 Space-borne instruments

It is clear today that satellite instruments constitute an essential contribution to the overall description of the spatial distribution of clouds and aerosols.

Space passive instruments (radiometers or spectrometers imagers or not, such as AVHRR - Advanced Very High Resolution Radiometer (Stowe et al., 1992), TOMS - Total Ozone Mapping Spectrometer (Herman et al., 1997), POLDER - Polarization and Directionality of Earths Reflectances (Deschamps et al., 1994), MISR - Multi-angle Imaging Spectro Radiometer (Diner et al., 1998), MODIS - MODerate resolution Imaging Spectroradiometer (Remer et al., 2005), OMI - Ozone Monitoring Instrument ((Levelt et al., 2006), SEVIRI - Spinning Enhanced Visible and Infra Red Imager (Sun and Pinker, 2007), etc.) measure the radiance scattered by aerosols and clouds in the satellite direction (nadir).

Active instruments use their own emitting source, usually impulse. The measuring principle is based on the analysis of the wave scattered by the particles located at the different levels of the atmosphere.

We can list for lidar(LITE - Lidar In-space Technology Experiment (Winker et al., 1996), GLAS - Geoscience Laser Altimeter System (Schutz et al., 2005), CALIOP - Cloud-Aerosol Lidar with Orthogonal Polarization (Winker et al.,

2010)) and for radar (TRMM - Tropical Rainfall Measuring Mission ([Kummerow et al., 2000](#))). They provide the altitude distribution of aerosols, cloud or precipitation structures.

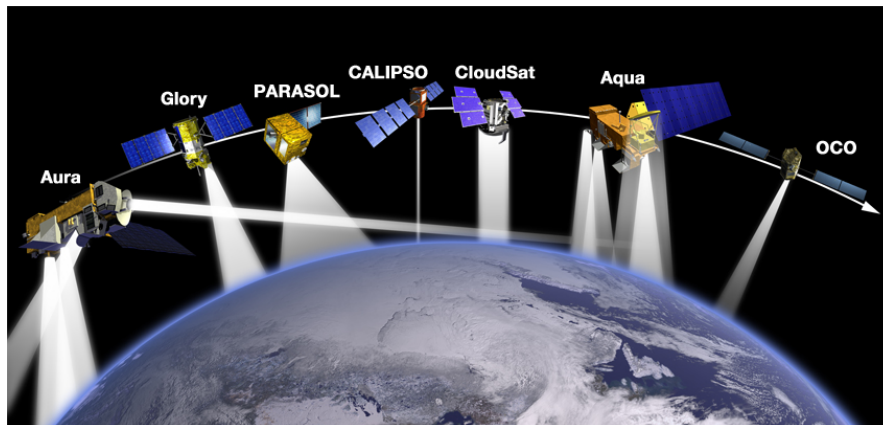


FIGURE 2.9: A-Train constellation.

The strong interest of a system resulting from the synergy between active and passive systems is to allow a quasi-three-dimensional analysis of aerosols, cloud and precipitation. Such an approach is possible with the A-Train ("Afternoon Train") satellite constellation (Fig. 2.9). It is a set of five satellites: Aqua (with 6 instruments including MODIS), Aura (4 instruments including OMI), PARASOL (with POLDER), CALIPSO (3 instruments including CALIOP), CloudSat.

2.4.5 In-situ measurements

In the opposite to remote sensing in-situ measurements mean direct contact with the respective subject such as air probes. ([McMurry, 2000b](#)). In-situ measurements of aerosol properties (size distribution, chemical composition, scattering and absorption) are performed at a number of sites, either at long-term monitoring sites, or specifically as part of intensive field campaigns. These measurements provide essential validation for global models, for example, by constraining aerosol concentrations at the surface and by providing high-quality information about chemical composition and local trends ([Flagan, 1998](#)). In addition, they provide key information about variability on various time scales. Comparisons of in situ measurements against those from global atmospheric models are complicated by

differences in meteorological conditions and because in situ measurements are representative of conditions mostly at or near the surface while the direct and indirect radiative forcings depend on the aerosol vertical profile. (IPCC, 2007).

Some of the available in situ measurement techniques are: Aerosol Mass Spectrometer (AMS) (Nash et al., 2006), Differential Mobility Analyzer (DMA) (Flanagan, 1998), Aerodynamic Particle Sizer (APS) (Volckens and Peters, 2005), Wide Range Particle Spectrometer (WPS) (Liu et al., 2010), Micro-Orifice Uniform Deposit Impactor (MOUDI) (Marple et al., 1991), Condensation Particle Counter (CPC) (McMurry, 2000a), Epiphaniometer (Gäggeler et al., 1989).

Chapter 3

Airborne sun photometer

PLASMA

Experiment is the only means of
knowledge at our disposal.
Everything else is poetry,
imagination.

Max Planck

3.1 Introduction and objectives

The initial purpose of the development of airborne multi-wavelength sun photometer was to have an instrument that would directly measure the vertical profiles of AOD at different wavelengths in order to make these data for validation of ground-based and space-borne lidar measurements. Lidar measures the backscattered laser light and the lidar equation cannot be solved without an additional constraint such as independent optical depth measurements easy to derive as long as the photometer is well calibrated. Thus, the first objective of PLASMA was to have a tool for the validation of lidar data.

It was decided to use a wide spectral range to be able to derive information on aerosol size distribution from AOD measurements (King et al., 1978). Thus, the second objective was to get the size distributions of aerosol particles at different altitudes.

Since last decades similar airborne sunphotometers were developed (Matsumoto et al., 1987; Schmid et al., 2003; Asseng et al., 2004) but the PLASMA feature is its lightness so that it can be easily installed on a small airplane or an automobile. That was the third objective: the mobility of the instrument.

As the instrument must be installed on the moving platform, the system requires accurate Sun tracking and connection to the GPS navigation system. Moreover, as the airplane speed is about 200 km/h, the frequency of the measurements at different channels must also be high enough for acquiring a whole data set within around one second. The installation on the body of the aircraft or on the roof of the automobile results in the necessity of complex computer control. A sophisticated software is required for the best automatization of the measurements.

In this chapter we'll describe the instrument, the data processing and provide illustrations of ground-based, airborne and automobile measurements.

3.2 Technical description

The instrument has two collimators both with approximately a 1.5° full angle of field of view (FOV) and a four-quadrant detector with a 6° angle of FOV. The first detector (Si) covers visible and near-infrared ranges ($0.343 \mu\text{m}$, $0.380 \mu\text{m}$, $0.441 \mu\text{m}$, $0.499 \mu\text{m}$, $0.553 \mu\text{m}$, $0.677 \mu\text{m}$, $0.869 \mu\text{m}$, $0.940 \mu\text{m}$, $1.023 \mu\text{m}$) and the second detector (InGaAs) covers middle infrared ($1.14 \mu\text{m}$, $1.24 \mu\text{m}$, $1.37 \mu\text{m}$, $1.60 \mu\text{m}$, $1.646 \mu\text{m}$, $2.25 \mu\text{m}$). The head can move in elevation ($0 - 90^\circ$) and azimuth ($0 - 360^\circ$) to be able to point any point of the sky. The rotation in azimuth can be continuous thanks to a ring power connector. Hereinafter, we will limit our study to the channels that are in atmospheric windows i.e. all channels except 0.94 , 1.14 and $1.37 \mu\text{m}$ that are located in water vapor absorption bands (Fig. 3.2).

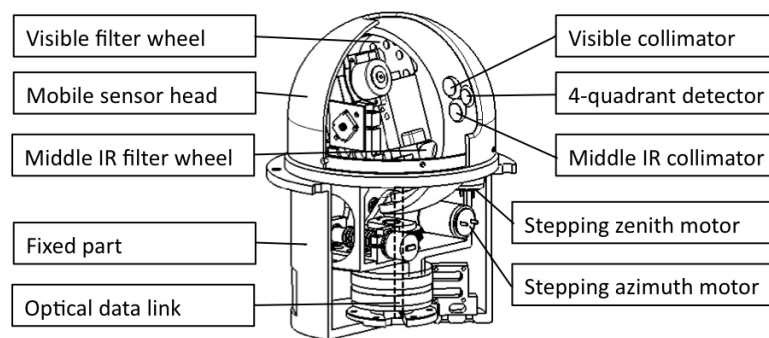


FIGURE 3.1: PLASMA scheme.

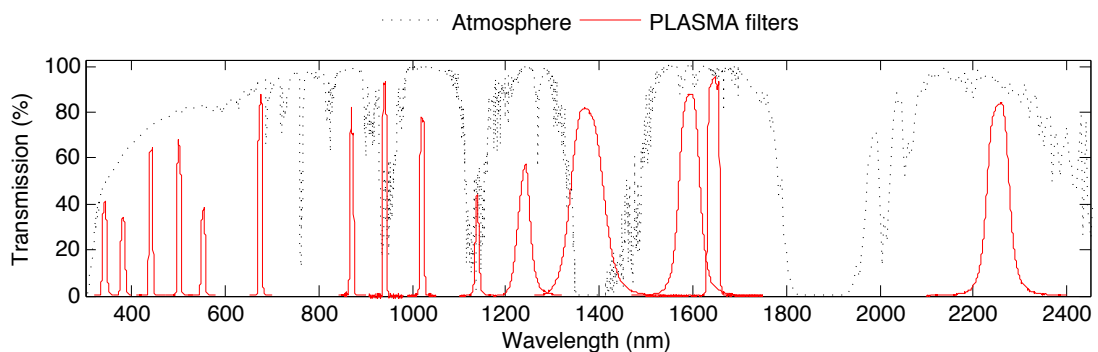


FIGURE 3.2: PLASMA filter's transmission.

A microprocessor computes the position of the Sun based on time, latitude, and longitude, provided by a GPS system. It directs the sensor head to the Sun, then the four-quadrant detector tracks precisely the Sun. If the tracking is disconnected when the aircraft is making a turn or due to the presence of clouds, then the GPS system takes over. The filters are located in two filter wheels which are rotated by a direct drive stepping motor. For a complete sequence, it takes 1.8 s for visible and near-infrared channels and 1.2 s for the middle infrared channels. For common aircraft speeds that are around of 200 km/h, it corresponds to a distance of 100 m and 66 m respectively.



FIGURE 3.3: PLASMA without jacket.

The voltage of both detectors is digitized by mean of a delta-sigma ADC. The instrument is operated with a PC that records digital count for the visible and middle infrared channels, latitude, longitude and altitude, speed and other flight parameters given by the GPS unit.

The 1.5° full angle field of view of PLASMA is comparable to the 1.2° of the CIMEL instrument of AERONET, which makes them less subject to diffuse light than instruments with broader FOV. If the effect of atmospheric forward scattering on direct solar irradiance measurements increases with particle size, aerosol optical depth and instrument FOV, it has been shown that the impact is negligible (less than 1% of AOD) for FOV smaller than 2° (Russell et al., 2004). A more recent

study (Zhao et al., 2012) confirms that in most cases for a CIMEL-like instrument, this effect can be neglected excepted for heavy dust loadings when for an AOD of 2 the relative error may reach 7%.

The InGaAs detector is temperature stabilized when the Si detector is not. Over the visible and near-infrared spectral range, the $1.023\mu\text{m}$ channel has been shown temperature sensitivity. A correction is applied throughout the processing using a coefficient of $0.35\%/^{\circ}\text{C}$ as estimated from laboratory measurements.

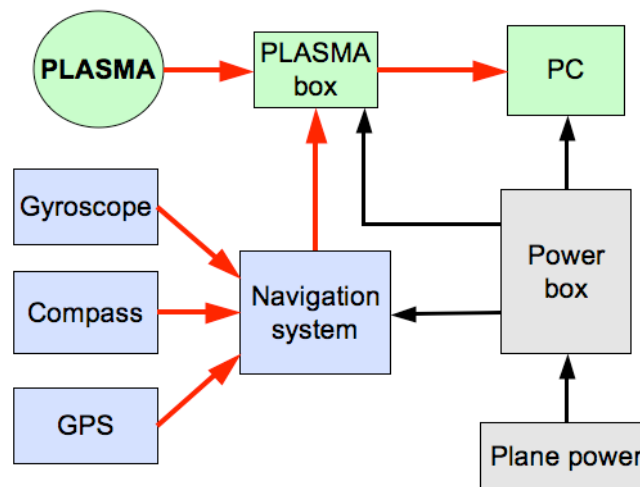


FIGURE 3.4: Scheme of the main hardware blocks.

Once installed on the aircraft, PLASMA is connected to a sophisticated navigation system, which includes a gyroscope, compass and GPS. The instrument and the PC are powered by the aircraft power (see Figure 3.4). When installed on roof of the automobile the instrument needs only GPS, and powered by the car's power.

Screenshot of PLASMA control is presented in the Figure 3.5. The program allows user to monitor the automatic operation of the tool, run it manually and to record the data.

After switching on PLASMA (1a, 1b in the Figure 3.5) immediately the head of the instrument starts to turn in order to aim the Sun (2a) according to GPS information. The position of a point on the 2b indicates the position of the sun spot on 4-quadrant detector. The signal level for the visible and infrared filters is

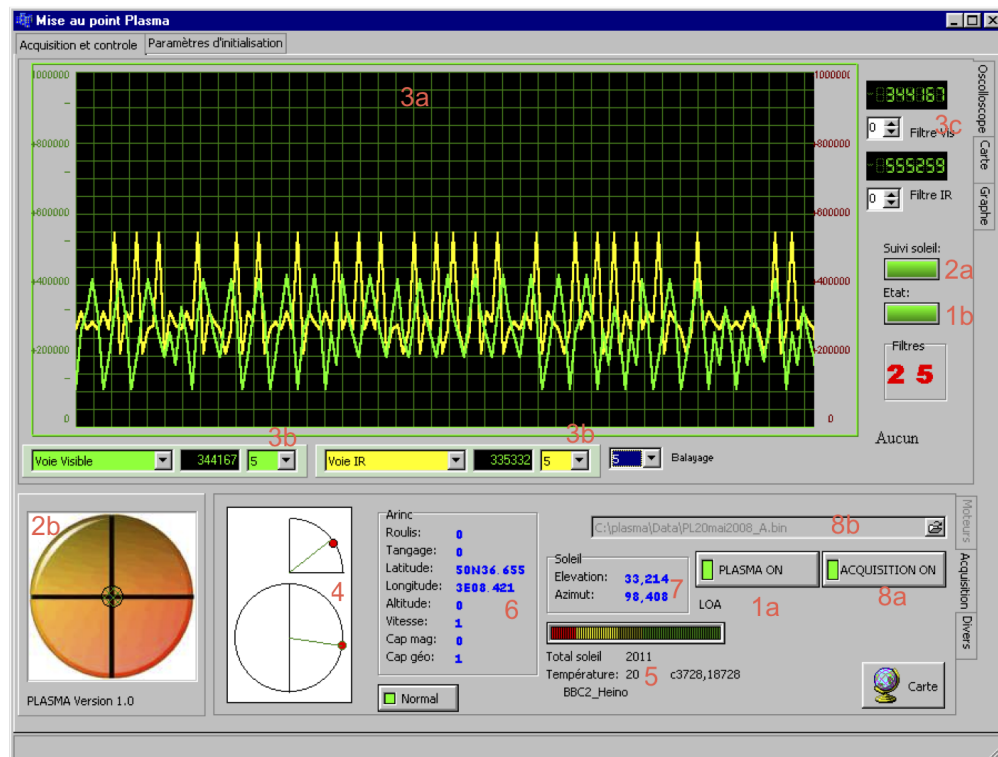


FIGURE 3.5: Screenshot of the program.

visualized on the oscilloscope 3a, with the possibility of a separate scale for both curves (3b). The user can see the signal level for each channel (3c), the position of collimators (4), the temperature of the instrument (5), the characteristics of the aircraft (automobile) movement (6) and the position of the sun (7). Once the operator checks that the instrument is working correctly, it is possible to start the data acquisition (8a), providing the file name and the path (8b).

3.3 Data processing

The digital signal ($DN(\lambda, z)$) measured by the instrument is proportional to sun irradiance $E(\lambda, z)$ (the relative Earth-Sun distance is taken to be imbedded in the extraterrestrial DN value in order to simplify the nomenclature) one can write:

$$DN(\lambda, z) = t_g(\lambda, z, \theta_s) DN_0(\lambda) e^{-\tau(\lambda, z)/\cos(\theta_s)} \quad (3.1)$$

From Eqs. (3.1) and (2.7) and after gaseous absorption correction we can obtain aerosol extinction optical depth:

$$\tau_{\text{ext}}^a(\lambda, z) = \frac{1}{m} [\ln(DN(\lambda)/t_g(\lambda, z)) - \ln(DN_0(\lambda))] - \tau_{\text{ext}}^m(\lambda, z) \quad (3.2)$$

To calculate gaseous absorption, i.e. absorption by oxygen, ozone, water vapor and other gases, we use spectral absorption lines provided in the 5S code and the mid-latitude summer atmospheric model (Tanré et al., 1990).

Molecular scattering optical depth at the altitude z is given by:

$$\tau_{\text{ext}}^m(\lambda, z) = \tau_{\text{ext}}^m(\lambda, z_0) \frac{P(z)}{P(z_0)} \quad (3.3)$$

where $\tau_{\text{ext}}^m(\lambda, z_0)$ is the molecular optical depth at the surface level z_0 and $P(z_0)$ the associated pressure.

In the UV spectral range the Rayleigh AOD is significant and has to be known with a good accuracy to be properly corrected for. Since it depends on the atmospheric pressure, a pressure gauge has been included in the PLASMA instrument. A pressure gauge was not installed on the early version of the instrument, so the pressure was estimated using the equation: $P(z) = P(z_0) \exp(-z/8.5)$, where z is the altitude of the aircraft expressed in km and 8.5 is the height scale for a standard molecular atmosphere.

3.4 Calibration

Calibration of a sun photometer consists in determining $DN_0(\lambda)$ in Eq. 3.1 for each spectral band. As band pass filters can degrade and instrument characteristics may change over time (Ichoku et al., 2002) the calibration has to be performed on a regular basis.

There are two ways to calibrate sun photometers as routinely done within the Aerosol Robotic Network (AERONET) (Holben et al., 1998): Langley method and intercalibration with master instrument (Lenoble et al., 2011). For PLASMA calibration we applied both methods. For intercalibration we used a master instrument of the AERONET/PHOTONS network.

3.4.1 Langley calibration

The typical approach to calibration is the so-called Langley (or Bouguer-Langley) method (Shaw et al., 1973), measuring the irradiance for a large range of solar zenith angles, and plotting $\ln DN(\lambda)$ versus airmass m . The extrapolation of the plotted line to $m = 0$ provides $DN_0(\lambda)$, and the slope is $-\tau(\lambda)$:

$$\ln(DN(\lambda)/t_g) = \ln(DN_0(\lambda)) - \tau(\lambda)m \quad (3.4)$$

Usually plots are made during the day for the airmass range between 5 and 2.

The calibration site has to be located in an area with very stable aerosol regime. The Langley method assumes that, during the measurements at different elevation angles, the atmosphere is temporally invariant and horizontally homogeneous (within about 50 km of the observer). Almost all calibrations of sunphotometers conducted at continental locations have the probability of being not accurate enough because of time-changing drifts in atmospheric properties. The solution is to use high-altitude mountain observatories known to present excellent optical conditions, such as the Mauna Loa (Hawaii, USA) and Izaña (Tenerife, Spain)

observatories. But even there the calibration procedure must be held during stable conditions in the mornings and performed over several days (Lenoble et al., 2011). The Langley calibration is very suitable since all spectral channels can be simultaneously calibrated but there are only few sites that meet the requirements (Shaw, 1983).

The deviation of the intercept $DN_0(\lambda)$ is a measure of the precision of the technique. If the aerosol loading is not constant, we may observe deviation from the linear regression line but such cases can be easily excluded at Mauna Loa and Izaña when Langley plots are performed.

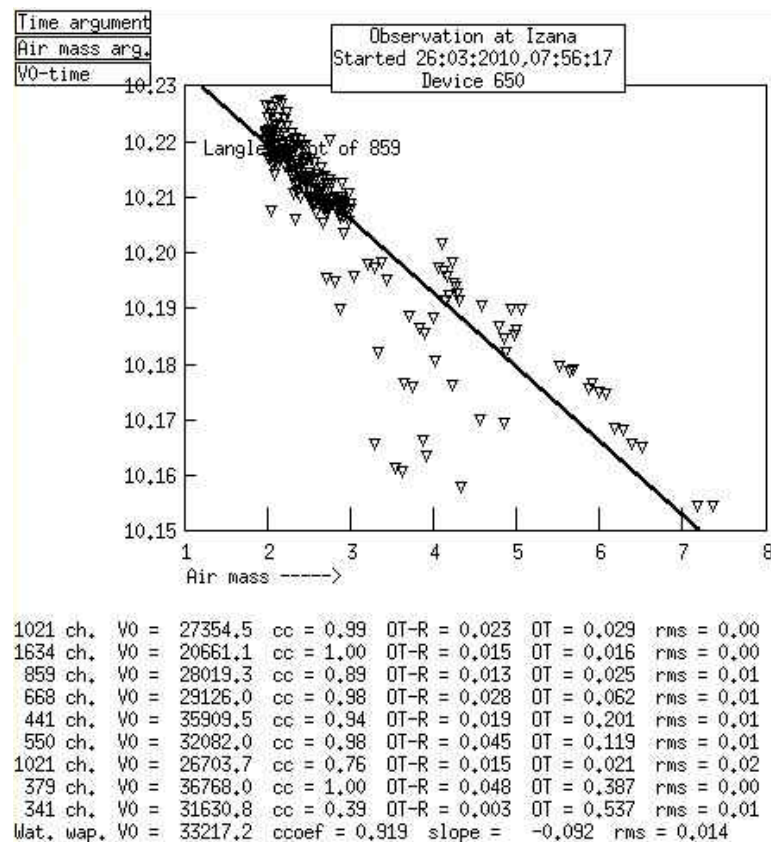


FIGURE 3.6: Langley plot provided by Demonstrat 26/03/2010.

As it is seen from Figure 3.6 the first attempt to calibrate PLASMA was unsuccessful due to instabilities of the atmosphere.

The accuracy of AOD depends on the accuracy of calibration coefficients. A 1% error in calibration coefficient leads to inaccuracy $\Delta\text{AOD} \approx 0.01$ at $m = 1$, with the error decreasing by a factor of $1/m$ as airmass increases. Usually the

profile flights last around 30 min around from 11 to 13 UTC; during this period the change of airmass is less than 5%. Since a miscalibration results in a bias in AOD but for constant airmass the value of the extinction coefficient that is the derivative of AOD is not impacted (see Eq. 3.2 and 2.9).

3.4.2 Intercalibration

When aerosol varies in time we cannot use the Langley method and calibration derived by inter comparing with another well calibrated instrument.

When the instruments are not perfectly identical, the pass bands and detector sensitivities of the two instruments (master and instrument undergoing calibration) have to be known and carefully considered in the comparison. When filters have slight differences in pass band characteristics, gaseous absorption feature can be different for one of the instruments (Lenoble et al., 2011).

Our intercalibration is performed using near-simultaneous measurements of sun irradiance by PLASMA and CIMEL sunphotometers at the same location. Spectral calibration coefficients can be found from the relation:

$$\frac{DN_0^{PLASMA}(\lambda)}{DN_0^{CIMEL}(\lambda)} = \frac{DN^{PLASMA}(\lambda)}{DN^{CIMEL}(\lambda)} \quad (3.5)$$

Several tools have been developed within the AERONET project for performing intercomparison exercise. In Fig. 3.7 we illustrate a tool included in the Demonstrat software that automatically compares AOD taken by two different instrument. In Fig. 3.8, we illustrate a second tool that computes the ratio of calibration coefficients for any spectral band.

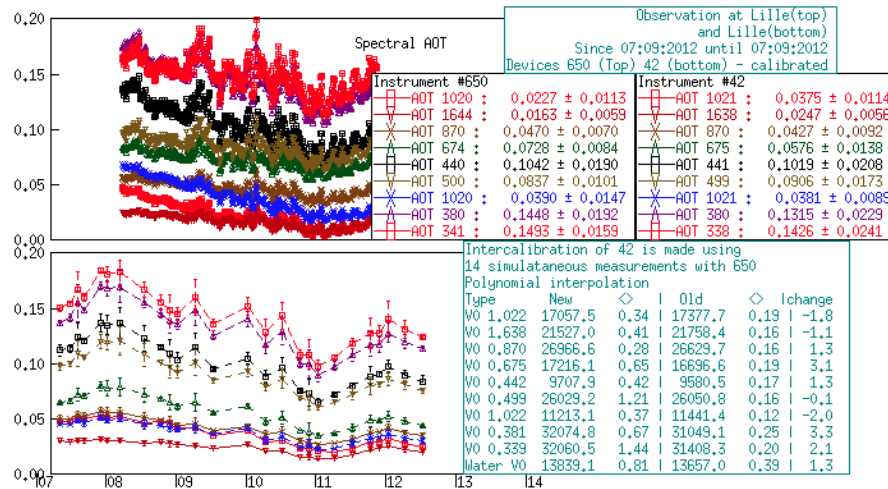


FIGURE 3.7: Illustration of the automatic calibration in Demonstrat.

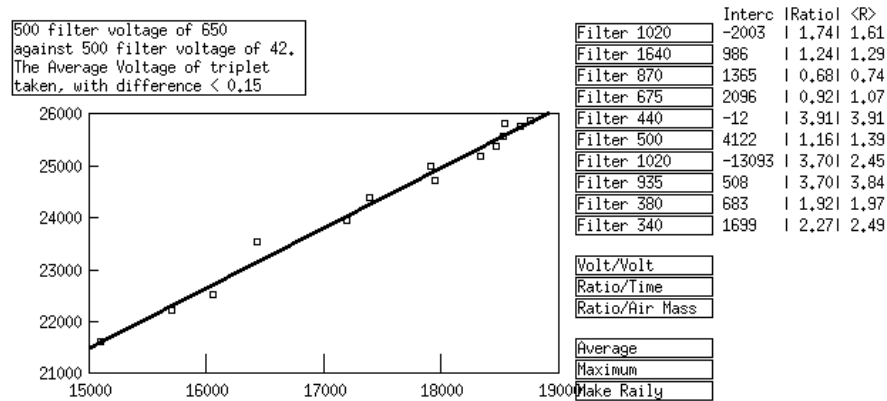


FIGURE 3.8: PLASMA vs. CIMEL digital count.

3.4.3 Evolution of the instrument and calibration campaigns

The first calibration campaign was organized in Izaña (28.3N 16.5W Elevation: 2391.0 m) Atmospheric Observatory (October 2009) and in Carpentras (44.1N 5.1E Elevation: 100.0 m) in March 2009.

The calibration coefficients calculated with Izaña and Carpentras data were applied to all data collected in Lille (50.6N 3.1E Elevation: 60.0 m) until March 2010 to obtain aerosol optical depth (AOD). The comparison with CIMEL at common wavelengths ($0.34\mu\text{m}$, $0.38\mu\text{m}$, $0.44\mu\text{m}$, $0.67\mu\text{m}$, $0.86\mu\text{m}$, $1.20\mu\text{m}$, $1.64\mu\text{m}$)

showed a good agreement between these two instruments with an accuracy ΔAOD from 0.01 to 0.02.

After modifications of some mechanical elements, a new calibration campaign was organized at Izaña in March 2010. Several measurements were then performed in LOA for different atmospheric conditions during 12 days in April–June 2010. A better agreement with CIMEL master instrument was obtained with rms AOD differences ~ 0.01 . The PLASMA calibration is not too far from the calibration requirements of AERONET master instruments ($0.002 < \Delta AOD < 0.009$) (Eck et al., 1999). A new campaign for Langley calibration was organized once again in Izaña in January 2011.

Once the technical development has been achieved, PLASMA was refurbished in March 2011. The stepping azimuth and zenith motors were replaced for better pointing capability and signal processing steps taken to improve the signal to noise ratio. We also replace all the filters, which required a new calibration of the instrument. After calibration the difference of AOD retrieved by PLASMA and CIMEL master instrument is less than 0.005 for all channels except 0.34 μm channel (see Fig. 3.10 in the Section 3.5.1).

3.5 Analysis of PLASMA ground-based, airborne and automobile measurements. Comparison with other instruments.

3.5.1 Ground-based measurements

After development of the instrument numerous measurements were performed in different places. Dates and number of measurements are presented in Table 3.1. These data are mostly integrated in the LOA Demonstrat tool to facilitate analysis.

TABLE 3.1: PLASMA ground-based measurements.

Site	Dates	Number of measurements
Lille	2010 April	8
	October	3
	2011 March	1
	April	4
	May	5
	September	1
	2012 February	2
	May	5
	July	1
	September	3
2013	February	3
	March	1
Izaña	2010 March	4
	2011 January	2
	2012 February	3
	2013 January	5
Beijing	2011 May	2
GSFC	2011 June	1
	2011 July	1
Dakar	2013 March	11
	2013 April	4
Cagliari	2013 June	5
Cap_d_En_F	2013 June	1

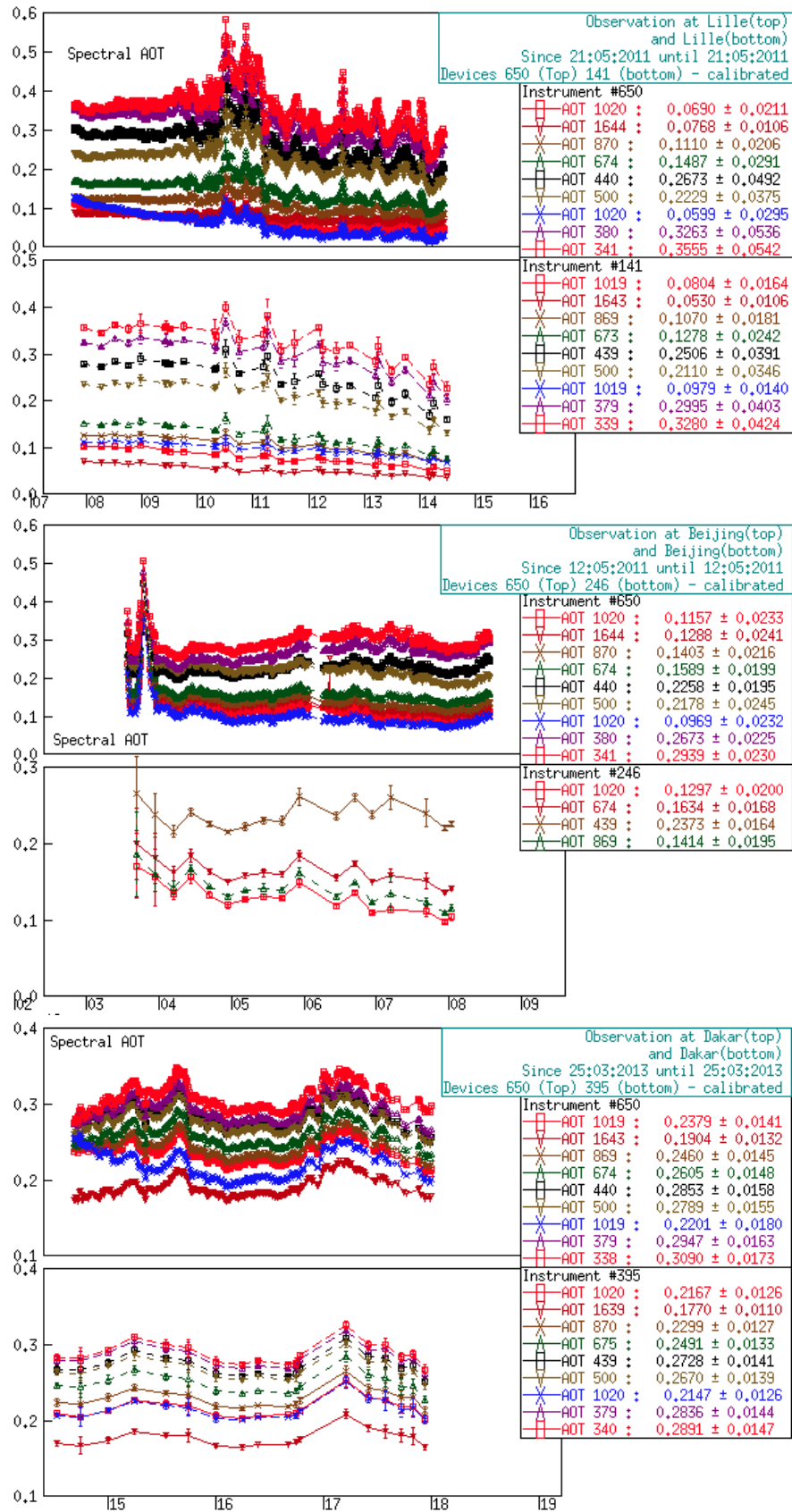


FIGURE 3.9: Examples of PLASMA ground-based measurements in Lille, Beijing and Dakar stations compared to CIMEL measurements at the same location.

On Figure 3.9 examples of PLASMA ground-based measurements in several places are presented in comparison with CIMEL instrument. Thanks to the PLASMA acquisition protocol, measurements are more frequent, which allows to better monitor the atmospheric variability.

Currently, we only analyzed results in spectral bands that are present on both PLASMA and CIMEL instruments. Of course, PLASMA covers a larger spectral range with a $2.25\mu\text{m}$ channel that is very important for aerosol size distribution inversion from spectral AOD's. Nevertheless at this stage we do not consider this wavelength since we cannot validate calibration coefficient with any other master instrument.

After the last upgrade of PLASMA in March 2011 the instrument is stable and AOD's are consistent with CIMEL measurements as reported in Fig. 3.10.

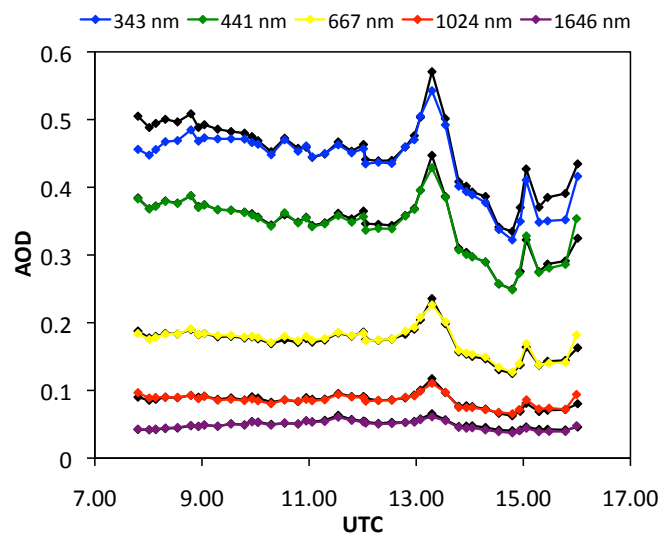


FIGURE 3.10: Comparison of simultaneous ground-based measurements of PLASMA (colored lines) and CIMEL CE-318 (black lines) 18/04/2011.

The differences observed before 9UTC and after 15UTC may come from filter out-of-band leakage resulting from incomplete blocking of solar energy from outside the filter bandpass as seen in some AERONET CIMEL instruments. In the laboratory, measurements of filters transmission such leakage wasn't observed over $\pm 100\text{ nm}$ from the central wavelength. Differences may also come from a miscalibration of this channel. Knowing the calibration coefficient within only 1%

error results in errors in the AOD of 0.025 for an airmass of 2.4 as anticipated around 7.30 in Lille in April. This effect would lead to a symmetrical behavior in the afternoon as observed in Fig. 3.10.

3.5.2 Airborne measurements

Since 2009 several airborne experiments were made in region of Lille. Except the flight on 28/05/2010, we do not report the technical flights since they were performed in any atmospheric conditions (presence of cirrus, presence of low clouds, etc.); our goal was to check the instrument and its capability to track the sun. We so present results for only 5 days (Table 3.2).

In M’Bour – Dakar region (Senegal) we flew 9 days and 17 measured profiles were acquired and processed (Table 3.2).

TABLE 3.2: PLASMA airborne measurements.

Place	Date	Time	Comments
Lille	28/05/2010	09:40 – 10:20	much instrumental noise
	12/10/2010	10:50 – 11:30	clear sky
	28/09/2011	14:50 – 15:30	clouds, turbidity
	29/09/2011	13:30 – 14:10	no data at 1700-3000 m (clouds)
	15/10/2011	08:50 – 09:20	clear sky, stable atmosphere
Dakar	26/03/2013	13:30 – 14:00	only up to 1000 m
	27/03/2013	14:00 – 14:30	stable atmosphere
		14:30 – 15:00	- // -
	28/03/2013	14:30 – 15:00	high atmospheric variability
		15:00 – 15:40	- // -
	30/03/2013	14:30 – 15:00	high atmospheric variability
		15:00 – 15:40	- //
	03/04/2013	15:00 – 15:50	clouds
		15:50 – 16:30	clear sky
	04/04/2013	14:10 – 14:40	high atmospheric variability
		14:40 – 15:10	more stable atmosphere
	05/04/2013	14:40 – 15:10	clouds
15:10 – 15:40		clear sky	
06/04/2013	14:30 – 15:00	clouds	
	15:00 – 15:30	- // -	
07/04/2013	13:00 – 13:30	clouds	
	13:30 – 14:00	- // -	

3.5.2.1 Airborne measurements in Lille region

For the airborne measurements PLASMA is mounted on the right side panel on the aircraft Piper PA-28RT-201T Turbo Arrow IV. The plane took off from the airfield Bondues and gaining altitude to the Touquet aerodrome. Because of the PLASMA location on the right door of the airplane, we could not get the sun in the instrument before making a 180° turn near the coast at an altitude of 3100m. The data recording continued until the aircraft touches the ground at the Bondues aerodrome or airport Lille Lesquin.



FIGURE 3.11: PLASMA on the plane.

Since PLASMA instrument was developed, several flights were performed in Lille: two technical flights in 2009, 6 flights in 2010 and 3 flights in 2011.

On Figure 3.12 the AOD and extinction coefficient compared with lidar measurements on 28th of May 2010 is presented. That time the ash layer from Eyjafjallajökull volcano eruption (that continued from 20 March to 23 June 2010) was observed over Lille. PLASMA operation was not stable due to technical problems and high atmospheric variability of aerosol layer and frequently occurred cirrus clouds. However, having an average over several measurements, it was possible to obtain a vertical profile of the extinction coefficient, which agrees well with the lidar.

The figure 3.13 represents the timebase of lidar measurements, which shows that the variable aerosol layer during the flight was located at an altitude of 1000-1500, as observed from PLASMA measurements.

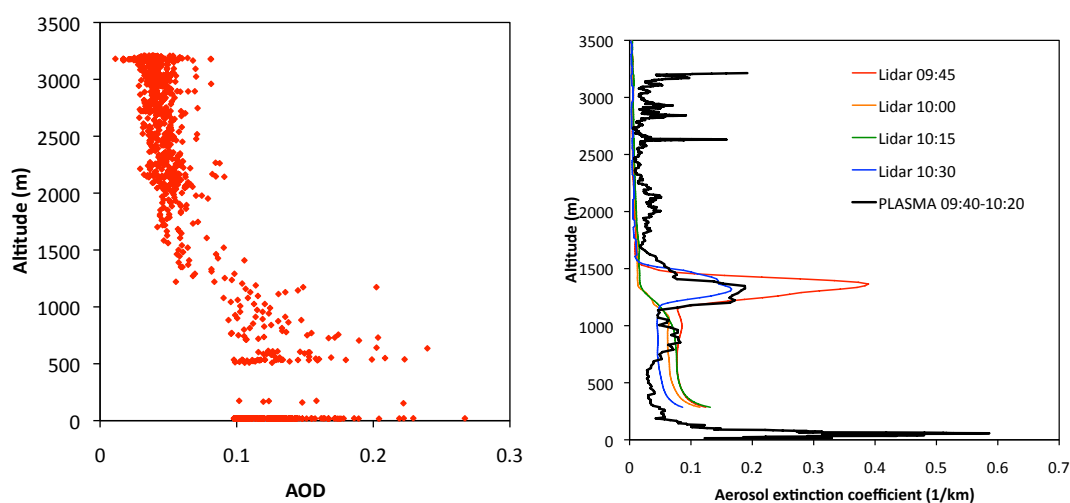


FIGURE 3.12: PLASMA AOD at 550 nm (left) and extinction coefficient compared with lidar (right) 28th of May 2010.

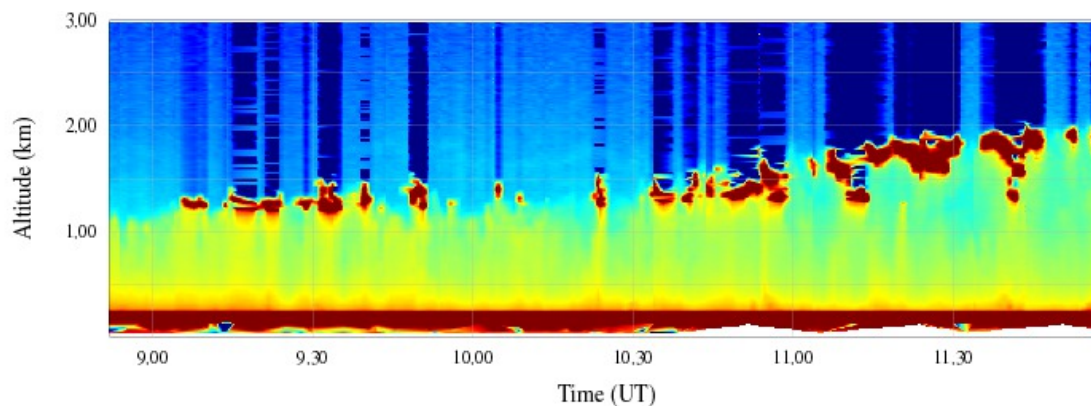


FIGURE 3.13: Timebase of lidar measurements in Lille 28th of May 2010.

During the flight, a layer of volcanic ash was observed by PLASMA and lidar (Fig. 3.14).

Figure 3.15 shows profiles of 4 flights in 2010–2011: 12/10/2010, 28/09/2011, 29/09/2011 and 15/10/2011 from the top to the bottom. The first column of graphs on the left presents the vertical profile of AOD at different wavelengths; the second (center) is the profile of extinction coefficient; the third column on the right presents the comparison of extinction at $0.553\mu\text{m}$ with lidar retrievals at $0.532\mu\text{m}$.

To get extinction profile we decided to remove all noisy data due to the presence of clouds and then to average over 10 measurements. It means that we assume



FIGURE 3.14: The picture taken during the flight over Lille 28th of May 2010 from an altitude around 1500 m.

that the state of the atmosphere was stable over 30–60 s, along 50–100 m in vertical direction and 2–4 km in horizontal direction. Altitudes below 500 m could not be observed by lidar but the profiles presented on figure 3.15 have been extended to the ground level by using the correction function based on independent measurements of AOD. Direct measurements of PLASMA can be used for validation of this function. The extinction profiles retrieved from lidar measurements are broadly consistent with PLASMA results, showing coarsely similar vertical attributes. The best agreement between aerosol extinction coefficient profiles retrieved from PLASMA and lidar data was observed 15 October 2011 when the atmosphere was stable enough as seen from AOD profile.

For other days, differences can be explained by time and space variability of aerosol and clouds. On 29 September 2011 clouds were present in the vicinity of the lidar location and the turbidity was rather high and variable, between 0.15 - 0.20 at $0.553 \mu\text{m}$ around noon; as a result data are noisier and a 50% difference of extinction coefficient at an altitude around 400 m is observed. Discrepancies can also result from spatial variability of the aerosol field; distance between both instruments was around 10 km when the airplane was on the ground, and more

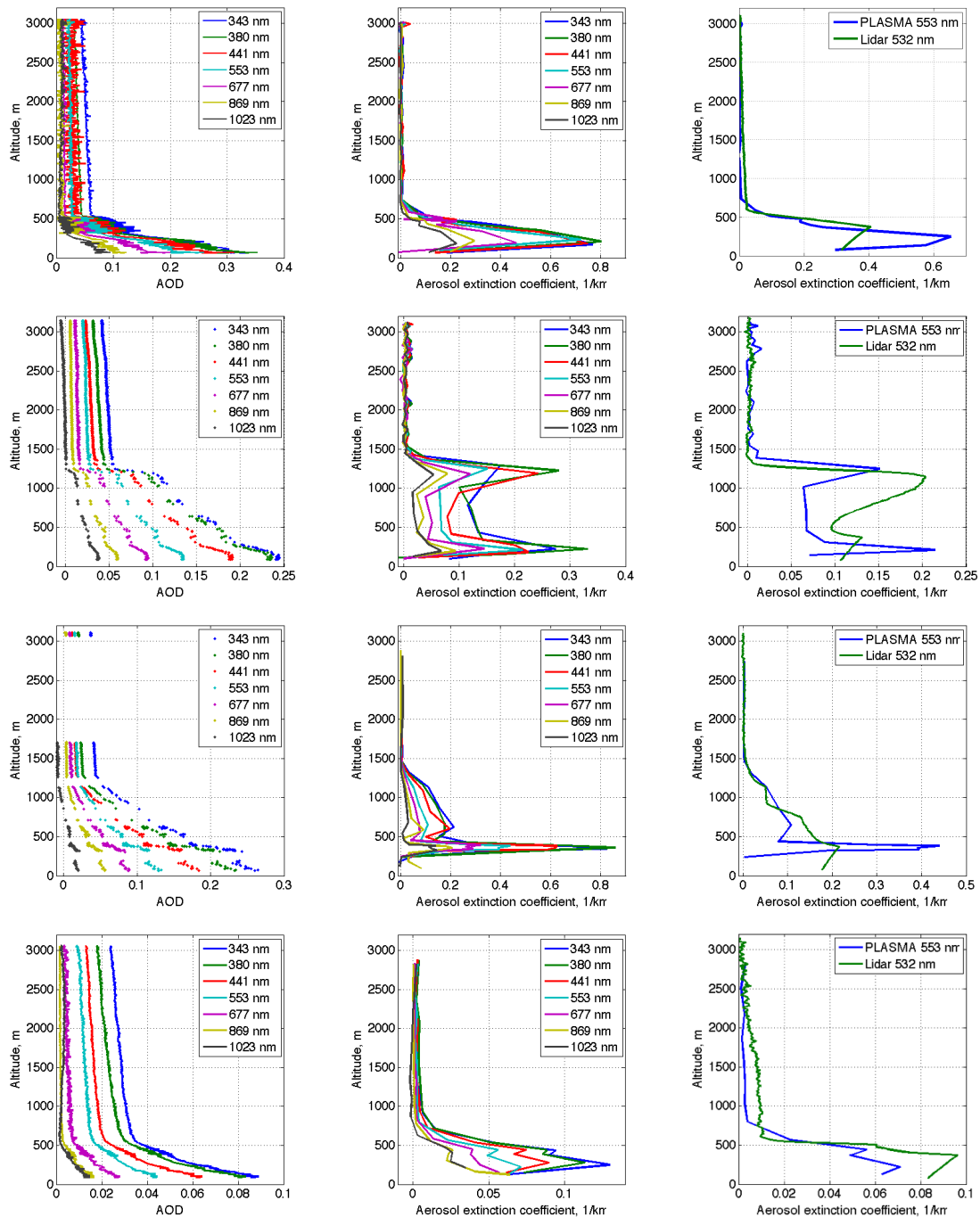


FIGURE 3.15: PLASMA AOD (left), aerosol extinction coefficient (center) at 7 channels and aerosol extinction coefficient compared with lidar (right) as a function of the altitude acquired near Lille region the 12th October 2010, 28th September, 29th September and 15th October 2011.

than 50 km when the plane was flying at the altitude of 3000 m. Moreover, the profiles take around 20 min and are compared to the nearest in time lidar profile ($\Delta t \approx 15$ min). Despite these differences, the aerosol layers are located at the same altitude and we can say that both vertical profiles are rather consistent.

3.5.2.2 M’Bour airborne experiment

From 26th of March to 7th April 2013 an airborne experiment was held with PLASMA in M’Bour, Senegal. We flew 9 days, each flight resulted in two vertical profiles from ground level up to 3100 m except the first technical flight up to 1200 m.

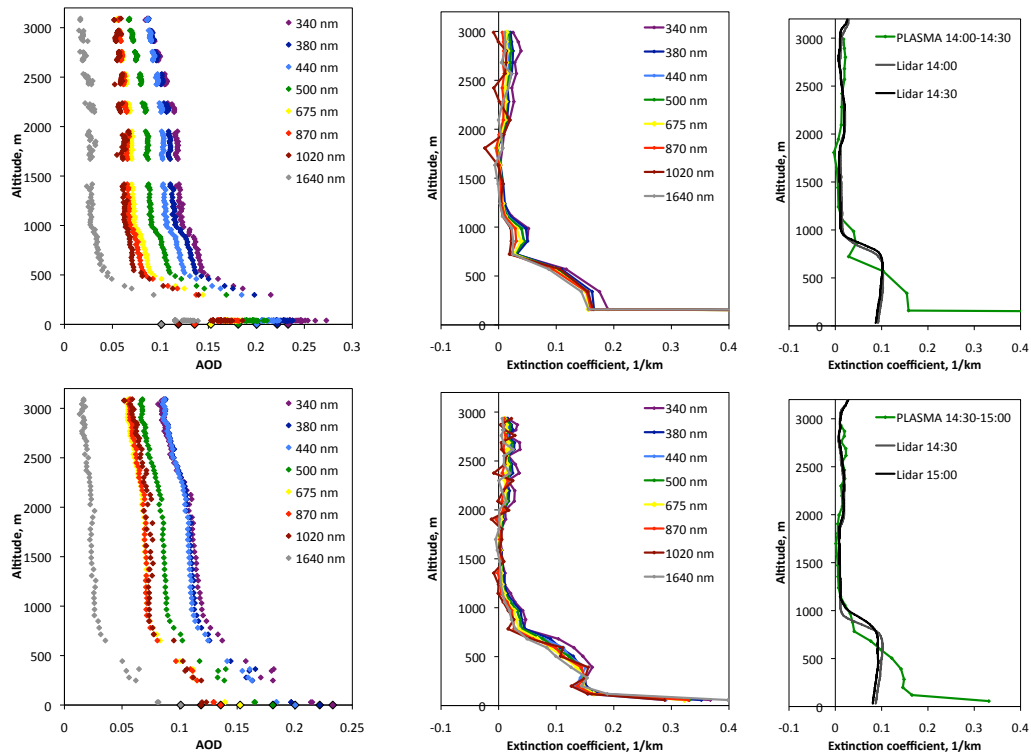


FIGURE 3.16: PLASMA AOD (left) and aerosol extinction coefficient (right) at 8 channels as a function of the altitude acquired near M’Bour region the 27th of March 2013.

In the Figures 3.16-3.21 AOD, derived extinction coefficients at the wavelengths $0.34 - 1.64\mu\text{m}$ are reported. We also report comparisons of the extinction coefficient profiles with the nearest in time lidar data. The figures also show the

AOT measurements of CIMEL sun photometer, which in most cases are in good agreement with the measurements of PLASMA at ground level.

27/03 (Fig. 3.16) stable atmospheric conditions allowed to make two profiles. The vertical profiles of the extinction coefficients are in good agreement with lidar retrieval except below 500 m where the lidar data are questionable.

28/03 and 30/03 (Fig. 3.17 and 3.18) due to higher atmospheric variability (see considerable noise in the second AOT profiles at an altitude of about 500 m) the consistency of the PLASMA and lidar measurements data below 1000 m is low.

3/04 (Fig. 3.19) due to the presence of clouds the first profile of the extinction coefficient was difficult to retrieve. The second profile is consistent with the lidar data.

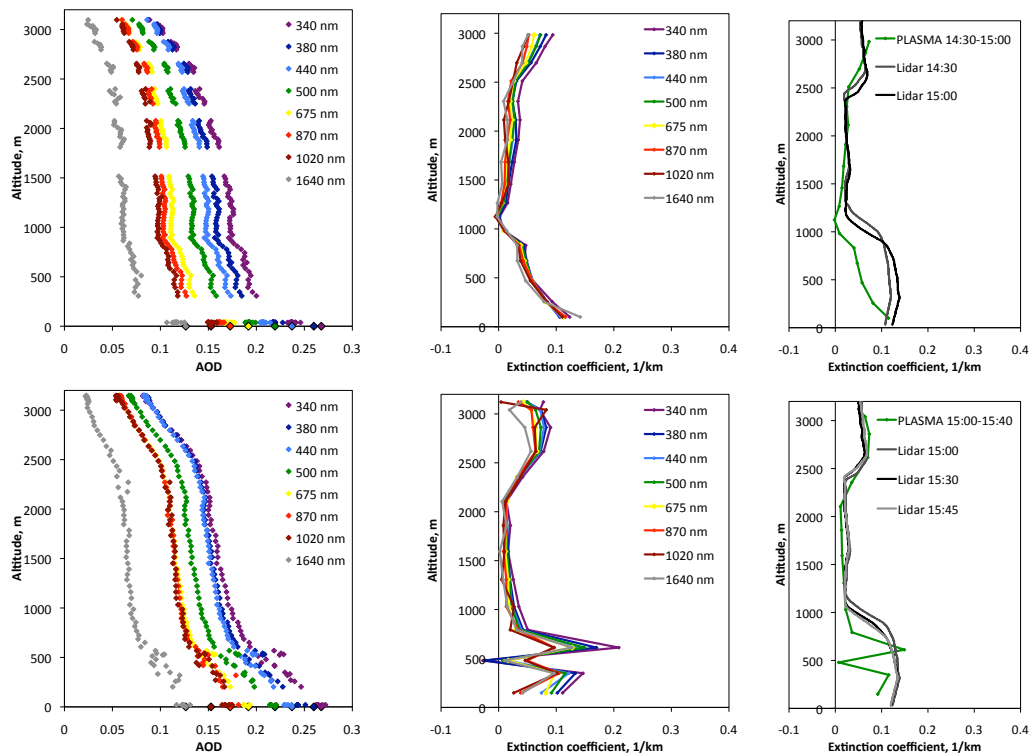


FIGURE 3.17: PLASMA AOD (left) and aerosol extinction coefficient (right) at 8 channels as a function of the altitude acquired near M' Bour region the 28th of March 2013.

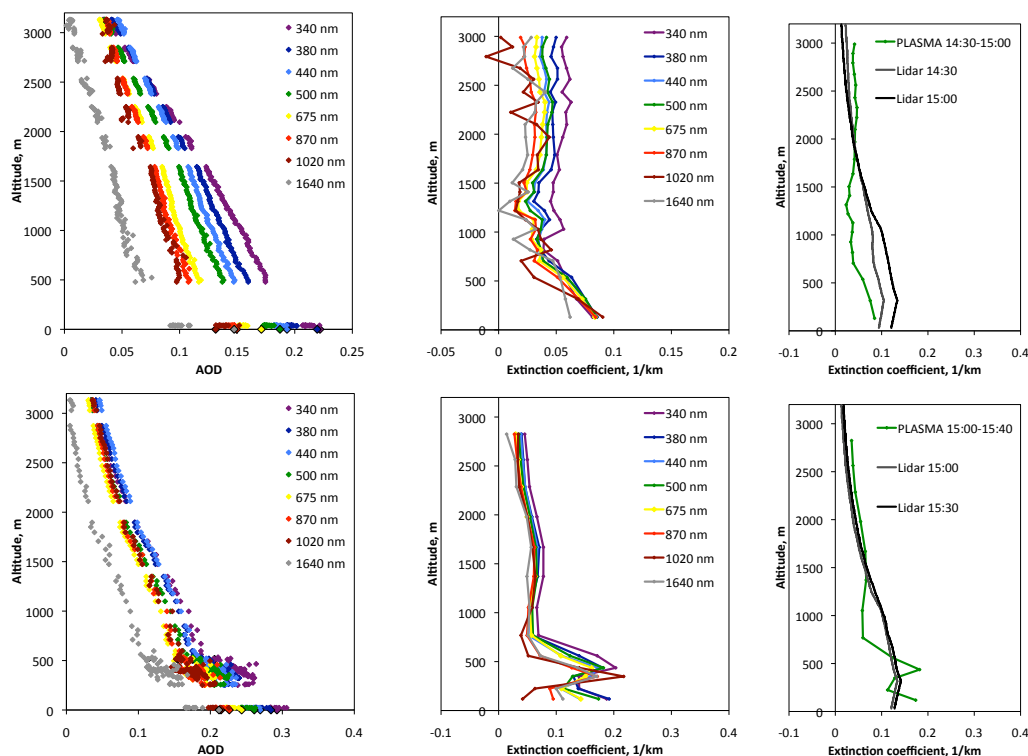


FIGURE 3.18: PLASMA AOD (left) and aerosol extinction coefficient (right) at 8 channels as a function of the altitude acquired near M'bour region the 30th of March 2013.

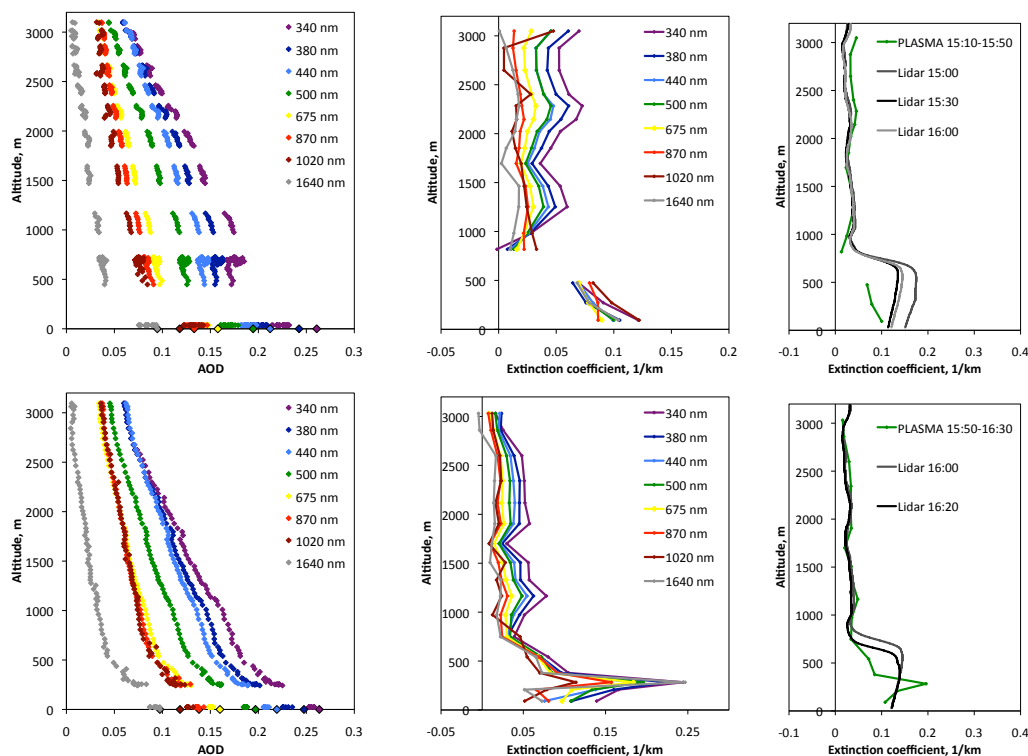


FIGURE 3.19: PLASMA AOD (left) and aerosol extinction coefficient (right) at 8 channels as a function of the altitude acquired near M'bour region the 3rd of April 2013.

4/04 (Fig. 3.20) while taking the first profile there was a strong atmospheric variability (possibly clouds), which results in the increasing of AOT with the altitude. At the same time PLASMA AOD on the ground was inconsistent with CIMEL measurements. The second profile AOT is smoother and therefore, the profile of the extinction coefficient is in good agreement with the lidar profiles.

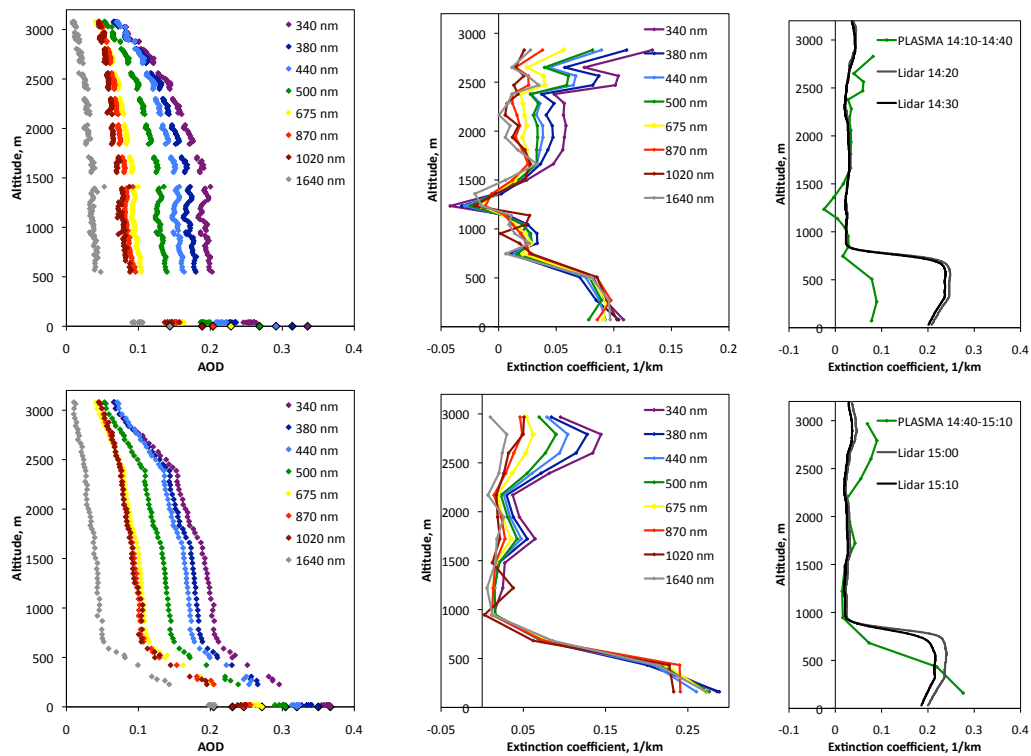


FIGURE 3.20: PLASMA AOD (left) and aerosol extinction coefficient (right) at 8 channels as a function of the altitude acquired near M’Bour region the 4th of April 2013.

5/04(Fig. 3.21) due to the presence of the clouds the AOT profiles have the incorrect dependence with increasing with the altitude and also much noise (approximately at 500 m and 1000-1500 m in the first profile). Consequently, the extinction coefficient has peaks which can not be considered as the aerosol layer, and negative values.

From the analysis of onboard measurements of PLASMA in M’Bour region we can conclude that in the case of low atmospheric variability and in the absence of clouds the photometer measures AOT with the high accuracy and hence the extinction coefficient is obtained correctly, including the altitudes below 500 m.

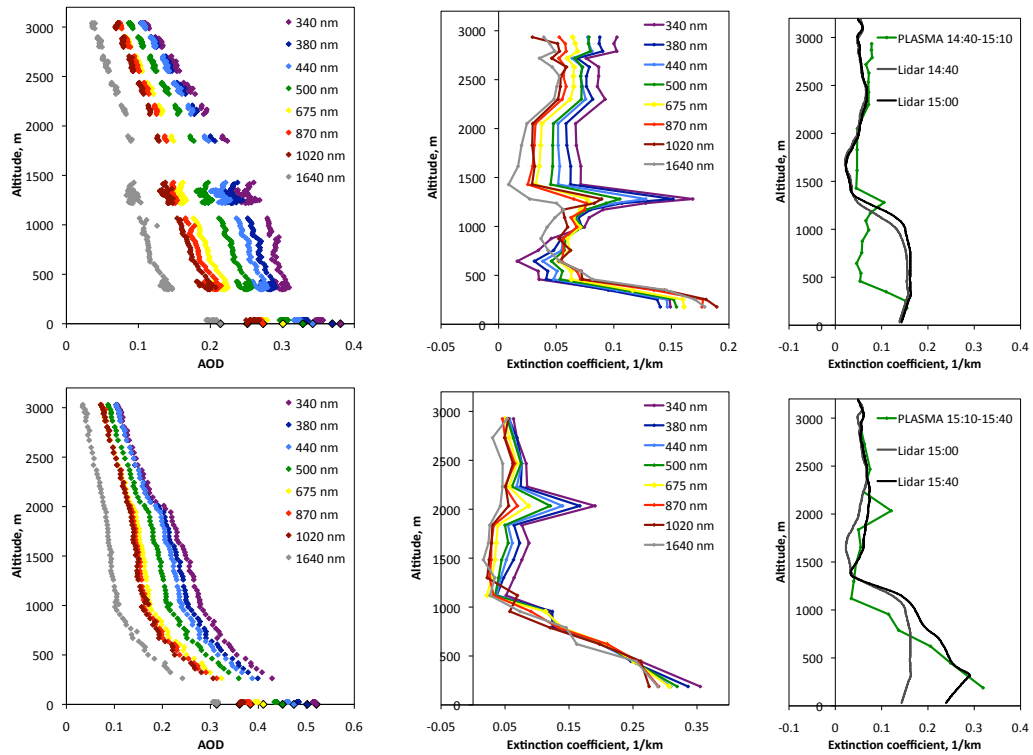


FIGURE 3.21: PLASMA AOD (left) and aerosol extinction coefficient (right) at 8 channels as a function of the altitude acquired near M'Bour region the 5th of April 2013.

This provides a basis for further corrections of processing algorithms of lidar measurements. The figures show that below 500 m the lidar profile of the extinction coefficient may not be reliable. The PLASMA data give a more complete picture of the distribution of aerosols at these altitudes. For example, 27/03, we believe that the PLASMA profiles are more accurate than lidar ones.

3.5.3 Automobile measurements

In addition to airborne measurements it is also possible to set up PLASMA on the roof of an automobile in order to obtain horizontal profiles of AOD. In mountain areas, we can also get vertical profiles using measurements performed at different altitudes.

Two automobile experiments were conducted, a first one in Tenerife island, Spain covering the altitude from 2400 m down to sea level and a second one campaign including the mobile lidar system in the frame of DRAGON campaign in Washington DC region, USA.

TABLE 3.3: PLASMA automobile measurements.

Place	Date	Time (UTC)
Tenerife	13/01/2011	09:50 – 12:50
		15:00 – 17:40
Washington DC	30/06/2011	13:10 – 17:30
	01/07/2011	13:50 – 18:50
	02/07/2011	14:00 – 18:30
	05/07/2011	10:50 – 15:10
	07/07/2011	12:30 – 20:30
	10/07/2011	14:00 – 17:00
	11/07/2011	12:00 – 22:10
	14/07/2011	12:10 – 18:00
	16/07/2011	12:10 – 20:50
	17/07/2011	12:30 – 14:00
	18/07/2011	12:10 – 17:30
	20/07/2011	14:30 – 18:20
21/07/2011	12:00 – 19:40	
22/07/2011	13:20 – 17:30	

3.5.3.1 Tenerife experiment

In January 2011 an experiment was successfully carried out on the island of Tenerife, Spain. In Tenerife island there are good conditions to carry out car experiment: altitude difference from the sea level to 2400 m is easily covered in around 1 hour, and there is only 30 km horizontal distance between the top and the bottom of the mountain.

PLASMA was installed on the top of a car of the Izaña Atmospheric Observatory (Fig. 3.22a). A trip to El Medano and back to the Observatory was performed for obtaining two profiles of AOD. The itinerary (Fig. 3.22a) was chosen for having less shadow. We had the opportunity to compare the PLASMA AOD with the Izaña AERONET site (alt. 2391m) very close to the road-way. There are also two additional AERONET sites, La Laguna (alt. 590 m) and Santa Cruz (alt. 54 m), that were located at a distance of 40 km from our measurements.

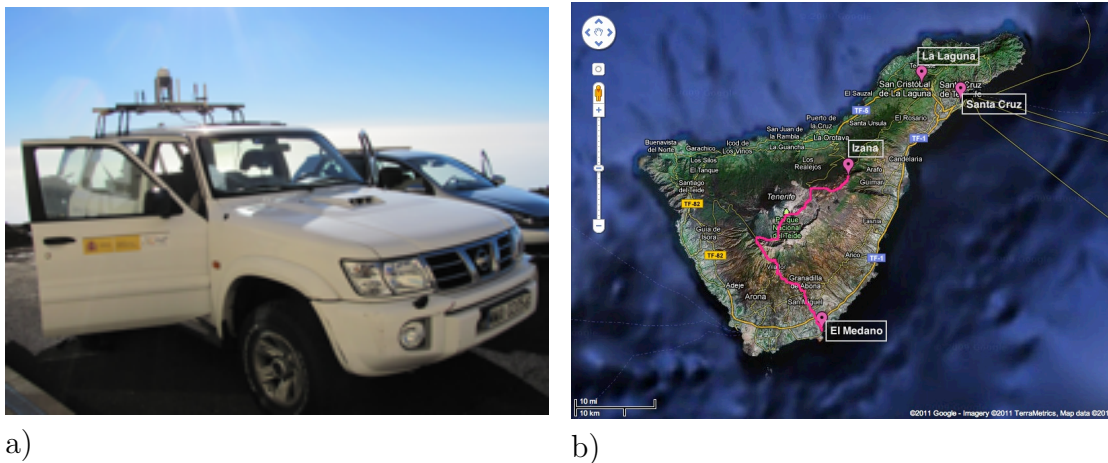


FIGURE 3.22: a) Installation on the AEMET car; b) PLASMA route on Tenerife and AERONET cites.

In the process of car-based measurements, PLASMA perfectly followed the Sun despite the shocks during the experiment. When passed through a shade with simultaneous turn of a road PLASMA looked at the sun again in few seconds. However, at an altitude of 200 m the electronic part of the instrument failed and data were very noisy. After restarting at the sea level PLASMA at the sea level,

it continued to work correctly all the way back to Izaña station but there were many clouds and haze, so we cannot analyze the upward path.

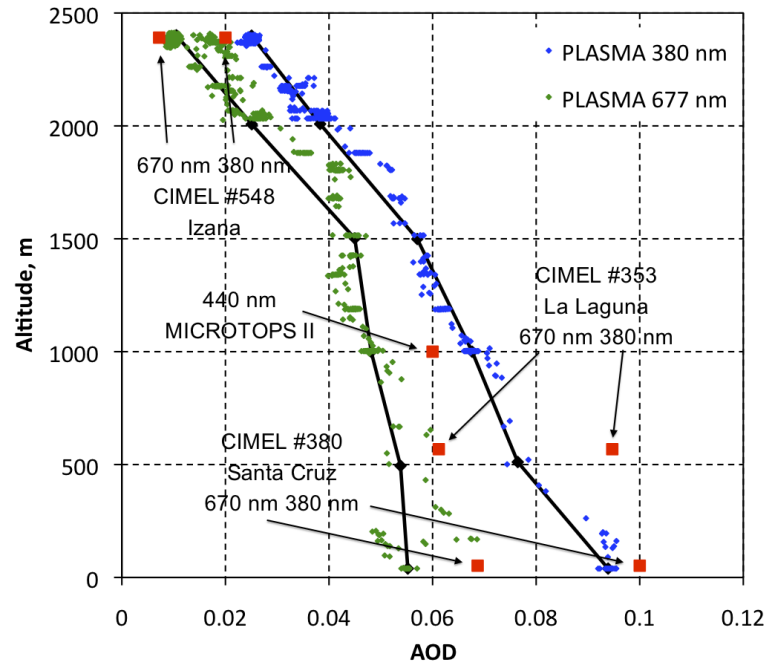


FIGURE 3.23: Vertical profiles of AOD during car experiment 13/01/2011 in Tenerife island, Spain.

The Figure 3.23 shows the vertical profiles of AOD at $0.380\mu\text{m}$ and $0.677\mu\text{m}$ compared to the three AERONET stations. Additional measurement performed at the altitude of 1000 m using a sunphotometer MICROTUPS II (Morys et al., 2001) is reported for $0.440\mu\text{m}$. Measurements of PLASMA are consistent with other instruments with $\Delta AOD \approx 0.01$ and the differences for the low altitude sites could clearly be explained by the distance between the instruments.

To retrieve the extinction coefficient from the measurement seems to be more challenging because of low values of optical depth. Nevertheless, already at this stage it is clear that the instrument can be used when installed on the roof of an automobile. It could be used both in places with different altitudes to obtain vertical profiles, and in flat areas to get the horizontal profiles of AOT.

3.5.3.2 DRAGON campaign

In July 2011 we took part for 15 days in the DRAGON (Distributed Regional Aerosol Gridded Observation Networks) campaign in the Washington DC and Baltimore USA region (Holben et al., 2011; Mortier et al., 2012). Washington DC metropolitan area has been selected in summer time since, climatologically, the greatest aerosol loading is observed in July and August (AOD at 500 nm close to 0.45 and Ångström exponent (between 440-870 nm) around 1.74). The goal was to obtain AOD horizontal profiles simultaneously with mobile lidar system between several sunphotometers in grid points.

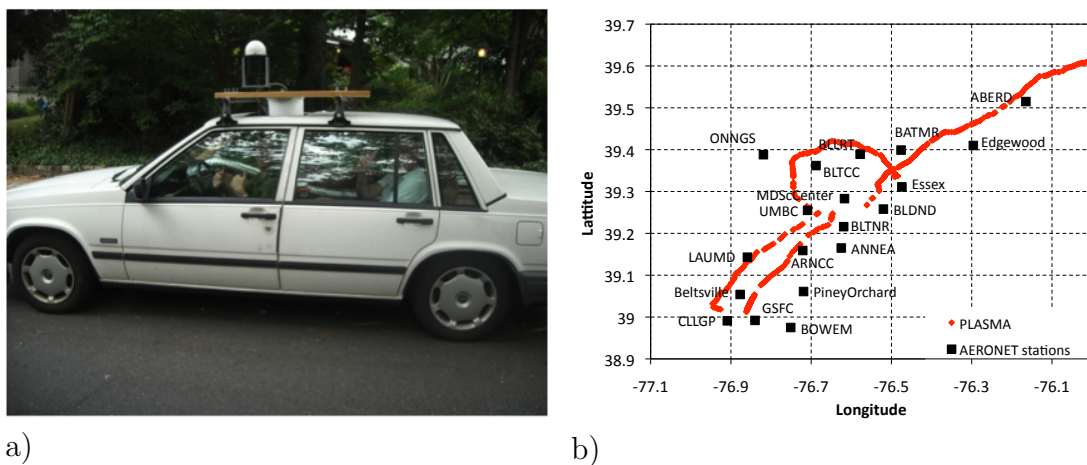


FIGURE 3.24: Installation of PLASMA and mobile lidar in the roof of the automobile (a) and PLASMA route 20/07/2011 and the closest AERONET stations during DRAGON campaign (b).

The mobile system (Fig. 3.24a) performed about 4300 km (≈ 80 hours of observation), mainly repeating the Hyattsville – Fair Hill or Hyattsville – Edgewood transects (back and forth). Fig. 3.24b shows the PLASMA path between AERONET-DRAGON stations. Here we analyze the measurements on 20/07/2011 since a high level AOD was observed with a strong spatial variability within the area.

Fig. 3.25 presents the AOD measured by PLASMA and AERONET CIMEL stations on the 20th of July 2011. The aerosol layer was not uniform over the area since from the GSFC to ABERD AERONET stations (1 hour drive) the

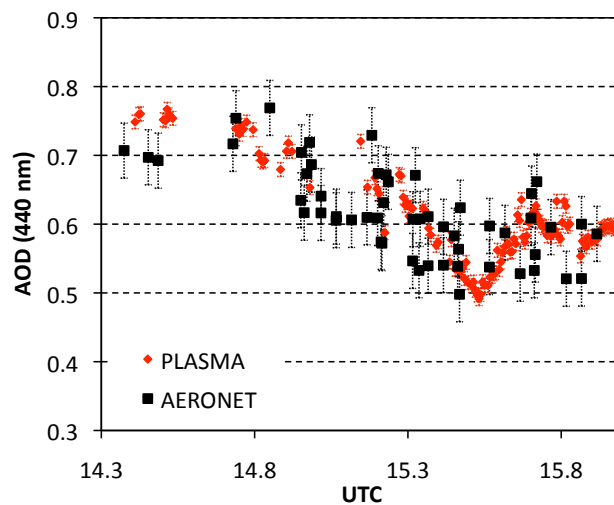


FIGURE 3.25: Comparison of PLASMA and AERONET AOD. AERONET measurements were at the distance 2-10 km.

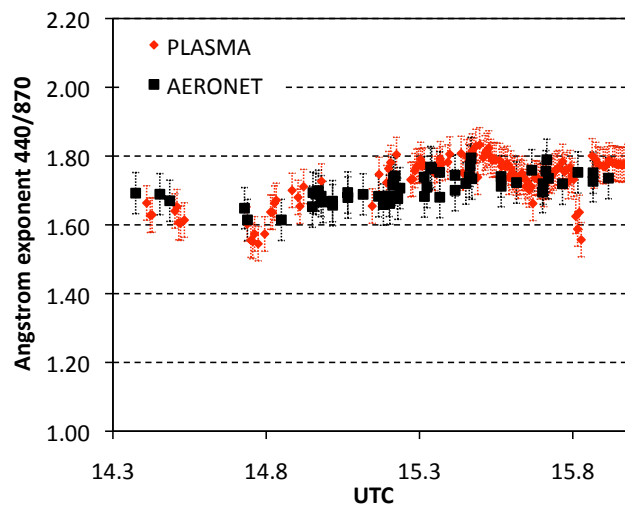


FIGURE 3.26: Comparison of PLASMA and AERONET Ångström exponent.

AOD (0.44 μm) varied from 0.44 to 0.72. PLASMA measured a maximum AOD at around 14.4UTC very close to GSFC station and a minimum AOD at about 15.5UTC, near the Essex station. More to the North, in the direction of the Edge-wood, AOD level increased. During the time of the experiment, each DRAGON stations never showed AOD time-variation larger than 0.05 over 1 hour (this variation is illustrated by confidence intervals on the Fig. 3.25). The differences between PLASMA and AERONET measurements for some stations can be explained considering the distances of 2-10 km between them as well as the high variability of

the aerosol field. The agreement observed again between the two data sets confirms that PLASMA provides reliable measurements with an accuracy comparable to AERONET.

The Ångström exponent derived from PLASMA is compared to level 2 AERONET data in Fig. 3.26. While the AOD varies by more than 50%, the Ångström exponent is more stable. The moderate variations around the mean value of 1.70 can result from cloud contamination or possible humidity effects. Both instruments display consistent spatial/temporal variations.

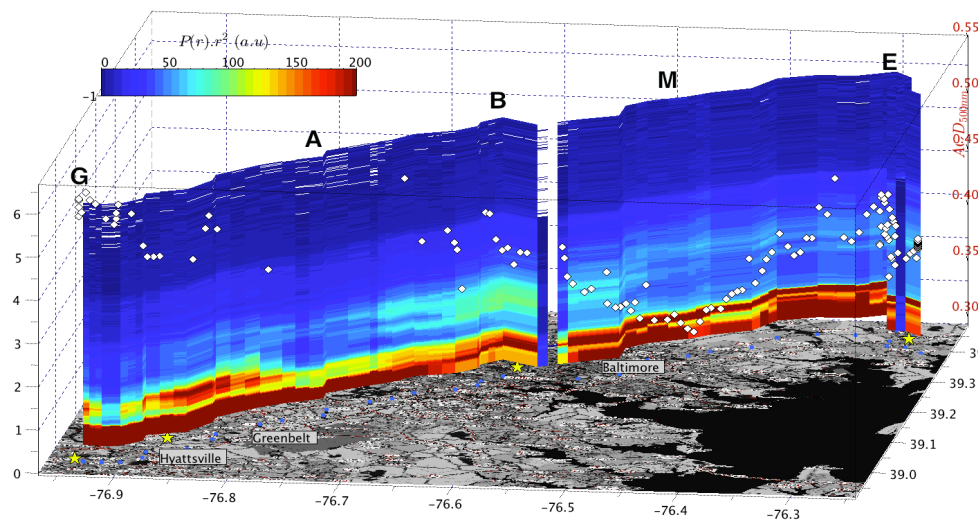


FIGURE 3.27: Attenuated backscattered lidar signal measured between Hyattsville (G) and Edgewood (E) with PLASMA AOD (white diamonds). From [Mortier et al. \(2012\)](#)

As PLASMA was installed on the automobile together with mobile lidar system we present here an example of combined measurements plot on Fig. 3.27 ([Mortier et al., 2012](#)). The high variability of aerosol along the path is also well observed. The vertical profiles show aerosol particles distributed up to 3,5-4 km with maximum particle concentration occurred near the ground, within the first kilometer. However, there was some secondary maximum between 1,5 and 2,5 km, as for example over Baltimore city (point B in Fig. 3.27). AOD measured over Baltimore city (0.4) smaller compared to the value (G, 0.54) measured near GSFC at the beginning of this transect. It can be explained by a lower particle concentration

within the first kilometer as shown by lidar on Fig. 3.27 over Baltimore. From B to M AOD continues to decrease and reaches a minimum of about 0.31. According to lidar profile, the atmospheric layer over point M is in general more transparent, especially over 1 km. Finally, from point M to Edgewood (E), at the end of this transect, AOD value increased up to 0.42 which can be mostly attributed to higher particle concentration within the first kilometer.

So, using mobile lidar-sunphotometer system we can obtain information about aerosol layer which is especially useful in areas with atmospheric inhomogeneities.

3.6 Conclusion

After three years of effort for improving the PLASMA technical part (adjustment, testing and calibration), we can now state that instrument performs high-precision measurements of AOT over a wide spectral range. The tests and comparisons with AERONET sunphotometer showed that the measurement error is only $\Delta(AOD) = 0.005$. This corresponds to the accuracy of master CIMEL instrument.

When installed on an aircraft or on an automobile, PLASMA accurately track the Sun through the 4-quadrant detector and provide high speed measurements of vertical or horizontal profiles of AOT in 15 wavelengths. The measurement error is $0.005 \leq \Delta(AOD) \leq 0.01$.

PLASMA measurements can be used as reference data for the validation of lidar measurements, since it provides direct sun measurements down to the ground level, while the lidar cannot observe below 300-500 m. Let us mention that using the mobile lidar-photometric system for taking horizontal transects of the atmosphere is very promising.

Chapter 4

Inversion of aerosol size distribution from spectral AOD measurements

The study and knowledge of the universe would somehow be lame and defective were no practical results to follow.

Marcus Tullius Cicero

4.1 Introduction

As airborne sunphotometer PLASMA has 15 channels over a wide spectral range, it is possible to retrieve the aerosol size distribution over a given size range which depends on the lower and upper wavelengths. Thanks to airborne data, we can obtain the size distribution of aerosol particles at different wavelengths at different altitudes.

A similar problem is solved in the framework of the AERONET network but both direct sun (over a smaller spectral range compared to PLASMA) and angular measurements of CIMEL CE-318 sunphotometer are used, and the retrieved vertically integrated parameters are the particle size distribution, refractive index, single scattering albedo and shape. The approach is attractive since it provides additional information on the vertical distribution of particle sizes.

In general, of course, in the absence of angular measurements the number of input data is too small for inversion of multiple parameters. For instance, it is not expected to retrieve the refractive index but in order to find out what are the limitations of the inversion technique of the atmospheric aerosol microphysical parameters using only the direct sun measurements, it is necessary to conduct a sensitivity study of the algorithm to changes in the various input parameters, in particular the complex refractive index and the noise level.

First, we describe the inversion algorithm, the sensitivity study to the refractive index (section 4.3.3) and to the measurement noise (Section 4.3.4). Then the results of measurement inversion are provided: the Section 4.4 is dedicated to the inversion of PLASMA data from ground-based measurements with its comparison with AERONET inversion; the results of DRAGON data retrieval are discussed in the Section 4.5; the most important results of airborne measurements inversion are reported in the Section 4.6.

4.2 Inversion algorithm

There are two steps in retrieving optical and microphysical properties of atmospheric aerosols from radiation measurements. The first is so-called "forward model" where the retrieval algorithm is used to simulate the atmospheric radiation assuming known atmospheric and surface properties. The second called "inversion" procedure where the inverse transformation is used for retrieving the aerosol properties from the radiation field.

At present, the forward-modeling doesn't present strong difficulties thanks to the powerful computers with fast operational processing. The inversion process is much more complicated especially for the case of simultaneous retrieval of many unknowns. Theoretically, the best solution of the problem is given by the best fitting of the measurements through the continuous space of all possible solutions. Unfortunately, often several different combinations of aerosol parameters produce the same, or nearly the same, radiation distribution. Therefore, the general solution is fundamentally nonunique mainly in the presence of noise in the measurements (Dubovik, 2004).

There are numerous inversion methods widely adopted in atmospheric remote sensing and other geophysical applications, such as the methods given by Kalman (1960); Philips (1962); Tikhonov (1963); Twomey (1963, 1975); Strand and Westwater (1968); Chanine (1968); Turchin and Nozik (1969); Rodgers (1976).

The inversion procedure presented by Dubovik and King (2000) proposes adding a priori assumptions on smoothness of the size distribution or spectral smoothness of the optical properties in the inversion procedure to constrain the solution while reproducing the measurement field within the error bars established for the measurements. This method is the one used in AERONET network to retrieve the aerosol properties from the measurements of the ground-based CIMEL sun-photometers. The modification of this method by excluding the angular measurements from input parameters is used in the present study. Its short description is presented below.

4.2.1 Forward problem

The atmospheric aerosol particles can be modeled as a mix of spherical particles. For a constant refractive index m at all wavelengths the relationship between the spectral AOD and the aerosol size distribution is given by the integral relation

(King et al., 1978):

$$\tau_a(\lambda) = \int_0^{\infty} \int_{z_1}^{z_2} \pi r^2 Q_{ext}(r, \lambda, m) n(r, z) dz dr \quad (4.1)$$

where r is particle radius; $n(r, z)$ is particles size distribution, i.e. aerosol number density in the radius range r to $r + dr$; $m(\lambda)$ is complex refractive index; Q_{ext} is extinction efficiency factor derived from Mie theory.

Assuming the same aerosol type along the vertical, we can write

$$\tau_a(\lambda) = \int_{r_{min}}^{r_{max}} K_{\tau}(r, \lambda, m) n_l(r) dr \quad (4.2)$$

where $n_l(r)$ is the size distribution in a layer of the atmosphere and $K_{\tau}(r, \lambda, m) = \pi r^2 Q_{ext}(r, \lambda, m)$ is the kernel function of optical thickness which can be computed from Mie theory for homogeneous spherical particles when the refractive index is known.

Eq. 4.2 can be rewritten in terms of a volume size distribution $v(\ln r) = dV(r)/dv \ln r$ where $v(\ln r)$ represents the volume of particles per unit area per unit log radius interval:

$$\begin{aligned} \tau_a(\lambda) &= \int_{r_{min}}^{r_{max}} \frac{3}{4\pi r^3} K_{\tau}(r, \lambda, m) v(\ln r) d \ln r, \\ &= \sum_{j=1}^q \int_{r_j}^{r_{j+1}} \frac{3}{4\pi r^3} K_{\tau}(r, \lambda, m) v(\ln r) d \ln r, \\ &\approx \mathbf{A}(r, \lambda, r) \mathbf{f}_l(\ln r) \end{aligned} \quad (4.3)$$

The variation of the optical thickness kernel function $(3/(4\pi r^3))K_{\tau}(r, \lambda, m)$ depends on r^3 in case of small particles (Rayleigh scattering limit) and on r^{-1} in case of large particles (geometric optics limit).

We can express Eq. 4.3 in terms of matrix

$$\mathbf{g} = \mathbf{A}\mathbf{f} + \epsilon \quad (4.4)$$

where $g_i = \tau_a \lambda_i$, $i = 1, 2, \dots, p$ is the vector representing AOT measurements at p discrete wavelengths; $f_j = v_l(\ln r_j)$ the volume aerosol size distribution at q discrete sizes; $\epsilon_i = \epsilon(\lambda_i)$ the vector of errors in $\tau_a(\lambda)$. The modified kernel function is approximated by matrix \mathbf{A}_τ as follows:

$$A_{i,j} = \int_{\ln r_j - \Delta \ln r / 2}^{\ln r_j + \Delta \ln r / 2} \frac{3}{4\pi r^3} K_\tau(r, \lambda, m) d \ln r \quad (4.5)$$

Solving Eq. 4.4 relatively to \mathbf{g} (i.e. finding the spectral optical thickness from known size distribution of the aerosol particles) is the forward problem.

4.2.2 Inversion problem

The forward problem consists in finding the vector \mathbf{g} from matrix equation 4.4. The retrieval problem is the inverse problem to solve this equation relative to \mathbf{f} , i.e. to find the size distribution of aerosol particles from known spectral AOT.

If we ignore the error vector ϵ in 4.4 the solution is

$$\mathbf{f} = \mathbf{A}^{-1}\mathbf{g}. \quad (4.6)$$

This equation is the special case when the number of measurements is equal to the number of unknowns. If the matrix \mathbf{A} has linearly independent and non-zero rows, Eq. 4.6 gives a unique solution. The measurement uncertainties lead to uncertainties in the solution vector according to

$$\Delta \mathbf{f} = \mathbf{A}^{-1}\epsilon. \quad (4.7)$$

The size distribution solution is stable if the rows of the matrix \mathbf{A} are linearly independent and very different. Usually the kernel function for one individual measurement is broad and overlaps the measurement next to it, the rows of the matrix \mathbf{A} differ slightly from one to another and are nearly linearly dependent, and by considering uncertainties $\Delta\mathbf{f}$ can be quite large, and the solution is unstable.

If the system of equations is overdetermined, i.e. there are more equations, or measurements, than unknowns (q), such situation can be used to minimize the solution errors. Usually the properties of the noise in the observations \mathbf{f} are known, and then the best solution of the overdetermined system of equations can be found by choosing the fitting errors as close as possible to the expected distribution of errors in \mathbf{f} .

The agreement of the fitting errors Δg with a known error distribution can be evaluated using the probability density function (PDF) as a function of modeled errors $P(\Delta\mathbf{g})$: the higher the $P(\Delta\mathbf{g})$ the closer the modeled $\Delta\mathbf{g}$ is to the known statistical properties. Thus, the best solution \mathbf{a}^{best} should result in modeled errors corresponding to the most probable error realization, i.e., to the PDF maximum:

$$P(\Delta\mathbf{g}) = P(\mathbf{g}^*(\hat{\mathbf{a}}) - \mathbf{g}) = P(\mathbf{g}^*(\hat{\mathbf{a}}) | \mathbf{g}) = \max \quad (4.8)$$

where $\mathbf{g}^*(\hat{\mathbf{a}})$ is the vector of retrieved measurements using the derived aerosol properties $\hat{\mathbf{a}}$ (aerosol size distribution, spectral real and imaginary refractive indices).

This principle is the well-known Maximum Likelihood Method (MLM). The PDF written as a function of measurements $P(\mathbf{g}^*(\hat{\mathbf{a}}) | \mathbf{g})$ is called the Likelihood Function. The MLM is one of the strategic principles of statistical estimation that provides statistically the best solution in many senses.

If the error PDF is described by a normal distribution, then the MLM is reduced to a particular case widely known as the least-square solution. The basic principle of this method relies on the fact that the normal (or Gaussian) distribution is the expected and most appropriate function for describing random noise. Hence the

normal PDF for each vector \mathbf{g} of measurements can be written in the form:

$$P(\mathbf{g}^*(\hat{\mathbf{a}}) | \mathbf{g}) = ((2\pi)^m \det(\mathbf{S}_\epsilon))^{-1/2} \exp\left(-\frac{1}{2} (\mathbf{g}^*(\hat{\mathbf{a}}) - \mathbf{g})^T \mathbf{S}_\epsilon^{-1} (\mathbf{g}^*(\hat{\mathbf{a}}) - \mathbf{g})\right) \quad (4.9)$$

where T denotes matrix transposition, \mathbf{S}_ϵ is the covariance matrix of the vector \mathbf{g} , $\det(\mathbf{S}_\epsilon)$ denotes the determinant of \mathbf{S}_ϵ , and p is the dimension of vectors \mathbf{g} and $\mathbf{g}^*(\hat{\mathbf{a}})$.

In the simplest case of only one source of data (e.g., spectral aerosol optical thickness as for PLASMA data inversion), the principle of maximum likelihood requires that the best estimate for the solution for the aerosol properties corresponds to the maximum value of Eq. 4.9, which in turn is equivalent to minimizing the term in the exponential in Eq. 4.9. Thus we seek to minimize the square norm defined by:

$$Q_1 = \epsilon^T \mathbf{S}_\epsilon^{-1} \epsilon = \sum_{i=1}^p \sum_{j=1}^p (\mathbf{g}_i^*(\hat{\mathbf{a}}) - \mathbf{g}_i) \mathbf{S}_\epsilon^{-1}_{ij} (\mathbf{g}_j^*(\hat{\mathbf{a}}) - \mathbf{g}_j) \quad (4.10)$$

where ϵ is the error vector denoting deviations from the measurements and the forward model, and defined in the same way as in Eq. 4.4.

[Dubovik and King \(2000\)](#) refer to the introduction of constraints as adding virtual measurements, where the constraints are treated mathematically in an identical way to real measurements. This is an obvious way of reducing the ambiguity associated with an ill-posed problem, but the introduction of erroneous constraints is itself equivalent to adding, along with more information, additional error. That error would have a non-random characteristic and would result in systematic errors, or biases. Thus it is important to add only valid and physically rational constraints to the possible solutions.

As an example, the constraint in the second derivative term of the size distribution can be introduced in the similar way that in Eq. 4.4:

$$Q_2 = \sum_{i=1}^p \sum_{j=1}^p f_i H_{ij} f_j \quad (4.11)$$

where H_{ij} is the matrix defined as

$$\begin{pmatrix} 1 & -2 & 1 & 0 & \dots & \dots & \dots & \dots & 0 \\ -2 & 5 & -4 & 1 & 0 & \dots & \dots & \dots & 0 \\ 1 & -4 & 6 & -4 & 1 & 0 & \dots & \dots & 0 \\ 0 & 1 & -4 & 6 & -4 & 1 & 0 & \dots & 0 \\ \dots & \dots \\ 0 & \dots & \dots & 0 & 1 & -4 & 6 & -4 & 1 \\ 0 & \dots & \dots & \dots & \dots & 0 & 1 & -2 & 1 \end{pmatrix} \quad (4.12)$$

The minimization process, now, should be applied over the new function Q defined as

$$Q = Q_1 + \gamma Q_2 \quad (4.13)$$

where γ is a non-negative Lagrange multiplier, which serves to weight the contribution of the smoothness constraint, relative to the contribution of the measurements.

Let us note that applying the methodology of MLM to the direct Sun measurements and using the same constrain as in Kings inversion, we get the same expressions and the solution that comes out is again (making $\sum_k (\partial Q / \partial f_k) = 0$):

$$\mathbf{f} = (\mathbf{A}^T \mathbf{S}_\epsilon^{-1} \mathbf{A} + \gamma \mathbf{H})^{-1} \mathbf{A}^T \mathbf{S}_\epsilon^{-1} \mathbf{g} \quad (4.14)$$

Dubovik and King (2000) proposes different constrains (logarithmic derivatives) but also retrieves the refractive index. After the introduction of the MLM theory, we can now formulate that the solution of the Duboviks inversion will be

given by the minimum of the function:

$$Q = \sum_{k=1}^5 \gamma_k [f_k^* - f_k(a)]^T (W_k)^{-1} [f_k^* - f_k(a)] \quad (4.15)$$

where the vector \mathbf{f}_1 correspond to the logarithms of $\tau(\lambda)$ at the selected wavelengths, the vector \mathbf{f}_2 correspond to the logarithms of the normalized radiance at the selected wavelengths, the vector \mathbf{f}_3 includes the values of the size distribution smoothing function, and \mathbf{f}_4 and \mathbf{f}_1 include the values of $n(\lambda)$ and $k(\lambda)$ smoothing functions. The matrix W_k are the weight matrices of random error in the input data sets. The vector a includes the logarithm of the retrieved values of the size distribution in the grid points and the values of the real and the imaginary part of the refractive index at the selected wavelengths. Finally, the Lagrange coefficients γ_k are defined from statistical considerations as the ratios of the error variances $\Delta_k = \epsilon_1^2 / \epsilon_2^2$. The multivariable search for the minimum of Eq. 4.15 is implemented by a stable numerical procedure combining matrix inversion and univariant relaxation according to [Dubovik et al. \(1998\)](#).

4.2.3 Inversion products

The AERONET inversion code provides aerosol optical properties in the total atmospheric column derived from the direct and diffuse radiation measured by AERONET Cimel sun/sky-radiometers. AERONET inversion development and research activities are described in the papers by [Dubovik and King \(2000\)](#); [Dubovik et al. \(2000, 2002a,b, 2006\)](#); [Sinyuk et al. \(2007\)](#). Hereinafter, we only consider AOD measurements but the assumption concerning aerosol properties are the same.

It was shown in many studies that a bimodal lognormal function is the most appropriate model for aerosol particle size distributions ([Whitby, 1978](#); [Shettle](#)

and Fenn, 1979; Remer and Kaufman, 1998):

$$\frac{dV(r)}{d \ln r} = \sum_{i=1}^2 \frac{C_{V,i}}{\sqrt{2\pi}\sigma_i} \exp \left[-\frac{(\ln r - \ln r_{V,i})^2}{2\sigma_i^2} \right] \quad (4.16)$$

where $C_{V,i}$ is the particle volume concentration, $r_{V,i}$ is the median radius, and σ_i is the standard deviation.

For both modes aerosol particles are assumed to be partitioned into two components: spherical and non-spherical. The spherical component is modeled by an ensemble of polydisperse, homogeneous spheres (complex index of refraction is the same for particles of all sizes). The non-spherical component is a mixture of polydisperse, randomly-oriented homogeneous spheroids. Atmosphere is assumed plane-parallel and vertical distribution of aerosol is assumed homogeneous in the almucantar inversion and bi-layered for the principal plane inversion. The statistically optimized inversion and corresponding retrieval error estimates are obtained under the assumption of uncorrelated log-normally distributed errors. This optimization accounts for different levels of accuracy in the measurements (e.g. the standard deviation for error in $\tau(\lambda)$ is assumed 0.01 for standard instrument and 0.005 for master instrument).

The AERONET retrieval provides aerosol parameters (i.e., size distribution, complex refractive index and partition of spherical/non-spherical particles) and products computed from the retrieved aerosol properties (e.g. phase function, single scattering albedo, spectral and broad-band fluxes, etc.). In addition, the output provides random and possible systematic (resulted from possible biases in measurements) errors for most of the retrieved characteristics.

The volume particle size distribution $dV(r)/d \ln r$ ($\mu\text{m}^3/\mu\text{m}^2$) is retrieved in 22 logarithmically equidistant bins in the range of sizes $0.05\mu\text{m} \leq r \leq 15\mu\text{m}$. The real $n(\lambda)$ ($1.33 \leq n(\lambda) \leq 1.6$) and imaginary $k(\lambda)$ parts of the complex refractive index ($0.0005 \leq k(\lambda) \leq 0.5$) are retrieved from the sky radiance measurements that are not available in our case, which requires to conduct a sensitivity study for this parameter (see next section). The inversion code finds the minimum within

the size interval from 0.194 to 0.576 μm . This minimum is used as a separation point between fine and coarse mode particles. Furthermore, the retrieval provides estimates of effective radius r_{eff} , standard deviation σ and volume concentrations $C_V(\mu m^3/\mu m^2)$ for both fine and coarse modes of the retrieved size distribution.

4.3 Sensitivity study of the inversion code

When the capabilities and limitations of the Dubovik's algorithm has been already largely described, the ability to retrieve microphysical parameters based on spectral AOD only using the same algorithm (as in the case of airborne sunphotometer PLASMA measurements) is not fully understood. Obviously, the inversion of the refractive index in this case is impossible, so we have to assume that it is known in advance. Such an assumption requires detailed consideration and sensitivity study to the refractive index for estimating the corresponding impact on the size parameters.

4.3.1 Description of the chosen aerosol types

We chose five types of aerosol (desert dust, biomass burning, urban clean, urban industrial and maritime aerosols) that cover most of the possible aerosol conditions. Long-term measurements of AERONET network show that these aerosol types in their pure forms are observed in the following sites: Solar Village (Saudi Arabia), Mongu (Zambia), Goddard Space Flight Center (Maryland, USA), Mexico (Mexico), Lanai (Hawaii, USA). The optical and microphysical parameters of these types were obtained and fully described by [Dubovik et al. \(2002a\)](#).

Solar Village - Desert dust aerosol

Solar Village (24.9N, 46.40E, Elevation: 790 m) is an important solar powered electricity generating system situated in the Arabian desert approximately 50 km northwest of Riyadh. The aerosol registered in this site present optical properties representative of the so-called pure desert dust, without contamination by urban pollution.

The size distribution is the function of the aerosol optical depth at 1020 nm. Values of the parameters for the fine and the coarse mode are computed using the expressions given in Table 4.1. The values of the imaginary part of the

refractive index at other wavelengths (340, 380, 500, 550, 1240, 1640, 2250 nm) were computed by the linear interpolation.

TABLE 4.1: Optical properties of aerosol in Solar Village (after Dubovik et al. (2002a)).

Range of optical thickness; $\langle\tau\rangle$	$0.1 \leq \tau(1020) \leq 1.5$; $\langle\tau(1020)\rangle = 0.17$
n	1.56 ± 0.03
$k(440/670/870/1020)$	$0.0029/0.0013/0.001/0.001 \pm 0.001$
$r_{Vf}(\mu m)$; σ_f	0.12 ± 0.05 ; 0.40 ± 0.05
$r_{Vc}(\mu m)$; σ_c	2.32 ± 0.03 ; 0.60 ± 0.03
$C_{Vf}(\mu m^3/\mu m^2)$	$0.02 + 0.02\tau(1020) \pm 0.03$
$C_{Vc}(\mu m^3/\mu m^2)$	$-0.02 + 0.98\tau(1020) \pm 0.04$

Mongu - Biomass burning aerosol

The AERONET station Mongu (15.25S, 23.15E, Elevation: 1107 m) is located in the airport of Mongu, the capital of the western region in Zambia. The aerosol in this region contains a lot of high-absorbing smoke due to the savanna burning annually from July to November.

Concentrations and radii of both modes of the size distribution are the functions of the aerosol optical depth at 440 nm (table 4.2). The values of the refractive index do not depend on the aerosol optical depth, its the imaginary part is one order of magnitude higher than in the other aerosol types.

TABLE 4.2: Optical properties of aerosol in Mongu (after Dubovik et al. (2002a)).

Range of optical thickness; $\langle\tau\rangle$	$0.1 \leq \tau(440) \leq 1.5$; $\langle\tau(440)\rangle = 0.38$
n ; k	1.51 ± 0.01 ; 0.021 ± 0.004
$r_{Vf}(\mu m)$; σ_f	$0.12 + 0.025\tau(440) \pm 0.01$; 0.40 ± 0.01
$r_{Vc}(\mu m)$; σ_c	$3.22 + 0.71\tau(440) \pm 0.043$; 0.73 ± 0.03
$C_{Vf}(\mu m^3/\mu m^2)$	$0.12\tau(440) \pm 0.04$
$C_{Vc}(\mu m^3/\mu m^2)$	$0.09\tau(440) \pm 0.02$

GSFC - Urban clean aerosol

The AERONET calibration center at NASA's Goddard Space Flight Center in Greenbelt, Maryland (38.99N, 76.84W, Elevation: 87 m) is located 20 km from Washington inside the Boston-Washington megalopolis which is a heavily urbanized area. The aerosol in GSFC has the lowest absorption values of the urban aerosol.

Concentrations and radii of both modes of the size distribution are the functions of the aerosol optical depth at 440 nm (table 4.3). The values of the real part of the refractive index also depends on $\tau(440)$ and the imaginary part is very low ($\langle k \rangle = 0.003$) as the aerosol is slightly absorbing.

TABLE 4.3: Optical properties of aerosol in GSFC
(after Dubovik et al. (2002a)).

Range of optical thickness; $\langle \tau \rangle$	$0.1 \leq \tau(440) \leq 1.0$; $\langle \tau(440) \rangle = 0.24$
n ; k	$1.41 - 0.03\tau(440) \pm 0.01$; 0.003 ± 0.003
$r_{Vf}(\mu\text{m})$; σ_f	$0.12 + 0.11\tau(440) \pm 0.03$; 0.38 ± 0.01
$r_{Vc}(\mu\text{m})$; σ_c	$3.03 + 0.49\tau(440) \pm 0.021$; 0.75 ± 0.03
$C_{Vf}(\mu\text{m}^3/\mu\text{m}^2)$	$0.15\tau(440) \pm 0.03$
$C_{Vc}(\mu\text{m}^3/\mu\text{m}^2)$	$0.01 + 0.04\tau(440) \pm 0.01$

Mexico - Urban industrial aerosol

The site is located in the high-populated and polluted Mexico city (19.33N, 99.18W, Elevation: 2268 m). The aerosol has the highest absorption among the urban aerosols with the mean value of the imaginary part of the refractive index of $\langle k \rangle = 0.014$.

Concentrations and radii of both modes of the size distribution are the functions of the aerosol optical depth at 440 nm (table 4.4).

TABLE 4.4: Optical properties of aerosol in Mexico
(after Dubovik et al. (2002a)).

Range of optical thickness; $\langle\tau\rangle$	$0.1 \leq \tau(440) \leq 1.8$; $\langle\tau(440)\rangle = 0.43$
n ; k	1.47 ± 0.03 ; 0.014 ± 0.006
$r_{Vf}(\mu m)$; σ_f	$0.12 + 0.04\tau(440) \pm 0.02$; 0.43 ± 0.03
$r_{Vc}(\mu m)$; σ_c	$2.72 + 0.60\tau(440) \pm 0.23$; 0.63 ± 0.05
$C_{Vf}(\mu m^3/\mu m^2)$	$0.12\tau(440) \pm 0.03$
$C_{Vc}(\mu m^3/\mu m^2)$	$0.11\tau(440) \pm 0.03$

Lanai - Maritime aerosol

The site is situated on the coast of Lanai island (20.74N, 156.92W, Elevation: 20 m) approximately 100 km from Honolulu. The aerosol in that location has very low optical thickness: $\tau(1020)$ varies from 0.01 to 0.2 with a mean value of $\langle\tau(1020)\rangle = 0.04$.

The concentration of the fine and coarse modes of the size distribution is the function of the aerosol optical depth at 1020 nm (table 4.5). The values of the imaginary part of the refractive index are the lowest among five examples chosen.

TABLE 4.5: Optical properties of aerosol in Lanai
(after Dubovik et al. (2002a)).

Range of optical thickness; $\langle\tau\rangle$	$0.01 \leq \tau(1020) \leq 0.2$; $\langle\tau(1020)\rangle = 0.04$
n ; k	1.36 ± 0.01 ; 0.0015 ± 0.001
$r_{Vf}(\mu m)$; σ_f	0.16 ± 0.02 ; 0.48 ± 0.04
$r_{Vc}(\mu m)$; σ_c	2.70 ± 0.04 ; 0.68 ± 0.04
$C_{Vf}(\mu m^3/\mu m^2)$	$0.40\tau(1020) \pm 0.01$
$C_{Vc}(\mu m^3/\mu m^2)$	$0.80\tau(1020) \pm 0.02$

4.3.2 Methodology of the sensitivity study

Inversions are made with a fixed refractive index but fixing the refractive index increases the number of input parameters in three times, i.e. if the inversion is made using AOD's at 11 wavelengths, then adding 11 values for the real and 11 values for the imaginary part of the refractive index results in 33 input parameters. Thus we made a couple of inversions in order to find out the impact of the actual refractive index on the retrieved size distribution.

Our methodology of the sensitivity study of inversion code to different parameters is the following. First, the aerosol optical thickness is calculated from given size distribution and complex refractive index using the forward code. We normalize the AOD to $\tau(440) = 0.2$ for biomass burning and urban aerosols and $\tau(1020) = 0.2$ for desert dust and maritime aerosols that are values commonly observed.

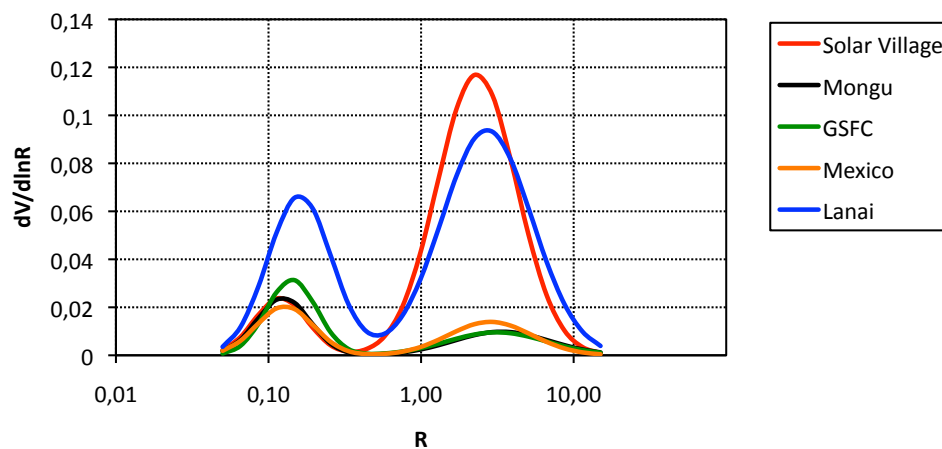


FIGURE 4.1: Size distributions of aerosol standard types when $AOD(440) = 0.2$ (biomass burning and urban aerosols) and $AOD(1020) = 0.2$ (desert dust and maritime aerosols).

The values of AOD in 8 channels of the extended CIMEL sunphotometer (0.34, 0.38, 0.44, 0.50, 0.67, 0.87, 1.02, 1.64 μm) and in the 11 channels of PLASMA (additional 0.55, 1.24 and 2.25 μm) are used as input parameters.

The spectral complex refractive index m is the second input parameter to the inversion. To estimate the sensitivity of the code the real part was fixed in five

values: average value $\langle n \rangle, \langle n \rangle \pm 0.01, \langle n \rangle \pm 0.05$; the imaginary part was fixed in three values: average value $\langle k \rangle, \langle k \rangle/2, \langle k \rangle * 2$ (see Fig. 4.2).

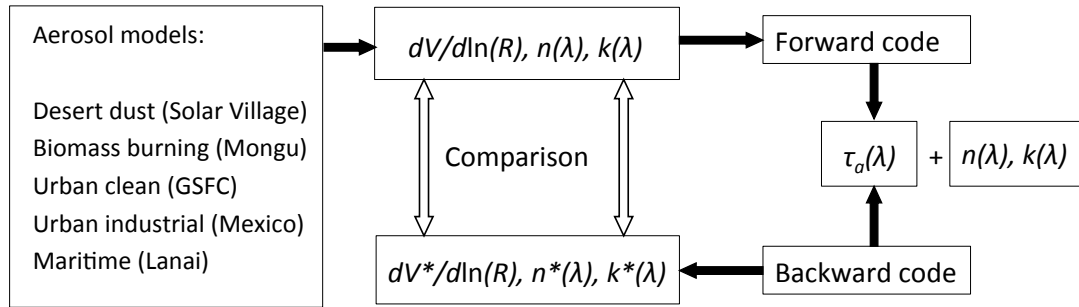


FIGURE 4.2: Scheme of the sensitivity study.

In all cases the same parameters of smoothness and the initial guess of the size distribution are used. Obviously, it is possible to predict with some precision the type of the aerosol in given region and then to change the input parameters in order to make the inversion results more accurate.

We present in the Appendix A the illustrations for the results discussed below. For two cases (8 and 11 wl inversion) first there are the tables with retrieved concentrations and effective radii of fine and coarse mode and the optical residual are given when the inversion is made with different refractive indices. Then the plots of size distributions are shown. At the end there are illustrations of 8 wl inversions with refractive index retrieved together with the size distribution. The second part of the Appendix A (Figures A.21-A.27) consists the illustrations of the sensitivity study of the inversion code to the noise level.

As seen from the Figures A.3, A.6, A.9, A.12, A.15 the inversion results when the refractive index is not fixed are not very different that when we fix the refractive index, but the retrieved value of the refractive index itself is not reliable. The real part, for example, can reach either maximum (1.6) or minimum (1.33) limits. However, AOD residual is smaller (usually it doesn't exceed 1%) than with fixed refractive index since the entire error goes to the wrong retrieval of the refractive index. Since the retrieval of the refractive index using only the AOD as input parameters is not possible we make the inversion with fixed refractive index.

4.3.3 Sensitivity to the refractive index

To illustrate the results of the study we compare the "model" and inverted size distributions assuming different refractive indices. Moreover, we calculated the concentrations of the fine and coarse mode and their effective radii:

$$r_{eff} = \frac{\int_{r_{min}}^{r_{max}} r^3 \frac{dN(r)}{d \ln r} d \ln r}{\int_{r_{min}}^{r_{max}} r^2 \frac{dN(r)}{d \ln r} d \ln r} \quad (4.17)$$

As it is well seen from the tables and figures (see Appendix A), the sensitivity of the inversion to real and imaginary parts of the refractive index varies with the aerosol type. Hereinafter, we present the impact on the effective radii. On the corresponding figures 4.3-4.7, the red points represent the model values, blue are the radii obtained with "true" values of refractive index and black points show the radii retrieved when the refractive index has been changed. The appropriate values are given in tables together with concentrations and AOD residual.

Desert dust aerosol (see Tables A.1, A.2 and Figures A.1, A.2) has low sensitivity to the variations of both real and imaginary parts from their true values. The effective radii of both fine ($R_{eff,f}$) and coarse ($R_{eff,c}$) modes are underestimated (Fig. 4.3). The values of effective radius are not sensitive to the changes of $Re(m)$ to 0.01 and $Im(m)$ part when the inversion is made at 11 wl with $\Delta R_{eff,c}/R_{eff,c} = 0.13 - 0.14$ and $\Delta R_{eff,f}/R_{eff,f} = 0.05 - 0.06$ (Table A.2, Fig. A.2). The concentration of the fine mode is overestimated by 10-15% and the coarse mode is underestimated by 33-35%. The coarse mode is less underestimated when inversion is made at 11 wl than at 8 wl. When inversion is made using 8 wl (Fig. 4.3) the effective radius of coarse mode is almost independent of the refractive index, while the underestimation is higher than at 11 wl inversion ($\Delta R_{eff,c}/R_{eff,c} = 0.26 - 0.28$), because of the high sensitivity of the inversion to 2.25 μm channel. When $Re(m)$ is overestimated, the underestimate of the fine mode is maximum with $\Delta R_{eff,f}/R_{eff,f} = 0.13 - 0.14$ for the inversion with 8 wl and $\Delta R_{eff,f}/R_{eff,f} = 0.09 - 0.13$ for the inversion with 11 wl (orange circles on the

Fig. 4.3). At the same time the concentration of fine mode is less overestimated. When $Re(m)$ is underestimated the impact using 8 or 11 wavelengths is different (green circles). Using the 8 wl inversion $R_{eff,f}$ is slightly overestimated and $R_{eff,c}$ is underestimated to the same extent, on the contrary the inversion using 11 wl leads the coarse mode to be slightly overestimated and the fine underestimated. The AOD residual is $< 1\%$ which means that the inversion converges well.

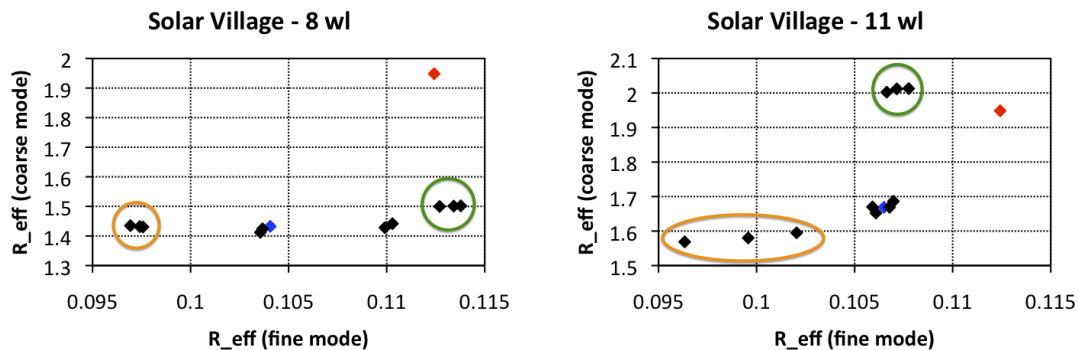


FIGURE 4.3: Effective radii retrieved from 8 and 11wl with different fixed refractive indices (desert dust).

The coarse mode of **biomass burning aerosol** (Tables A.3, A.4 and Figures A.4, A.5) is sensitive to the changes of the imaginary part of the refractive index: by overestimating it, the coarse mode is essentially underestimated especially when we are using only 8 wl (Table A.3, Fig. A.4). The effective radius of the coarse mode is overestimated for both 8 and 11 wl inversions; the highest overestimation of $R_{eff,c}$ is observed when the imaginary part of the refractive index $k = 2k_{mod}$: $\Delta R_{eff,c}/R_{eff,c} = 0.78$ for 8 wl inversion and $\Delta R_{eff,c}/R_{eff,c} = 0.34$ for 11 wl inversion (Fig. 4.4). The fine mode varies only slightly in all cases with the increase of its concentration around mean radius for 50-80% (Tables A.3, A.4); the total concentration of the fine mode is consistent with the model. The inversion at 11 wl shows better retrieval with smaller underestimation of the coarse mode (Fig. A.5). The residual is high (from 1.8 to 13.6%) that means that the inversion doesn't converge well.

Inversion of the **urban clean aerosol** (GSFC) (Tables A.5, A.6 and Figures A.7, A.8) has low sensitivity to the both parts of the refractive index with

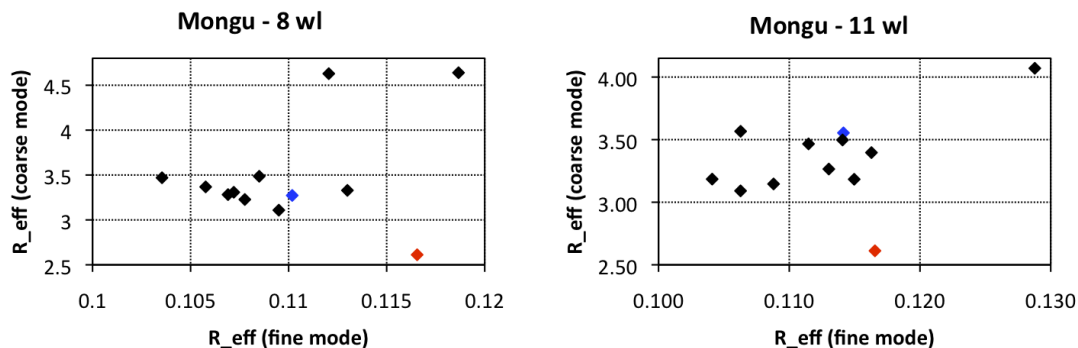


FIGURE 4.4: Effective radii retrieved from 8 and 11wl with different fixed refractive indices (biomass burning).

$0.2\% < \text{AOD residual} < 0.5\%$ independent from the number of wavelengths used. The fine mode is overestimated by 31% when the real part of the refractive index is underestimated by 0.05. Effective radius of the coarse mode is overestimated both for 8 wl and 11 wl inversion. (Fig. A.7, A.8). Effective radius of the fine mode is similarly underestimated for the 11 wl and 8 wl inversion depending on the real part of the refractive index. $\Delta R_{eff,f}/R_{eff,f} = 0.11 - 0.12$ when $n = n_{mod} + 0.05$ and $\Delta R_{eff,f}/R_{eff,f} = 0.04 - 0.05$ when $n = n_{mod} - 0.05$ (Fig. 4.5).

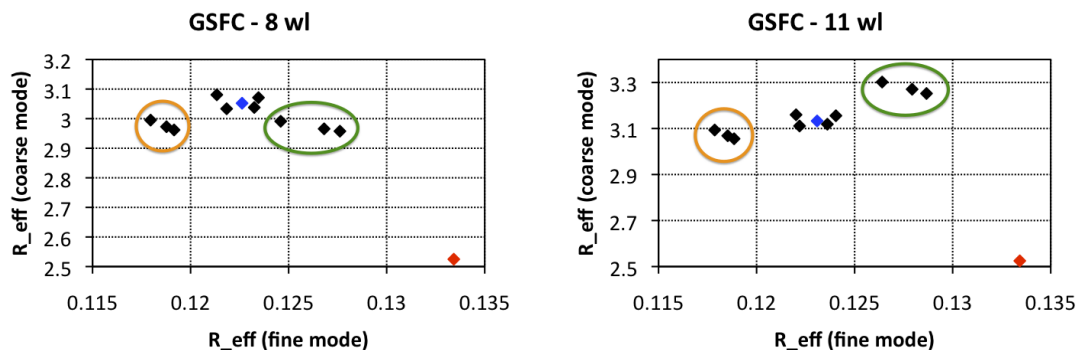


FIGURE 4.5: Effective radii retrieved from 8 and 11wl with different fixed refractive indices (urban clean).

Urban polluted aerosol in Mexico (Tables A.7, A.8 and Figures A.10, A.11), which has almost equal concentration of the fine and coarse modes, is more challenging to invert. The coarse mode is rather accurately retrieved with low sensitivity to the changes of the refractive index but the fine mode displays large variation with the real part of the refractive index. The best fit is when the real part is

overestimated by 0.05 when the fine mode is overestimated by 32% for a underestimate of the real part (Figures A.10, A.11). The residual varies in the range between 0.1% and 4.1% (Tables A.7, A.8). Effective radius of the coarse mode is less overestimated using the 11 wl inversion ($\Delta R_{eff,c}/R_{eff,c} = 0.10 - 0.35$) than using the 8 wl inversion ($\Delta R_{eff,c}/R_{eff,c} = 0.14 - 0.61$). $R_{eff,f}$ is underestimated for the 11 wl inversion ($\Delta R_{eff,f}/R_{eff,f} = 0.03 - 0.15$). Using 8 wl inversion $R_{eff,f}$ is retrieved accurately when $n = n_{mod}$ (Fig. 4.6 and Tables A.7, A.8).

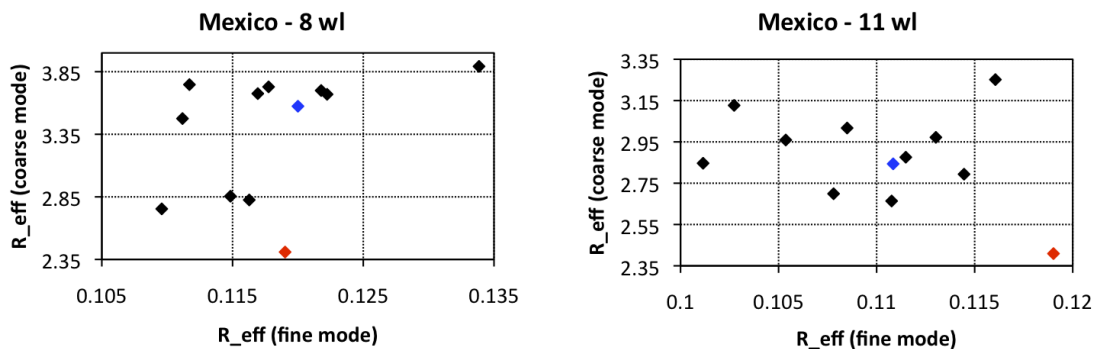


FIGURE 4.6: Effective radii retrieved from 8 and 11wl with different fixed refractive indices (urban industrial).

The inversion of the **maritime aerosol** (Lanai) is the most difficult since it presents high sensitivity to the changes of the real part of the refractive index (Tables A.9, A.10 and Figures A.13, A.14). The underestimation of the real part by 0.05 leads to the overestimation of the fine mode by 42% and of the coarse mode by 55%. At the same time the residual increases up to 35%. Overestimation of the real part leads to the underestimation of the coarse mode by 28%. There is no sensitivity to the changes of the imaginary part of the refractive index (Fig. A.13, A.14). The effective radius of the coarse mode is underestimated for 11 wl inversion with lower value $\Delta R_{eff,c}/R_{eff,c} = 0.12$ when $n = n_{mod} + 0.05$. For 8 wl inversion $R_{eff,c}$ is respectively underestimated (overestimated) with overestimation (underestimation) of the real part of refractive index and overestimated with its underestimation ($\Delta R_{eff,c}/R_{eff,c} = 0.09$). $R_{eff,f}$ is underestimated when $n = n_{mod} + 0.05$ and overestimated when $n = n_{mod} - 0.05$ with $\Delta R_{eff,f}/R_{eff,f} = 0.01 - 0.05$ and $\Delta R_{eff,f}/R_{eff,f} = 0.14 - 0.15$ respectively (Fig. 4.7).

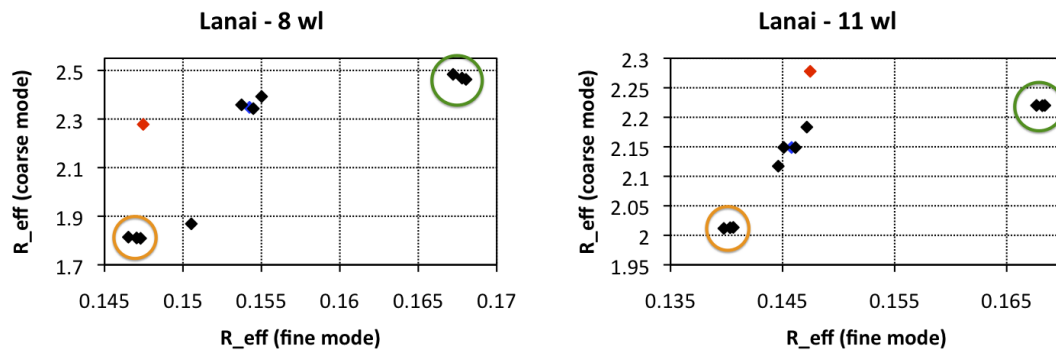


FIGURE 4.7: Effective radii retrieved from 8 and 11wl with different fixed refractive indices (maritime).

4.3.4 Sensitivity to the AOD noise

The sensitivity of the inversion process to the instrumental noise is very important to study in. Let us remind that the accuracy of the CIMEL sunphotometer is 0.01 for standard instrument and 0.005 for master instrument.

For our study, we first took a relative error of 5% and 10% of the AOD for all wavelengths. We simulated noise as a random variable normally distributed with a standard distribution of $\Delta\tau = 0.05\tau$ and $\Delta\tau = 0.1\tau$ (see Figure 4.8).

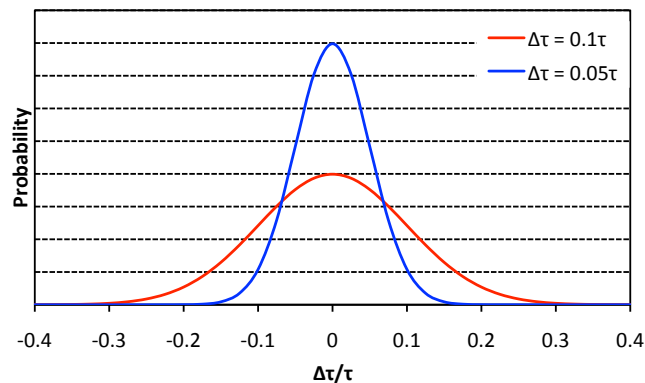


FIGURE 4.8: Distribution of the AOD noise.

For statistical sampling we have generated five cases of noise for each aerosol type. In figures (see Appendix A) the results of inversion of the size distribution for the standard types of aerosols are shown. We report in Figures A.16-A.20 the inversion results with 5% noise as well as the distributions retrieved without noise.

In Figures A.21-A.25 the inversion results and the spectral dependence of AOD for each noise case are shown.

4.3.4.1 Sensitivity to the AOD noise $\Delta\tau = 0.05\tau$.

The inversion results with AOD noise $\Delta\tau = 0.05\tau$ differ from the aerosol type (Figures A.16 - A.20). Below we comment each type.

The standard deviation of 5% AOD noise of aerosol in Solar Village for 340 nm is 0.025, which is 2.5 times greater than the precision of a standard instrument CIMEL and 5 times greater than the precision of the master instrument and of airborne sunphotometer PLASMA, so the data with such noise would not be reliable. However, some of the cases are retrieved adequately and residual ranges from 2% to 10.7% (Fig. A.16).

Inversion of the size distribution of aerosol in Mongu has high accuracy with respect to inversion with the data without noise except the case 3 and 5 for 11 wl inversion (Fig. A.17).

The size distribution of aerosol in GSFC is retrieved very accurately so as for 8 and 11 wl inversions with residual from 1.2% to 5.4%, which means a low sensitivity of the inversion to AOD noise (Fig. A.18).

Aerosol in Mexico City is also retrieved quite accurately with respect to the inversion on the data without noise with the residual from 2.4% to 7.5%. (Fig. A.19).

Retrieval of the size distribution of aerosol in Lanai is highly dependent on the noisy AOD spectrum and can be as relatively accurate (case 4) either very inadequate (case 2), despite the low value of the residuals for all cases (Fig. A.20).

4.3.4.2 Sensitivity to the AOD noise $\Delta\tau = 0.1\tau$.

None of the cases of size distribution inversion with AOD noise for desert dust (Solar Village) model has adequate results (Fig. A.21). Probably, the point is

that the noise value is 10% of AOD; $\Delta\tau(340)$ means the absolute value of 0.05, which is 5 times more than the error of the CIMEL sunphotometer. The spectral dependence of AOD shows that the noise is very significant and it is unlikely that such data should be considered as reliable.

In the inversion of biomass burning (Mongu) aerosol only cases 2 and 5 can be considered as satisfactory as for 11 either at 8 wl inversions. This is due to the fact that the spectral behavior of a noisy AOD still has right dependence (Fig. A.22).

The size distribution of urban clean aerosol in the GSFC is retrieved adequately with the exception of case 3 which for 11 wl inversion has the wrong size distribution, that can be explained by the reversed spectral dependence of AOD in the 340-380 nm range (Fig. A.23). The fact that the inversion at the 8 wavelengths is better we explain as in (reference) that the smaller is the number of wavelength the smaller is the noise affecting the quality of inversion. In this case, the noise outweigh the importance of the channel 2250 nm for the inversion.

The size distribution of aerosol in Mexico adequately retrieved only for the cases 1, 2 and 3, with the inversion at the 8 wavelengths, while with the inversion at 11 wavelengths none of the cases give the distribution similar to the model (Fig. A.24). The residual ranges from 6.6 to 44.6%, indicating a the inversion does not well converge.

Inversion of maritime aerosol in Lanai is very different for the 8 and 11 wavelengths (Fig. A.25). For example, case 1: the inversion at 11 wavelengths gives the most precise fit with the lowest residual of 3.7%, while inversion at 8 wavelengths on the contrary, gives the worst retrieval with the greatest residual of 14.1%. This is despite the fact that the noise creates a reverse AOD spectrum. The inversion at 8 wavelengths gives the most accurate result for the case 3 with the residual of 3.2%, and in the case of inversion at 11 wavelengths residual is relatively low (4.8%), but the coarse mode is overestimated as in cases 2 and 5. Of course, data with such noise (that is 0.08 at 340 nm, which is 8 times more than CIMEL measurement error) never used for inversion.

We can conclude from the above that the least sensitivity to AOD noise when retrieving the size distribution of particles has the urban aerosol even with $\Delta\tau = 0.1\tau$. The inversion results are highly dependent not only on the noise value, but also on its configuration. Thus, the reversed spectral dependence in some segments of the AOD leads to the inaccurate inversion of the size distribution.

4.3.4.3 Sensitivity of the inversion code with $\tau = \langle \tau \rangle$ and standard instrumental noise $\Delta\tau = 0.005$ and $\Delta\tau = 0.01$

As it is shown in Chapter 4, the measurement error of PLASMA is 0.005 in the case of ground-based measurements and 0.01 in the case of automobile and airborne measurements. CIMEL sunphotometer has a standard error of 0.01 for the usual device and 0.005 for the master instrument. Therefore, we have chosen two more versions of noise $\Delta\tau = 0.005$ and $\Delta\tau = 0.01$.

In addition, we have chosen the average values of AOD and the size distributions of the studied typical aerosols. The figure 4.9 shows the distribution of these average distributions. So we have standard aerosols and the standard noise. The refractive index is assumed to be known. Inversion is made out for 11 and 8 wavelengths as usual.

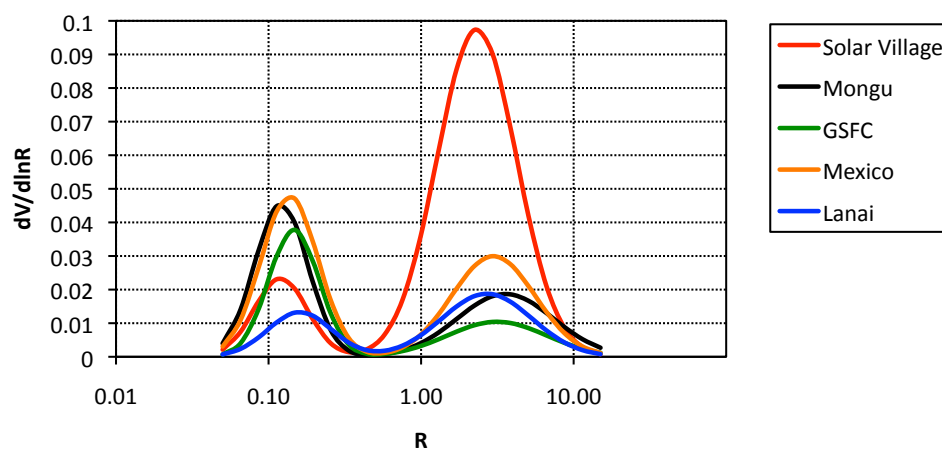


FIGURE 4.9: Size distributions of aerosol standard types when $AOD(\lambda) = \langle AOD(\lambda) \rangle$.

Aerosol in Solar Village is retrieved much more accurately if compared with previous retrievals. When inversion is made with the noise $\Delta\tau = 0.005$ the results are better for 11 wl than for 8 wl inversion (Fig. A.26 - A.27). Three from five cases of 11 wl inversion with the noise $\Delta\tau = 0.01$ are adequate (Fig. A.28). However inversion at 8 wl with the same noise has four accurate distributions (Fig. A.29). Optical residuals vary from minimum 0.6% – 2.5% when inversion is made using 11 wl with the noise $\Delta\tau = 0.005$ to maximum 1.4% – 10.6% when inversion is made using 11 wl with the noise $\Delta\tau = 0.01$.

Biomass burning aerosol in Mongu is retrieved accurately for all cases of noise and number of wavelengths despite the high value of AOD residual which varies from 2.4% to 38% (Figures A.28 - A.27).

The best inversion results of urban aerosol in GSFC is for 8 wl inversion with the noise $\Delta\tau = 0.005$ when AOD residual varies from 0.24% to 7.9% and for 11 wl inversion with the noise $\Delta\tau = 0.005$ when AOD residual varies from 1.4% to 10.5%. Inversions with the noise $\Delta\tau = 0.01$ for 11 wl inversion have residual up to 27.8%.

Inversion of urban aerosol in Mexico has underestimation of the coarse mode when made at 8 wl with the noise $\Delta\tau = 0.01$. Other cases have enough accurate results of size distributions however the AOD residual varies from 0.71% to 15.9%.

The worst results have inversions of maritime aerosol in Lanai because of its low optical depth. Most of the cases results in inaccurate distribution with high AOD residual. Only few cases are retrieved adequately (e.g. case 5 on Fig. A.27).

4.3.5 Conclusion of the sensitivity study

Sensitivity study of the inversion have shown that under certain conditions it is possible to derive the size distribution of aerosol particles from measurements of the optical thickness in the range of $0.34 - 2.25 \mu m$ or $0.34 - 1.64 \mu m$.

Different aerosol types have various sensitivity to the refractive index changes and to measurement noise. Desert dust aerosol is not sensitive to changes of the complex refractive index but the coarse mode is constantly underestimated for around 30%. Biomass burning aerosol is not sensitive to the changes of the real part of the refractive index. Only the fine mode of urban clean and urban polluted aerosols are sensitive to the underestimation of the real part of the refractive index for 0.05. The change of n for 0.01 does not affect the shape of the distribution. The maritime aerosol is sensitive to the changes of the real part of the refractive index: with its underestimation for 0.05 both modes are overestimated and with its overestimation the coarse mode is underestimated. The change for 0.01 affects only slightly to the shape of the distribution. Only the biomass burning aerosol show the sensitivity to the imaginary part of the refractive index: with overestimation of k the coarse mode is underestimated.

Thus, we conclude that it is possible to derive the size distribution from PLASMA data with the assumption that the real part of the refractive index is known with the accuracy of 0.05 (0.01 for maritime aerosol), and the imaginary part within $\pm 50\%$.

Study of the sensitivity to AOD noise showed that with the instrumental noise of 0.005, all aerosol types except maritime aerosol with low optical depth (Lanai) are retrieved with a sufficient accuracy. With the noise of 0.01 only certain aerosol types (biomass burning and urban clean) could be retrieved accurately.

4.4 Inversion of PLASMA ground-based measurements

We hereinafter invert PLASMA data acquired in Lille and Beijing.

In Lille a large number of measurements was made (see Table 3.1) and we present results for the 19th of April, 2011. We inverted the AOD data using 8 wavelengths from 0.34 to 1.64 μm as only these channels are well calibrated, got the size distributions of aerosol particles and compared them with AERONET inversions. As it is seen from the figure, AERONET gives stable inversions for the 3 data sets, whereas PLASMA shows that the size distribution is changing. PLASMA is giving the same coarse mode as AERONET at 8:48 but very different results at other times but the spectral AOD is well fitted. It means that when the contribution of the fine mode is significant, it is difficult to retrieve the contribution of the coarse mode although the location of the central radius is more or less at the right position.

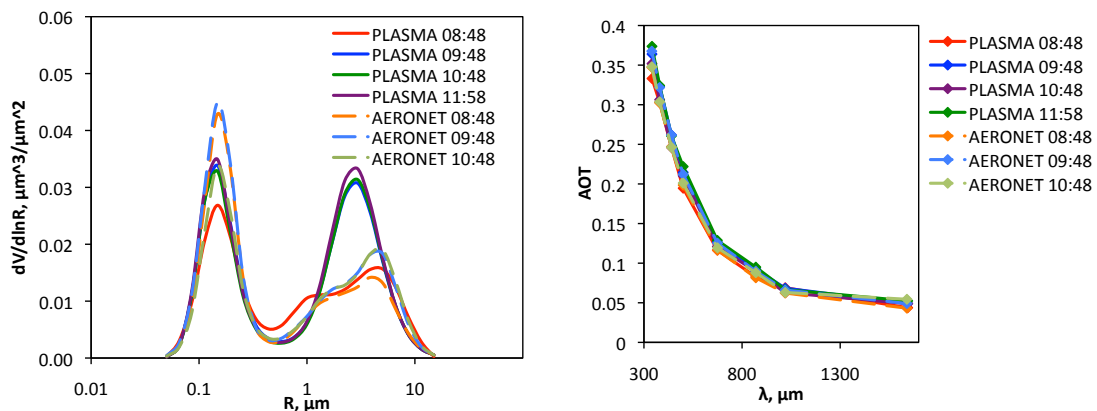


FIGURE 4.10: Aerosol size distribution derived from PLASMA ground-based measurements in Lille 19/04/2011.

Aerosol in Beijing has high values of AOD. During the measurements using PLASMA there was a strong atmospheric variability. On May 11, 2011 from 00:23 to 8:02 AOT increased by 2 times and changed its spectral dependence. Due to the fact that there is no simultaneous measurements of PLASMA and CIMEL we cannot compare their data for full consistency. We can only see that the PLASMA

size distribution is in the range of the AERONET distribution. The discrepancy is less than 3%. Also there is underestimation of the coarse mode and the central radius moved towards fine particles. This means that the algorithm is insensitive to the AOD measurements at 1640 nm wavelength and for determining the coarse mode angular measurements are required.

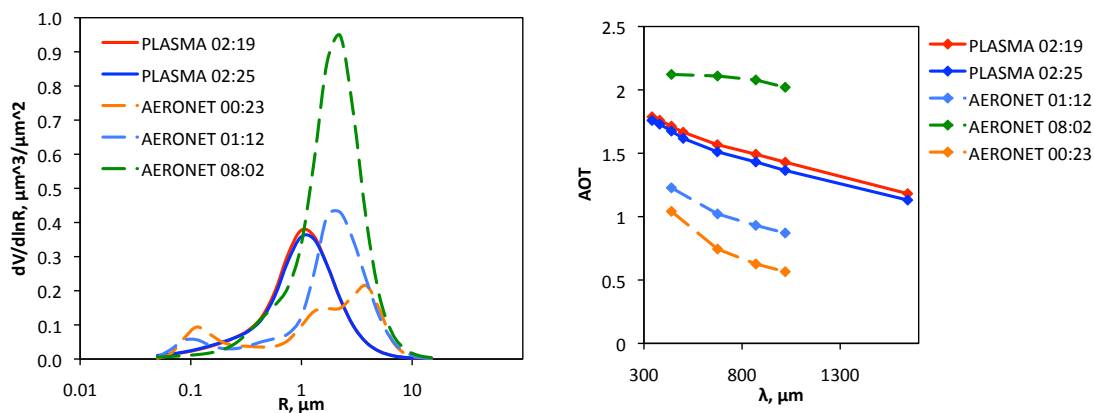


FIGURE 4.11: Aerosol size distribution derived from PLASMA ground-based measurements in Beijing 11/05/2011.

4.5 Inversion of the DRAGON campaign data

During the DRAGON campaign, PLASMA was installed on the roof of the automobile together with a mobile lidar. We present below the results of inversion for July 20, 2011. The comparison of PLASMA AOD and Ångström exponent was presented in Section 3.5.3.2. We selected five locations on the PLASMA route close in time and space to AERONET stations. Thus, we can compare the size distributions of aerosol particles retrieved from direct sun PLASMA measurements at 8 wavelengths with AERONET inversion at direct sun and angular measurements at 4 wavelengths. We also performed an inversion at 7 wavelengths (excluding 1640 nm channel) to show the ability of the inversion code to retrieve the size distribution from direct sun measurements of standard instrument CIMEL CE-318.

Inversion results are shown in Fig. 4.12. The fine mode is retrieved with good precision, while the coarse mode has a lower accuracy. So, near the Aldino, Beltsville and Kentsland stations the inversion of PLASMA data overestimates

the coarse mode, and the central radius shifted towards the large particles. Inversion at 7 wavelengths gives the central radius more shifted towards large particles. Near the station Edgewood concentration of the coarse mode is accurately retrieved but the central radius does not match the AERONET value. At the UMBC station the concentration of the coarse mode was higher than at other places, and is underestimated.

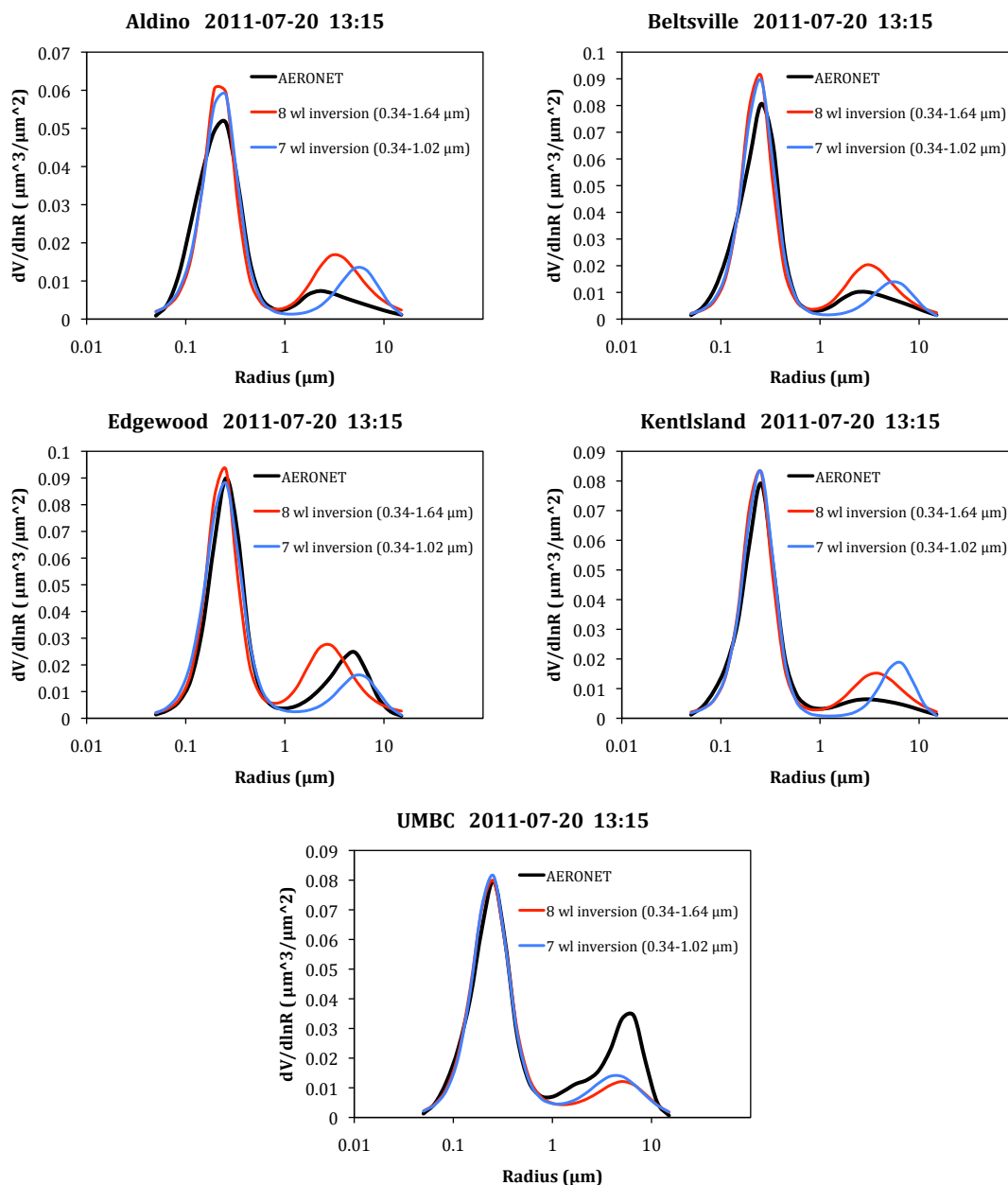


FIGURE 4.12: Comparison between PLASMA inversion on 7 and 8 wavelengths with the AERONET inversion.

4.6 Inversion of airborne measurements

The innovative contribution of PLASMA (from the point of view of new information on aerosols in the atmosphere) is the retrieval of the size distribution of aerosol particles at different altitudes. The multi-wavelength lidars could provide only information about the total concentration of separate fine and coarse mode and this issue is still under development (Cuesta et al., 2008; Chaikovsky et al., 2012; Lopatin et al., 2013).

Study of the sensitivity of the inversion code to different parameters (refractive index, noise) led to the conclusion that the available spectral range and number of wavelengths is sufficient to retrieve the size distribution of aerosol particles with enough accuracy.

4.6.1 Flights over Lille

Fig. 4.13 shows the size distribution retrieved from PLASMA airborne measurements in the region of Lille at different altitudes. The figures also shows the size distributions from AERONET at the surface level which corresponds to the vertical integrated size distribution.

It should be noted that PLASMA ground-based measurements were carried out at a distance of about 10 km from the station in Lille, so we cannot expect full consistency with AERONET. The concentrations of both small and coarse modes differ. Thus, the inversion on PLASMA data on 12/10/2010 gives a large concentration of both modes, and a much smaller 28/09/2011. On 28/09/2011 and 15/10/2011 the fine modes are moreless similar, but the coarse modes from PLASMA are smaller.

To retrieve the size distributions we have taken the following points: ground level (65 - 90 m), 250 m, 500 m, 1000 m, 2000 m and a maximum altitude (3000 - 3100 m).

The discrepancy in the AOD was not more 5%.

12/10/2010 as we see from the size distribution plots most of the aerosols contained below the altitude of 500 m. The coarse mode is defined in the layer of 250-500 m, and the fine mode probably uniformly distributed. Over 500 m there was a slight amount of aerosol.

28/09/2011 the fine mode was uniformly distributed over the whole atmospheric column (at least below 3000 m). The coarse mode is constant at altitudes of 90-500 m, and after 1000 m there is a decrease of its concentration. This suggests that the larger particles were at the altitude between 500 m and 2000.

15/10/2011 aerosols were uniformly distributed. Coarse and fine modes decrease with approximately the same intensity. Most of the coarse mode is at the altitudes below 250 m.

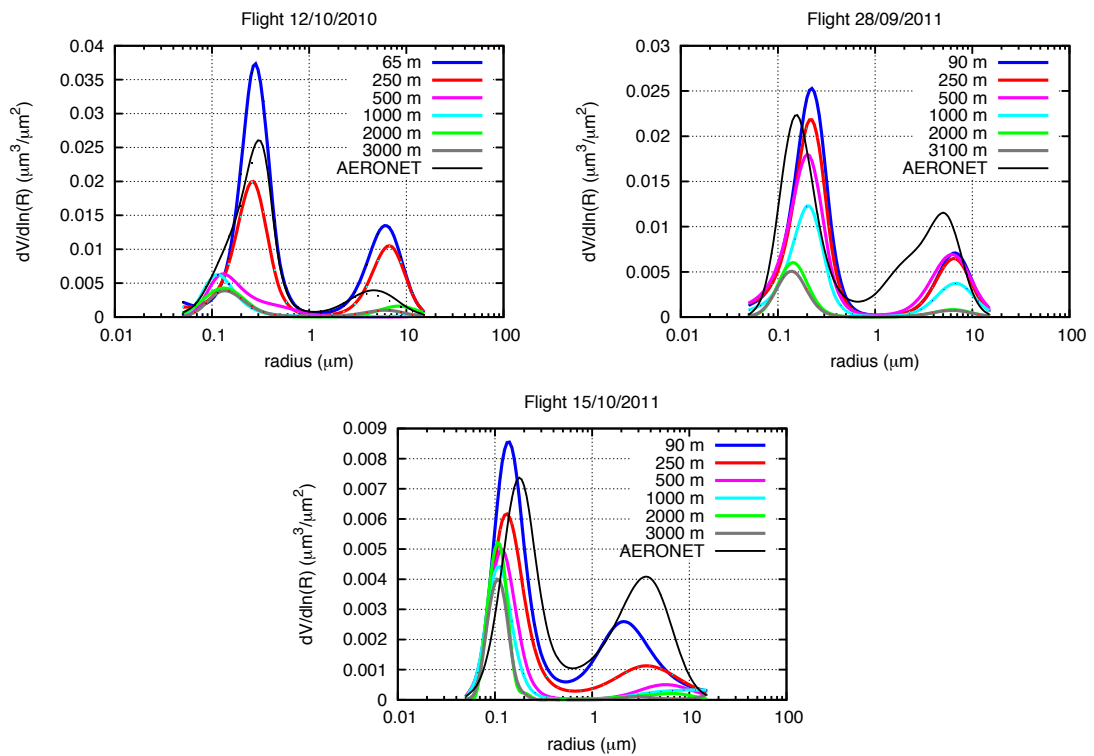


FIGURE 4.13: Size distributions at different altitudes obtained during the airborne measurements by PLASMA sunphotometer over Lille.

4.6.2 Flights over M’Bour –Dakar

The distribution of aerosol particles in the region M’bour – Dakar is very different from Lille continental aerosol. This region is characterized by a constant presence of desert dust, i.e. there is high concentration of large particles.

The figures show the retrieved particle’s size distributions at different altitudes compared to AERONET retrievals at ground level. The inversion was performed at 7 wavelengths in the range 340 - 1020 nm. Unfortunately due to the incorrect calibration of infrared channels, the 1640 nm wavelength could not be included in the inversion. The calibration coefficient for this wavelength was underestimated and so the inversion results are very much different from the expected with the AOD residual up to 20%. An example of such retrieval is shown on Fig. 4.14.

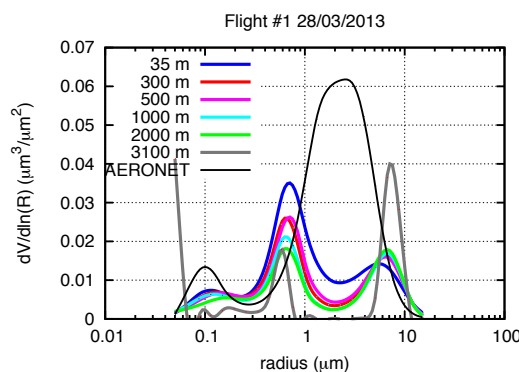


FIGURE 4.14: Example of the size distribution retrieved from airborne measurements including 1640 nm channel that has wrong calibration.

Because it was necessary to exclude 1640 nm that is sensitive to large particles the majority of retrievals underestimate the coarse mode. However, it is possible to determine the general trend of aerosol vertical distribution if not quantitatively but at least qualitatively.

We report below three days of measurements i.e. six inversions that are the most representative: 28/03/2013, 6/04/2013, 7/04/2013.

28/03 (Fig. 4.15) there was a uniform decrease of both modes with the altitude. Between 1000 m and 2000 m the coarse mode remained stable, so we can assume

that there were at least 2 aerosol layers: one at the altitude below 1000 m and the second over 2000 m. This fits the profile of extinction on Fig. 3.17.

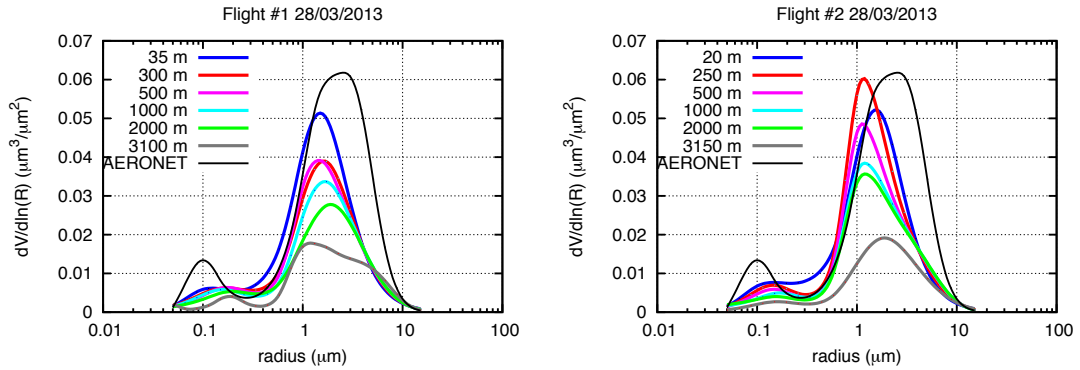


FIGURE 4.15: Size distributions at different altitudes obtained during the airborne measurements by PLASMA sunphotometer over M'bour on 28/03/2013.

6/04 there was the decrease in the concentration of the coarse mode from the first flight to the second, while at an altitude of 500 m concentration increased. This suggests the redistribution of aerosols at different altitudes: there was the decrease of aerosol concentration in the total column but there was its increase at the altitudes below 2000 m.

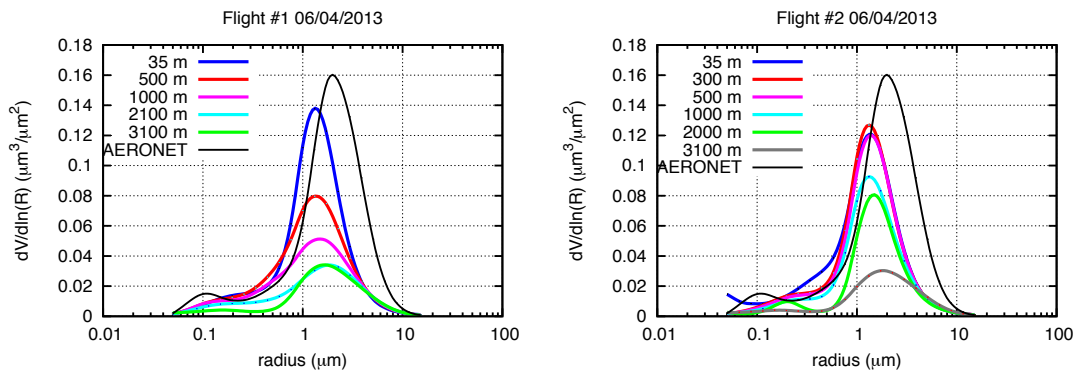


FIGURE 4.16: Size distributions at different altitudes obtained during the airborne measurements by PLASMA sunphotometer over M'bour on 06/04/2013.

7/04 the aerosol concentration increased while at an altitude of 2000 m and 3000 m it was not changed. At an altitude of 1000 m the coarse mode did not reduced. It can be concluded that between the flights the aerosol layer with large particles appeared between 1000 and 2000 m.

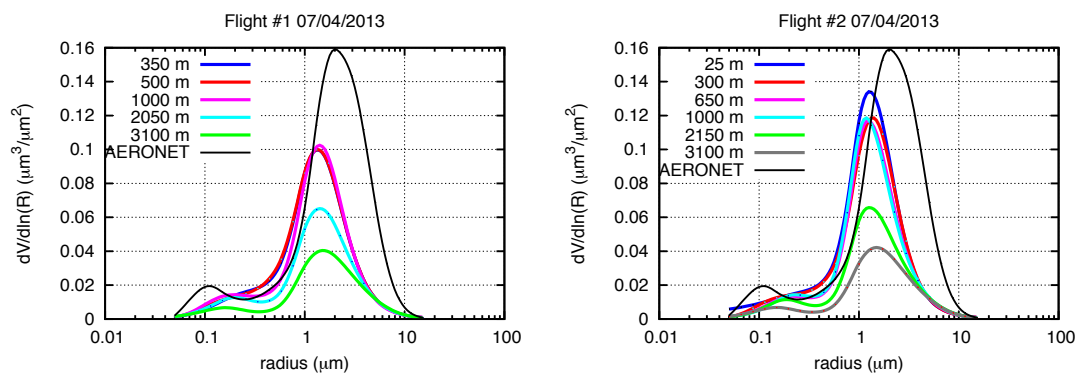


FIGURE 4.17: Size distributions at different altitudes obtained during the airborne measurements by PLASMA sunphotometer over M’Bour on 07/04/2013.

We see that with several airborne measurements in one day the evolution of the aerosol layers can be observed. This information can help to better understand the processes that aerosols undergo in the atmosphere.

4.7 Conclusion of PLASMA data inversion

From the sensitivity study the inversion code can be used for deriving the size distribution of aerosol particles from only spectral AOD measurements. First, we inverted PLASMA ground-based measurements and compared the results with AERONET inversions. Then we inverted automobile and airborne measurements. The size distributions at different altitudes cannot be compared with any other measurements but from their shapes and decreasing behavior with the altitude we can conclude that the results are promising.

The inversion code used for this study performs high precision for the ranges $0.34-1.64 \mu m$ and $0.34-1.02 \mu m$ and so it can be used not only for PLASMA data processing but also for derivation of the size distribution of aerosol particles from sun measurements of CIMEL instrument. Sun measurements are more frequent than sky measurements, so the inversion of spectral AOD data can supplement the standard AERONET inversion.

Chapter 5

General conclusion

Realists do not fear the results of their study.

Fyodor Dostoevsky

Last years significant work was done in the development of new instrumentation for atmospheric aerosol investigation. International photometric and lidar observation networks were established, several satellites with research instruments on board were launched. It is believed that measurements from one instrument complement the others and used in synergy for getting a clear picture of complex atmospheric processes.

Airborne sun photometer PLASMA was developed to validate and complement data from other instruments such as lidar data. Furthermore, PLASMA can be used independently from other systems as a reliable source of information about the distribution of aerosol particles in the atmosphere.

During the development of the instrument a number of technical problems were solved and the current version meets our goal, AOD accuracy is around $0.005 < \Delta(AOD) < 0.01$, which is comparable to the accuracy of sun photometers CIMEL CE- 318. A large number of ground-based, airborne, and automobile experiments were carried out all over the world (Lille, Tenerife, Beijing, Dakar, Washington

DC, Cagliari) and the PLASMA data were compared with the photometric and lidar data.

PLASMA ground-based measurements are consistent with AERONET data. When installed on an aircraft or on an automobile, PLASMA accurately tracks the Sun through the 4-quadrant detector and provides high speed measurements of vertical or horizontal profiles of AOT in 15 wavelengths. Airborne measurements of vertical profiles of aerosol extinction coefficient were compared to the lidar profiles. In most cases measurements are consistent. When discrepancies are observed, part of them can be explained by various environmental factors such as atmospheric variability or time and space differences between the two instruments (Section 3.5.2). We observe the largest discrepancies near the surface (300-500 m) where the lidar cannot measure and requires an extrapolation procedure in the retrieval algorithm. PLASMA measurements can be used as reference data for the validation of lidar measurements, since it provides direct sun measurements down to the ground level, while the lidar cannot observe below 300-500 m. The instrument was also used to obtain horizontal (DRAGON campaign) profiles of AOD being installed on the roof of automobile. During the campaign, mobile lidar system was used together with PLASMA and the photometric data were implemented as independent AOD measurements in lidar data processing. Using the mobile lidar-photometric system for taking horizontal transects of the atmosphere is very promising.

Inversion code of spectral AOD to retrieve aerosol size distribution has been developed. Oleg Dubovik's code used in AERONET network has been adapted to the process the AOD data over a wide spectral range for retrieving the size distribution of aerosol particles without the use of angular measurements. Using only spectral AOD's, it is impossible to retrieve simultaneously the aerosol size as well as the complex refractive index. Since we have to assume a priori values, a sensitivity study of the retrieval to changes of the refractive index was performed. It turned out that for some aerosol type it is possible to retrieve the size distribution without knowing the refractive index precisely but with the assumption that the real part of the refractive index is known with the accuracy of 0.05 (0.01 for

maritime aerosol), and the imaginary part within $\pm 50\%$. (Section 4.3). Study of the sensitivity to AOD noise showed that with the instrumental noise of 0.005, all aerosol types except maritime aerosol with low optical depth (Lanai) are retrieved with a sufficient accuracy.

A comparison of PLASMA and AERONET size distributions from stations in Lille, Beijing and Cagliari have shown that the inversion algorithm performs well. The inversion code used for this study performs high precision for the ranges $0.34-1.64 \mu m$ and $0.34-1.02 \mu m$ and so it can be used not only for PLASMA data processing but also for derivation of the size distribution of aerosol particles from sun measurements of CIMEL instrument. Sun measurements are more frequent than sky measurements, so the inversion of spectral AOD data can supplement the standard AERONET inversion.

Inversion of DRAGON automobile experiment presents good consistency with AERONET retrievals. Finally we applied the code to retrieve the size distributions at different altitudes from airborne measurements in Lille and Dakar; although the accuracy of the measurements still needs to be improved, the variation of the derived size as a function of the altitude is consistent with expected physical process.

Appendix A

Illustrations for the sensitivity study to the refractive index and AOD noise

In this appendix the tables and figures concerning the sensitivity study of the inversion code to the complex refractive index and AOD noise are shown.

Desert Dust (Solar Village)

$$C_{Vf}^{model} = 0.024\mu m^3/\mu m^2, R_{eff,f}^{model} = 0.112\mu m$$

$$C_{Vc}^{model} = 0.176\mu m^3/\mu m^2, R_{eff,c}^{model} = 1.95\mu m$$

TABLE A.1: Sensitivity study results: 8 wl inversion (Solar Village)

a) Sensitivity to the real part of complex refractive index

n	$n = n_{model}$	$n = n_m - 0.01$	$n = n_m + 0.01$	$n = n_m - 0.05$	$n = n_m + 0.05$
$C_{Vf}, \mu m^3/\mu m^2$	0.0277(+14%)	0.0269(+12%)	0.0271(+13%)	0.0292(+21%)	0.0266(+10%)
$C_{Vc}, \mu m^3/\mu m^2$	0.126(-34%)	0.117(-33%)	0.114(-35%)	0.123(-30%)	0.116(-34%)
$R_{eff,f}, \mu m$	0.104	0.110	0.104	0.113	0.097
$R_{eff,c}, \mu m$	1.43	1.44	1.41	1.50	1.43
AOD residual	0.66%	0.63%	0.65%	0.65%	0.85%

b) Sensitivity to the imaginary part of complex refractive index

k	$k = k_{mod}/2$	$k = 2k_{mod}$
$C_{Vf}, \mu m^3/\mu m^2$	0.0277(+15%)	0.0264(+10%)
$C_{Vc}, \mu m^3/\mu m^2$	0.115(-34%)	0.116(-34%)
$R_{eff,f}, \mu m$	0.104	0.110
$R_{eff,c}, \mu m$	1.42	1.43
AOD residual	0.64%	0.64%

c) Sensitivity to the real and imaginary parts of complex refractive index

n	$n = n_{mod} - 0.05$	$n = n_{mod} + 0.05$	$n = n_{mod} - 0.05$	$n = n_{mod} + 0.05$
k	$k = k_{mod}/2$	$k = k_{mod}/2$	$k = 2k_{mod}$	$k = 2k_{mod}$
$C_{Vf}, \mu m^3/\mu m^2$	0.0292(+21%)	0.0266(+10%)	0.0292(+21%)	0.0267(+11%)
$C_{Vc}, \mu m^3/\mu m^2$	0.123(-30%)	0.116(-34%)	0.123(-30%)	0.117(-34%)
$R_{eff,f}, \mu m$	0.114	0.098	0.113	0.097
$R_{eff,c}, \mu m$	1.50	1.43	1.50	1.44
AOD residual	0.66%	0.86%	0.63%	0.83%

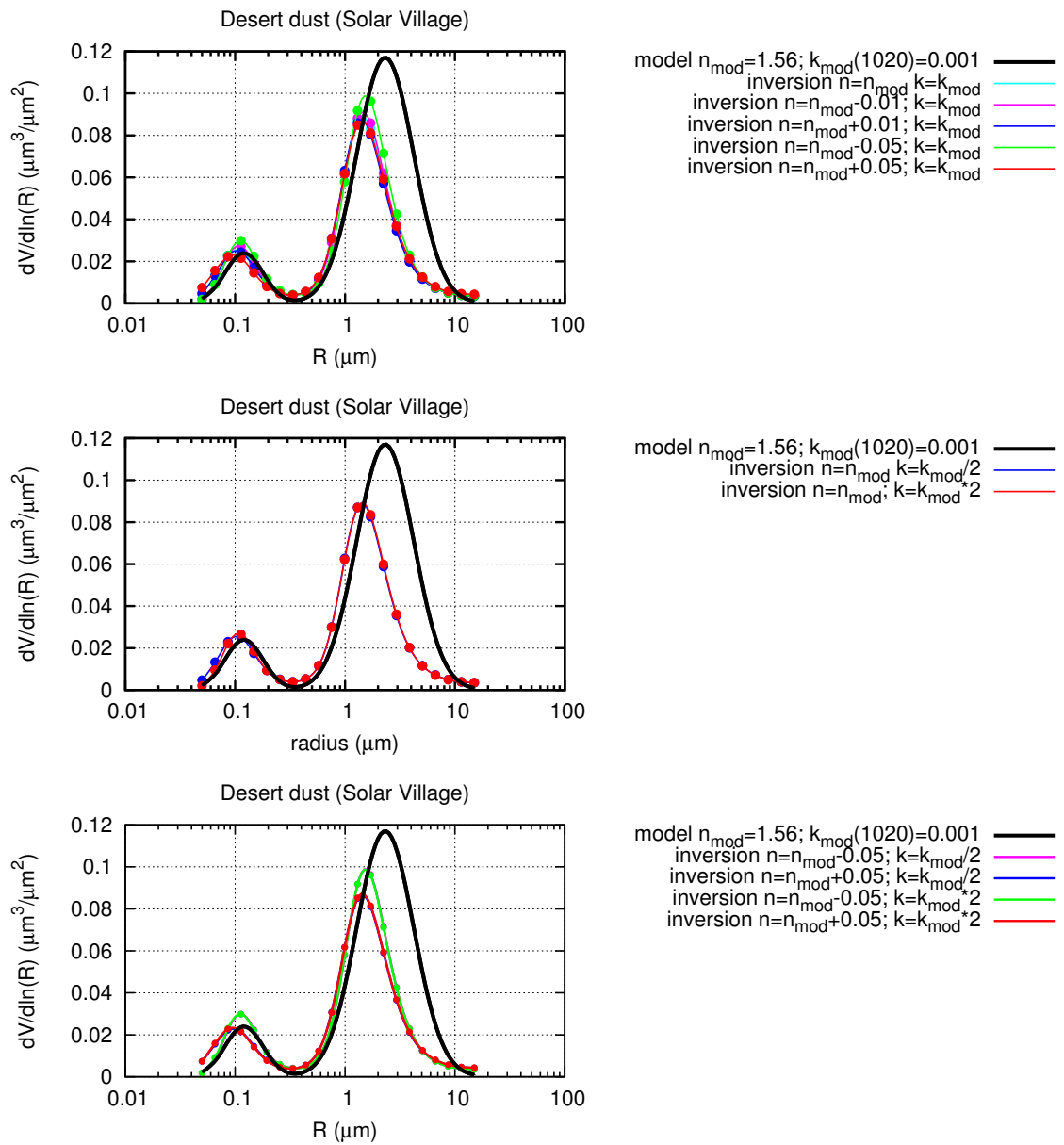


FIGURE A.1: Size distributions retrieved from 8 wl with different refractive indices (fixed) - Solar Village.

TABLE A.2: **Sensitivity study results: 11 wl inversion (Solar Village)**

a) Sensitivity to the real part of complex refractive index

n	$n = n_{model}$	$n = n_m - 0.01$	$n = n_m + 0.01$	$n = n_m - 0.05$	$n = n_m + 0.05$
$C_{Vf}, \mu m^3 / \mu m^2$	0.0261(+9%)	0.0267(+11%)	0.0256(+6%)	0.0294(+21%)	0.0253(+5%)
$C_{Vc}, \mu m^3 / \mu m^2$	0.143(-18%)	0.145(-17%)	0.141(-19%)	0.178(+15%)	0.134(-24%)
$R_{eff,f}, \mu m$	0.106	0.107	0.106	0.107	0.100
$R_{eff,c}, \mu m$	1.67	1.69	1.65	2.01	1.58
AOD residual	0.57%	0.57%	0.56%	0.58%	0.70%

b) Sensitivity to the imaginary part of complex refractive index

k	$k = k_{mod}/2$	$k = 2k_{mod}$
$C_{Vf}, \mu m^3 / \mu m^2$	0.0261(+9%)	0.0261(+8%)
$C_{Vc}, \mu m^3 / \mu m^2$	0.143(-18%)	0.143(-18%)
$R_{eff,f}, \mu m$	0.106	0.107
$R_{eff,c}, \mu m$	1.67	1.67
AOD residual	0.55%	0.56%

c) Sensitivity to the real and imaginary parts of complex refractive index

n	$n = n_{mod} - 0.05$	$n = n_{mod} + 0.05$	$n = n_{mod} - 0.05$	$n = n_{mod} + 0.05$
k	$k = k_{mod}/2$	$k = k_{mod}/2$	$k = 2k_{mod}$	$k = 2k_{mod}$
$C_{Vf}, \mu m^3 / \mu m^2$	0.0293(+22%)	0.0247(+26%)	0.0294(+22%)	0.0260(+8%)
$C_{Vc}, \mu m^3 / \mu m^2$	0.179(+2%)	0.136(-23%)	0.177(+1%)	0.133(-24%)
$R_{eff,f}, \mu m$	0.108	0.102	0.107	0.096
$R_{eff,c}, \mu m$	2.01	1.59	2.00	1.57
AOD residual	0.58%	0.70%	0.57%	0.72%

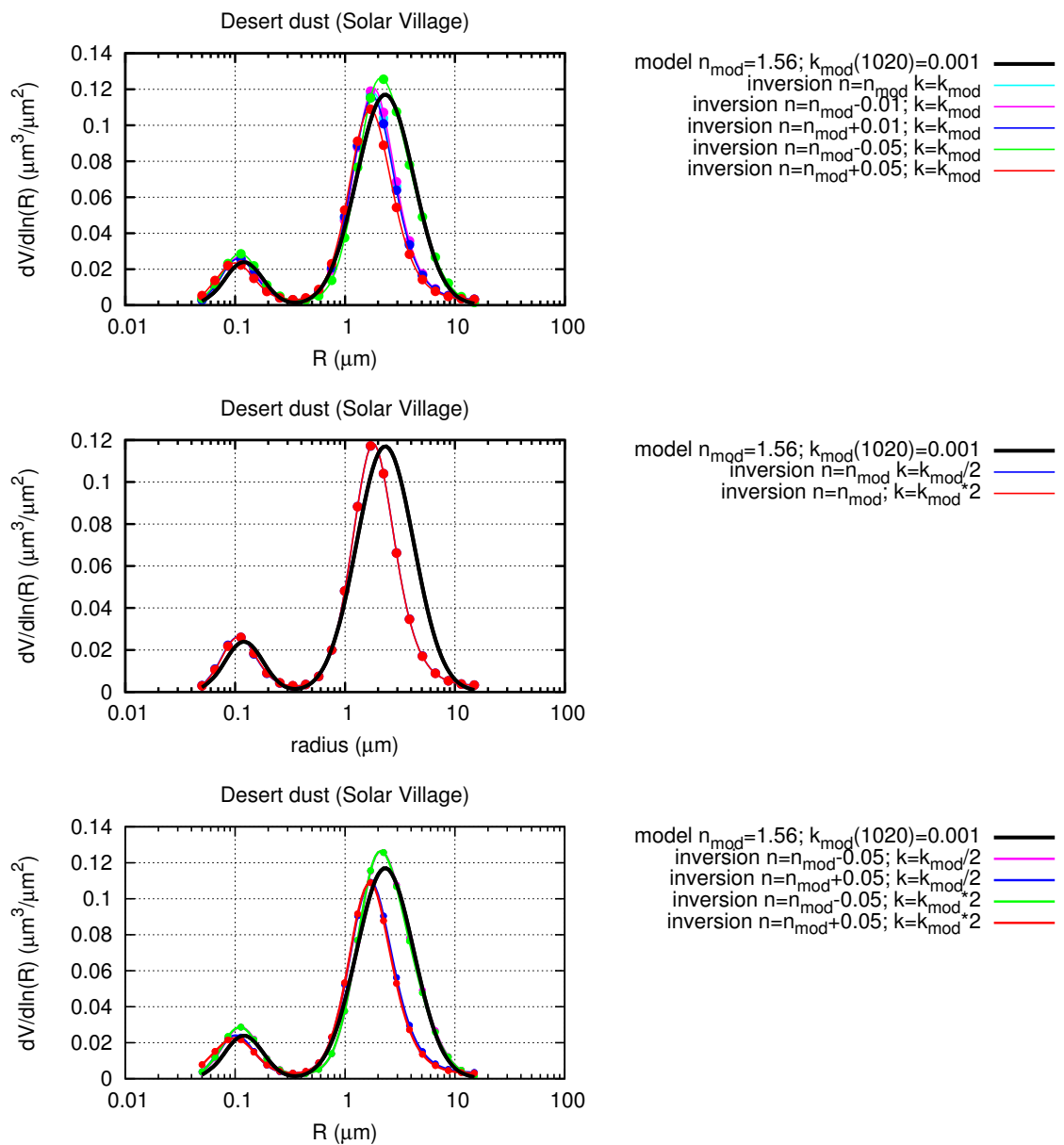


FIGURE A.2: Size distributions retrieved from 11 wl with different refractive indices (fixed) - Solar Village.

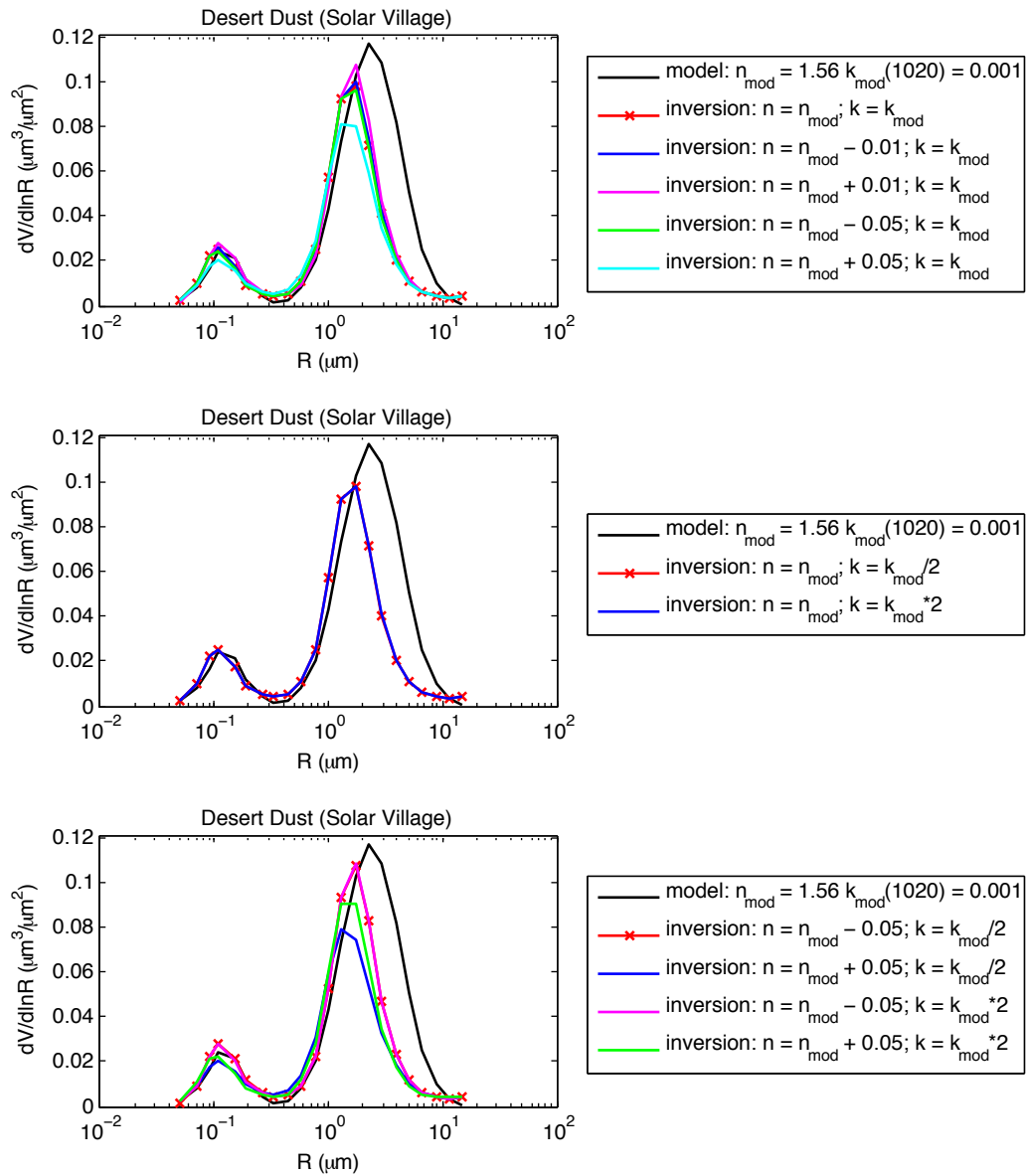


FIGURE A.3: Size distributions retrieved from 8 wl with different initial refractive indices (retrieved together with size distributions) - Solar Village.

Biomass burning(Mongu)

$$C_{Vf}^{model} = 0.024\mu m^3/\mu m^2, R_{eff,f}^{model} = 0.117\mu m$$

$$C_{Vc}^{model} = 0.018\mu m^3/\mu m^2, R_{eff,c}^{model} = 2.61\mu m$$

TABLE A.3: **Sensitivity study results: 8 wl inversion (Mongu)**

a) Sensitivity to the real part of complex refractive index

n	$n = n_{model}$	$n = n_m - 0.01$	$n = n_m + 0.01$	$n = n_m - 0.05$	$n = n_m + 0.05$
$C_{Vf}, \mu m^3/\mu m^2$	0.0245(+2%)	0.0246(+2%)	0.0244(+2%)	0.0300(+25%)	0.0220(-8%)
$C_{Vc}, \mu m^3/\mu m^2$	0.0120(-32%)	0.0118(-33%)	0.0122(-31%)	0.0110(-38%)	0.0141(-20%)
$R_{eff,f}$	0.110	0.113	0.108	0.107	0.106
$R_{eff,c}$	3.27	3.33	3.23	3.31	3.37
AOD residual	3.63%	4.28%	3.16%	3.85%	2.41%

b) Sensitivity to the imaginary part of complex refractive index

k	$k = k_{mod}/2$	$k = 2k_{mod}$
$C_{Vf}, \mu m^3/\mu m^2$	0.0253(+6%)	0.0224(-7%)
$C_{Vc}, \mu m^3/\mu m^2$	0.0141(-21%)	0.0034(-81%)
$R_{eff,f}$	0.109	0.119
$R_{eff,c}$	3.11	4.64
AOD residual	2.31%	12.04%

c) Sensitivity to the real and imaginary parts of complex refractive index

n	$n = n_{mod} - 0.05$	$n = n_{mod} + 0.05$	$n = n_{mod} - 0.05$	$n = n_{mod} + 0.05$
k	$k = k_{mod}/2$	$k = k_{mod}/2$	$k = 2k_{mod}$	$k = 2k_{mod}$
$C_{Vf}, \mu m^3/\mu m^2$	0.0305(+27%)	0.0221(-8%)	0.0274(+14%)	0.0216(-10%)
$C_{Vc}, \mu m^3/\mu m^2$	0.0156(-12%)	0.0160(-10%)	0.0028(-84%)	0.0088(-50%)
$R_{eff,f}$	0.109	0.107	0.112	0.104
$R_{eff,c}$	3.49	3.28	4.63	3.47
AOD residual	2.74%	1.75%	9.66%	5.11%

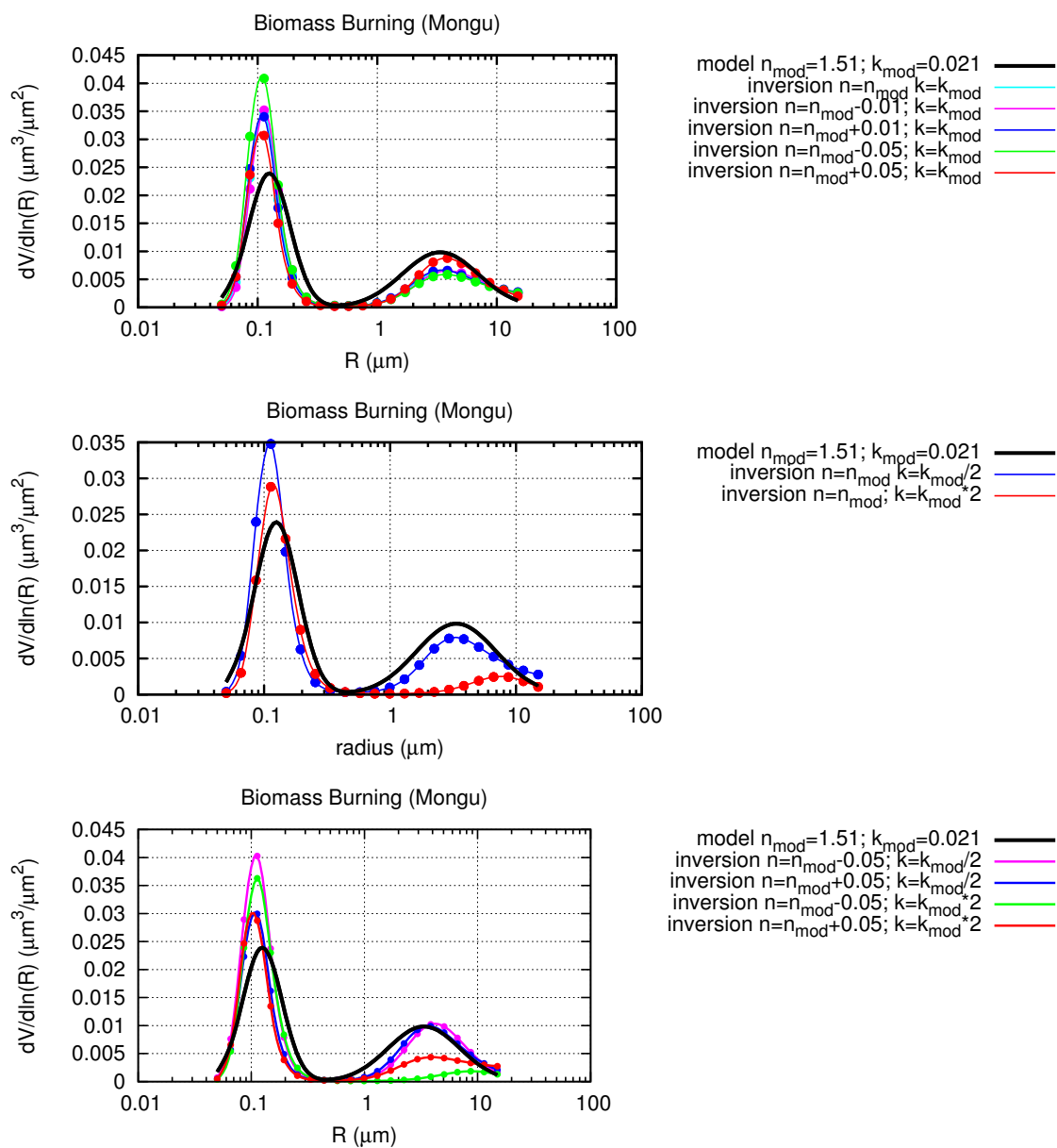


FIGURE A.4: Size distributions retrieved from 8 wl with different refractive indices (fixed) - Mongu.

TABLE A.4: **Sensitivity study results: 11 wl inversion (Mongu)**

a) Sensitivity to the real part of complex refractive index

n	$n = n_{model}$	$n = n_m - 0.01$	$n = n_m + 0.01$	$n = n_m - 0.05$	$n = n_m + 0.05$
$C_{Vf}, \mu m^3 / \mu m^2$	0.0232(-3%)	0.0255(+7%)	0.0232(-3%)	0.0269(+12%)	0.0223(-7%)
$C_{Vc}, \mu m^3 / \mu m^2$	0.0157(-11%)	0.0132(-26%)	0.0155(-12%)	0.0137(-23%)	0.0146(-17%)
$R_{eff,f}$	0.114	0.109	0.111	0.116	0.104
$R_{eff,c}$	3.55	3.15	3.47	3.40	3.18
AOD residual	5.13%	4.63%	4.58%	6.29%	3.49%

b) Sensitivity to the imaginary part of complex refractive index

k	$k = k_{mod}/2$	$k = 2k_{mod}$
$C_{Vf}, \mu m^3 / \mu m^2$	0.0243(+2%)	0.0217(-10%)
$C_{Vc}, \mu m^3 / \mu m^2$	0.0165(-7%)	0.0107(-40%)
$R_{eff,f}$	0.113	0.114
$R_{eff,c}$	3.27	3.50
AOD residual	2.90%	10.14%

c) Sensitivity to the real and imaginary parts of complex refractive index

n	$n = n_{mod} - 0.05$	$n = n_{mod} + 0.05$	$n = n_{mod} - 0.05$	$n = n_{mod} + 0.05$
k	$k = k_{mod}/2$	$k = k_{mod}/2$	$k = 2k_{mod}$	$k = 2k_{mod}$
$C_{Vf}, \mu m^3 / \mu m^2$	0.0286(+19%)	0.0222(-7%)	0.0222(-7%)	0.0205(-15%)
$C_{Vc}, \mu m^3 / \mu m^2$	0.0152(-14%)	0.0158(-11%)	0.0113(-36%)	0.0125(-29%)
$R_{eff,f}$	0.115	0.106	0.129	0.106
$R_{eff,c}$	3.18	3.09	4.07	3.57
AOD residual	3.53%	2.34%	13.64%	7.37%

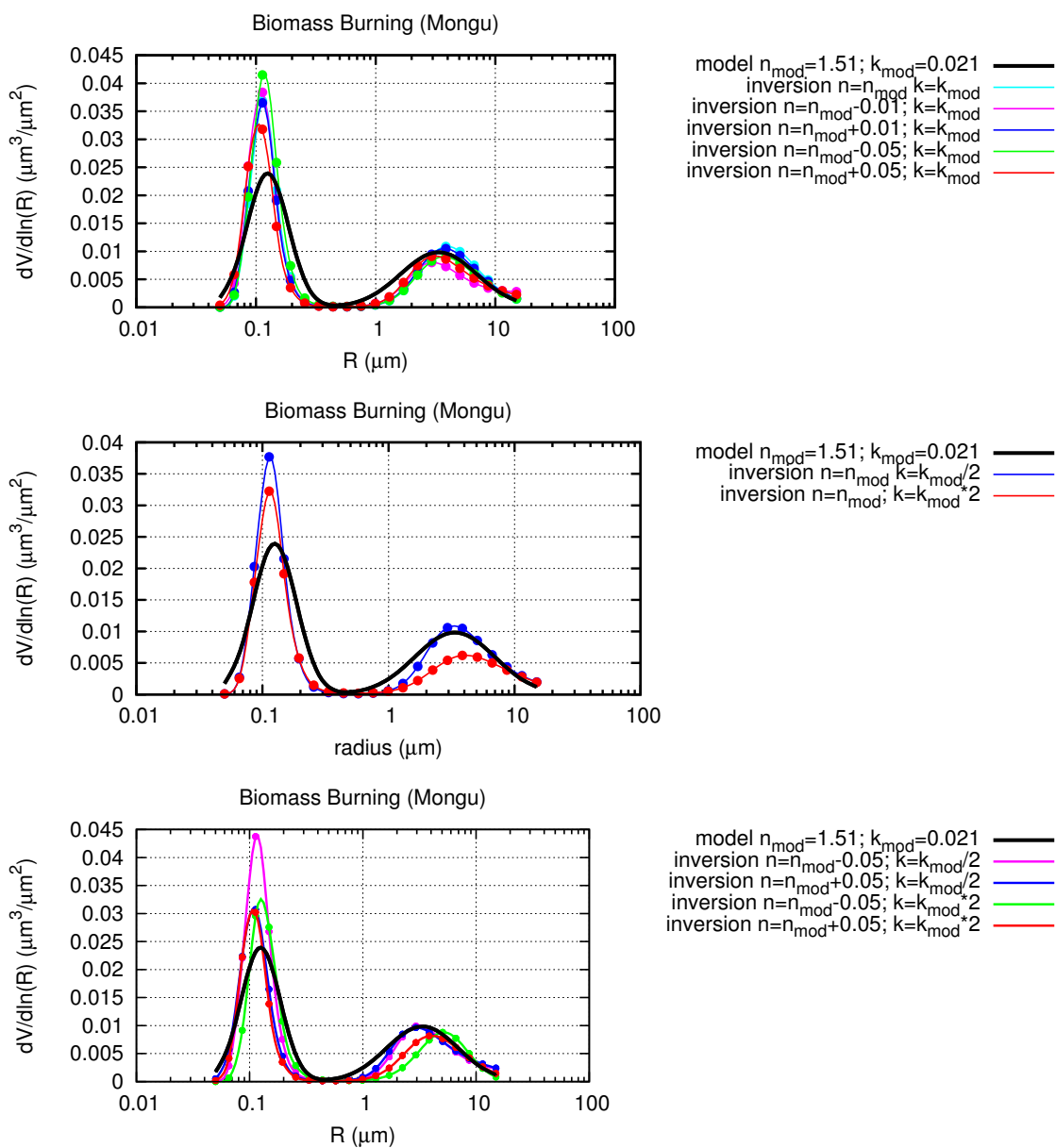


FIGURE A.5: Size distributions retrieved from 11 wl with different refractive indices (fixed) - Mongu.

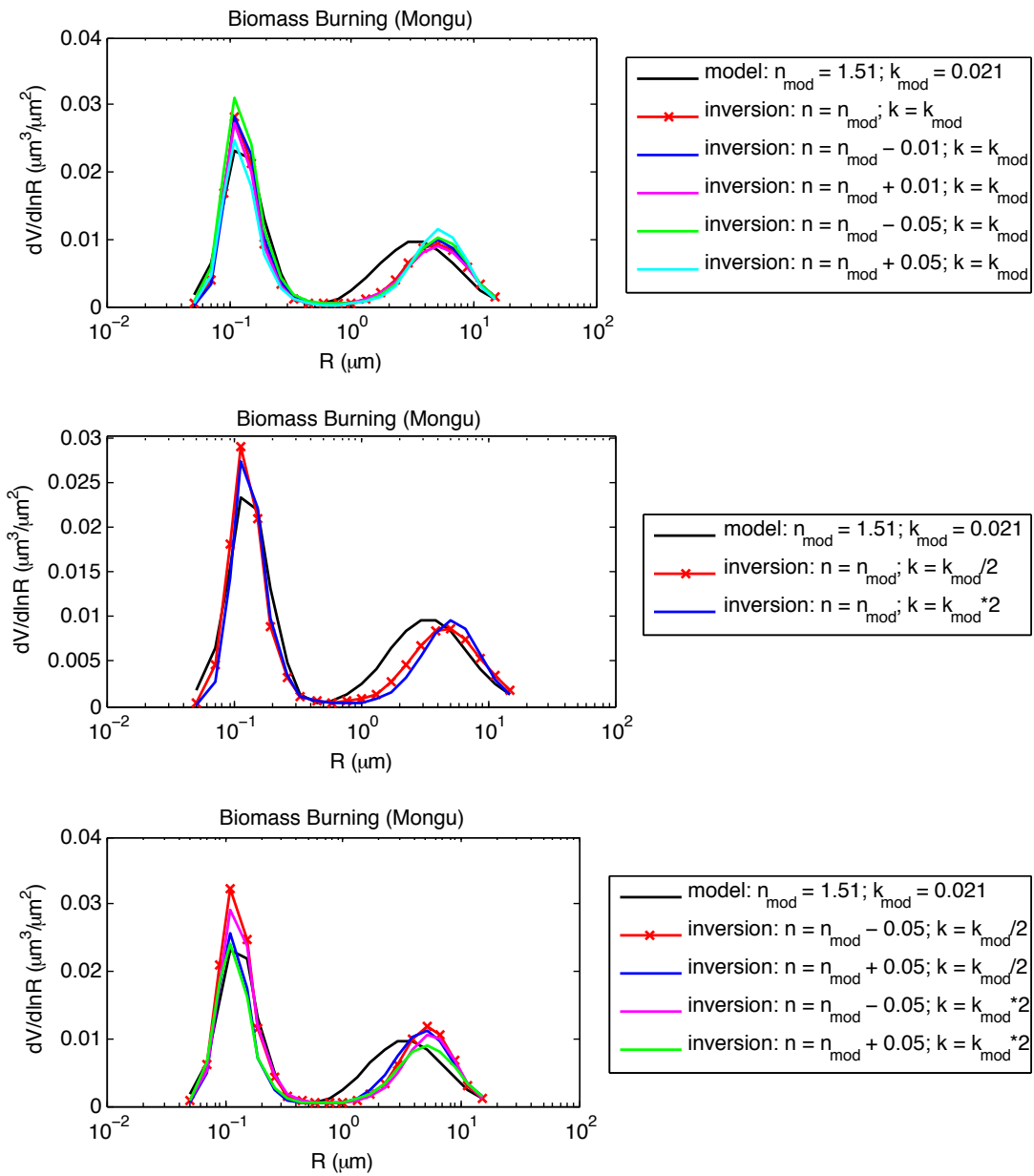


FIGURE A.6: Size distributions retrieved from 8 wl with different initial refractive indices (retrieved together with size distributions) - Mongu.

Urban clean (GSFC)

$$C_{Vf}^{model} = 0.03\mu m^3/\mu m^2, R_{eff,f}^{model} = 0.133\mu m$$

$$C_{Vc}^{model} = 0.018\mu m^3/\mu m^2, R_{eff,c}^{model} = 2.52\mu m$$

TABLE A.5: **Sensitivity study results: 8 wl inversion (GSFC)**

a) Sensitivity to the real part of complex refractive index

n	$n = n_{model}$	$n = n_m - 0.01$	$n = n_m + 0.01$	$n = n_m - 0.05$	$n = n_m + 0.05$
$C_{Vf}, \mu m^3/\mu m^2$	0.0328(+9%)	0.0339(+13%)	0.0317(+5%)	0.0394(+31%)	0.0281(-7%)
$C_{Vc}, \mu m^3/\mu m^2$	0.0205(+16%)	0.0206(+17%)	0.0204(+15%)	0.0194(+10%)	0.0199(+13%)
$R_{eff,f}$	0.123	0.123	0.122	0.127	0.119
$R_{eff,c}$	3.05	3.07	3.03	2.97	2.97
AOD residual	0.24%	0.25%	0.24%	0.27%	0.22%

b) Sensitivity to the imaginary part of complex refractive index

k	$k = k_{mod}/2$	$k = 2k_{mod}$
$C_{Vf}, \mu m^3/\mu m^2$	0.0327(+9%)	0.0329(+9%)
$C_{Vc}, \mu m^3/\mu m^2$	0.0207(+17%)	0.0200(+13%)
$R_{eff,f}$	0.123	0.121
$R_{eff,c}$	3.04	3.08
AOD residual	0.23%	0.26%

c) Sensitivity to the real and imaginary parts of complex refractive index

n	$n = n_{mod} - 0.05$	$n = n_{mod} + 0.05$	$n = n_{mod} - 0.05$	$n = n_{mod} + 0.05$
k	$k = k_{mod}/2$	$k = k_{mod}/2$	$k = 2k_{mod}$	$k = 2k_{mod}$
$C_{Vf}, \mu m^3/\mu m^2$	0.0393(+31%)	0.0281(-7%)	0.0399(+33%)	0.0282(-6%)
$C_{Vc}, \mu m^3/\mu m^2$	0.0197(+12%)	0.0201(+14%)	0.0186(+5%)	0.0196(+11%)
$R_{eff,f}$	0.128	0.119	0.125	0.118
$R_{eff,c}$	2.96	2.96	2.99	3.00
AOD residual	0.26%	0.21%	0.50%	0.23%

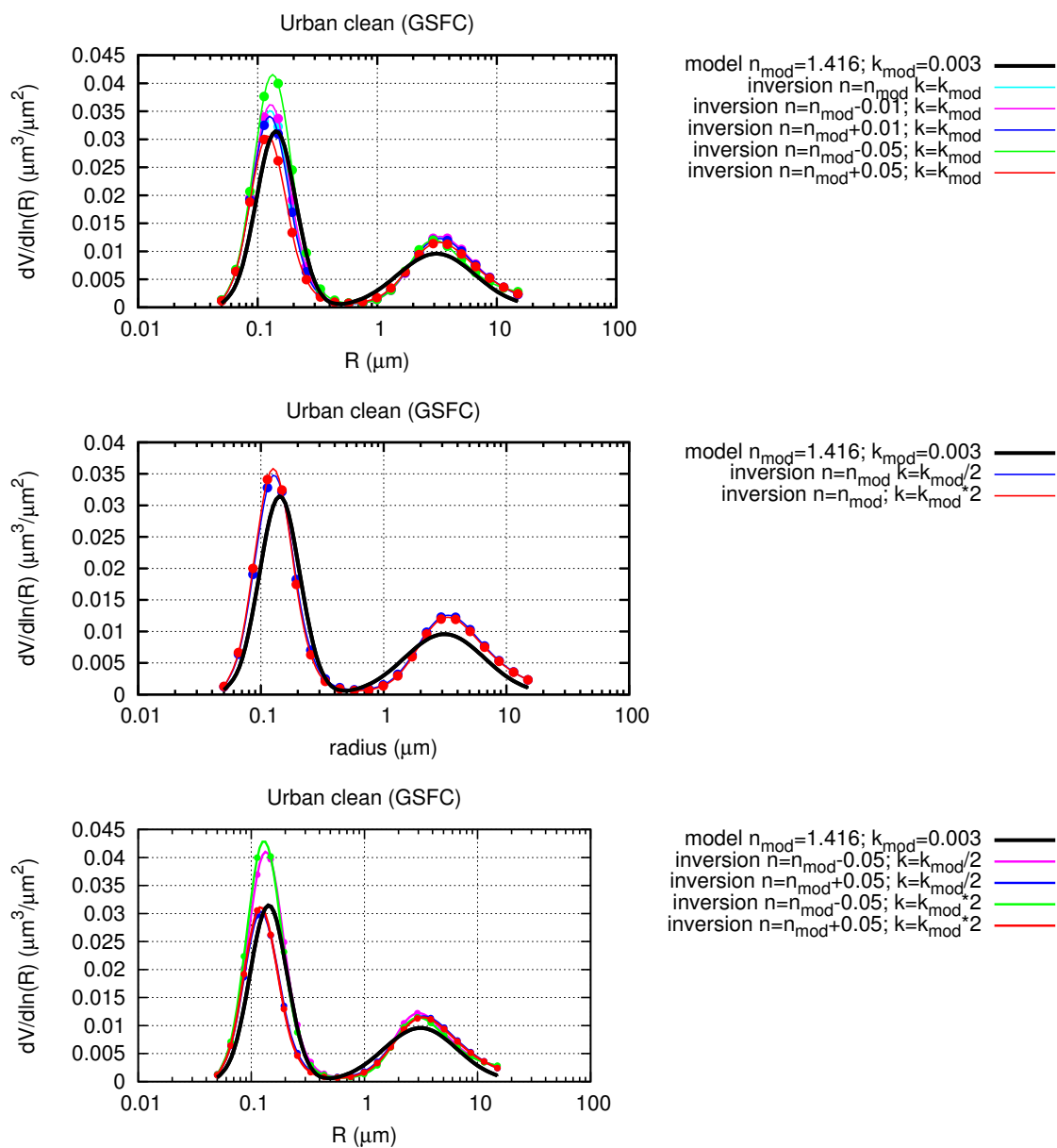


FIGURE A.7: Size distributions retrieved from 8 wl with different refractive indices (fixed) - GSFC.

TABLE A.6: **Sensitivity study results: 11 wl inversion (GSFC)**

a) Sensitivity to the real part of complex refractive index

n	$n = n_{model}$	$n = n_m - 0.01$	$n = n_m + 0.01$	$n = n_m - 0.05$	$n = n_m + 0.05$
$C_{Vf}, \mu m^3 / \mu m^2$	0.0327(+9%)	0.0338(+12%)	0.0317(+5%)	0.0391(+30%)	0.0282(-6%)
$C_{Vc}, \mu m^3 / \mu m^2$	0.0208(+18%)	0.0210(+19%)	0.0207(+17%)	0.0217(+23%)	0.0203(+15%)
$R_{eff,f}$	0.123	0.124	0.122	0.128	0.119
$R_{eff,c}$	3.13	3.16	3.11	3.27	3.07
AOD residual	0.26%	0.27%	0.26%	0.29%	0.24%

b) Sensitivity to the imaginary part of complex refractive index

k	$k = k_{mod}/2$	$k = 2k_{mod}$
$C_{Vf}, \mu m^3 / \mu m^2$	0.0327(+9%)	0.0328(+9%)
$C_{Vc}, \mu m^3 / \mu m^2$	0.0210(+19%)	0.0204(+15%)
$R_{eff,f}$	0.124	0.122
$R_{eff,c}$	3.12	3.16
AOD residual	0.25%	0.28%

c) Sensitivity to the real and imaginary parts of complex refractive index

n	$n = n_{mod} - 0.05$	$n = n_{mod} + 0.05$	$n = n_{mod} - 0.05$	$n = n_{mod} + 0.05$
k	$k = k_{mod}/2$	$k = k_{mod}/2$	$k = 2k_{mod}$	$k = 2k_{mod}$
$C_{Vf}, \mu m^3 / \mu m^2$	0.0390(+30%)	0.0282(-6%)	0.0393(+31%)	0.0282(-6%)
$C_{Vc}, \mu m^3 / \mu m^2$	0.0220(+25%)	0.0205(+16%)	0.0210(+19%)	0.0200(+13%)
$R_{eff,f}$	0.129	0.119	0.126	0.118
$R_{eff,c}$	3.25	3.06	3.30	3.09
AOD residual	0.28%	0.23%	0.31%	0.25%

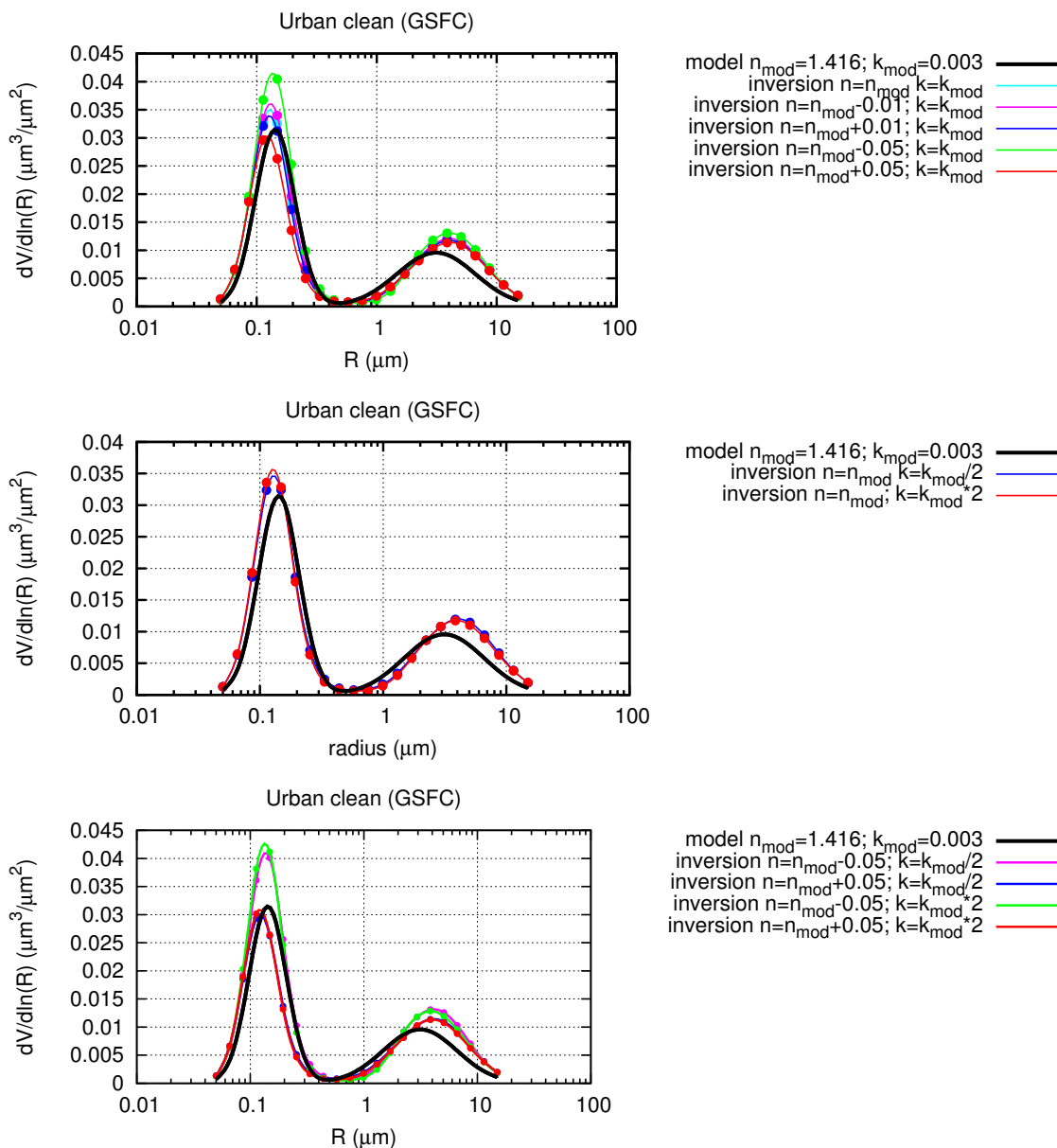


FIGURE A.8: Size distributions retrieved from 11 wl with different refractive indices (fixed) - GSFC.

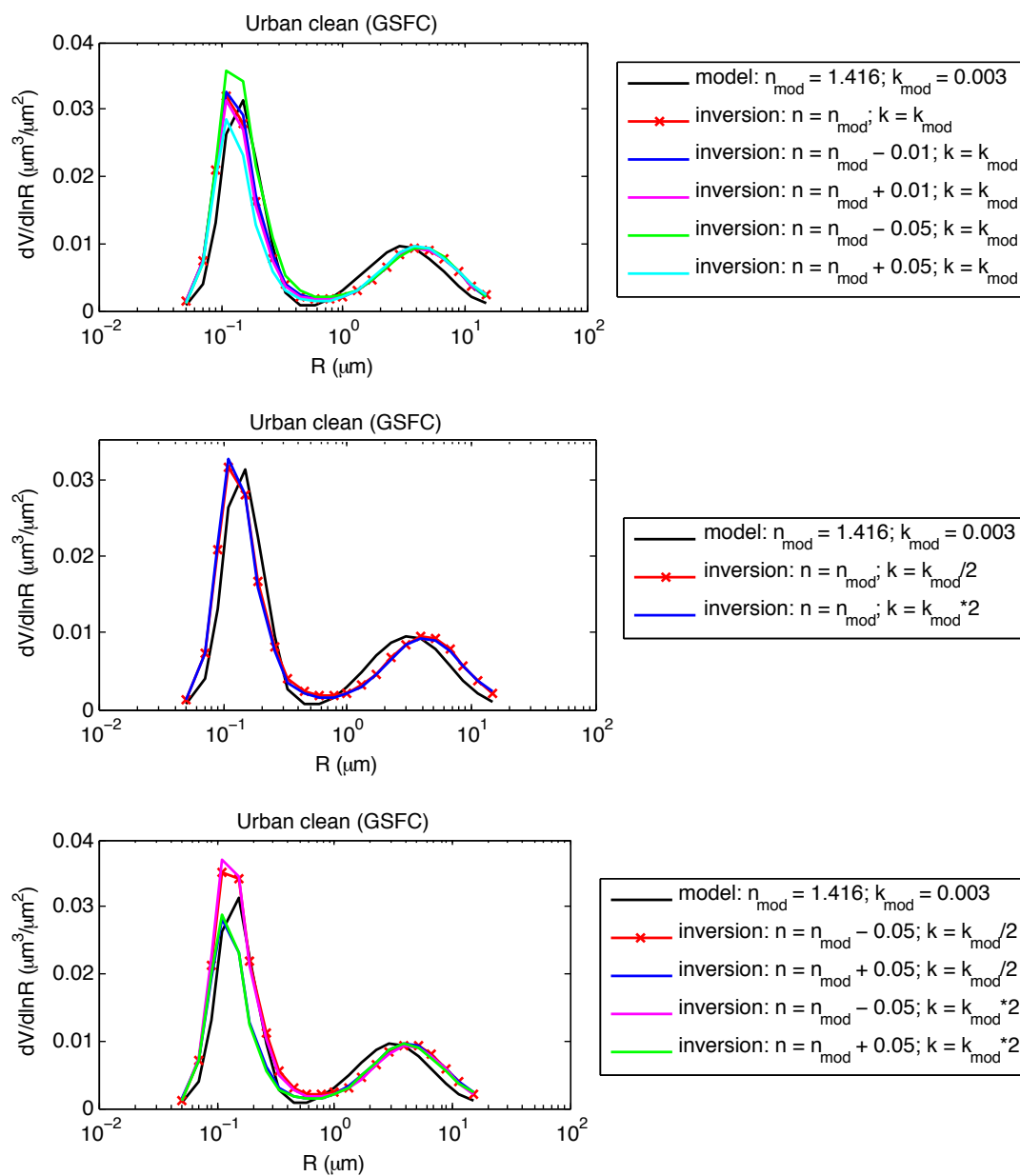


FIGURE A.9: Size distributions retrieved from 8 wl with different initial refractive indices (retrieved together with size distributions) - GSFC.

Urban polluted (Mexico)

$$C_{Vf}^{model} = 0.024\mu m^3/\mu m^2, R_{eff,f}^{model} = 0.119\mu m$$

$$C_{Vc}^{model} = 0.022\mu m^3/\mu m^2, R_{eff,c}^{model} = 2.41\mu m$$

TABLE A.7: **Sensitivity study results: 8 wl inversion (Mexico)**

a) Sensitivity to the real part of complex refractive index

n	$n = n_{model}$	$n = n_m - 0.01$	$n = n_m + 0.01$	$n = n_m - 0.05$	$n = n_m + 0.05$
$C_{Vf}, \mu m^3/\mu m^2$	0.0238(+8%)	0.0242(+10%)	0.0235(+7%)	0.0289(+32%)	0.0219(-1%)
$C_{Vc}, \mu m^3/\mu m^2$	0.0186(-15%)	0.0186(-15%)	0.0184(-16%)	0.0179(-18%)	0.0186(-15%)
$R_{eff,f}$	0.120	0.122	0.118	0.117	0.111
$R_{eff,c}$	3.57	3.67	3.73	3.67	3.48
AOD residual	1.80%	1.89%	1.73%	2.27%	1.44%

b) Sensitivity to the imaginary part of complex refractive index

k	$k = k_{mod}/2$	$k = 2k_{mod}$
$C_{Vf}, \mu m^3/\mu m^2$	0.0239(+9%)	0.0233(+3%)
$C_{Vc}, \mu m^3/\mu m^2$	0.0212(-3%)	0.0179(-18%)
$R_{eff,f}$	0.116	0.122
$R_{eff,c}$	2.83	3.70
AOD residual	1.43%	2.64%

c) Sensitivity to the real and imaginary parts of complex refractive index

n	$n = n_{mod} - 0.05$	$n = n_{mod} + 0.05$	$n = n_{mod} - 0.05$	$n = n_{mod} + 0.05$
k	$k = k_{mod}/2$	$k = k_{mod}/2$	$k = 2k_{mod}$	$k = 2k_{mod}$
$C_{Vf}, \mu m^3/\mu m^2$	0.0293(+34%)	0.0217(-1%)	0.0254(+16%)	0.0218(-1%)
$C_{Vc}, \mu m^3/\mu m^2$	0.0202(-8%)	0.0208(-5%)	0.0192(-12%)	0.0174(-20%)
AOD residual	1.84%	0.10%	4.07%	2.09%
$R_{eff,f}$	0.115	0.110	0.134	0.112
$R_{eff,c}$	2.85	2.75	3.89	3.75

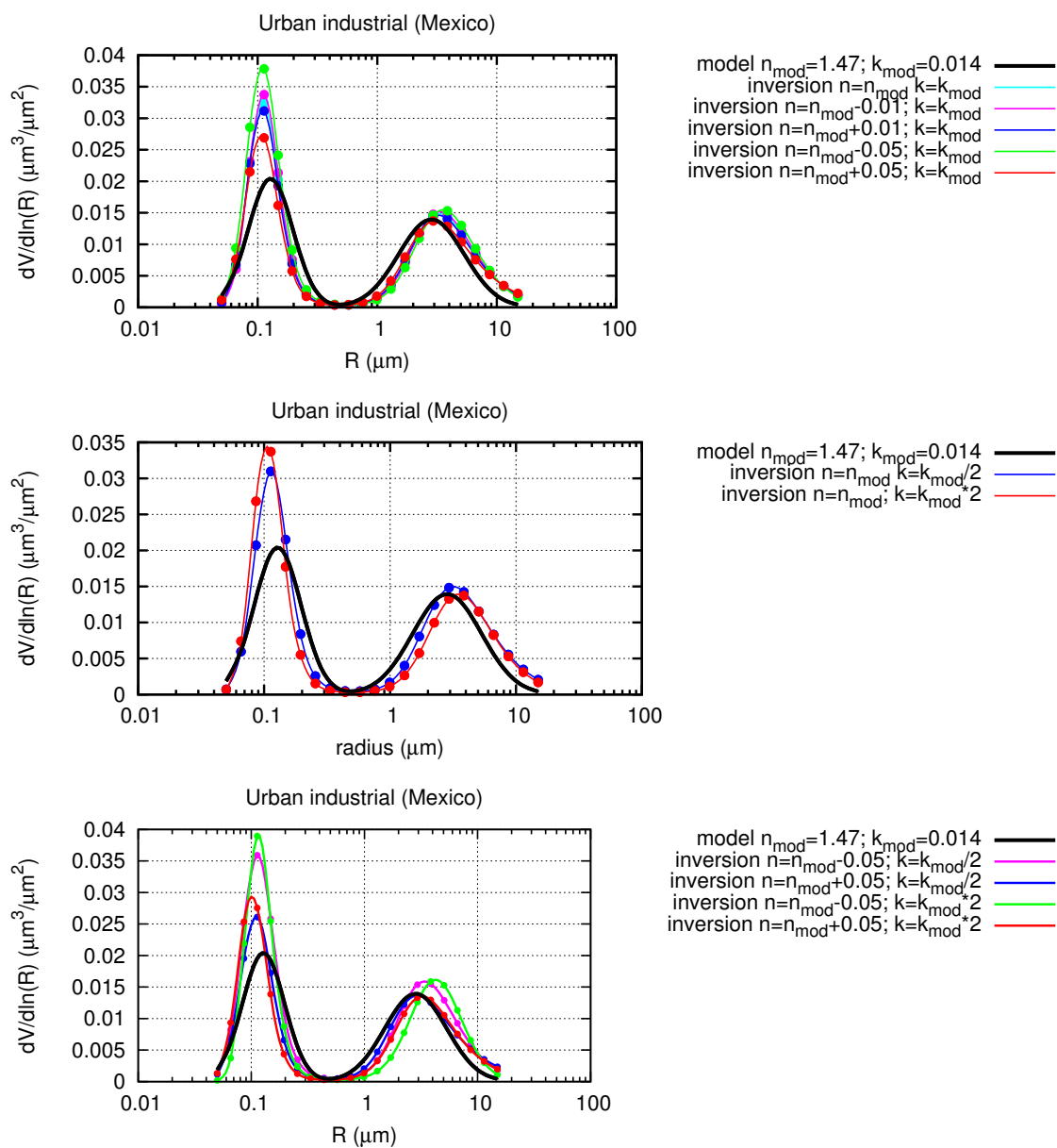


FIGURE A.10: Size distributions retrieved from 8 wl with different refractive indices (fixed) - Mexico.

TABLE A.8: **Sensitivity study results: 11 wl inversion (Mexico)**

a) Sensitivity to the real part of complex refractive index

n	$n = n_{model}$	$n = n_m - 0.01$	$n = n_m + 0.01$	$n = n_m - 0.05$	$n = n_m + 0.05$
$C_{Vf}, \mu m^3 / \mu m^2$	0.0250(+14%)	0.0258(+18%)	0.0229(+4%)	0.0310(+42%)	0.0217(-1%)
$C_{Vc}, \mu m^3 / \mu m^2$	0.0222(+1%)	0.0224(+2%)	0.0232(+6%)	0.0229(+5%)	0.0213(-3%)
$R_{eff,f}$	0.111	0.111	0.116	0.108	0.108
$R_{eff,c}$	2.84	2.88	3.25	3.02	2.70
AOD residual	1.54%	1.65%	0.012%	2.22%	1.05%

b) Sensitivity to the imaginary part of complex refractive index

k	$k = k_{mod}/2$	$k = 2k_{mod}$
$C_{Vf}, \mu m^3 / \mu m^2$	0.0245(+12%)	0.0257(+17%)
$C_{Vc}, \mu m^3 / \mu m^2$	0.0227(+4%)	0.0208(-5%)
$R_{eff,f}$	0.114	0.105
$R_{eff,c}$	2.79	2.96
AOD residual	0.93%	2.96%

c) Sensitivity to the real and imaginary parts of complex refractive index

n	$n = n_{mod} - 0.05$	$n = n_{mod} + 0.05$	$n = n_{mod} - 0.05$	$n = n_{mod} + 0.05$
k	$k = k_{mod}/2$	$k = k_{mod}/2$	$k = 2k_{mod}$	$k = 2k_{mod}$
$C_{Vf}, \mu m^3 / \mu m^2$	0.0301(+37%)	0.0213(-3%)	0.0316(+44%)	0.0227(+4%)
$C_{Vc}, \mu m^3 / \mu m^2$	0.0240(+10%)	0.0216(-2%)	0.0204(-7%)	0.0208(-5%)
$R_{eff,f}$	0.113	0.111	0.103	0.101
$R_{eff,c}$	2.97	2.66	3.13	2.85
AOD residual	1.48%	0.54%	3.98%	2.34%

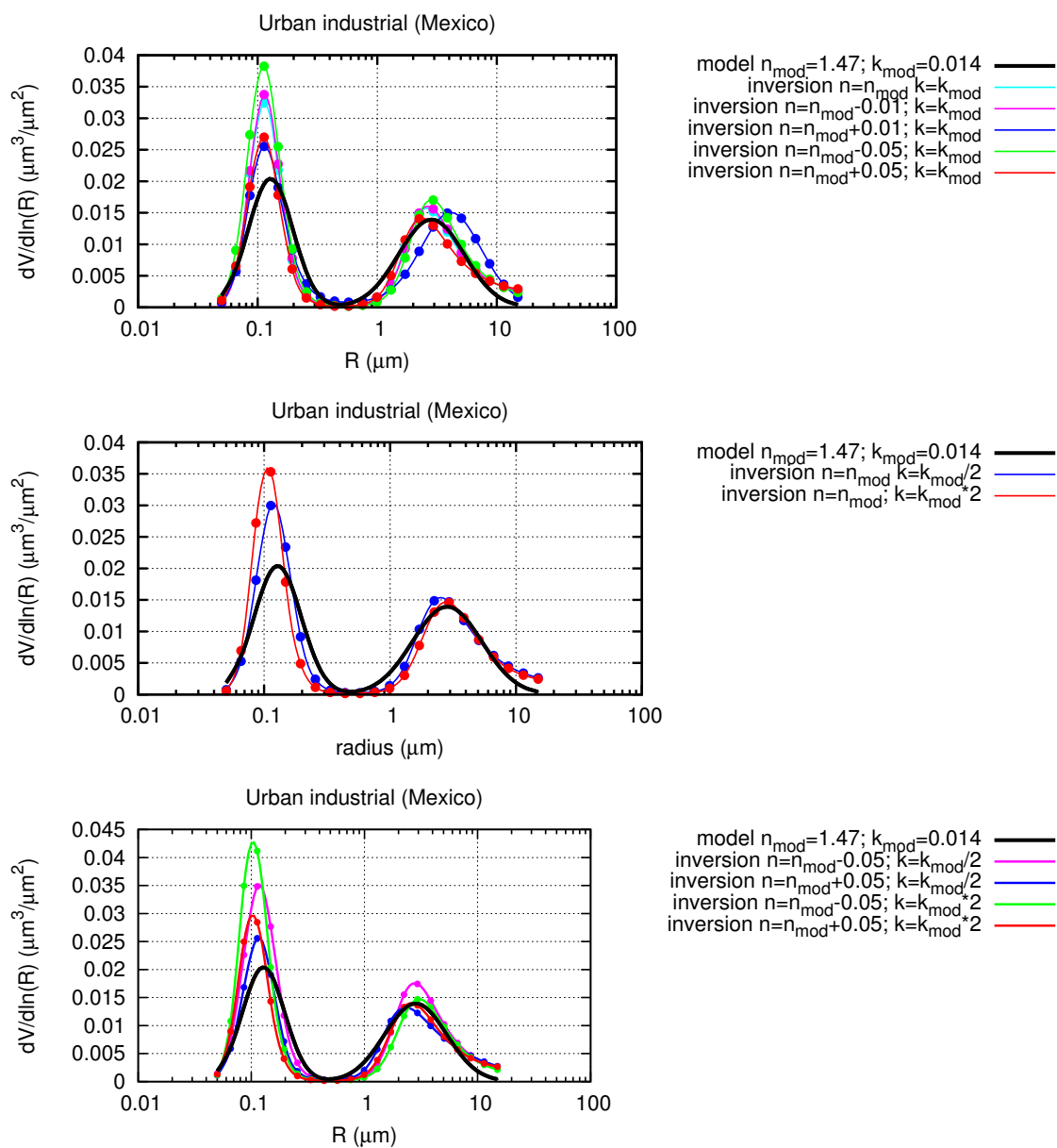


FIGURE A.11: Size distributions retrieved from 11 wl with different refractive indices (fixed) - Mexico.

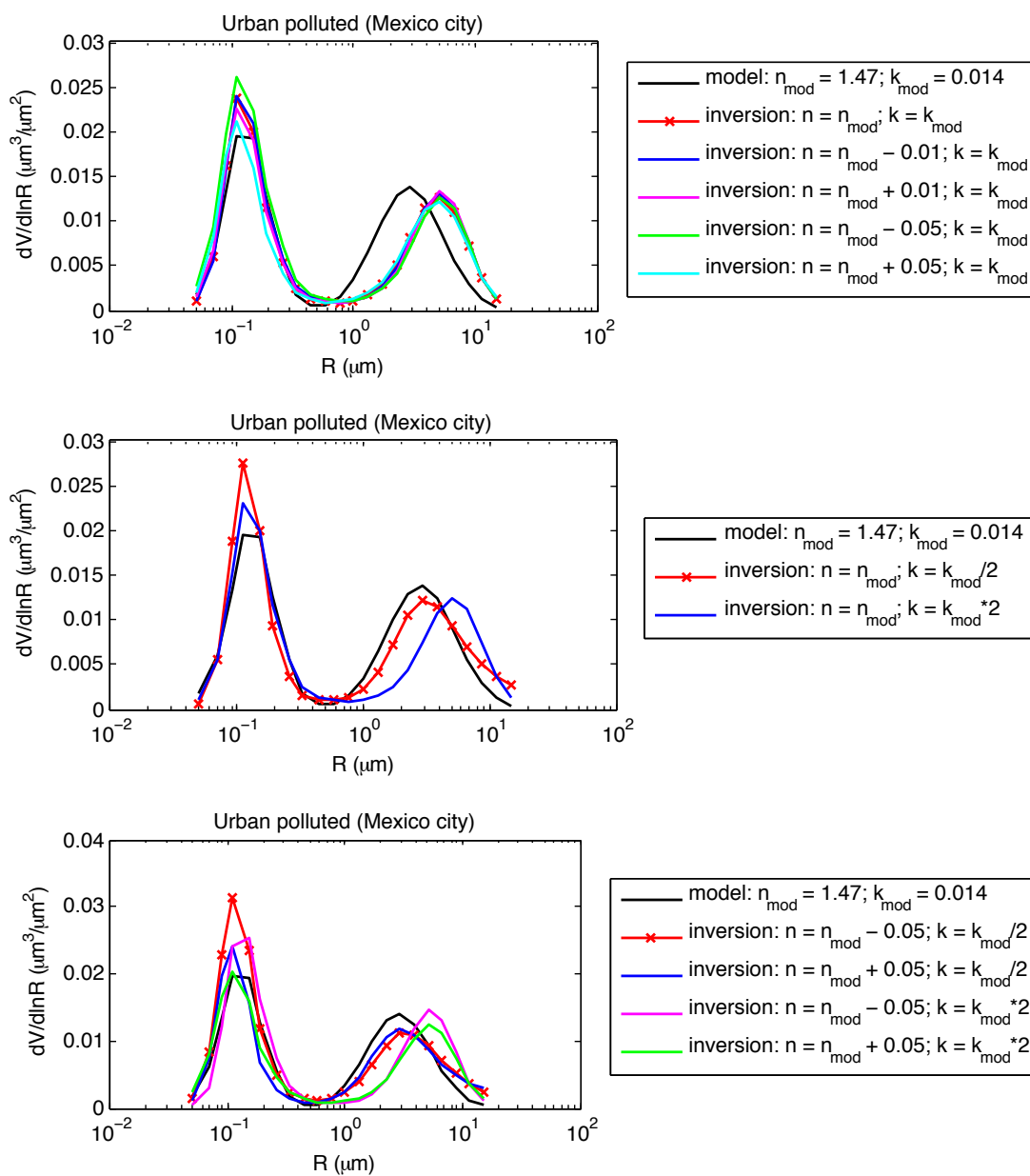


FIGURE A.12: Size distributions retrieved from 8 wl with different initial refractive indices (retrieved together with size distributions) - Mexico.

Maritime (Lanai)

$$C_{Vf}^{model} = 0.08\mu m^3/\mu m^2, R_{eff,f}^{model} = 0.147\mu m$$

$$C_{Vc}^{model} = 0.16\mu m^3/\mu m^2, R_{eff,c}^{model} = 2.28\mu m$$

TABLE A.9: Sensitivity study results: 8 wl inversion (Lanai)

a) Sensitivity to the real part of complex refractive index

n	$n = n_{model}$	$n = n_m - 0.01$	$n = n_m + 0.01$	$n = n_m - 0.05$	$n = n_m + 0.05$
$C_{Vf}, \mu m^3/\mu m^2$	0.0778(-3%)	0.0805(+1%)	0.0773(-4%)	0.114(+42%)	0.0668(-14%)
$C_{Vc}, \mu m^3/\mu m^2$	0.161(+1%)	0.166(+4%)	0.1209(-24%)	0.247(+55%)	0.114(-29%)
$R_{eff,f}$	0.154	0.155	0.151	0.168	0.147
$R_{eff,c}$	2.35	2.39	1.87	2.47	1.81
AOD residual	0.30%	0.30%	0.27%	34.13%	0.28%

b) Sensitivity to the imaginary part of complex refractive index

k	$k = k_{mod}/2$	$k = 2k_{mod}$
$C_{Vf}, \mu m^3/\mu m^2$	0.0778(-3%)	0.0778(-3%)
$C_{Vc}, \mu m^3/\mu m^2$	0.161(+1%)	0.162(+2%)
AOD residual	0.30%	0.31%
$R_{eff,f}$	0.154	0.154
$R_{eff,c}$	2.34	2.36

c) Sensitivity to the real and imaginary parts of complex refractive index

n	$n = n_{mod} - 0.05$	$n = n_{mod} + 0.05$	$n = n_{mod} - 0.05$	$n = n_{mod} + 0.05$
k	$k = k_{mod}/2$	$k = k_{mod}/2$	$k = 2k_{mod}$	$k = 2k_{mod}$
$C_{Vf}, \mu m^3/\mu m^2$	0.114(+42%)	0.0688(-14%)	0.0115(+43%)	0.0688(-14%)
$C_{Vc}, \mu m^3/\mu m^2$	0.246(+55%)	0.114(-29%)	0.250(+57%)	0.114(-29%)
$R_{eff,f}$	0.168	0.147	0.167	0.147
$R_{eff,c}$	2.46	1.81	2.48	1.81
AOD residual	33.79%	0.28%	34.83%	0.28%

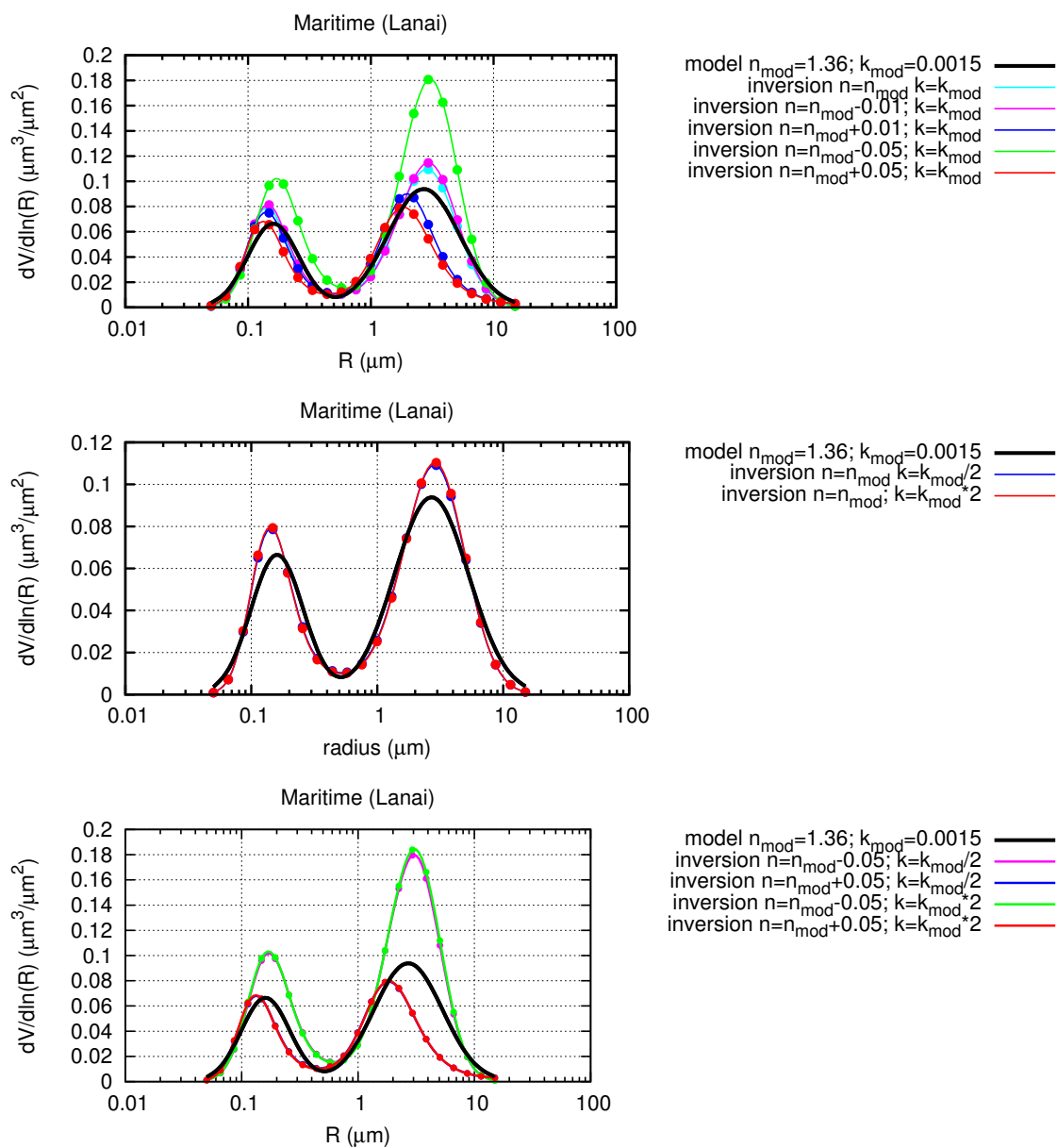


FIGURE A.13: Size distributions retrieved from 8 wl with different refractive indices (fixed) - Lanai.

TABLE A.10: **Sensitivity study results: 11 wl inversion (Lanai)**

a) Sensitivity to the real part of complex refractive index

n	$n = n_{model}$	$n = n_m - 0.01$	$n = n_m + 0.01$	$n = n_m - 0.05$	$n = n_m + 0.05$
$C_{Vf}, \mu m^3 / \mu m^2$	0.0828(+3%)	0.0856(+7%)	0.0801(+0%)	0.113(+40%)	0.0712(-11%)
$C_{Vc}, \mu m^3 / \mu m^2$	0.146(-8%)	0.149(-6%)	0.143(-10%)	0.211(+32%)	0.132(-17%)
$R_{eff,f}$	0.146	0.147	0.145	0.168	0.140
$R_{eff,c}$	2.15	2.18	2.12	2.22	2.01
AOD residual	0.26%	0.26%	0.26%	32.60%	0.26%

b) Sensitivity to the imaginary part of complex refractive index

k	$k = k_{mod}/2$	$k = 2k_{mod}$
$C_{Vf}, \mu m^3 / \mu m^2$	0.0827(+3%)	0.0829(+3%)
$C_{Vc}, \mu m^3 / \mu m^2$	0.146(-8%)	0.145(-9%)
$R_{eff,f}$	0.146	0.145
$R_{eff,c}$	2.15	2.15
AOD residual	0.25%	2.26%

c) Sensitivity to the real and imaginary parts of complex refractive index

n	$n = n_{mod} - 0.05$	$n = n_{mod} + 0.05$	$n = n_{mod} - 0.05$	$n = n_{mod} + 0.05$
k	$k = k_{mod}/2$	$k = k_{mod}/2$	$k = 2k_{mod}$	$k = 2k_{mod}$
$C_{Vf}, \mu m^3 / \mu m^2$	0.112(+40%)	0.0711(-11%)	0.113(+41%)	0.0712(-11%)
$C_{Vc}, \mu m^3 / \mu m^2$	0.210(+32%)	0.132(-17%)	0.211(+33%)	0.132(-17%)
$R_{eff,f}$	0.168	0.141	0.168	0.140
$R_{eff,c}$	2.22	2.01	2.22	2.01
AOD residual	32.30%	0.27%	33.19%	0.27%

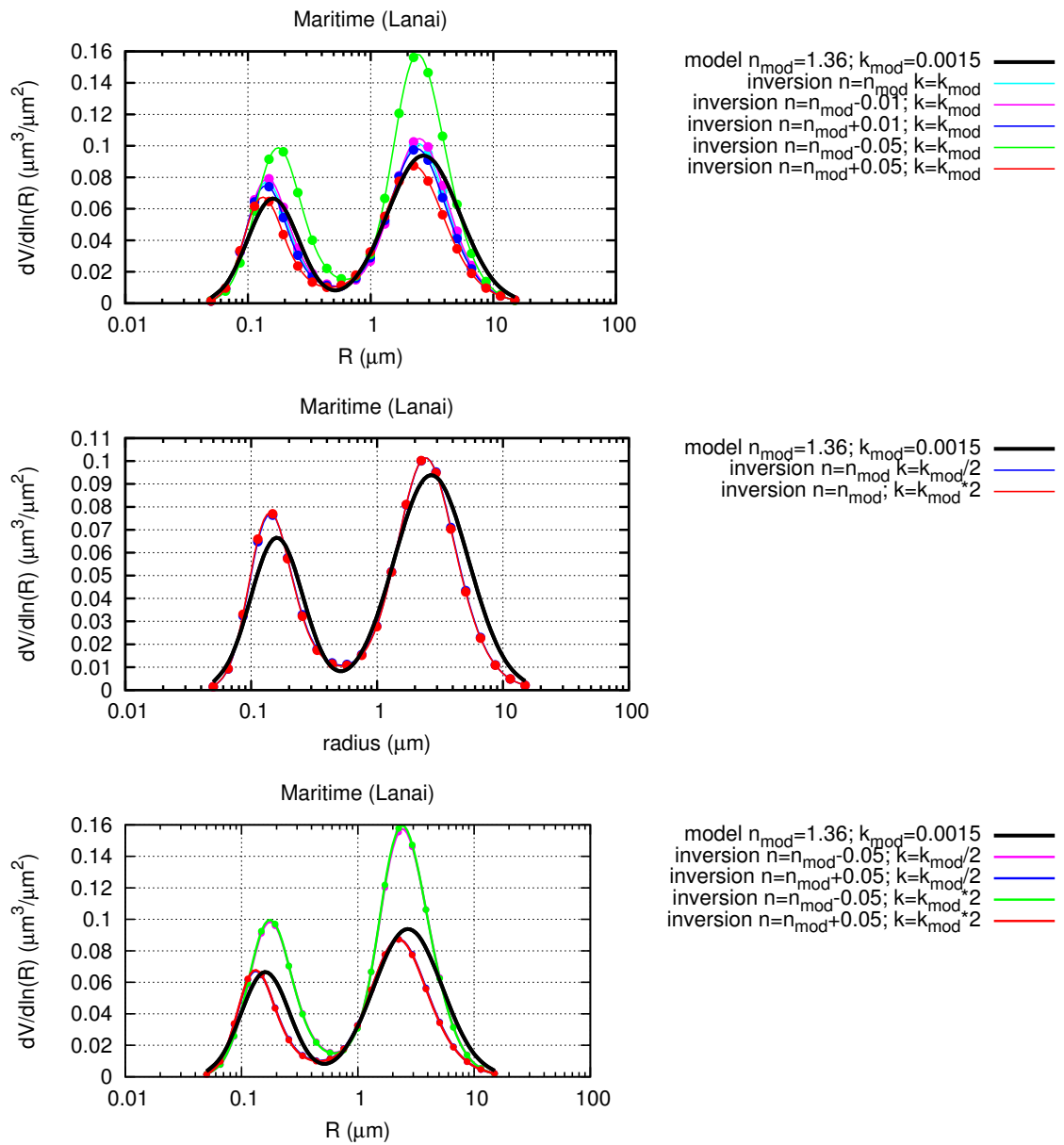


FIGURE A.14: Size distributions retrieved from 11 wl with different refractive indices (fixed) - Lanai.

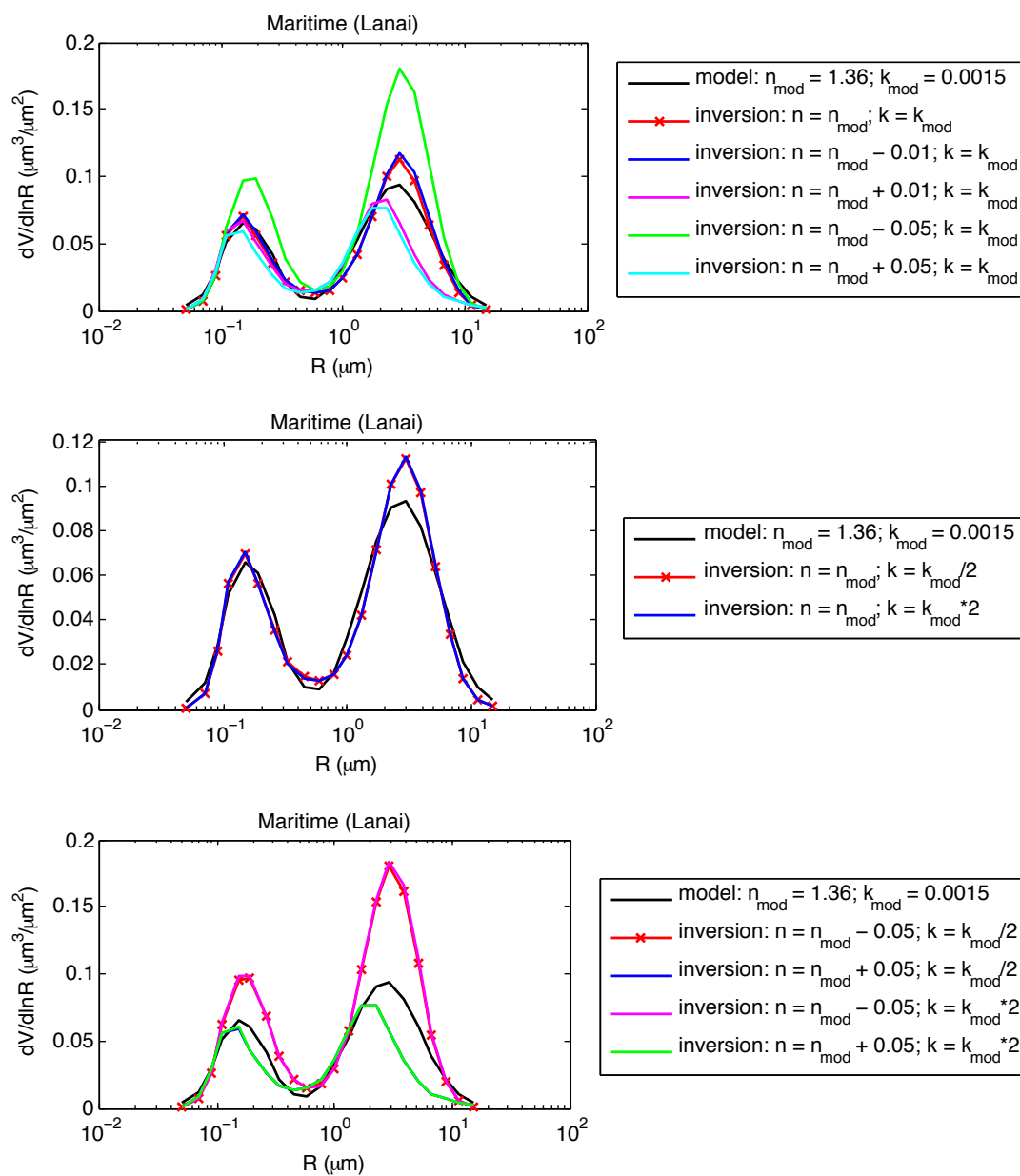
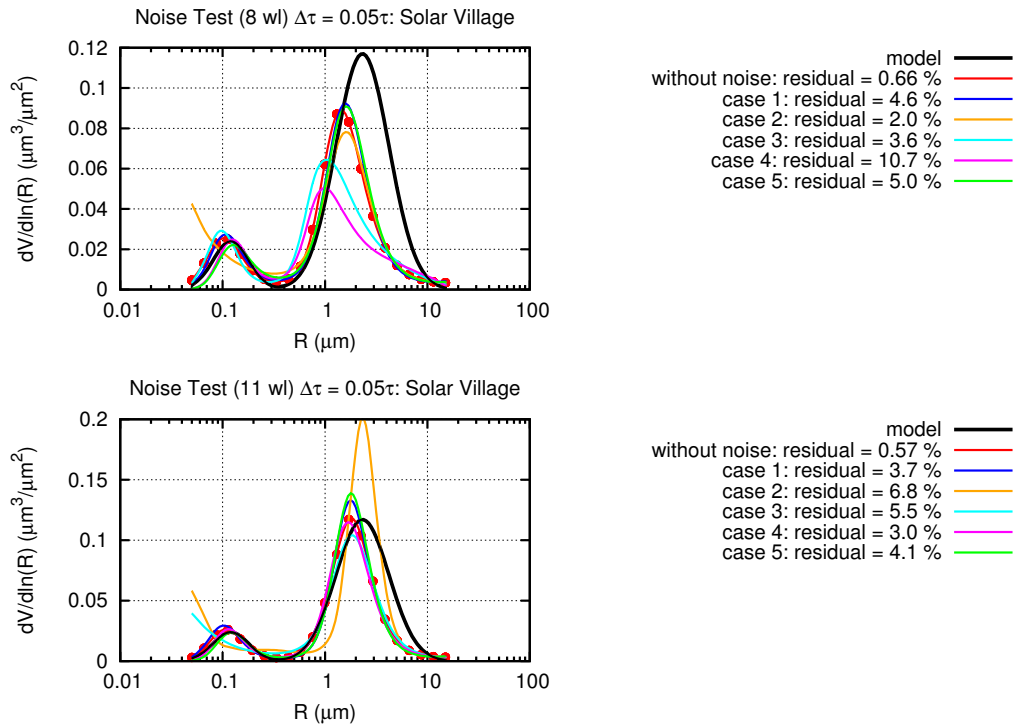
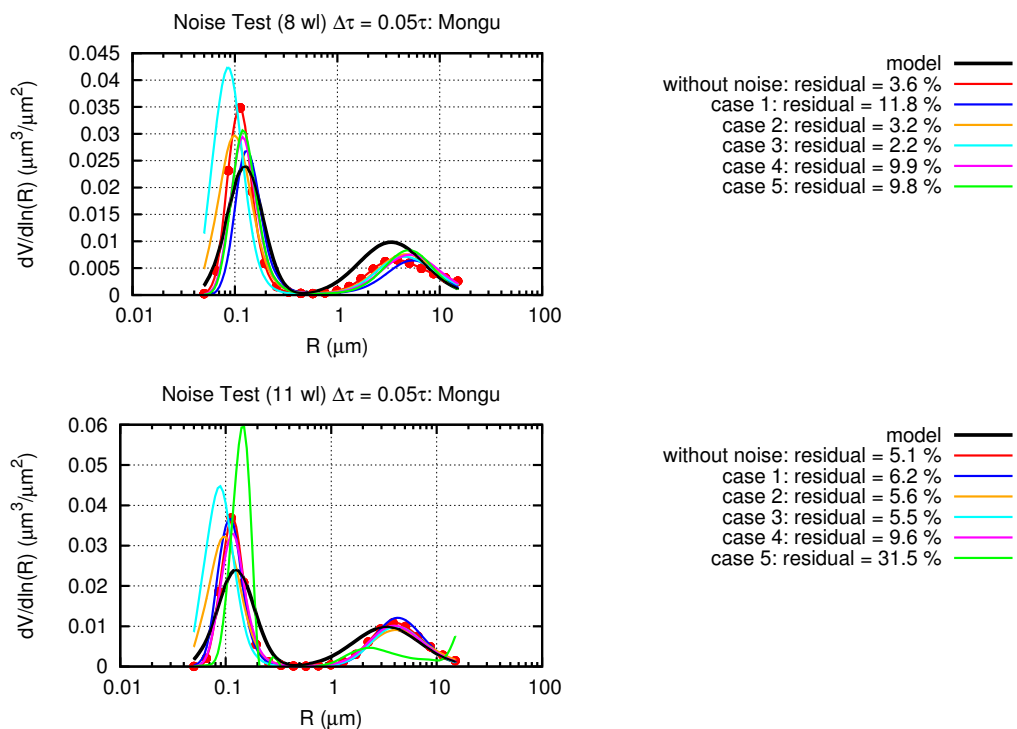
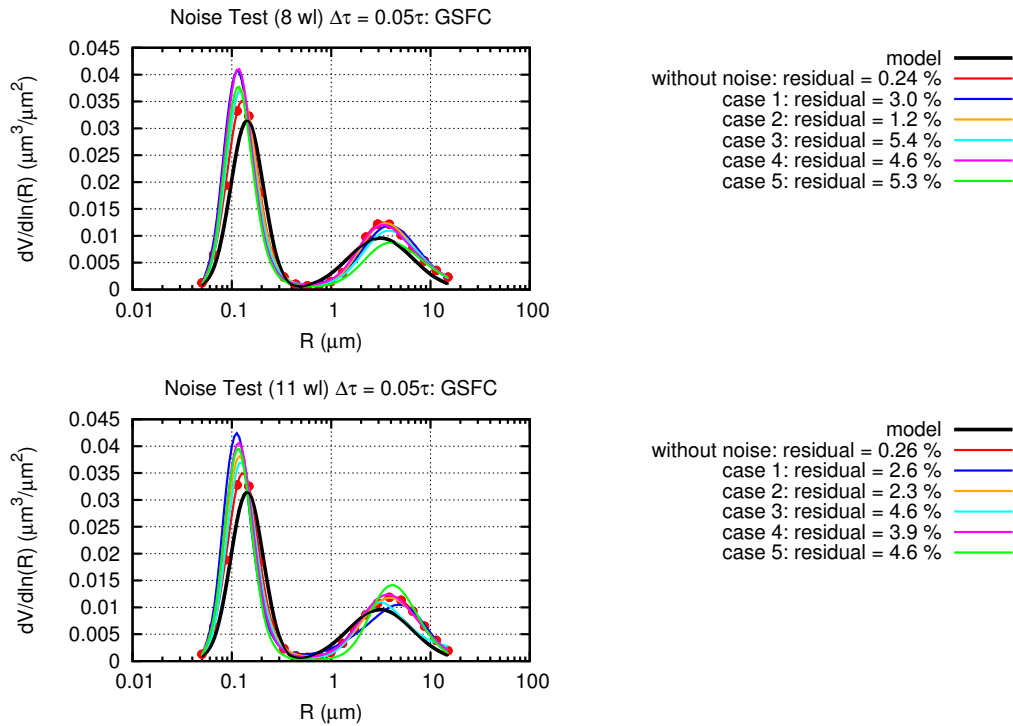
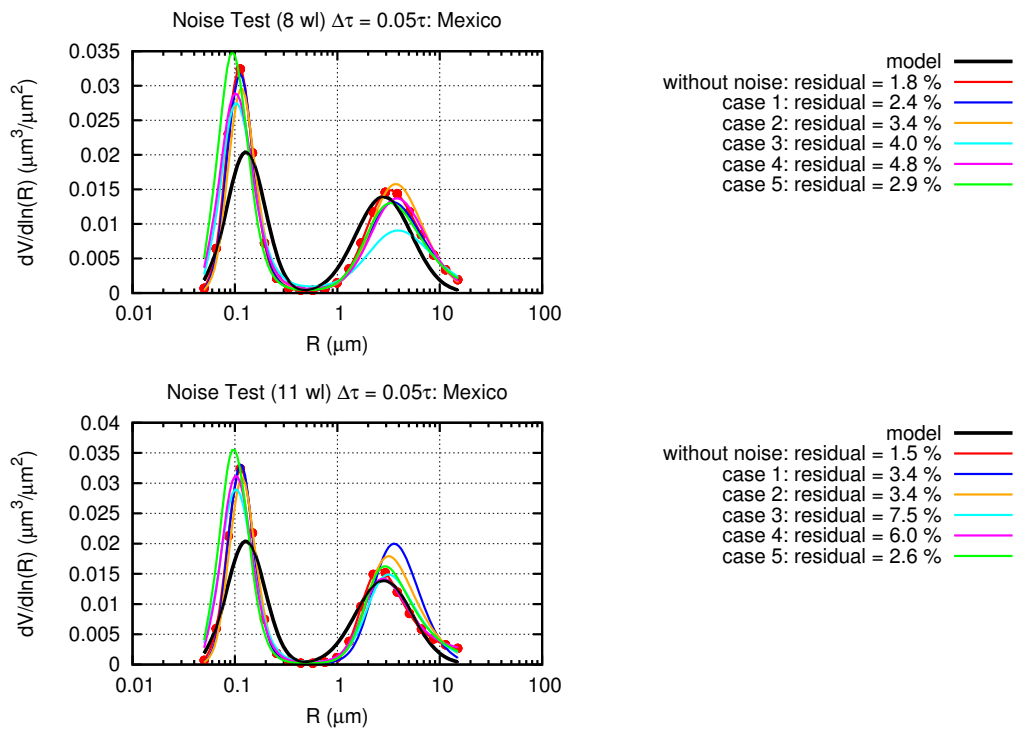
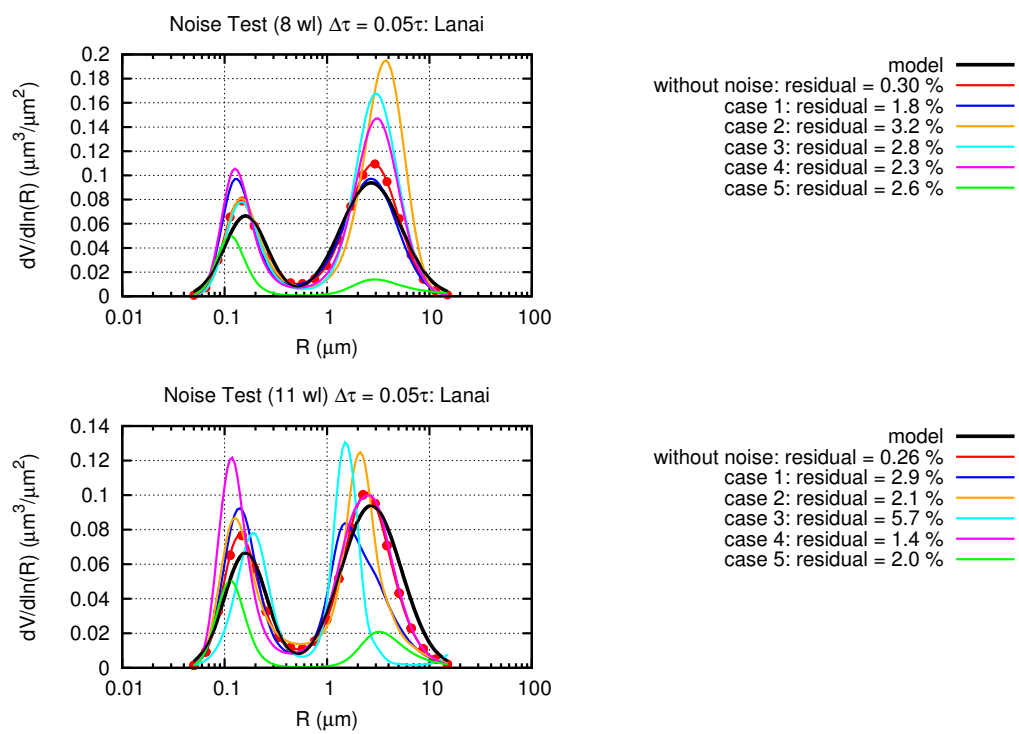


FIGURE A.15: Size distributions retrieved from 8 wl with different initial refractive indices (retrieved together with size distributions) - Lanai.

FIGURE A.16: Sensitivity to the AOD noise $\Delta\tau = 0.05\tau$ - Solar Village.FIGURE A.17: Sensitivity to the AOD noise $\Delta\tau = 0.05\tau$ - Mongu.

FIGURE A.18: Sensitivity to the AOD noise $\Delta\tau = 0.05\tau$ - GSFC.FIGURE A.19: Sensitivity to the AOD noise $\Delta\tau = 0.05\tau$ - Mexico.

FIGURE A.20: Sensitivity to the AOD noise $\Delta\tau = 0.05\tau$ - Lanai.

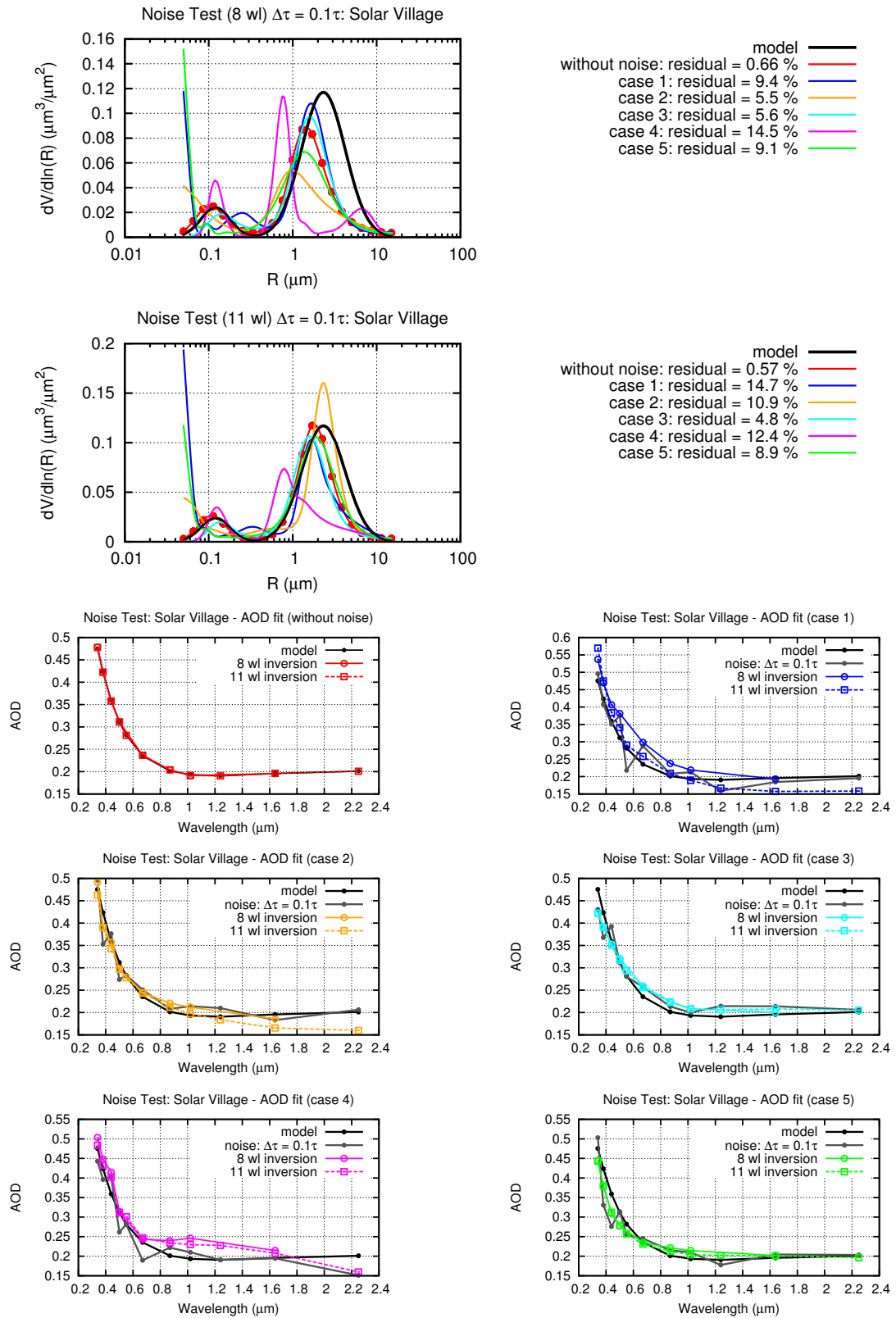


FIGURE A.21: Sensitivity to the AOD noise $\Delta\tau = 0.1\tau$ - Solar Village.

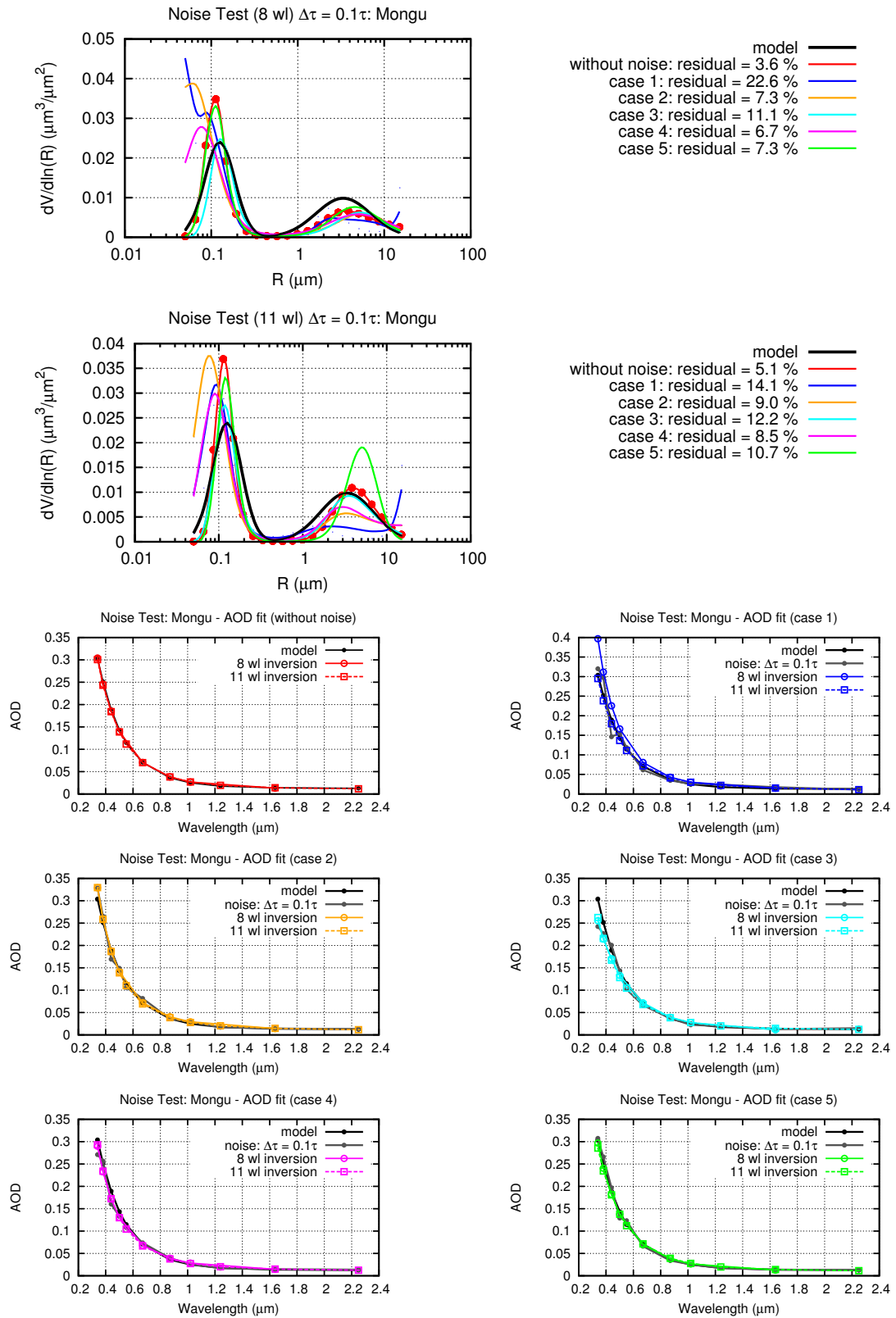


FIGURE A.22: Sensitivity to the AOD noise $\Delta\tau = 0.1\tau$ - Mongu.

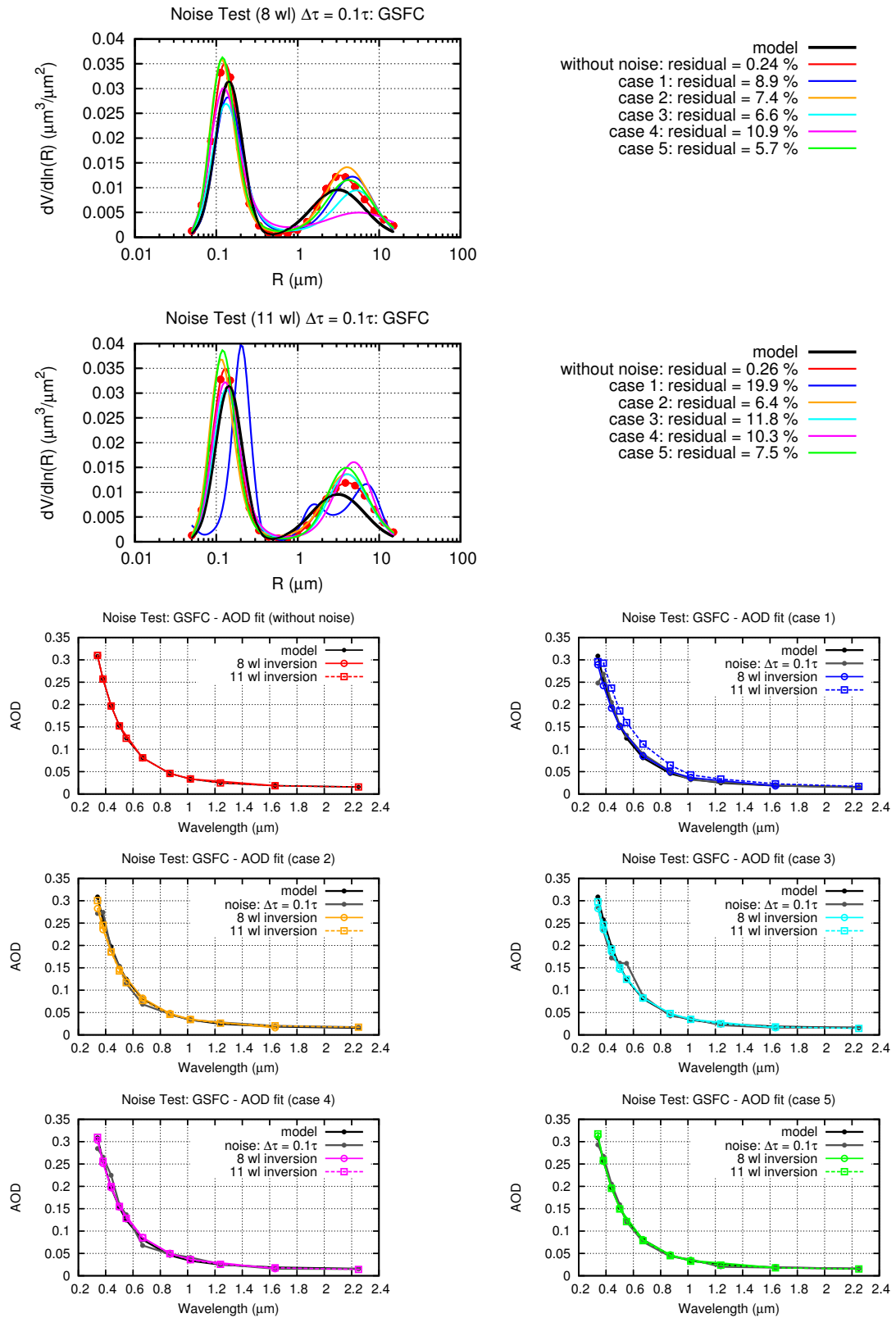


FIGURE A.23: Sensitivity to the AOD noise $\Delta\tau = 0.1\tau$ - GSFC.

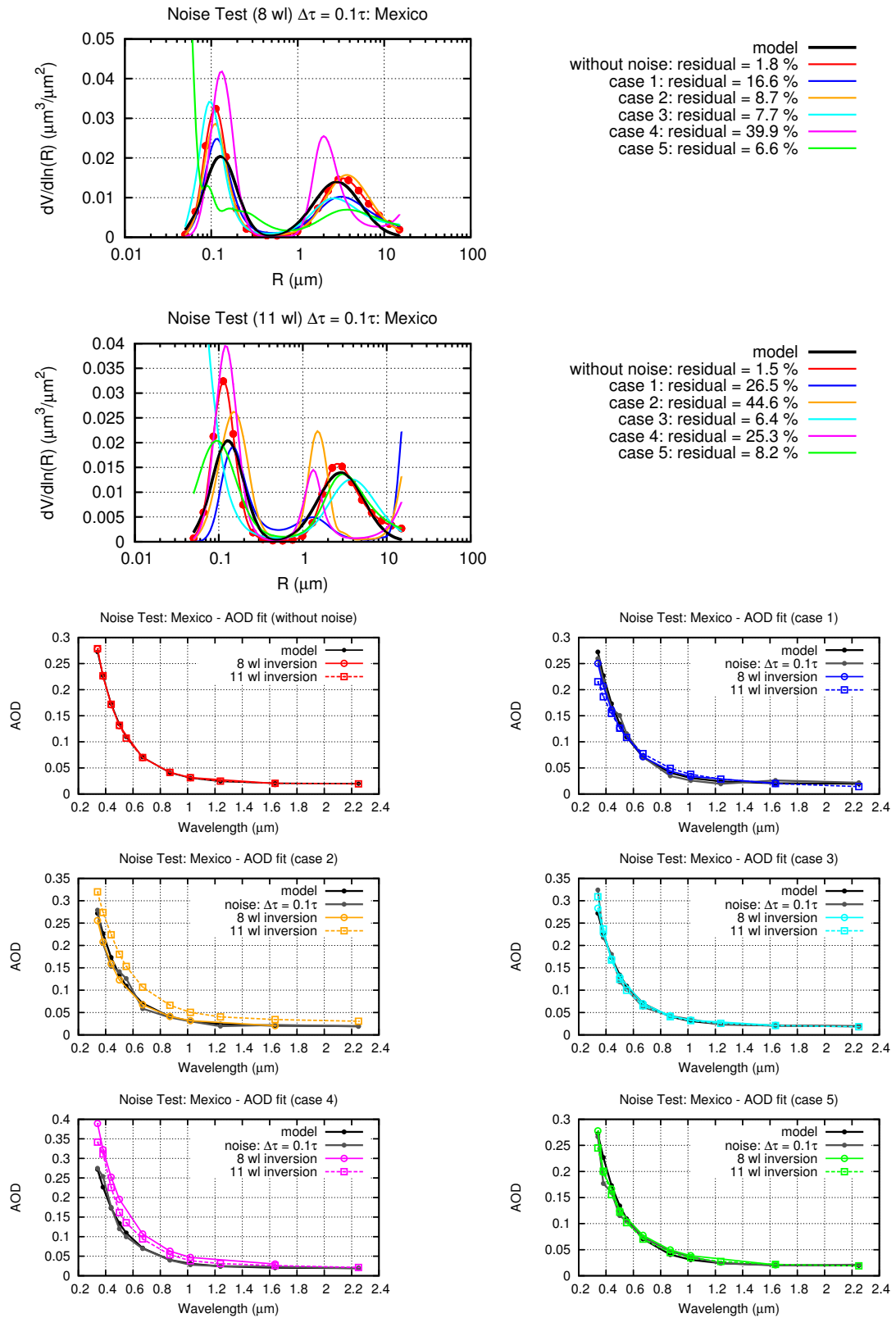


FIGURE A.24: Sensitivity to the AOD noise $\Delta\tau = 0.1\tau$ - Mexico.

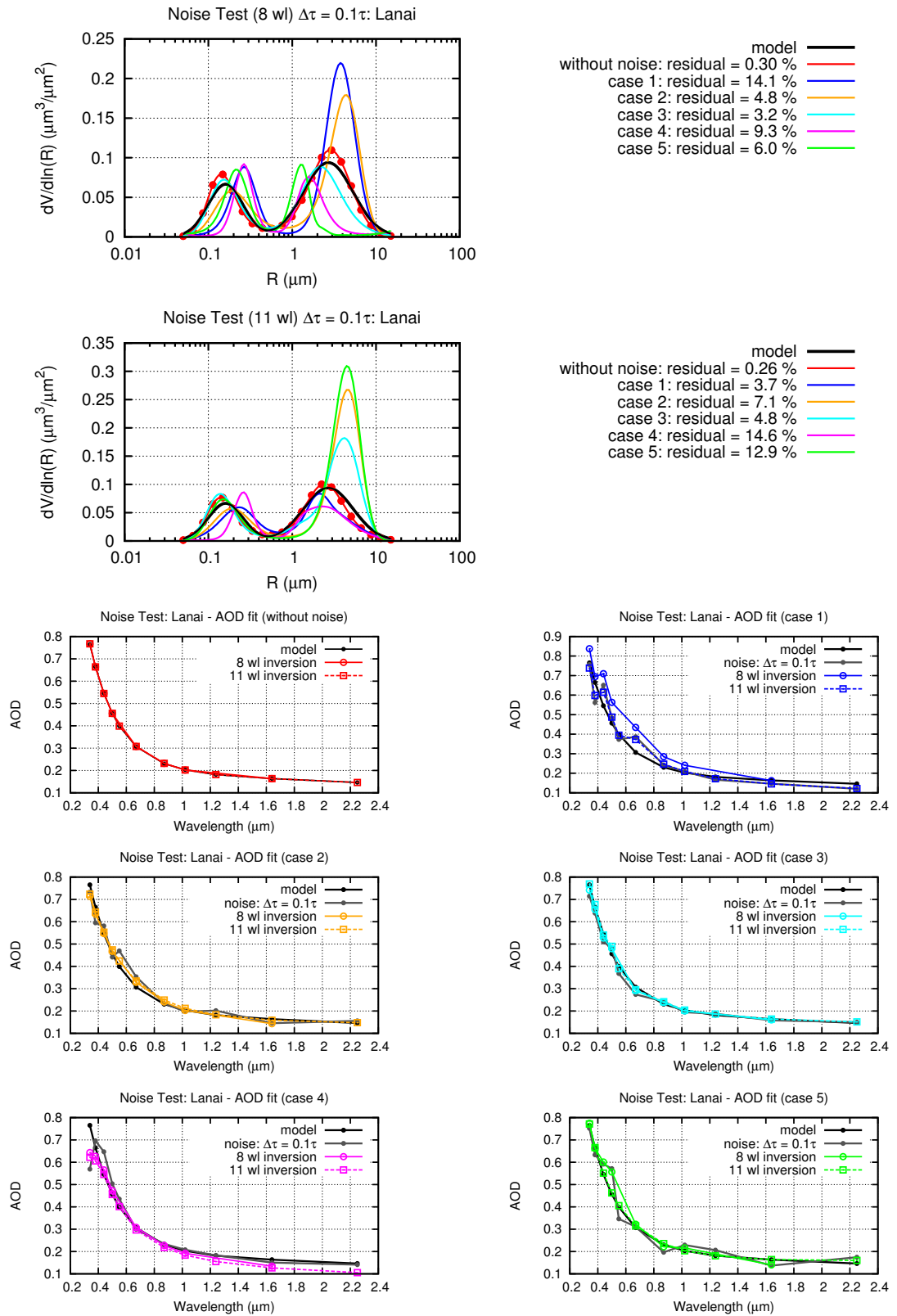


FIGURE A.25: Sensitivity to the AOD noise $\Delta\tau = 0.1\tau$ - Lanai.

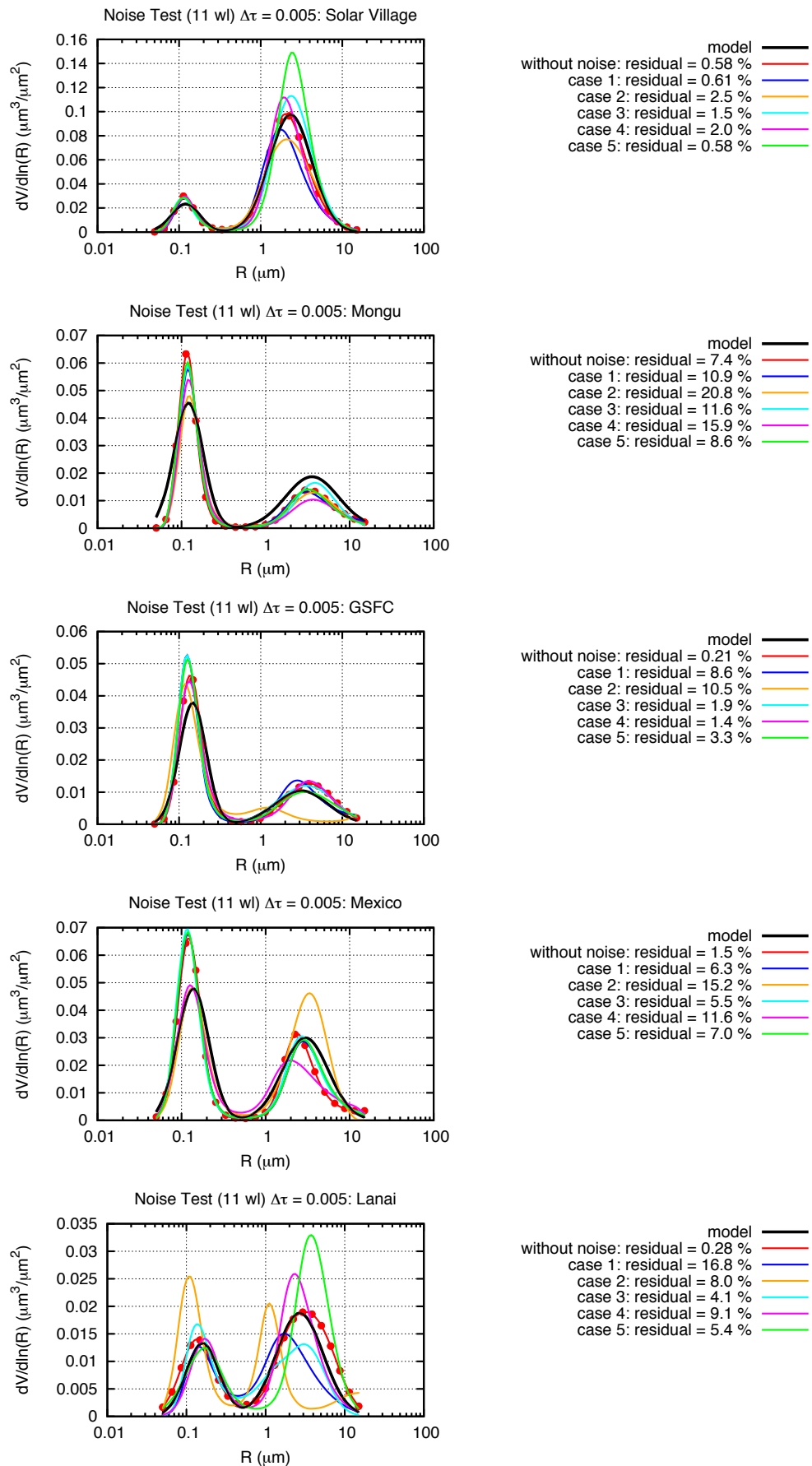


FIGURE A.26: Sensitivity of 11 wl inversion to the AOD noise $\Delta\tau = 0.005$ when $\tau = \langle \tau \rangle$.

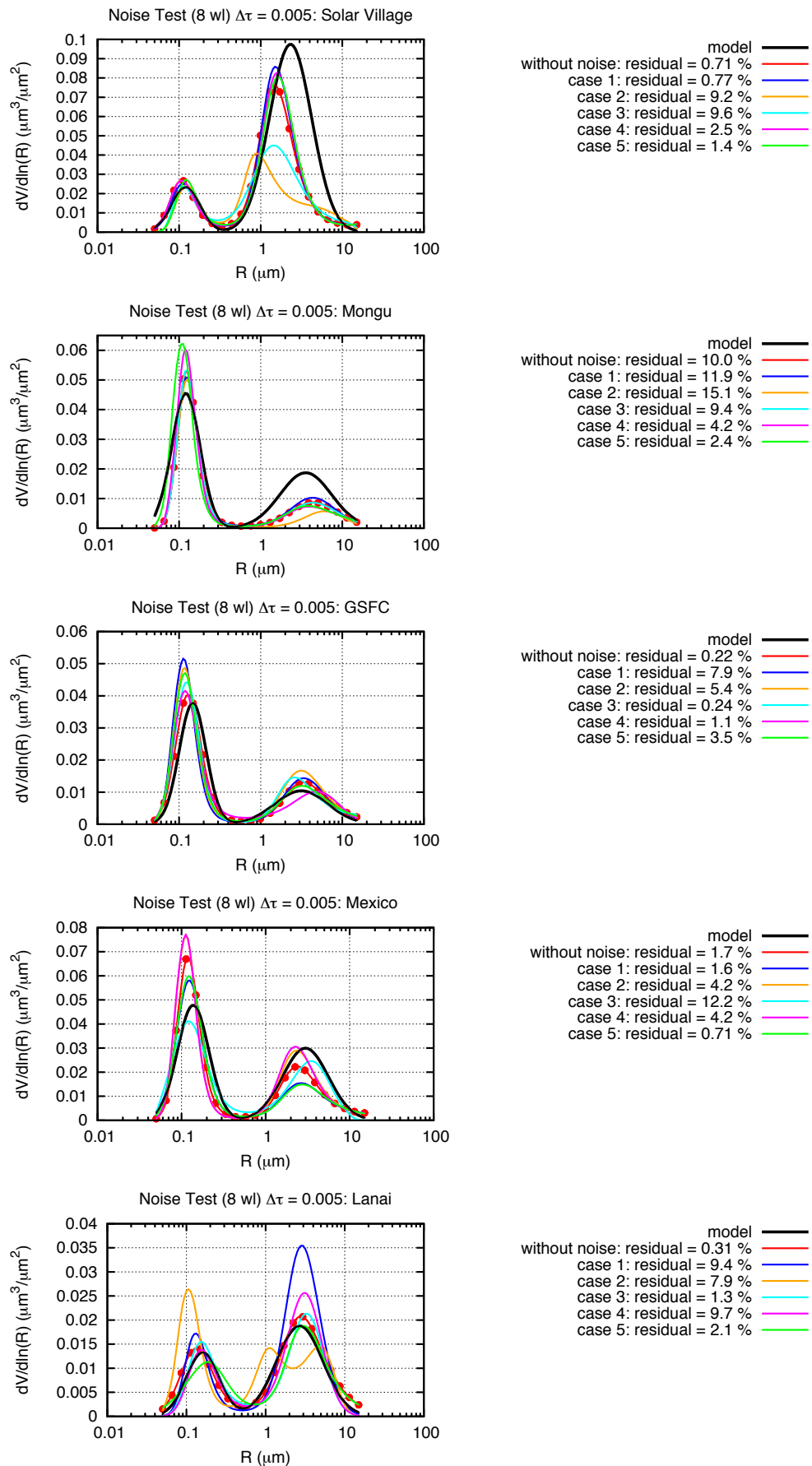


FIGURE A.27: Sensitivity of 8 wl inversion to the AOD noise $\Delta\tau = 0.005$ when $\tau = \langle \tau \rangle$.

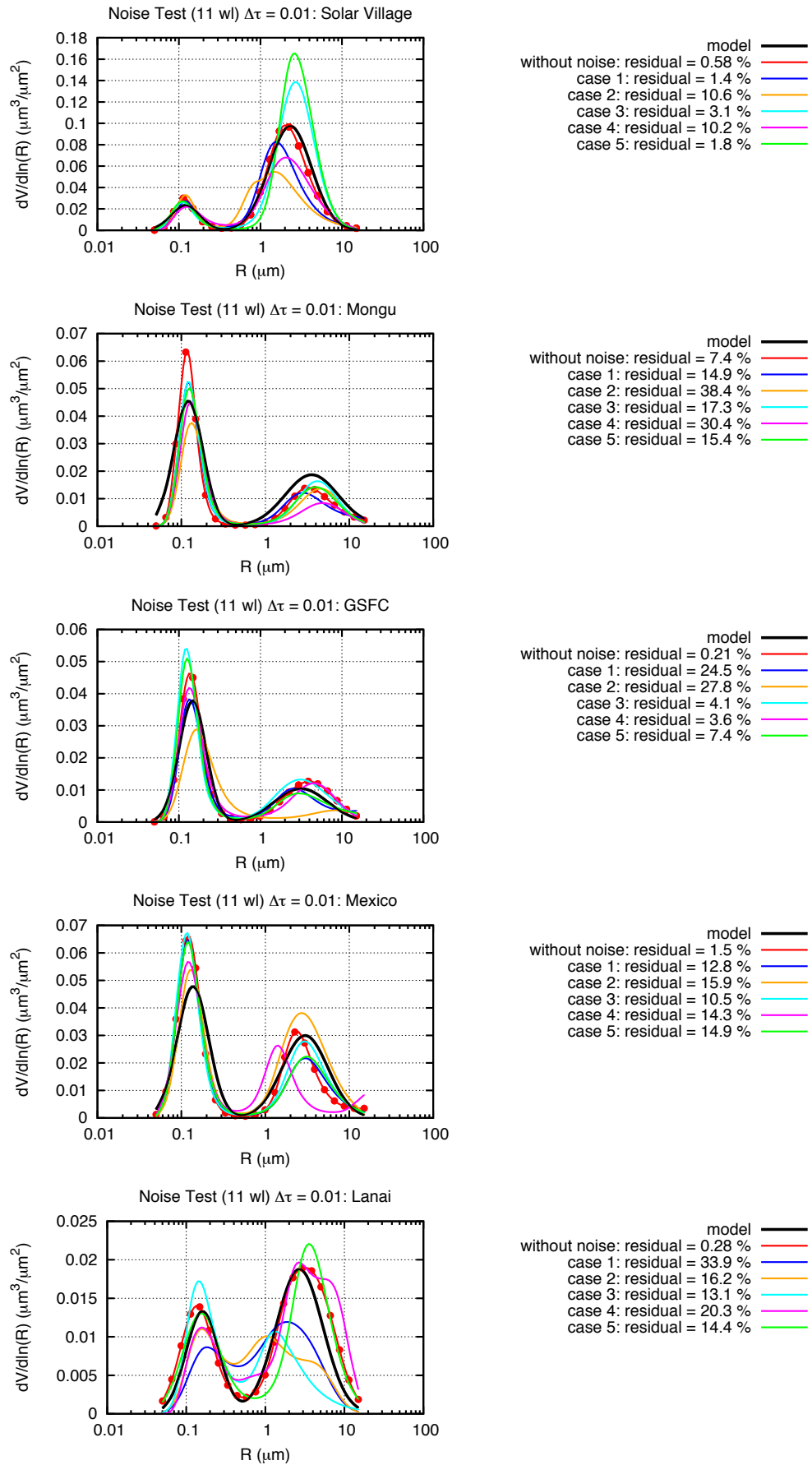


FIGURE A.28: Sensitivity of 11 wl inversion to the AOD noise $\Delta\tau = 0.01$ when $\tau = \langle \tau \rangle$.

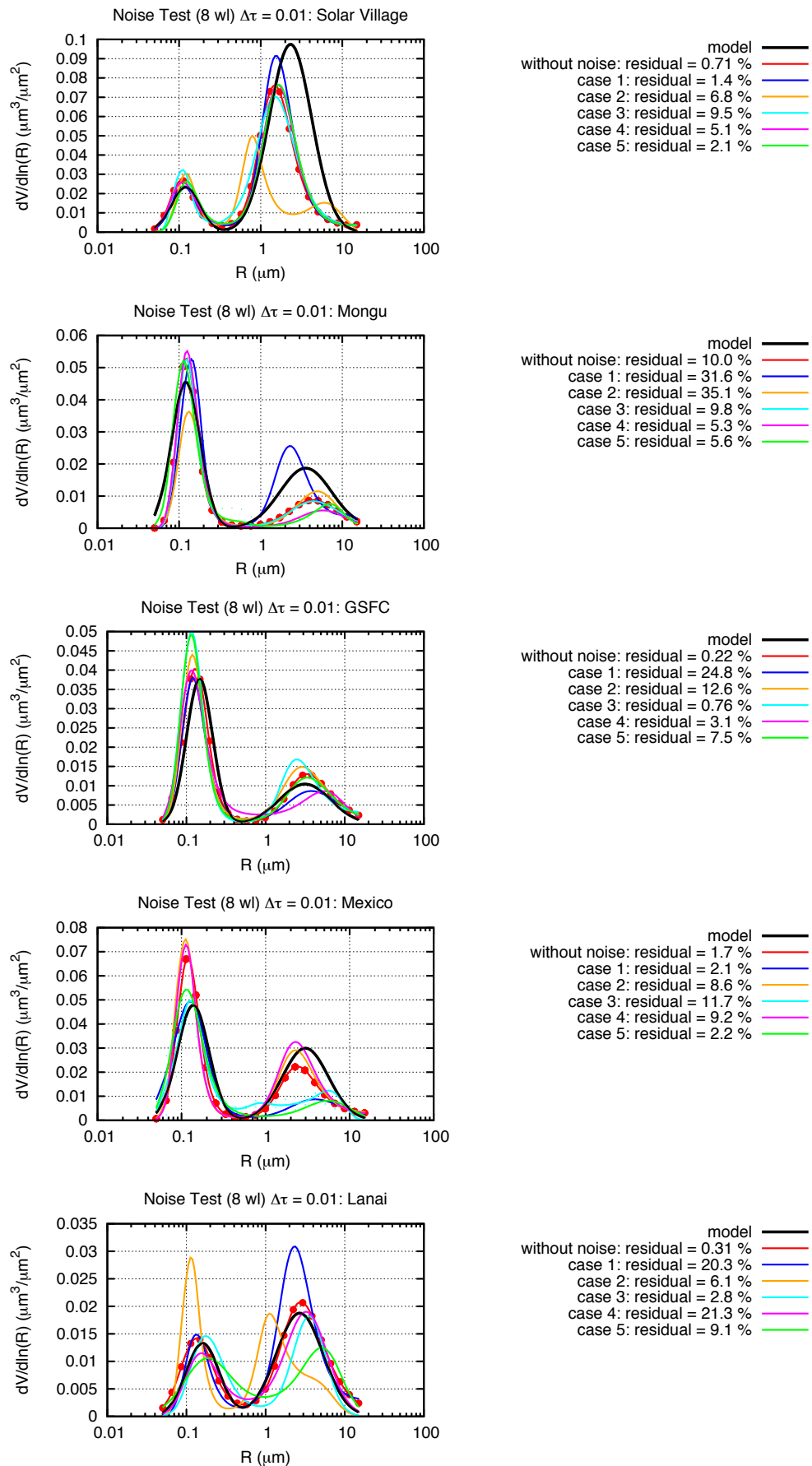


FIGURE A.29: Sensitivity of 8 wl inversion to the AOD noise $\Delta\tau = 0.01$ when $\tau = \langle \tau \rangle$.

Appendix B

The paper published during the study

The paper published in 2013 in "Atmospheric Measurement Techniques", volume 6, pages 2383 – 2389. It concerns to PLASMA technical description, calibration, first results and is the part of the Chapter [4](#).



Airborne sun photometer PLASMA: concept, measurements, comparison of aerosol extinction vertical profile with lidar

Y. Karol^{1,2}, D. Tanré¹, P. Goloub¹, C. Ververaerde¹, J. Y. Balois¹, L. Blarel¹, T. Podvin¹, A. Mortier¹, and A. Chaikovsky²

¹Laboratoire d'Optique Atmosphérique (LOA), UMR8518, CNRS – Université des Sciences et Technologies de Lille, 59655 Villeneuve d'Ascq, France

²B. I. Stepanov Institute of Physics National Academy of Sciences of Belarus, 68, Nezavisimosti av., 220072 Minsk, Belarus

Correspondence to: Y. Karol (yana.karol@ed.univ-lille1.fr)

Received: 1 August 2012 – Published in Atmos. Meas. Tech. Discuss.: 19 September 2012

Revised: 5 August 2013 – Accepted: 5 August 2013 – Published: 16 September 2013

Abstract. A 15-channel airborne sun-tracking photometer has been developed. The instrument provides aerosol optical depths over a wide spectral range (0.34–2.25 μm) with an accuracy (ΔAOD) of approximately 0.01. Taking measurements at different altitudes allow us to derive the aerosol extinction vertical profile. Thanks to the wide spectral range of the instrument, information on the aerosol size distribution along the vertical is also available.

1 Introduction

Atmospheric aerosols play a role in the earth radiative budget (see, for example, Hansen et al., 1997; Ramanathan et al., 2001 or Kaufman et al., 2002). Due to their interaction with solar and thermal radiation, aerosols first cool the atmosphere–surface system (aerosol direct effect) and by absorbing sunlight in the atmosphere, they further cool the surface but warm the atmosphere. They also modify the temperature and humidity profiles which creates a more stable temperature profile that results in less cumulus cloud cover (semi-direct effect) (Hansen et al., 1997; Koren et al., 2004). Aerosols also impact the cloud properties by acting as cloud condensation nuclei and ice nuclei (indirect effects). To investigate aerosol–cloud interactions, it is important to determine the 3-D distribution of aerosol properties. There are several satellite sensors (imagers or scanners) that provide a 2-D distribution but the aerosol vertical repartition is not sampled. Satellite missions that include lidars such as CALIPSO (Winker et al., 2010) are useful tools for

measuring vertical profiles of aerosols on the satellite track; however, elastic backscatter lidars have limitations since the lidar equation cannot be solved without an additional constraint such as independent optical depth measurement.

An airborne sun-tracking photometer named PLASMA (for Photomètre Léger Aéroporté pour la Surveillance des Masses d'Air) has been developed. Aerosol optical depths (AOD) at several wavelengths are derived from measurements of the extinction of solar radiation by molecular and aerosol scattering and absorption processes. Aerosol size distribution information can be retrieved from the AOD spectral dependence when the spectral range is large enough (King et al., 1978). Naturally, flying at different altitudes provides the information along the vertical.

Deriving photometric AODs is quite obvious as long as the instrument is well calibrated. There is no analog to the restrictive satellite constraint of signal contamination by highly reflective pixels and there is comparatively little dependence on particle properties of the aerosols. Indeed sun photometric measurements such as those made by AERONET (Holben et al., 1998) are the principal means of validating satellite-based AOD retrievals (Remer et al., 2005; Kahn et al., 2010; Tanré et al., 2011). With an airborne version like PLASMA, we can easily sample different locations within a few minutes. It can also be used to validate extinction vertical profiles obtained from ground-based or space-borne lidars such as CALIPSO on CALIPSO (Winker et al., 2010).

Similar airborne sun photometers from last decades were successfully developed (Matsumoto et al., 1987; Schmid et al., 2003; Asseng et al., 2004). Compared to AATS-14

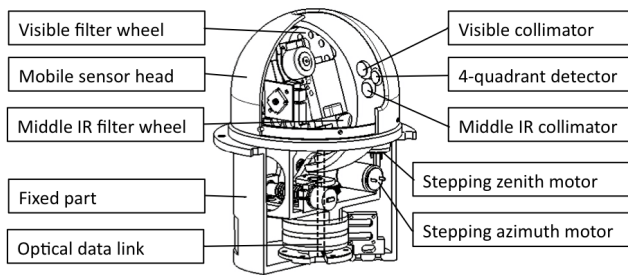


Fig. 1. PLASMA scheme.

(Ames Airborne Tracking Sun photometer) and FUBISS-ASA2 (Free University Berlin Integrated Spectrographic System – Aureole and Sun Adapter), the spectral range is similar. The main advantage of PLASMA is its small size and lightness. The weight of the optical head (mobile part) is 3.5 kg and the weight of the electronic modules is around 4 kg. The optical head has been designed to be easily set up on any mobile platform like a small aircraft or an automobile. It can be used for sampling, in a few minutes, aerosol plumes that are not horizontally uniform or for precisely retrieving aerosol vertical profile.

In this paper we first present the technical characteristics, the calibration procedure and a discussion on the recent evolutions of the instrument. Preliminary results of ground-based, airborne and automobile measurements are discussed and a comparison with lidar profiles is finally provided.

2 Description of the instrument

This instrument has two collimators both with approximately a 1.5° full angle of field of view (FOV) and a four-quadrant detector with a 6° angle of FOV. The first detector (Si) covers visible and near-infrared ranges (0.343 μm , 0.380 μm , 0.441 μm , 0.499 μm , 0.553 μm , 0.677 μm , 0.869 μm , 0.940 μm , 1.023 μm) and the second detector (InGaAs) covers middle infrared (1.14 μm , 1.24 μm , 1.60 μm , 1.646 μm , 2.25 μm). PLASMA interference filters are similar to AERONET CIMEL sun photometer filters (Holben et al., 1998). The head can move in elevation (0 – 90°) and azimuth (0 – 360°), and rotation in azimuth can be continuous thanks to a ring power connector (Fig. 1). Hereinafter, we will limit our study to the channels that are in atmospheric windows (Fig. 2).

A microprocessor computes the position of the Sun based on time, latitude, and longitude, provided by a GPS system. It directs the sensor head to the Sun at which point the four-quadrant detector precisely tracks the Sun. If the tracking is disconnected when the aircraft is making a turn or due to the presence of clouds, then the GPS system takes over. The filters are located in two filter wheels which are rotated by a direct drive stepping motor. For a complete sequence, it takes 1.8 s for visible and near-infrared channels

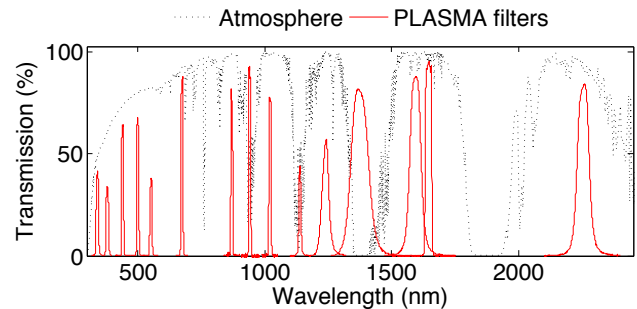


Fig. 2. PLASMA filter's transmission.

and 1.2 s for the middle-infrared channels. For common aircraft speeds $\sim 200 \text{ km h}^{-1}$, a complete filter sequence corresponds to a distance of 100 m and 66 m.

The voltage of both detectors is digitized by means of a delta-sigma ADC. The instrument is operated with a PC that records digital count for the visible and middle-infrared channels, latitude, longitude and altitude, speed and other flight parameters given by the GPS unit.

The 1.5° full angle field of view of PLASMA is comparable to the 1.2° of the CIMEL instrument. This relatively small FOV ensures that the instrument is less sensitive to atmospheric scattering into the FOV than instruments with broader FOV. The effect of atmospheric forward scattering on direct solar irradiance measurements increases with particle size, aerosol optical depth and instrument FOV; it has been shown that the impact is negligible (less than 1 % of AOD) for FOV smaller than 2° (Russell et al., 2004). A more recent study (Sinyuk et al., 2012) confirms that in most cases for a CIMEL-like instrument, this effect can be neglected excepted for heavy dust loadings where the relative error may reach $\sim 1\%$ for an AOD of 3.5.

The InGaAs detector is temperature stabilized while the Si detector is not. The 1.023 μm channel has been shown to be temperature sensitive. A correction derived from our laboratory measurements is applied to the detector signal using a coefficient of $0.35\% \text{ }^\circ\text{C}^{-1}$.

3 Theoretical background

AOD is derived from measurements of the atmospheric spectral transmission. Due to Bouguer–Lambert–Beer law the sun irradiance $E(\lambda, z)$ at a given wavelength λ and at an altitude z above sea level is expressed as (Bohren and Huffman, 1998):

$$E(\lambda, z) = t_g(\lambda, z) E_0(\lambda) e^{-\tau(\lambda, z)m}, \quad (1)$$

where $E_0(\lambda)$ is the extraterrestrial sun irradiance; $t_g(\lambda, z)$ the gaseous transmission; m the air mass given by $1/\cos(\theta_s)$ when refraction and atmospheric curvature are neglected; θ_s the solar zenith angle and $\tau(\lambda, z)$ the total optical depth of the

atmosphere that is the sum of aerosol extinction and molecular (Rayleigh) optical depths:

$$\tau(\lambda, z) = \tau_{\text{ext}}^a(\lambda, z) + \tau_{\text{ext}}^m(\lambda, z). \quad (2)$$

The digital signal ($DN(\lambda, z)$) measured by the instrument is proportional to sun irradiance $E(\lambda, z)$ (the relative Earth–Sun distance is taken to be imbedded in the extraterrestrial DN value in order to simplify the nomenclature) one can write:

$$DN(\lambda, z) = t_g(\lambda, z)DN_0(\lambda)e^{-\tau(\lambda, z)/\cos(\theta_s)}. \quad (3)$$

From Eqs. (3) and (2) and after gaseous absorption correction, we can obtain aerosol extinction optical depth:

$$\tau_{\text{ext}}^a(\lambda, z) = \frac{1}{m} [\ln(DN(\lambda)/t_g(\lambda, z)) - \ln(DN_0(\lambda))] - \tau_{\text{ext}}^m(\lambda, z). \quad (4)$$

To calculate gaseous absorption, i.e. absorption by oxygen, ozone, water vapor and other gases, we use spectral absorption lines provided in the 5S code and the mid-latitude summer atmospheric model (Tanré et al., 1990).

Molecular scattering optical depth at the altitude z is given by

$$\tau_{\text{ext}}^m(\lambda, z) = \tau_{\text{ext}}^m(\lambda, z_0) \frac{P(z)}{P(z_0)}, \quad (5)$$

where $\tau_{\text{ext}}^m(\lambda, z_0)$ is the molecular optical depth at the surface level z_0 and $P(z_0)$ the associated pressure.

In the UV spectral range, the Rayleigh AOD is significant and has to be known with good accuracy to be properly corrected for. Since it depends on the atmospheric pressure, a pressure gauge has been included in the PLASMA instrument. Unfortunately, the measurements were not available at the time of our experiment and a crude estimate was performed using the equation: $P(z) = P(z_0)\exp(-z/8.5)$, where z is the altitude of the aircraft expressed in km.

Since the aerosol extinction coefficient is the altitude derivative of AOD

$$\sigma_{\text{ext}}^a = \frac{d\tau_{\text{ext}}^a}{dz}, \quad (6)$$

we can compare aerosol extinction coefficient derived by PLASMA and inferred from lidar backscatter profiles to validate lidar retrieval procedure.

In addition to the aerosol content, PLASMA can provide information on the aerosol size through the Ångström exponent. Based on spectral AODs, angstrom exponent is defined by Eq. (7) and is sensitive to the aerosol size (Schuster et al., 2006).

$$\tau(\lambda) = \tau(\lambda_0) \left(\frac{\lambda}{\lambda_0} \right)^{-\alpha} \quad (7)$$

More advanced retrieval (King et al., 1978) using spectral information have been developed and shown able to derive information on the aerosol size distribution $n(r, z)$ by inverting the following equation:

$$\tau_{\text{ext}}^m(\lambda, z) = \int_z^\infty dz' \int_{r_{\text{min}}}^{r_{\text{max}}} \pi r^2 Q_{\text{ext}}(m(\lambda), \frac{2\pi r}{\lambda}) n(r, z') dr, \quad (8)$$

where r is particle radius; $n(r, z)$ particle's size distribution; $m(\lambda)$ complex refractive index; Q_{ext} extinction efficiency factor. Equation (8) assumes that the aerosol type does not depend on the altitude.

4 Calibration and ground-based measurements

For PLASMA calibration we used Langley method and intercalibration with master sun photometer CIMEL CE-318 that is used in Aerosol Robotic Network (AERONET) (Holben et al., 1998).

Langley plots are made to determine the spectral extraterrestrial voltage. The site has to be located at high altitude and in an area with a very stable aerosol regime. The Langley plot is a log of the DN against the optical air mass during the day (from Eq. 3) for the optical air mass range between 5 and 2. The intercept is the calibration coefficient, and the slope the optical thickness. The deviation of the intercept is a measure of the precision of the technique. If the aerosol loading is not constant, we may observe deviation from the linear regression line but such cases can be easily excluded at Mauna Loa and Izaña when Langley plots are performed. The Langley calibration is suitable for all spectral channels but the procedure is not straightforward since there are only a few sites that meet the requirements (Shaw, 1983).

Intercalibration between instruments is easier and of an accuracy comparable to Langley plots and can be done with near-simultaneous measurements of sun irradiance by PLASMA and CIMEL sun photometers at the same location. Spectral extraterrestrial voltage can be found from the relation:

$$\frac{DN_0^{\text{PLASMA}}(\lambda)}{DN_0^{\text{CIMEL}}(\lambda)} = \frac{DN^{\text{PLASMA}}(\lambda)}{DN^{\text{CIMEL}}(\lambda)}. \quad (9)$$

The accuracy of AOD depends on the accuracy of calibration coefficients. A 1% error in calibration coefficient leads to inaccuracy $\Delta\text{AOD} \approx 0.01$ at $m = 1$, with the error decreasing by a factor of $1/m$ as air mass increases. Usually the profile flights last around 30 min from 11:00 to 13:00 UTC; during this period the change of air mass is less than 5%. Since a miscalibration results in a bias in AOD and the air mass is constant, it does not impact the value of the extinction coefficient that is the derivative of AOD (see Eqs. 4 and 6).

The first calibration campaign was organized at the Atmospheric Observatory in Izaña (28.3° N, 16.5° W; alt. 2391 m)

in October 2009 for Langley approach and in Carpentras (44.1° N, 5.1° E; alt. 100 m) in March 2009 for intercalibration.

The calibration coefficients calculated with Izaña and Carpentras data in 2009 were applied to all data collected in Lille (50.6° N, 3.1° E; alt. 60 m) until March 2010 to obtain aerosol optical depth (AOD). The comparison with CIMEL measurements at common wavelengths (0.34 μm , 0.38 μm , 0.44 μm , 0.67 μm , 0.86 μm , 1.02 μm , 1.64 μm) showed a good agreement between the two instruments with rms AOD differences being between 0.01 and 0.02.

After modifications of some mechanical elements, a new calibration campaign was organized at Izaña in March 2010. Several measurements were then performed in LOA to sample different atmospheric conditions during 12 days in April–June 2010 and a better agreement with CIMEL master instrument was obtained with rms AOD differences ~ 0.01 . The PLASMA calibration is not too far from the calibration of AERONET reference instruments ($0.002 < \Delta\text{AOD} < 0.009$) (Eck et al., 1999).

Once the technical development has been achieved, PLASMA was refurbished in March 2011. The stepping azimuth and zenith motors were replaced for better pointing capability and signal processing steps taken to improve the signal to noise ratio. We also replace all the filters, which required a new calibration of the instrument. After calibration the difference of AOD retrieved by PLASMA and CIMEL master instrument is less than 0.005 for all channels except 0.34 μm channel (see Fig. 3).

The differences observed before 09:00 UTC and after 15:00 UTC may come from filter out-of-band leakage resulting from incomplete blocking of solar energy from outside the filter bandpass as seen in some AERONET CIMEL instruments. In the laboratory measurements of filters transmission, such leakage was not observed over ± 100 nm from the central wavelength. Differences may also come from a miscalibration of this channel. Knowing the calibration coefficient within 1 % error only results in errors in the AOD of 0.025 for an air mass of 2.4 as anticipated around 07:30 in Lille in April. This effect would lead to a symmetrical behavior in the afternoon as observed in Fig. 3.

Since PLASMA has the same interference filters as CIMEL, we follow the AERONET calibration policy and the instrument is going to be calibrated every year.

Currently, we analyze only results in spectral bands that are present on both PLASMA and CIMEL instruments. Of course, PLASMA covers a larger spectral range with a 2.25 μm channel that is very important for AOD inversion. Nevertheless at this stage we do not consider this wavelength since we cannot validate calibration coefficient with any other instrument.

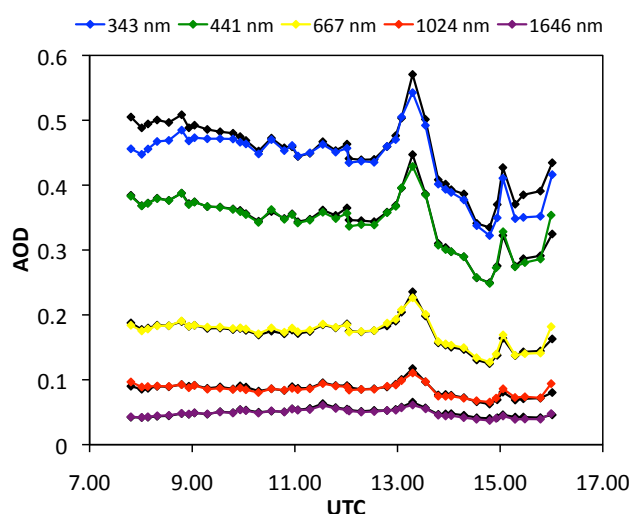


Fig. 3. Comparison of simultaneous ground-based measurements of PLASMA (colored lines) and CIMEL CE-318 (black lines) 18 April 2011.

5 Airborne measurements

In addition to ground-based measurements, several flights were performed in Lille: two technical flights in 2009, 6 flights in 2010 and 3 flights in 2011. We provide hereinafter results for flights performed after first improvements, i.e. since October 2010 only.

Figure 4 shows profiles of 4 flights in 2010–2011: 12 October 2010, 28 September 2011, 29 September 2011 and 15 October 2011 from the top to the bottom. The first column of graphs on the left presents the vertical profile of AOD at different wavelengths; the second is the profile of extinction coefficient; the third column on the right presents the comparison of extinction at 0.553 μm with lidar retrievals at 0.532 μm . We use the Cloud and Aerosol Micro-LIDAR (CAML) CE 3702 manufactured by CIMEL. The instrument has been already described in Pelon et al. (2008) and Léon et al. (2009). The aerosol extinction profile as well as the effective extinction-to-backscatter ratio are retrieved using combination of lidar data and sun-photometer AOD (Léon et al., 2009).

To get extinction profile we decided to remove all noisy data due to the presence of clouds and then to average over 10 measurements. It means that we assume that the state of the atmosphere was stable over 30–60 s, along 50–100 m in vertical direction and 2–4 km in horizontal direction. Altitudes below 500 m could not be observed by lidar. Lidar profiles presented on Fig. 4 are extended to the ground level by using the correction function based on independent measurements of AOD. Direct measurements of PLASMA can be used for validation of this function. The extinction profiles retrieved from lidar measurements are broadly consistent with PLASMA results, showing coarsely similar vertical

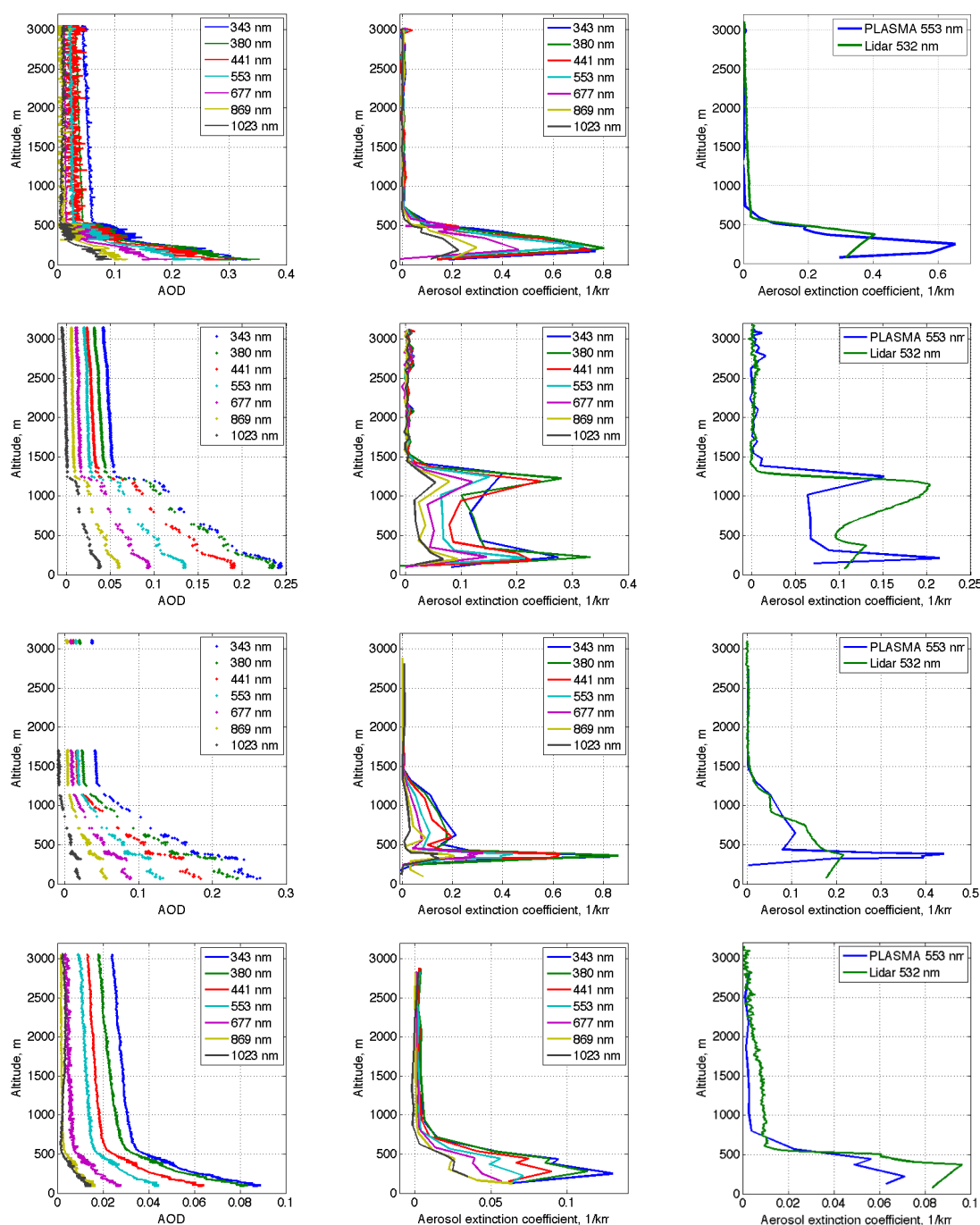


Fig. 4. PLASMA AOD (left), aerosol extinction coefficient (center) at 7 channels and aerosol extinction coefficient compared with lidar (right) as a function of the altitude acquired near Lille region the 12 October 2010, 28 September 2011, 29 September 2011 and 15 October 2011.

attributes. The best agreement between aerosol extinction coefficient profiles retrieved from PLASMA and lidar data was observed 15 October 2011 when the atmosphere was stable enough as seen from AOD profile.

For other days, differences might be explained by time and space variability of aerosol and clouds. On 29 September 2011 clouds were present in the vicinity and the turbidity

was rather high and variable, between 0.15–0.20 at 0.553 μm around noon; as a result the data are noisier and a 50 % difference of extinction coefficient at an altitude around 400 m is observed. Discrepancies can also result from spatial variability of the aerosol field; distance between both instruments was around 10 km when the airplane was on the ground, and more than 50 km when the plane was flying at the altitude

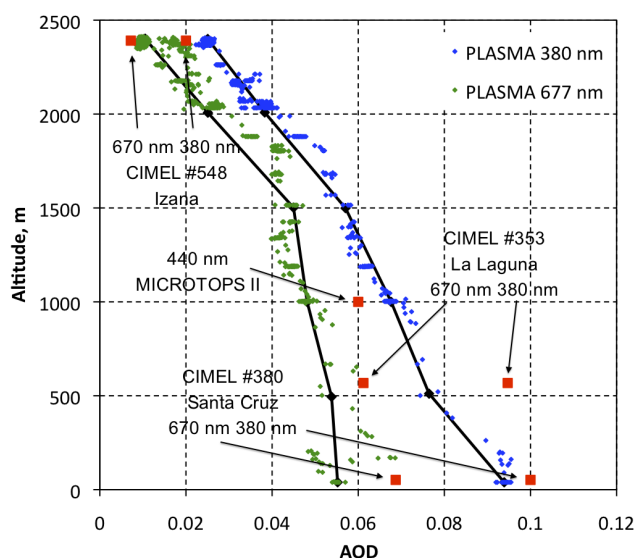


Fig. 5. Vertical profiles of AOD during automobile experiment 13 January 2011 on Tenerife island, Spain.

of 3000 m. Moreover, the profiles take around 20 min and are compared to the nearest in the time lidar profile ($\Delta t \approx 15$ min). Despite these differences, the aerosol layers are located at the same altitude and we can say that both vertical profiles are coarsely consistent.

6 Automobile measurements

In addition to airborne measurements it is also possible to set up PLASMA on the roof of an automobile in order to obtain horizontal transects of AOD. In mountain areas, we can also get vertical profiles using measurements performed at different altitudes.

In January 2011 an experiment was successfully carried out on the island of Tenerife, Spain. The measurements were made from sea level to an altitude of 2400 m in one hour. Horizontal coverage area was about 30 km and we had the opportunity to compare the PLASMA AOD with the Izaña AERONET site (alt. 2391 m) very close to the roadway. There are also two additional AERONET sites, La Laguna (alt. 590 m) and Santa Cruz (alt. 54 m), that were located at a distance of 40 km from our measurements.

The vertical profiles of AOD at $0.380 \mu\text{m}$ and $0.677 \mu\text{m}$ is compared to the three AERONET stations in Fig. 5. An additional measurement performed at the altitude of 1000 m using a sun photometer MICROTOPS II (Morys et al., 2001) is reported for $0.44 \mu\text{m}$. Measurements of PLASMA are consistent with other instruments with $\Delta\text{AOD} \sim 0.01$ and the differences for the low altitude sites could be explained by the distance between the instruments.

7 Conclusions

The new sun photometer that we have developed has been fully described. Following the calibration procedure recommended by AERONET, PLASMA provides AOD measurements with an accuracy of $0.005 < \Delta\text{AOD} < 0.01$ over a wide spectral range.

Its capability to follow the sun when it moves is very attractive. Installed on an aircraft, vertical profiles of AOD and aerosol extinction coefficient can be so derived and compared to lidar retrievals. Overall, PLASMA is a user-friendly instrument, easy to install on moving platforms and performing well compared to other instruments.

Acknowledgements. This study has been funded by CNES (Centre National d'Études Spatiales), CNRS (Centre National de la Recherche Scientifique), the University of Lille, and Région Nord-Pas-de-Calais. Y. Karol is supported by a fellowship from CNES and CNRS. PLASMA calibration was performed at Izaña observatory using AERONET-EUROPE calibration center, supported by ACTRIS from European Union Seventh Framework Program (FP7/2007-2013) under grant agreement no. 262254. Emilio Cuevas-Agullo from the Meteorological State Agency of Spain (AEMET) is acknowledged for his help during the experiment in Tenerife. The authors are very thankful to AERONET for establishing and maintaining the sites used in this work.

Edited by: O. Dubovik



The publication of this article is financed by CNRS-INSU.

References

- Asseng, H., Ruhtz, T., and Fischer, J.: Sun and Aureole Spectrometer for Airborne Measurements to Derive Aerosol Optical Properties, *Appl. Optics*, 43, 2146–2155, doi:10.1364/AO.43.002146, 2004.
- Bohren, C. and Huffman, D.: *Absorption and Scattering of Light by Small Particles*, Wiley science paperback series, Wiley-VCH, 1998.
- Eck, T. F., Holben, B. N., Reid, J. S., Dubovik, O., Smirnov, A., O'Neill, N. T., Slutsker, I., and Kinne, S.: Wavelength dependence of the optical depth of biomass burning, urban, and desert dust aerosols, *J. Geophys. Res.*, 104, 31333–31349, doi:10.1029/1999JD900923, 1999.
- Hansen, J., Sato, M., and Ruedy, R.: Radiative forcing and climate response, *J. Geophys. Res.*, 102, 6831–6864, doi:10.1029/96JD03436, 1997.
- Holben, B., Eck, T., Slutsker, I., Tanré, D., Buis, J., Setzer, A., Vermote, E., Reagan, J., Kaufman, Y., Nakajima, T., Lavenu, F., Jankowiak, I., and Smirnov, A.: AERONET – A Federated Instrument Network and Data Archive for Aerosol Character-

- ization, *Remote Sens. Environ.*, 66, 1–16, doi:10.1016/S0034-4257(98)00031-5, 1998.
- Kahn, R., Gaitley, B., Garay, M., Diner, D., Eck, T., Smirnov, A., and Holben, B.: Multiangle Imaging SpectroRadiometer global aerosol product assessment by comparison with the Aerosol Robotic Network, *J. Geophys. Res.*, 115, D23209, doi:10.1029/2010JD014601, 2010.
- Kaufman, Y. J., Tanré, D., and Boucher, O.: A satellite view of aerosols in the climate system, *Nature*, 419, 215–223, 2002.
- King, M., Byrne, D., Herman, B., and Reagan, J.: Aerosol Size Distributions Obtained by Inversions of Spectral Optical Depth Measurements, *J. Atmos. Sci.*, 35, 2153–2167, doi:10.1175/1520-0469(1978)035<2153:ASDOBI>2.0.CO;2, 1978.
- Koren, I., Kaufman, Y. J., Remer, L. A., and Martins, J. V.: Measurement of the Effect of Amazon Smoke on Inhibition of Cloud Formation, *Science*, 303, 1342–1345, doi:10.1126/science.1089424, 2004.
- Léon, J.-F., Derimian, Y., Chiapello, I., Tanré, D., Podvin, T., Chatenet, B., Diallo, A., and Deroo, C.: Aerosol vertical distribution and optical properties over M'Bour (16.96° W; 14.39° N), Senegal from 2006 to 2008, *Atmos. Chem. Phys.*, 9, 9249–9261, doi:10.5194/acp-9-9249-2009, 2009.
- Matsumoto, T., Russell, P., Mina, C., Ark, W. V., and Banta, V.: Airborne Tracking Sunphotometer, *J. Atmos. Ocean. Tech.*, 4, 336–339, 1987.
- Morys, M., Forrest, M., Hagerup, S., Anderson, S., Baker, A., Kia, J., and Walkup, T.: Design, calibration, and performance of MICROTOS II handheld ozone monitor and Sun photometer, *J. Geophys. Res.*, 106, 14573–14582, 2001.
- Pelon, J., Mallet, M., Mariscal, A., Goloub, P., Tanré, D., Karam, D. B., Flamant, C., Haywood, J., Pospichal, B., and Victori, S.: Microlidar observations of biomass burning aerosol over Djougou (Benin) during African Monsoon Multidisciplinary Analysis Special Observation Period 0: Dust and Biomass-Burning Experiment, *J. Geophys. Res.*, 113, D00C18, doi:10.1029/2008JD009976, 2008.
- Ramanathan, V., Crutzen, P., Kiehl, J., and Rosenfeld, D.: Aerosols, Climate, and the Hydrological Cycle, *Science*, 294, 2119–2124, doi:10.1126/science.1064034, 2001.
- Remer, L., Kaufman, Y., Tanré, D., Mattoo, S., Chu, D., Martins, J., Li, R., Ichoku, C., Levy, R., Kleidman, R., Eck, T., Vermote, E., and Holben, B.: The MODIS Aerosol Algorithm, Products, and Validation, *J. Atmos. Sci.*, 62, 947–973, doi:10.1175/JAS3385.1, 2005.
- Russell, P. B., Livingston, J. M., Dubovik, O., Ramirez, S. A., Wang, J., Redemann, J., Schmid, B., Box, M., and Holben, B. N.: Sunlight transmission through desert dust and marine aerosols: Diffuse light corrections to Sun photometry and pyr heliometry, *J. Geophys. Res.*, 109, D08207, doi:10.1029/2003JD004292, 2004.
- Schmid, B., Redemann, J., Russell, P., Hobbs, P., Hlavka, D., McGill, M., Holben, B., Welton, E., Campbell, J., Torres, O., Kahn, R., Diner, D., Helmlinger, M., Chu, D., Robles-Gonzalez, C., and de Leeuw, G.: Coordinated airborne, spaceborne, and ground-based measurements of massive thick aerosol layers during the dry season in southern Africa, *J. Geophys. Res.-Atmos.*, 108, 8496, doi:10.1029/2002JD002297, 2003.
- Schuster, G. L., Dubovik, O., and Holben, B. N.: Angstrom exponent and bimodal aerosol size distributions, *J. Geophys. Res.*, 111, D07207, doi:10.1029/2005JD006328, 2006.
- Shaw, G.: Sun Photometry, *Bulletin of the American Meteorological Society*, 64, 4–10, doi:10.1175/1520-0477(1983)064<0004:SP>2.0.CO;2, 1983.
- Sinyuk, A., Holben, B., Smirnov, A., Eck, T., Slutsker, I., Schafer, J., Giles, D., and Sorokin, M.: Assessment of error in aerosol optical depth measured by AERONET due to aerosol forward scattering, *Geophys. Res. Lett.*, 39, L23806, doi:10.1029/2012GL053894, 2012.
- Tanré, D., Deroo, C., Duhaut, P., Herman, M., Morcrette, J., Perbos, J., and Deschamps, P.: Description of a computer code to simulate the satellite signal in the solar spectrum: the 5S Code, *Int. J. Remote Sens.*, 11, 659–668, 1990.
- Tanré, D., Bréon, F. M., Deuzé, J. L., Dubovik, O., Ducos, F., François, P., Goloub, P., Herman, M., Lifermann, A., and Waquet, F.: Remote sensing of aerosols by using polarized, directional and spectral measurements within the A-Train: the PARASOL mission, *Atmos. Meas. Tech.*, 4, 1383–1395, doi:10.5194/amt-4-1383-2011, 2011.
- Winker, D., Pelon, J., Coakley, J., Ackerman, S., Charlson, R., Colarco, P., Flamant, P., Fu, Q., Hoff, R., Kittaka, C., Kubar, T., Le Treut, H., McCormick, M., Mégie, G., Poole, L., Powell, K., Trepte, C., Vaughan, M., and Wielicki, B.: The CALIPSO Mission: A Global 3D View of Aerosols and Clouds, *B. Am. Meteorol. Soc.*, 91, 1211–1229, doi:10.1175/2010BAMS3009.1, 2010.

Bibliography

- Ackerman, A. S., Toon, O. B., Taylor, J. P., Johnson, D. W., Hobbs, P. V., and Ferek, R. J.: Effects of aerosols on cloud albedo: evaluation of twomey's parameterization of cloud susceptibility using measurements of ship tracks, *J. Atmos. Sci.*, 57, 2684–2695, URL [http://dx.doi.org/10.1175/1520-0469\(2000\)057<2684:EJOACA>2.0.CO;2](http://dx.doi.org/10.1175/1520-0469(2000)057<2684:EJOACA>2.0.CO;2), 2000.
- Adams, P., Seinfeld, J., and Koch, D.: Global concentrations of tropospheric sulphate, nitrate and ammonium aerosol simulated in a general circulation model, *J. Geophys. Res.*, 104, 13 79113 823, 1999.
- Albrecht, B.: Aerosols, Cloud Microphysics, and Fractional Cloudiness, *Science*, 245, 1227–1230, doi:10.1126/science.245.4923.1227, 1989.
- Andreae, M.: Climatic effects of changing atmospheric aerosol levels, in: *World Survey of Climatology*, edited by Henderson-Sellers, A., vol. 16: *Future Climates of the World*, pp. 341–392, Elsevier, Amsterdam, 1995.
- Andreae, M. and Crutzen, P.: Atmospheric Aerosols: Biogeochemical Sources and Role in Atmospheric Chemistry, *Science*, 276, 1052–1058, doi:10.1126/science.276.5315.1052, 1997.
- Ångström, A. K.: On the atmospheric transmission of Sun radiation and on dust in the air, *Geogr. Ann.*, 11, 156–166, 1929.
- Asseng, H., Ruhtz, T., and Fischer, J.: Sun and Aureole Spectrometer for Airborne Measurements to Derive Aerosol Optical Properties, *Appl. Opt.*, 43, 2146–2155, doi:10.1364/AO.43.002146, URL <http://ao.osa.org/abstract.cfm?URI=ao-43-10-2146>, 2004.
- Bergstrom, R., Pilewskie, P., Schmid, B., and Russell, P.: Estimates of the spectral aerosol single scattering albedo and aerosol radiative effects during SAFARI 2000, *Journal of Geophysical Research*, 108, 8474, doi:10.1029/2002JD002435, 2003.
- Bohren, C. and Huffman, D.: *Absorption and Scattering of Light by Small Particles* (Wiley science paperback series), Wiley-VCH, 1998.
- Bond, T. and Bergstrom, R.: Light Absorption by Carbonaceous Particles: An Investigative Review, *Aerosol Science and Technology*, 40, 27–67, doi:10.1080/02786820500421521, 2006.

- Bösenberg, J.: EARLINET: A European Aerosol Research Lidar Network to Establish an Aerosol Climatology, Max-Planck-Institut Report No. 348, 2003.
- Bösenberg, J. and Hoff, R.: Plan for the implementation of the GAW Aerosol Lidar Observation Network GALION, GAW report 178, World Meteorological Organization, Hamburg, Germany, 2007.
- Chaikovsky, A., Dubovik, O., Goloub, P., Tanré, D., Chaikovskaya, L., Denisov, S., Grudo, Y., Lopatsin, A., Karol, Y., Lapyonok, T., Korol, M., Osipenko, F., Savitski, D., and Slesar, A.: Combined lidar and radiometric sounding of atmospheric aerosol: algorithm of data processing, software, dissemination, in: Proceedings of XVIII International symposium "Atmospheric and ocean optics. Atmosphere physics ", Irkutsk, Russian Federation, 2—6 July, pp. C1—C4, 2012.
- Chaikovsky, A. P., Ivanov, A. P., Balin, Y. S., Elnikov, A. V., Tulinov, G. F., Plusnin, I. I., Bukin, O. A., and Chen, B. B.: CIS-LiNet lidar network for monitoring aerosol and ozone: methodology and instrumentation, *Atmospheric and oceanic optics*, 18, 2005.
- Chanine, M.: Determination of the Temperature Profile in an Atmosphere from its Outgoing Radiance, *J. Opt. Soc. Am.*, 58, 1634–1637, doi:10.1364/JOSA.58.001634, URL <http://www.opticsinfobase.org/abstract.cfm?URI=josa-58-12-1634>, 1968.
- Chowdhary, J., Cairns, B., Mishchenko, M., Hobbs, P., Cota, G., Redemann, J., Rutledge, K., Holben, B., and Russell, E.: Retrieval of Aerosol Scattering and Absorption Properties from Photopolarimetric Observations over the Ocean during the CLAMS Experiment, *Journal of the Atmospheric Sciences*, 62, 1093–1117, doi:10.1175/JAS3389.1, 2005.
- Cooke, W. F., Lioussé, C., Cachier, H., and Feichter, J.: Construction of a $1^\circ \times 1^\circ$ fossil fuel emission data set for carbonaceous aerosol and implementation and radiative impact in the ECHAM4 model, *J. Geophys. Res.*, 104(D18), 22 137–22 162, 1999.
- Cuesta, J., Flamant, H. P., and Flamant, C.: Synergetic technique combining elastic backscatter lidar data and sunphotometer AERONET inversion for retrieval by layer of aerosol optical and microphysical properties, *APPLIED OPTICS*, 47, 4598–4611, 2008.
- Davis, D. L., Bell, M. L., , and Fletcher, T.: A look back at the London smog of 1952 and the half century since, *Environ. Health Perspect.*, 110, 734–735, 2002.
- Deschamps, P.-Y., Breon, F.-M., Leroy, M., Podaire, A., Bricaud, A., Buriez, J.-C., and Seze, G.: The POLDER mission: instrument characteristics and scientific objectives, *Geoscience and Remote Sensing, IEEE*, 32, 598–615, 1994.
- Diner, D., Beckert, J., Reilly, T., Bruegge, C., Conel, J., Kahn, R., Martonchik, J., Ackerman, T., Davies, R., Gerstl, S., Gordon, H., Muller, J.-P., Myneni,

- R., Sellers, R., Pinty, B., and Verstraete, M.: Multi-angle Imaging Spectro-Radiometer (MISR) description and experiment overview, *IEEE Trans. Geosci. Rem. Sens.*, 36(4), 1072–1087, 1998.
- Donaldson, K., Stone, V., Seaton, A., and MacNee, W.: Ambient particle inhalation and the cardiovascular system : potential mechanisms, *Environ. Health Perspect.*, 109, 523–527, 2001.
- Dubovik, O.: Optimization of Numerical Inversion in Photopolarimetric Remote Sensing, in: *Photopolarimetry in Remote Sensing*, edited by Videen, G., Yatskiv, Y., and Mishchenko, M., pp. 65–106, Kluwer Academic Publishers, Dordrecht, The Netherlands, 2004.
- Dubovik, O. and King, M.: A flexible inversion algorithm for retrieval of aerosol optical properties from Sun and sky radiance measurements, *Journal of Geophysical Research*, 105, 20 673–20 696, 2000.
- Dubovik, O., Yokota, T., and Sasano, Y.: Improved technique for data inversion and its application to the retrieval algorithm for ADEOS/I-LAS, *Advances in Space Research*, 21, 397 – 403, doi:[http://dx.doi.org/10.1016/S0273-1177\(97\)00920-4](http://dx.doi.org/10.1016/S0273-1177(97)00920-4), URL <http://www.sciencedirect.com/science/article/pii/S0273117797009204>, 1998.
- Dubovik, O., Smirnov, A., Holben, B., King, M., Kaufman, Y., Eck, T., and Slutsker, I.: Accuracy assessments of aerosol optical properties retrieved from Aerosol Robotic Network (AERONET) Sun and sky radiance measurements, *Journal of Geophysical Research*, 105, doi:10.1029/2000JD900040, 2000.
- Dubovik, O., Holben, B., Eck, T., Smirnov, A., Kaufman, Y., King, M., Tanré, D., and Slutsker, I.: Variability of Absorption and Optical Properties of Key Aerosol Types Observed in Worldwide Locations, *J. Atmos. Sci.*, 59, 590–608, doi:10.1175/1520-0469(2002)059<0590:VOAAOP>2.0.CO;2, 2002a.
- Dubovik, O., Holben, B. N., Lapyonok, T., Sinyuk, A., Mishchenko, M. I., Yang, P., and Slutsker, I.: Non-spherical aerosol retrieval method employing light scattering by spheroids, *Geophys. Res. Lett.*, 10, doi:10.1029/2001GL014506, 2002b.
- Dubovik, O., Sinyuk, A., Lapyonok, T., Holben, B. N., Mishchenko, M., Yang, P., Eck, T. F., Volten, H., Munoz, O., Veihelmann, B., van der Zander, W., Sorokin, M., and Slutsker, I.: Application of light scattering by spheroids for accounting for particle non-sphericity in remote sensing of desert dust, *J. Geophys. Res.*, 111, doi:10.1029/2005D006619, 2006.
- Eck, T. F., Holben, B. N., Reid, J. S., Dubovik, O., Smirnov, A., O’Neill, N. T., Slutsker, I., and Kinne, S.: Wavelength dependence of the optical depth of biomass burning, urban, and desert dust aerosols, *J. Geophys. Res.*, 104, 31 333–31 349, doi:10.1029/1999JD900923, 1999.
- Flagan, R.: History of Electrical Aerosol Measurements, *Aerosol Science and Technology*, 28, 301–380, doi:10.1080/02786829808965530, 1998.

- Frenkel, J.: A theory of the fundamental phenomena of atmospheric electricity, *Journal of Physics*, 8, 285–304, 1944.
- Gäggeler, H. W., Baltensperger, U., Emmenegger, M., Jost, D. T., Schmidt-Ott, A., Haller, P., and Hofmann, M.: The epiphaniometer, a new device for continuous aerosol monitoring, *Journal of Aerosol Science*, 20, 557–564, URL <http://www.sciencedirect.com/science/article/pii/0021850289901018>, 1989.
- Gong, S., Barrie, L., Blanchet, J.-P., and Spacek, L.: Modeling size-distributed sea salt aerosols in the atmosphere: An application using Canadian climate models, in: *Air Pollution Modeling and Its Applications XII*, edited by Gryning, S.-E. and Chaumerliac, N., Plenum Press, New York, 1998.
- Graf, H.-F., Feichter, J., and Langmann, B.: Volcanic sulphur emissions: Estimates of source strength and its contribution to the global sulphate distribution, *J. Geophys. Res.*, 102, 10 72710 738, 1997.
- Hansen, J., Sato, M., and Ruedy, R.: Radiative forcing and climate response, *Journal of Geophysical Research*, 102, 6831–6864, doi:10.1029/96JD03436, 1997.
- Havers, N., Burba, P., Lambert, J., and Klockow, D.: Spectroscopic Characterization of Humic-Like Substances in Airborne Particulate Matter, *Journal of Atmospheric Chemistry*, 29, 45–54, URL <http://dx.doi.org/10.1023/A:1005875225800>, 10.1023/A:1005875225800, 1998.
- Haywood, J. and Boucher, O.: Estimates of the direct and indirect radiative forcing due to tropospheric aerosols: A review, *Reviews of Geophysics*, 38, 513–543, 2000.
- Haywood, J. and Ramaswamy, V.: Global sensitivity studies of the direct radiative forcing due to anthropogenic sulfate and black carbon aerosols, *Journal of Geophysical Research*, 103, 6043–6058, doi:10.1029/97JD03426, 1998.
- Herman, J., Bhartia, P. K., Torres, O., Hsu, C., Seftor, C., and Celarier, E.: Global distributions of UV-absorbing aerosols from Nimbus 7/TOMS data, *J. Geophys. Res.*, 102, 16 911 –16 923, 1997.
- Hess, M., Koepke, P., and Schult, I.: Optical Properties of Aerosols and Clouds: The Software Package OPAC., *Bulletin of the American Meteorological Society*, 79, 831–844, 1998.
- Hinds, W.: *Aerosol Technology: Properties, Behavior, and Measurement of Airborne Particles* (Wiley-Interscience), Wiley-Interscience, 1999.
- Holben, B., Eck, T., Slutsker, I., Tanré, D., Buis, J., Setzer, A., Vermote, E., Reagan, J., Kaufman, Y., Nakajima, T., Lavenu, F., Jankowiak, I., and Smirnov, A.: AERONET - A Federated Instrument Network and Data Archive for Aerosol Characterization, *Remote Sensing of Environment*, 66, 1 – 16, doi:10.1016/S0034-4257(98)00031-5, URL <http://www.sciencedirect.com/science/article/pii/S0034425798000315>, 1998.

- Holben, B., Eck, T., Schafer, J., Giles, D., and Sorokin, M.: Distributed Regional Aerosol Gridded Observation Networks (DRAGON) White Paper, available from http://aeronet.gsfc.nasa.gov/new_web/dragon.html, 2011.
- Huebert, B., Bates, T., Russell, P., Shi, G., Kim, Y., Kawamura, K., Carmichael, G., and Nakajima, T.: An overview of ACE-Asia: Strategies for quantifying the relationships between Asian aerosols and their climatic impacts, *Journal of Geophysical Research*, 108, 8633, doi:10.1029/2003JD003550, 2003.
- Ichoku, C., Levy, R., Kaufman, Y., Remer, L., Li, R.-R., Martins, V., Holben, B., Abuhassan, N., Slutsker, I., Eck, T., and Pietras, C.: Analysis of the performance characteristics of the five-channel Microtops II Sun photometer for measuring aerosol optical thickness and precipitable water vapor, *Journal of Geophysical Research*, 107, 4179, doi:10.1029/2001jd001302, 2002.
- InVS/Afsse: Estimation de l'impact sanitaire d'une pollution environnementale et évaluation quantitative des risques sanitaires, Tech. Rep. 157 p., Ed. InVS/Afsse, 2005.
- IPCC: Climate Change 2001 : The Scientific Basis, Cambridge University Press, 2001.
- IPCC: Climate Change 2007: The Physical Science Basis, Cambridge University Press, 2007.
- Jacobson, M. Z.: Global direct radiative forcing due to multicomponent anthropogenic and natural aerosols, *J. Geophys. Res.*, 106, 1551–1568, doi:10.1029/2000JD900514, URL <http://dx.doi.org/10.1029/2000JD900514>, 2001.
- Jones, A., Roberts, D. L., and Slingo, A.: A climate model study of indirect radiative forcing by anthropogenic sulphate aerosols, *Nature*, 370, 450–453, URL <http://dx.doi.org/10.1038/370450a0>, 1994.
- Junge, C. E.: The size distribution and aging of natural aerosols as determined from electrical and optical data on the atmosphere, *J. Meteorol.*, 12, 13–25, 1955.
- Junge, C. E.: Air chemistry and radioactivity, vol. 4 of *International Geophysics Series*, Academic Press, 1963.
- Kacenenbogen, M.: Application de la télédétection spatiale à la surveillance de la pollution en aérosols, Ph.D. thesis, Université de Lille 1, Villeneuve d'Ascq, France, 2008.
- Kahn, R., Gaitley, B., Garay, M., Diner, D., Eck, T., Smirnov, A., and Holben, B.: Multiangle Imaging SpectroRadiometer global aerosol product assessment by comparison with the Aerosol Robotic Network, *Journal of Geophysical Research*, 115, D23 209, doi:10.1029/2010JD014601, 2010.
- Kalman, R.: A new approach to linear filtering and prediction problems, *Journal of Basic Engineering*, 82, 35–45, doi:10.1115/1.3662552, 1960.

- Karol, Y., Tanré, D., Goloub, P., Ververaerde, C., Balois, J. Y., Blarel, L., Podvin, T., Mortier, A., and Chaikovskiy, A.: Airborne sun photometer PLASMA: concept, measurements, comparison of aerosol extinction vertical profile with lidar, *Atmospheric Measurement Techniques*, 6, 2383–2389, doi:10.5194/amt-6-2383-2013, URL <http://www.atmos-meas-tech.net/6/2383/2013/>, 2013.
- Kaufman, Y. J., Tanré, D., and Boucher, O.: A satellite view of aerosols in the climate system, *Nature*, 419, 215–223, URL <http://www.nature.com/nature/journal/v419/n6903/full/nature01091.html?lang=en>, 2002.
- King, M. D., Byrne, D. M., Herman, B. M., and Reagan, J. A.: Aerosol Size Distributions Obtained by Inversions of Spectral Optical Depth Measurements, *Journal of the Atmospheric Sciences*, 35, 2153–2167, doi:10.1175/1520-0469(1978)035<2153:ASDOBI>2.0.CO;2, URL [http://dx.doi.org/10.1175/1520-0469\(1978\)035<2153:ASDOBI>2.0.CO;2](http://dx.doi.org/10.1175/1520-0469(1978)035<2153:ASDOBI>2.0.CO;2), 1978.
- Kummerow, C., Simpson, J., Thiele, O., Barnes, W., Chang, A. T. C., Stocker, E., Adler, R. F., Hou, A., Kakar, R., Wentz, F., Ashcroft, P., Kozu, T., Hong, Y., Okamoto, K., Iguchi, T., Kuroiwa, H., Im, E., Haddad, Z., Huffman, G., Ferrier, B., Olson, W. S., Zipser, E., Smith, E. A., Wilhelm, T. T., North, G., Krishnamurti, T., and Nakamura, K.: The Status of the Tropical Rainfall Measuring Mission (TRMM) after Two Years in Orbit, *Journal of Applied Meteorology*, 39, 1965–1982, doi:10.1175/1520-0450(2001)040<1965:TSOTTR>2.0.CO;2, URL [http://dx.doi.org/10.1175/1520-0450\(2001\)040<1965:TSOTTR>2.0.CO;2](http://dx.doi.org/10.1175/1520-0450(2001)040<1965:TSOTTR>2.0.CO;2), 2000.
- Lacis, A. A. and Mishchenko, M. I.: Climate forcing, sensitivity and response, in: *Aerosol forcing of climate*, edited by Charlson, R. J. and Heintzenberg, J., pp. 11–42, John Wiley, New York, 1995.
- Lenoble, J., Remer, J., Remer, L., and Tanre, D.: *Aerosol Remote Sensing*, Springer Praxis Books, Springer London, Limited, URL <http://books.google.by/books?id=QeWvkgEACAAJ>, 2011.
- Léon, J., Derimian, Y., Chiapello, I., Tanré, D., Podvin, T., Chatenet, B., Diallo, A., and Deroo, C.: Aerosol vertical distribution and optical properties over M’Bour, Senegal from 2006 to 2008, *Atmospheric Chemistry and Physics*, 9(23), 9249–9261, 2009.
- Levelt, P. F., Hilsenrath, E., Leppelmeier, G. W., van den Oord, G. H. J., Bhartia, P. K., de Haan, J. T. J. F., and Veefkind, J. P.: Science objectives of the Ozone Monitoring Instrument, *IEEE Trans. Geosci. Remote Sens.*, 44(5), 1093–1101, 2006.
- Liao, D., Creason, J., Shy, C., Williams, R., Watts, R., and Zweidinger, R.: Daily variation of particulate air pollution and poor cardiac autonomic control in the elderly, *Environ. Health Perspect.*, 107, 521–525, 1999.

- Liu, B. Y., Romay, F. J., Dick, W. D., Woo, K.-S., and Chiruta, M.: A Wide-Range Particle Spectrometer for Aerosol Measurement from 0.010 μm to 10 μm , *Aerosol and Air Quality Research*, 10, 125–139, 2010.
- Lopatin, A., Dubovik, O., Chaikovsky, A., Goloub, P., Lapyonok, T., Tanré, D., and Litvinov, P.: Enhancement of aerosol characterization using synergy of lidar and sun-photometer coincident observations: the GARRLiC algorithm, *Atmospheric Measurement Techniques*, 6, 2065–2088, doi:10.5194/amt-6-2065-2013, URL <http://www.atmos-meas-tech.net/6/2065/2013/>, 2013.
- Lyapustin, A., Gatebe, C. K., Kahn, R., Brandt, R., Redemann, J., Russell, P., King, M. D., Pedersen, C. A., Gerland, S., Poudyal, R., Marshak, A., Wang, Y., Schaaf, C., Hall, D., and Kokhanovsky, A.: Analysis of snow bidirectional reflectance from ARCTAS spring-2008 campaign, *Atmos. Chem. Phys.*, 10, 4359–4375, 2010.
- Marple, V. A., Rubow, K. L., and Behm, S. M.: A Microorifice Uniform Deposit Impactor (MOUDI): Description, Calibration, and Use, *Aerosol Science and Technology*, 14, 434–446, 1991.
- Marticorena, B., Bergametti, G., Aumont, B., Callot, Y., Ndoume, C., and Legrand, M.: Modeling the atmospheric dust cycle. 2. Simulation of Saharan dust sources, *J. Geophys. Res. Atmos.*, 102, 43874404, 1997.
- Matsumoto, T., Russell, P., Mina, C., Ark, W. V., and Banta, V.: Airborne Tracking Sunphotometer, *J. Atmos. Ocean . Tech.*, 4, 336–339, 1987.
- McCartney, E. J.: *Optics of the Atmosphere*, Wiley, New York, 1976.
- McMurry, P.: The history of CPCs, *Aerosol Sci. Technol.*, 33, 297–322, 2000a.
- McMurry, P.: A review of atmospheric aerosol measurements, *Atmospheric Environment*, 34, 1959–1999, doi:10.1016/S1352-2310(99)00455-0, 2000b.
- Mészáros, E.: *Fundamentals of atmospheric aerosol chemistry*, Akadémiai Kiadó, Budapest, 1999.
- Miller, R. L. and Tegen, I.: Climate Response to Soil Dust Aerosols, *Journal of Climate*, 11, 3247–3267, doi:10.1175/1520-0442(1998)011<3247:CRTSDA>2.0.CO;2, URL [http://dx.doi.org/10.1175/1520-0442\(1998\)011<3247:CRTSDA>2.0.CO;2](http://dx.doi.org/10.1175/1520-0442(1998)011<3247:CRTSDA>2.0.CO;2), 1998.
- Millikan, R. A.: The Isolation of an Ion, a Precision Measurement of its Charge, and the Correction of Stokes’s Law, *Science*, 32, 436–448, doi:10.1126/science.32.822.436, URL <http://www.sciencemag.org/content/32/822/436.short>, 1910.
- Mortier, A., Goloub, P., Holben, B., Podvin, T., Blarel, L., Verwaerde, C., Karol, Y., Slutsker, I., Balois, J.-Y., Tanre, D., Berkoff, T., Victori, S., and Mathieu, R.: Aerosol Spatial Distribution during DRAGON experiment as seen by a mobile ground-based LIDAR-sunphotometer system-Preliminary results, in:

- Reviewed and revised papers of the 26th International Lidar Radar Conference, pp. 411–414, Porto Heli, Peloponnesus, Greece, 2012.
- Morys, M., Forrest, Hagerup, S., Anderson, S., Baker, A., Kia, J., and Walkup, T.: Design, calibration, and performance of MICROTOPS II handheld ozone monitor and Sun photometer, *Journal of Geophysical Research*, 106, 14573–14582, 2001.
- Mulot, J. U., Baeza, A., Blanchard, O., Delmas, V., Elichegaray, C., Lefranc, A., Ramel, M., Slama, R., and Vendel, J.: Pollution par les particules dans l'air ambiant. Synthèses des éléments sanitaires en vue d'un appui à l'élaboration de seuils d'information et d'alerte du public pour les particules dans l'air ambiant., Rapport d'expertise collective de l'AFFSET, 2009.
- Nash, D. G., Baer, T., and Johnston, M. V.: Aerosol mass spectrometry: An introductory review, *International Journal of Mass Spectrometry*, 258, 2 – 12, doi: 10.1016/j.ijms.2006.09.017, URL <http://www.sciencedirect.com/science/article/pii/S1387380606004362>, 2006.
- Pelon, J., Mallet, M., Mariscal, A., Goloub, P., Tanré, D., Karam, D. B., Flamant, C., Haywood, J., Pospichal, B., and Victori, S.: Microlidar observations of biomass burning aerosol over Djougou (Benin) during African Monsoon Multi-disciplinary Analysis Special Observation Period 0: Dust and Biomass-Burning Experiment, *J. Geophys. Res.*, 113, D00C18, doi:10.1029/2008JD009976, 2008.
- Penner, J. E., Chuang, C. C., and Grant, K.: Climate forcing by carbonaceous and sulfate aerosols, *Climate Dynamics*, 14, 839–851, URL <http://dx.doi.org/10.1007/s003820050259>, 10.1007/s003820050259, 1998.
- Penner, J. E., Hegg, D., and Leaitch, R.: Unravelling the role of aerosols in climate change, *Environ. Sci. Technol.*, 35, 332 A–340 A, 2001.
- Philips, D.: A technique for the numerical solution of certain integral equations of the first kind, *J. Assoc. Comp. Mach.*, 9, 84–97, 1962.
- Pincus, R. and Baker, M.: Effect of precipitation on the albedo susceptibility of clouds in the marine boundary layer, *Nature*, 372, 250–252, doi:10.1038/372250a0, 1994.
- Ramanathan, V., Crutzen, P., Kiehl, J., and Rosenfeld, D.: Aerosols, Climate, and the Hydrological Cycle, *Science*, 294, 2119–2124, doi:10.1126/science.1064034, 2001.
- Ramgolam, K., Favez, O., Cachier, H., Gaudichet, A., Marano, F., Martinon, L., and Baeza-Squiban, A.: Size-partitioning of an urban aerosol to identify particle determinants involved in the proinflammatory response induced in airway epithelial cells, *Particle and Fibre Toxicology*, 6, 10, doi:10.1186/1743-8977-6-10, 2009.
- Remer, L. and Kaufman, Y.: Dynamic aerosol model: Urban/industrial aerosol, *Journal of Geophysical Research*, 103, doi:10.1029/98JD00994, 1998.

- Remer, L., Kaufman, Y., Tanré, D., Mattoo, S., Chu, D., Martins, J., Li, R., Ichoku, C., Levy, R., Kleidman, R., Eck, T., Vermote, E., and Holben, B.: The MODIS Aerosol Algorithm, Products, and Validation, *Journal of the Atmospheric Sciences*, 62, 947–973, doi:10.1175/JAS3385.1, 2005.
- Rocadenbosch, F., Mattis, I., Ansmann, A., Wandinger, U., Bockmann, C., Pappalardo, G., Amodeo, A., Bosenberg, J., Alados-Arboledas, L., Apituley, A., Balis, D., Chaikovsky, A., Comeron, A., Munoz, C., Sicard, M., Freudenthaler, V., Wiegner, M., Gustafsson, O., Hansen, G., Mamouri, R.-E., Papayannis, A., Mitev, V., Nicolae, D., Perez, C., Perrone, M., Pietruczuk, A., Pujadas, M., Putaud, J.-P., Ravetta, F., Rizi, V., Simeonov, V., Spinelli, N., Stoyanov, D., and Trickl, T.: The European Aerosol Research Lidar Network (EARLINET): An Overview, in: *Geoscience and Remote Sensing Symposium, 2008. IGARSS 2008. IEEE International*, vol. 2, pp. II-410 –II-413, doi:10.1109/IGARSS.2008.4779015, 2008.
- Rodgers, C. D.: Retrieval of Atmospheric Temperature and Composition From Remote Measurements of Thermal Radiation, *Rev. Geophys. and Space Phys.*, 14, 609 – 624, 1976.
- Russell, P. B., Livingston, J. M., Dubovik, O., Ramirez, S. A., Wang, J., Redemann, J., Schmid, B., Box, M., and Holben, B. N.: Sunlight transmission through desert dust and marine aerosols: Diffuse light corrections to Sun photometry and pyr heliometry, *J. Geophys. Res.*, 109, D08 207, doi: 10.1029/2003JD004292, 2004.
- Schmid, B., Livingston, J. M., Russell, P. B., Durkee, P. A., Jonsson, H. H., Collins, D. R., Flagan, R. C., Seinfeld, J. H., Gassó, S., Hegg, D. A., Öström, E., Noone, K. J., Welton, E. J., Voss, K. J., Gordon, H. R., Formenti, P., and Andreae, M. O.: Clear sky closure studies of lower tropospheric aerosol and water vapor during ACE-2 using airborne sunphotometer, airborne in-situ, space-borne, and ground-based measurements, *Tellus B*, 52, 568–593, 2000.
- Schmid, B., Redemann, J., Russell, P., Hobbs, P., Hlavka, D., McGill, M., Holben, B., Welton, E., Campbell, J., Torres, O., Kahn, R., Diner, D., Helmlinger, M., Chu, D., Robles-Gonzalez, C., and de Leeuw, G.: Coordinated airborne, spaceborne, and ground-based measurements of massive thick aerosol layers during the dry season in southern Africa, *Journal of Geophysical Research - Atmospheres*, 108, 8496, doi:10.1029/2002JD002297, 2003.
- Schnell, R. C. and Vali, G.: Biogenic ice nuclei: Part I. Terrestrial and marine sources, *J. Atmos. Sci.*, 33, 15541564, 1976.
- Schuster, G. L., Dubovik, O., and Holben, B. N.: Angstrom exponent and bimodal aerosol size distributions, *J. Geophys. Res.*, 111, D07 207, doi:10.1029/2005JD006328, URL <http://dx.doi.org/10.1029/2005JD006328>, 2006.
- Schutz, B. E., Zwally, H. J., Shuman, C. A., Hancock, D., and DiMarzio, J. P.: Overview of the ICESat Mission, *Geophys. Res. Lett.*, 32, L21S01, doi:10.1029/2005GL024009, URL <http://dx.doi.org/10.1029/2005GL024009>, 2005.

- Shaw, G.: Sun Photometry, *Bulletin of the American Meteorological Society*, 64, 4–10, doi:10.1175/1520-0477(1983)064<0004:SP>2.0.CO;2, 1983.
- Shaw, G. E., Reagan, J. A., and Herman, B. M.: Investigations of atmospheric extinction using direct solar radiation measurements made with multiple wavelength radiometer, *J. Appl. Meteor.*, 12 374, 1973.
- Shettle, E. P. and Fenn, R. W.: Models of aerosols of lower troposphere and the effect of humidity variations on their optical properties, AFCRL Tech. Rep. 79 0214, 100 pp., Air Force Cambridge Res. Lab., Hanscom, Air Force Base, Mass., 1979.
- Sinyuk, A., Dubovik, O., Holben, B., Eck, T. F., Breon, F.-M., Martonchik, J., Kahn, R., Diner, D. J., Vermote, E. F., Roger, J.-C., Lapyonok, T., and Slutsker, I.: Simultaneous retrieval of aerosol and surface properties from a combination of AERONET and satellite data, *Remote Sensing of Environment*, 107, 90 – 108, doi:http://dx.doi.org/10.1016/j.rse.2006.07.022, URL <http://www.sciencedirect.com/science/article/pii/S0034425706004111>, 2007.
- Sokolik, I. N. and Toon, O. B.: Incorporation of mineralogical composition into models of the radiative properties of mineral aerosol from UV to IR wavelengths, *J. Geophys. Res.*, 104, 9423–9444, doi:10.1029/1998JD200048, URL <http://dx.doi.org/10.1029/1998JD200048>, 1999.
- Stenchikov, G., Kirchner, I., Robock, A., Graf, H.-F., Antuña, J., Grainger, R., Lambert, A., and Thomason, L.: Radiative forcing from the 1991 Mount Pinatubo volcanic eruption, *Journal of Geophysical Research*, 103, 13 837–13 857, doi:10.1029/98JD00693, 1998.
- Stowe, L. L., Carey, R. M., and Pellegrino, P. P.: Monitoring the Mt. Pinatubo aerosol layer with NOAA/AVHRR data, *Remote Sens. Environ.*, 60, 22–34, 1992.
- Strand, O. N. and Westwater, E. R.: Statistical Estimation of the Numerical Solution of a Fredholm Integral Equation of the First Kind, *J. Assoc. Comp. Mach.*, 15, doi:10.1145/321439.321445, 1968.
- Stull, R. B.: An introduction to boundary layer meteorology, Kluwer Academic Publishers, Dordrecht, 1988.
- Sun, D. and Pinker, R.: Retrieval of surface temperature from the MSG-SEVIRI observations: Part I. Methodology, *International Journal of Remote Sensing*, 28, 5255–5272, doi:10.1080/01431160701253246, 2007.
- Tanré, D., Deroo, C., Duhaut, P., Herman, M., Morcrette, J., Perbos, J., and Deschamps, P.: Description of a computer code to simulate the satellite signal in the solar spectrum: the 5S Code, *Int. J. Remote Sensing*, 11, 659–668, 1990.
- Tanré, D., Kaufman, Y. J., Holben, B. N., Chatenet, B., Karnieli, A., Lavenue, F., Blarel, L., Dubovik, O., Remer, L. A., and Smirnov, A.: Climatology of dust aerosol size distribution and optical properties derived from remotely sensed data in the solar spectrum, *J. Geophys. Res.*, 106(D16), 18 205–18 217, 2001.

- Tanré, D., Bréon, F. M., Deuzé, J. L., Dubovik, O., Ducos, F., François, P., Goloub, P., Herman, M., Lifermann, A., and Waquet, F.: Remote sensing of aerosols by using polarized, directional and spectral measurements within the A-Train: the PARASOL mission, *Atmospheric Measurement Techniques*, 4, 1383–1395, doi:10.5194/amt-4-1383-2011, URL <http://www.atmos-meas-tech.net/4/1383/2011/>, 2011.
- Tegen, I., Lacis, A., and Fung, I.: The influence on climate forcing of mineral aerosols from disturbed soils, *Nature*, 380, 419–422, doi:10.1038/380419a0, 1996.
- ten Brink, H. M., Veefkind, J. P., Waijers-Ijpelaan, A., and van der Hage, J. C.: Aerosol light-scattering in the Netherlands, *Atmos. Environ.*, 30, 4251–4261, 1996.
- Tikhonov, A. N.: On the solution of ill-posed problems and the method of regularization, *Dokl. Akad. Nauk SSSR*, 151, 1963.
- Turchin, V. and Nozik, V.: Statistical regularization of solution of noncorrect problems, *Izv. Akad. Nauk SSSR, Ser. Fiz. Atmos. Okeana*, 5, 1969.
- Twomey, S.: On the Numerical Solution of Fredholm Integral Equations of the First Kind by the Inversion of the Linear System Produced by Quadrature, *J. ACM*, 10, 97–101, doi:10.1145/321150.321157, 1963.
- Twomey, S.: Pollution and the planetary albedo, *Atmospheric Environment* (1967), 8, 1251–1256, doi:10.1016/0004-6981(74)90004-3, 1974.
- Twomey, S.: Comparison of constrained linear inversion and an iterative nonlinear algorithm applied to the indirect estimation of particle size distributions, *Journal of Computational Physics*, 18, 188–200, doi:10.1016/0021-9991(75)90028-5, 1975.
- Veefkind, J. P.: Aerosol Satellite Remote Sensing, Ph.D. thesis, Universiteit Utrecht, 1999.
- Volckens, J. and Peters, T.: Counting and particle transmission efficiency of the aerodynamic particle sizer, *Journal of Aerosol Science*, 36, 1400–1408, doi:10.1016/j.jaerosci.2005.03.009, 2005.
- Waquet, F., Cairns, B., Knobelspiesse, K., Chowdhary, J., Travis, L., Schmid, B., and Mishchenko, M.: Polarimetric remote sensing of aerosols over land, *Journal of Geophysical Research*, 114, D01 206, doi:10.1029/2008JD010619, 2009.
- Weber, R., McMurry, P., Mauldin III, R., Tanner, D., Eisele, F., Clarke, A., and Kapustin, V.: New particle formation in the remote troposphere: A comparison of observations at various sites, *Geophys. Res. Lett.*, 26, 307–310, 1999.
- Welton, E. J., Campbell, J. D. S., and Scott, V. S.: Global monitoring of clouds and aerosols using a network of micro-pulse lidar systems, in *Lidar Remote Sensing for Industry and Environmental Monitoring*, Proc. SPIE, 4153, 151–158, 2001.

- Whitby, K.: The physical characteristics of sulfate aerosols, *Atmospheric Environment*, 12, 135–159, 1978.
- Wilson, C. T. R.: On the ionisation of atmospheric air, Royal Soc., London, 1901.
- Winker, D., Pelon, J., Coakley, J., Ackerman, S., Charlson, R., Colarco, P., Flamant, P., Fu, Q., Hoff, R., Kittaka, C., Kubar, T., Le Treut, H., McCormick, M., Mégie, G., Poole, L., Powell, K., Trepte, C., Vaughan, M., and Wielicki, B.: The CALIPSO Mission: A Global 3D View of Aerosols and Clouds, *Bulletin of the American Meteorological Society*, 91, 1211–1229, doi:10.1175/2010BAMS3009.1, 2010.
- Winker, D. M., Couch, R. H., and McCormick, M. P.: An overview of LITE: NASA's Lidar In-space Technology Experiment, *Proc. IEEE*, 84, 164–180, 1996.
- WMO/GAW: Strategic Plan: 2008-2015 - A Contribution to the Implementation of the WMO Strategic Plan: 2008-2011 (WMO TD No. 1384), GAW report 172, World Meteorological Organization, 2007.
- Zhao, F., Tan, Y., Li, Z., and Gai, C.: The effect and correction of aerosol forward scattering on retrieval of aerosol optical depth from Sun photometer measurements, *Geophysical Research Letters*, doi:10.1029/2012GL052135, 2012.
- Zieger, P., Ruhtz, T., Preusker, R., and Fischer, J.: Dual-aureole and sun spectrometer system for airborne measurements of aerosol optical properties, *Appl. Opt.*, 46, 8542–8552, doi:10.1364/AO.46.008542, URL <http://ao.osa.org/abstract.cfm?URI=ao-46-35-8542>, 2007.